UNIVERSITÀ DI PARMA

UNIVERSITA' DEGLI STUDI DI PARMA

DOTTORATO DI RICERCA IN
Scienza e Tecnologia dei Materiali

CICLO XXXVI

Development of bioactive bioceramics as delivery systems for regenerative medicine

Coordinatore:
Chiar.mo Prof. Enrico Dalcanale

Tutore:
Dr. Simone Sprio
Co-tutore:
Dr. Ing. Massimiliano Dapporto

Dottoranda: *Marta Tavoni, M. sc*

Anni Accademici 2020/2021 – 2022/2023

AIM OF THE WORK

Bone disorders associated with traumas or degenerative diseases, including osteoporosis, bone infections, and tumors, are major causes of pain, disability, mortality, and are steadily increasing in the worldwide population, representing a critical clinical problem.

A common approach for the treatment of these conditions involves systemic drug administration and eventually the surgical removal of damaged bone. Hence, the main goal is repairing the affected bone and providing effective medical treatments. However, such an approach features various problems related to systemic drug administration, such as the need of large doses to achieve effective local drug concentration, which can yield toxicity and other side-effects. Hence, new methods to provide drug accumulation in the target anatomical district are greatly needed and explored. In such a context the present work is dedicated to the design and development of bioactive porous bioceramic scaffolds as drug delivery systems, aimed to develop new effective therapies for the treatment of various bone disorders and diseases. It has been carried out at the Institute of Science, Technology and Sustainability for Ceramics, belonging to the National Research Council of Italy (ISSMC-CNR), during my PhD in Materials Science and Technology.

Bone tissue regeneration requires the use of three-dimensional porous scaffolds able to provide physiological cell response and permit the regrowth of new healthy bone tissue. In this context, substantial research over the last decades has been devoted to the development of scaffolds based on calcium phosphate (CaP) and hydroxyapatite (HA), as elective materials to combine bioactivity, osteointegration and tissue regeneration, thanks to their mimicry with the bone mineral phase. In the present work different types of CaP-based scaffolds have been developed depending on the specific bone district of interest, particularly: macroporous sintered scaffolds (particularly suitable in cranioplasty and maxillofacial surgery), bone cements (that can be used in minimally invasive surgery such as vertebroplasty and spinal fusion or as bone filler or in procedures of joint replacement), biomorphic scaffolds (designed for the regeneration of load-bearing bone segments), and 3D-printed scaffold (to regenerate bone defects with complex morphology).

After a general introduction on bone tissue physiology and an overview of the analytical methods involved in the research (Chapter 1 and Chapter 2, respectively), this thesis focuses on the preparation of the above-mentioned calcium phosphate bone scaffolds as drug delivery systems to favour the regeneration of bone tissue, while also releasing biomolecules with therapeutic actions.

In particular, Chapter 3 describes the preparation of macroporous sintered scaffolds by direct foaming, a template-free processing technique capable of providing open and interconnected macroporosity, useful to enhance osteointegration and also for the delivery of antibiotics. Chapter 4 is dedicated to the development of apatitic bone cements, obtained by appositely synthesized self-hardening pastes, able to set in physiological conditions and characterized by diffuse microporosity, suitable for bone anchoring and for the local delivery of various therapeutics, where optimizing the drug loading was optimized depending on the chemical properties of the drug. Finally, Chapter 5 describes the functionalization of biomorphic scaffolds (kindly provided by *GreenBone Ortho S.p.A*), characterized by hierarchically organized structure and porosity, with anticancer drugs.

In addition, in the present work I correlated the physico-chemical and microstructural properties of scaffolds with the mechanisms underlying the drug release in the various scaffolds. In this respect, the experimental data were fitted by semi-empirical mathematical models (i.e., Korsmeyer-Peppas model).

DEVELOPMENT OF BIOACTIVE BIOCERAMICS AS DELIVERY SYSTEMS FOR REGENERATIVE MEDICINE

TABLE OF CONTENT

FIGURE INDEX

TABLE INDEX

List of Acronyms

ACP: Amorphous Calcium Phosphate

AIOM: Italian Association of Medical Oncology

AIRC: Italian Association for Cancer Research

ANOVA: One-Way Analysis of Variance Test

API: Active Pharmaceutic Ingredient

BET: Brunauer–Emmett–Teller Theory

BM: Bone metastasis

BTE: Bone Tissue Engineering

BTR: Bone Tissue Regeneration

Caki-2: human clear cell renal cell carcinoma

CaP/CaPs: Calcium Phosphate(s)

CaP-Ac: Calcium Phosphate Nanoparticles Stabilized with Acetate

CaPCO: Carbonated Calcium Phosphate Nanoparticles Stabilized with Citrate

CPC: Calcium Phosphate-Based Cement

DCPD: Dicalcium Phosphate Dihydrate, Brushite

DDS: Drug Delivery System

Den: Denosumab

DLS: Dynamic Light Scattering

Dox: Doxorubicin

ECM: extracellular matrix

Ev: Everolimus

FT-IR: Fourier Transform Infra-Red Spectroscopy

FWHM: Full-Width Half Maximum Peak Parameter

GB: Biomorphic Scaffold

HA: Hydroxyapatite

HA-NPs: Hydroxyapatite Nanoparticles

HEPES:(4-(2-Hydroxyethyl)-1-Piperazineethanesulfonic Acid)

ICP-OES: Inductively Coupled Plasma Optical Emission Spectroscopy

IgG: Immunoglobulin G

L/P: Liquid to Powder Ratio

MCS: mesenchymal cell line

MDAMB-231: triple-negative human breast adenocarcinoma cell line

MMS: Macroporous Sintered Scaffold

MSF-7: human breast cancer cell line with estrogen, progesterone, and glucocorticoid receptor

mTOR: mammalian target of rapamycin

MTX: Methotrexate

NIR: near infra-red

NPs: Nanoparticles

OA: Osteoarthritis

OBs: Osteoblast

OCs: Osteoclast

OM: Osteomyelitis

OS: Osteosarcoma

PBMCs: human peripheral blood mononuclear cell line

PXRD: Powder X-Ray Diffraction

RANKL: receptor activator of nuclear factor kappa-B ligand

SEM: Scanning Electron Microscopy

SrCPC: Strontium-Doped Calcium Phosphate-Based Cement

SSA: Specific Surface Area

TC: Tetracycline

TCP: Tricalcium Phosphate

TGA: Thermogravimetric Analysis

UV-Vis: Ultraviolet-Visible

XRD: X-Ray Diffraction

CHAPTER 1 – INTRODUCTION

1.1. Bone tissue

The adult human skeleton is made up of 206 bones namely providing structural support for the body (Figure 1). In addition, several other functions are associated to bones, including: i) movement and locomotion by providing leverage for the muscles, ii) protection of vital internal organs from damage, iii) maintenance of mineral homeostasis and iv) a vital environment for haematopoiesis within the bone marrow[1,2]. Although the skeleton is mostly considered to be a rigid framework, the bone tissue is a dynamic, metabolically active, and highly vascularized organ[3]. It is characterized by complex structures that are constantly undergoing dynamic remodeling due to the complex interaction of several biochemical processes[3,4].

***Figure 1**. The human skeleton*[1]

Part of the content of Chapter 1 was published in Journal of Composite Science 5, 227 (2021) as "*Tavoni, M., Dapporto, M., Tampieri, A. & Sprio, S. - Bioactive Calcium Phosphate-Based Composites for Bone Regeneration.";* in Biomimetics, 2022, 7, 112, as "*Pupilli F., Ruffini A., Dapporto M, Tavoni M., Tampieri A., Sprio S. - Design Strategies and Biomimetic Approaches for Calcium Phosphate Scaffolds in Bone Tissue Regeneration"*.

Bone remodeling supports calcium mobilization to maintain calcium balance, replacement of old bone tissue, an adaptation of the entire skeleton and individual sites to varying loads, weight, and strain, and repair of damaged bone[3].

Bone cells, including osteoblasts, osteocytes, and osteoclasts, are responsible for repairing, maintaining and adapting bone[3,5,6]:

-*Osteoblasts*, also known as *bone builders*, derived from mesenchymal stem cells (MSC) in the bone marrow and present as cuboidal cells that form a continuous layer on the bone surface[3]. Their primary role is the production of the organic matrix: type I collagen, which is suitable for subsequent mineralization to form bone tissue, osteocalcin, osteonectin, and bone morphogenetic proteins.

-*Osteoclasts*, also known as *bone resorbers*, are multinucleated giant cells derived from bone marrow monocytes coming from the hematopoietic stem cells (HSC). Their main function is the acid degradation of the mineral phase and the surface destruction of old and fractured bone. Furthermore, their activity is regulated by chemical signals (hormones, low calcium levels) or mechanical signals that stimulate the activity of osteoclasts to destroy some lamellae and deposit new lamellae with a different orientation, thus stabilizing the applied load.

-*Osteocytes*, also called *bone controllers*, develop from osteoblasts and remain in the bone matrix until the bone part is degraded[3,5,6]. Osteocytes use interconnected cytoplasmic channels called canaliculi to deliver nutrients to the surrounding tissue. They cannot produce or destroy the bone tissue. However, their ability to sense mechanical stress via cytoplasmic extensions can stimulate other cells to deposit or resorb the mineral phase.

-*Endosteal lining cells,* also called *bone housekeepers*, are flat cells that cover approximately 80-95% of the inner bone surface, forming a protective layer. They are associated with a thin collagenous membrane that covers the mineralized bone surface, the osteocytic lacunae, and their canaliculi.

The bone microstructure is, therefore, the result of the biomineralization of Type I collagen, secreted by fibroblasts and osteoblasts cells, as a major component of the extracellular matrix (ECM) of skin, tendon, and bone[7]. Therefore, osteoblasts create the nanocomposite structure of bone by secreting the ions responsible for the formation of apatite crystals, and the ECM in turn influences adhesion, proliferation, and differentiation of osteoblasts, osteoclasts, and osteocytes [8,9]. The ECM consists of inorganic and organic phases and water: the organic component consists of collagen and non-collagenous proteins and the inorganic component contains calcium phosphate (mainly plate-like nanocrystalline hydroxyapatite, HA), calcium carbonate, magnesium phosphate, and magnesium fluoride, doped with various anionic (HPO_4^{2-}, CO_3^{2-}, Cl^-) and cationic species (Na^+, K^+, Mg^{2+}, Sr^{2+}, Zn^{2+}, Ba^{2+}, Cu^{2+}, Al^{3+}, Fe^{2+}, and Si^{2+}) trapped in the crystal structure. Carbonate ions are present up to 8 wt.% while Na^+, Mg^{2+}, K^+, Sr^{2+}, Zn^{2+}, Ba^{2+}, Cu^{2+}, Al^{3+}, $Fe^{2+/3+}$, F^-, Cl^- and Si^{4+} ions are present in a trace amounts (<1wt.%)[10]. Biogenic HA in bone tissue is non-stoichiometric with a Ca/P ratio between 1.5 and 1.67, with the inclusion of foreign ions in the crystal structure affecting solubility, bioactivity, surface chemistry, and morphology[11,12]. The general chemical formula for biogenic apatite is: $Ca_{10-x}(PO_4)_{6-x}(HPO_4 \text{ or } CO_3)_x(OH \text{ or } ½\ CO_3)_{2-x}$ where $0 \leq x \leq 2$. One of the most common doping ions in biogenic HA is CO_3^{2-}, which can replace both phosphate and hydroxyl ions (resulting in Type B and Type A carbonated apatite, respectively). It was observed that B-type carbonated-HA inhibits the crystal growth and decreases the crystallinity; this structural disorder increases the chemical reactivity and improves the solubility without altering the affinity of the osteoblast cells[11,13]. Other possible anionic substitutions are with fluoride and chloride ions[11,13]. Cationic substitutions generally involve monovalent and divalent cations in the calcium sites of the HA crystal lattice, as reported in Table I [4,11,13–15]

Table I. Relevant cation substitutions in natural HA crystal structure

Cations	Biological effects
Magnesium	Enhancing skeletal metabolism and bone growth
Strontium	Increasing bone mass: stimulating bone formation and reducing bone resorption (anti-osteoporotic agent)
Silicon	Stimulating extracellular matrix formation and mineralization
Zinc	Stimulating osteoblastic activity *in vitro* and inhibiting bone resorption *in vivo*

The bone structure has a complex hierarchical architecture resulting from the complex interactions of multi-level components, from micrometric osteons to apatite nanocrystals (Figure 2).

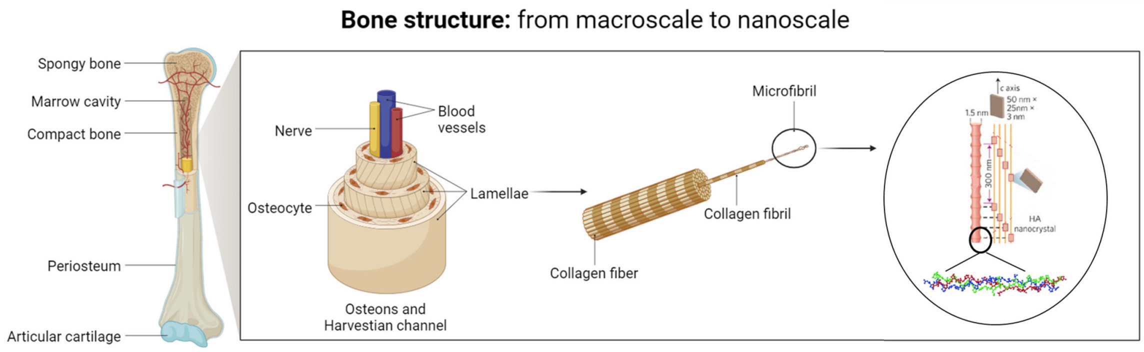

***Figure 2**. Bone structure: from macroscale to nanoscale.*

It is possible to classify the levels and structures of bone components as follows:

- Macrostructure: cancellous and cortical bone.
- Microstructure: (10-500 mm): Haversian channel, osteons, single trabeculae.
- Sub-microstructure (1-10 mm): lamellae.
- Nanostructure (100 nm-1 mm): fibrillar collagen and embedded mineral.
- Sub-nanostructures (< 100 nm): molecular structure of constituent elements, such as minerals, collagen, and non-collagenous proteins [16].

Concerning the **macrostructure**, an important distinction must be made between the two classes of bone tissue present in vertebras, with specific functionalities: *cortical* and *cancellous bone*[17].

-*Cortical bone,* also known as compact bone, is a dense structure organized as regular layers of lamellae tissue, with different thicknesses depending on the bone location. The cortical bone tissue location is on the outer layer of bone tissue, constituting about 80% of the total skeleton mass. Transverse sections of lamellae arrangement in load-bearing bones, such as the femur and other lower extremity bones exhibit a denser and thicker structure compared with other tissues, such as lateral and posterior cortex[17,18].

-*Cancellous bone,* also known as *trabecular bone* or *spongiosa*, is less dense tissue in which collagen fibers, and lamellae are irregularly arranged, interconnecting and forming the trabecular tissue network. Cancellous bone is located within metaphysis and epiphysis at the end of long bones and in short bones as well. Metabolic activity, such as bone cell production and mineral exchange is higher in cancellous bone compared with the cortical one as its porous structure is highly vascularized and contains the red bone marrow [17,18].

The **microstructure** consists of a planar arrangement of mineralized collagen called *lamellae,* 3 to 7 µm thick, which can wrap in concentric layers (3-8 lamellae) around canals, such as blood vessels to form a cylindrical structure, called osteon, 100-120 µm in diameter, extending parallel to the long axis of the bone. Osteons can directly form de novo from vascularized channels, called primary osteons, or they can be reproduced from the bone remodeling process, called a secondary osteon. Secondary osteons, or *Harvestian systems,* are the most common in the mature skeleton and are characterized by the presence of a cement line as the outer layer of the osteon itself, a sign of cessation of the resorption process[17]. The central canals facilitate the attachment of each series of lamellae within the lamellar bundle and may branch or combine with the prevailing direction, which is along the bone axis and the cement outer layer[17,19].

The **sub-microstructure** consists of lamellar bone, the most common material forming bone tissue, which consists of a series of lamellae. From TEM and SEM micrographs have shown that the orientation of a series of lamellae does not follow a strict parallel arrangement of mineralized collagen fibers, but consists of highly interlaced bundles of fibres with different densities in adjacent layers[17,20]. The recruitment of osteocyte-differentiating osteoblasts could be indicated by the alternation of dense and loose density layers. The secretion of densely interlaced fibrillar matrix by osteoblast overlaps with the loose fibrillar matrix already laid down by pre-osteocytes during their transformation from osteoblast to osteocytes. A similar arrangement of lamellae has been found in woven bone, a transient tissue with a disordered fibrous structure that is formed during bone remodeling processes, and fracture repair. Unlike lamellar bone, woven bone is composed of mineralized collagen fibril bundles with little or no 3D orientation[17,19].

In the **nanostructure**, the most prominent structures observed are collagen fibers that are covered with heterogeneously nucleated minerals. The collagen fibrils consist of a collection of collagen molecules, 300 nm long and 1.5 nm wide, which are deposited in the extracellular space by osteoblasts and assembled into fibrils with a diameter of about 100 nm. Adjacent molecules to the fibrils are staggered by $D \approx 67$ nm along the axial direction, creating a characteristic pattern of gap zones 35 nm long and overlap zones 32 nm long within the fibril[21]. Immunohistological studies have shown a preferential and periodical assembly of the constituting macromolecules into fibers[22]. Mineralized collagen fibrils *in* *vivo* self-assemble in a complex fashion, apparently starting in the osteoblast endoplasmic reticulum, then in compartments outside the cytoplasm, and finally moving to the extracellular space. The diameters of these arrays can vary from less than a micron to several microns and fibril arrays are only present in the ordered material. Most fibrils in the disordered material appear as individual fibrils and show little preferred orientation compared with the ordered material[17,19].

In the **molecular structure**, mineralized collagen fibrils at the nanometric level are composed of three main materials: crystals, collagens and non-collagenous organic proteins. Plate-shaped crystals occupy periodical spaces within the collagen fibrils, limiting their crystal growth and therefore their dimension at a nanometric scale, with average lengths and widths of the plates at about 50 × 25 nm and crystal thickness of 2–3 nm[16]. The mineral crystals, composed of mainly apatite with small impurities, such as Na^+, K^+, Mg^{2+}, HPO_4^{2-} and carbonates, grow with c-axes of the crystal roughly parallel to the long axes of the collagen fibrils[17]. While the X-ray diffraction pattern is the HA, the near absence or absence of the hydroxyl group has been proven repeatedly by chemical methods and FTIR, 1D-NMR and 2D-NMR spectroscopy [17,23,24]. The primary organic component of the matrix is Type I collagen, secreted by osteoblasts and self-assembled into fibrils with a specific tertiary structure. Non-collagenous organic proteins, including phosphoproteins, such as osteopontin, sialoprotein, osteonectin and osteocalcin, may function to regulate the size, orientation and crystal habit of the mineral deposits. Through chelation of calcium or enzymatic release of phosphorus from these proteins, they may serve as a reservoir for calcium or phosphate ions for mineral formation[17,25]

The bone formation in mammals follows a complex cascade of phenomena known as *biomineralization*[17]. This physiological process is regulated by the interaction of apatite precursor minerals, such as octacalcium phosphate $Ca_8H_2(PO_4)_6{\cdot}5H_2O$ (OCP) and amorphous calcium phosphate $Ca_3(PO_4)_2{\cdot}nH_2O$ (ACP), in addition to the organic extracellular molecules that drive the formation of hierarchal structured hybrid organic-inorganic tissue. Several control mechanisms activated by the bio-organic matrix regulate the formation and organization of the mineral phase at the multi-scale. This guides the formations of nanoplate-sized HA parallel-oriented to the collagen fibril axial structures with a complex hierarchal organization, that is able to withstand mechanical strain and adapt to constant external stimuli[17,21,26]:

- *Chemical factors*: precipitation of ions naturally present in the environment, mediated by a complex macromolecular organic structure, which acts as sites of heterogeneous nucleation and control specific chemical interaction.
- *Spatial factors*: confinement of the nuclei growth, as well as a constraint in their shape and contact with the organic structure.
- *Structural factors*: inducing peculiar crystallographic features driven by the interaction between the mineral phase and the organic template.
- Morphologic factors (*morphogenesis*): where the mineral phase takes place in a complex architecture on a macroscopic scale, strictly dependent on the combination of various phenomena above-mentioned, which hierarchically occur on different dimensional scale in correspondence with the sites of heterogeneous nucleatio[17,27].

The formation of calcium phosphate phases in bone tissue includes the sequestration of calcium and phosphorous ions into ACP stable precursors and the templating of these clusters into ordered forms [28]. Formation and evolution of relatively stable amorphous phases have been studied to perform an in-depth examination of biomineralization processes. In vitro studies monitored with micro-Raman spectroscopy combined with solid state NMR, for example, have been used to show that ACP is first formed and subsequently transforms into OCP, then progressively turns into carbonated apatite[29,30] . Mineralization evolution of apatite precursors is further regulated by the presence of non-collagenic proteins, such as albumin and osteocalcin. OCP crystallization studies in vitro in the presence of albumin prove that significant localized variations in albumin concentration in body fluids can effectively inhibit crystal growth, especially during the early stages of biomineral formation[31], while osteocalcin is found to be attached to the collagen structure and interacts with the Ca-sites, participating in the alignment of apatite crystallites during mineralization[32,33]. Development and better understanding of mineralized fibril formation have also been focused on the re-evaluation of the role of collagen during biomineralization. Collagen was long believed to only serve as a structural matrix and considered to be inactive in biomineralization. Recently, collagen was discovered to play an active role in templating apatite mineralization process by the discovery of a positively charged region existing in collagen fibrils at the interface of the gap and overlap[28]. Cryo-TEM studies of collagen fibrils mineralization showed, for example, that once ACP particles enter the fibril structure, collagen with its charged amino acid groups acts as a nucleation site for the formation of nanosized apatite[34]. Despite extensive efforts to understand biomineralization processes, to date, only simplified biomimetic structures have been achieved.

Bone remodelling is defined as the process of bone formation by osteoblasts or bone resorption by osteoclasts on a given surface. Bone modelling processing occurs solely on pre-existing bone surfaces and has the function of increasing bone mass and altering bone shape. During bone modelling, osteoclast and osteoblast activity are not strictly coupled, thus the two processes occur in a relatively independent manner of one another [17,35].

Bone modelling is the process by which bone is renewed to maintain bone strength and mineral homeostasis and it is characterized by the sequential action of both osteoclast in bone resorption and osteoblast in bone formation in the same spatial location[17]. Remodelling involves continuous removal of discrete packets of old bone, replacement of these packets with a newly synthetized collagen matrix and subsequent mineralization repairing micro-damages present on the surface of bone tissue [17,36]

One remodelling cycle of trabecular bone takes approximately 120 days, while the surface of spongiosa is total remodelled every 2 years. The remodelling cycle has been divided into six phases [3,6,37] (Figure 3).

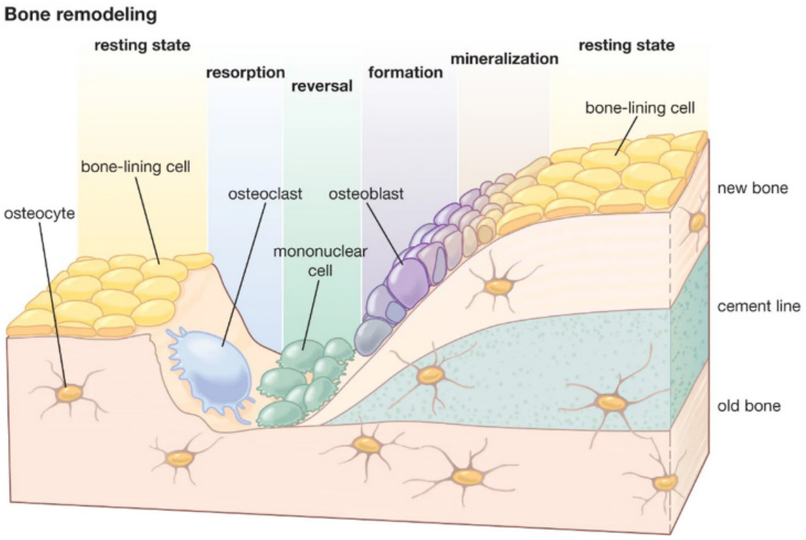

***Figure 3**. Steps of bone remodelling in adult trabecular bone* [38]

Quiescence and activation phases: a layer of flat-lining cells over a thin collagenous membrane covers the surface of the bone and it is prepared for resorption. This involves retraction of the endosteal lining cells and removal of the thin collagenous membrane covering the bone surface. The osteoclast precursors differentiate to mature and functional osteoclasts.

Resorption phase: recruitment and fusion of osteoclastic precursors, preparation of osteoclasts for resorption and development of the ruffled membrane; osteoclasts resorb the bone, which leads to the formation of lacunae or pits; osteoclasts migrate slowly or undergo apoptosis.

Reversal phase: osteoblast progenitors are attracted to the resorption cavity, while monocytes and endosteal lining cells prepare the surface of the resorption pit for new bone production by removal of the debris left by the osteoclasts.

Formation phase: osteoblasts lay down an unmineralized organic matrix (osteoid), which is primarily composed of type I collagen fibers and serves as a template for inorganic HA crystal. Hence, active osteoblasts produce the osteoid.

Mineralization phase: the final phase is the process of calcification or mineralization of the osteoid.

Quiescence/termination phase: following the mineralization, the bone enters the quiescent phase and the amount of bone formed equals the amount resorbed.

1.2. Bone metabolic dysfunction and diseases

Bone homeostasis and metabolism depend on the communication between bone cells, particularly between osteoclast and osteoblast[39]. Communication between bone cells, specifically osteoclasts, and osteoblasts, is essential for bone homeostasis and metabolism. An example of bone cell regulation comes from the RANKL/RANK/OPG pathway, highlighting that the activation of osteoclasts precursors is mostly related to an osteoblast-secreting factor (RANKL). Bone homeostasis imbalances have been associated with several degenerative bone diseases, and a wide range of skeletal disorders including osteoporosis, bone infections, and bone cancer, causing disability, pain and mortality [40–43].

1.2.1. Osteoporosis

Osteoporosis is a metabolic bone disease caused by the disruption in homeostasis between bone formation and resorption[39]. This imbalance in bone remodeling leads to a reduction in bone mass and micro-architectural deterioration of bone tissue. The increased fragility of the bone and its susceptibility to fracture can cause bone/joint pain, back pain, loss of mobility and height loss[40,44] (Figure 4).

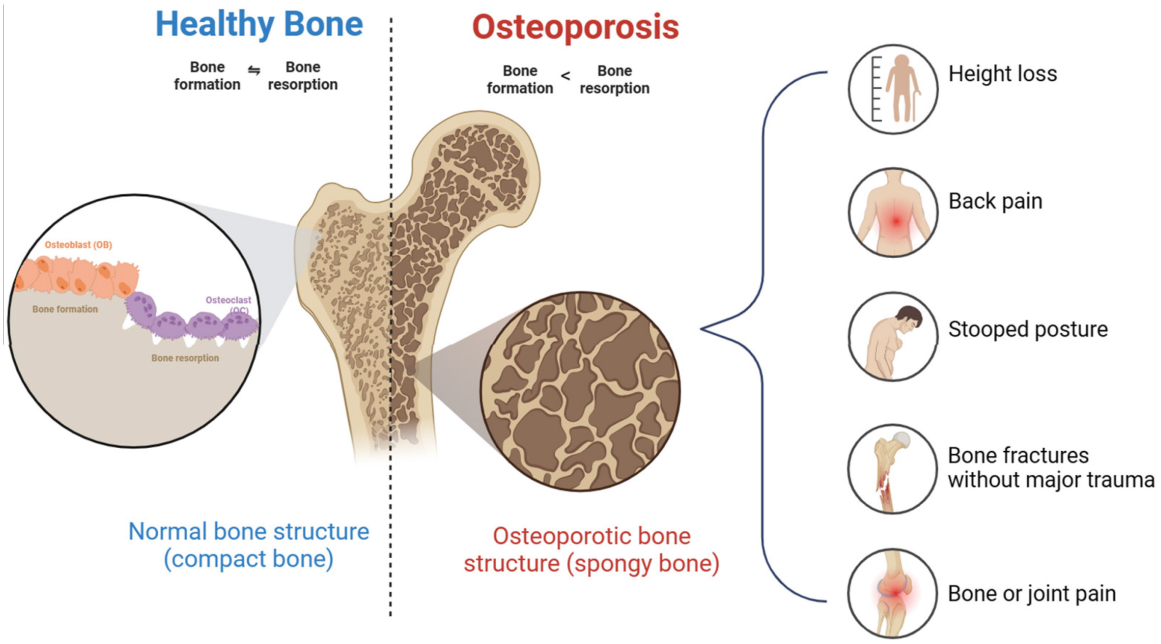

Figure 4. *Comparison between healthy and osteoporotic bone structures and the common symptoms of osteoporosis. Created with Biorender.com*

Osteoporosis can be classified into primary and secondary osteoporosis:

- Primary osteoporosis is usually the result of age-related changes and is likely to occur in the elderly and include post-menopausal, senile and idiopathic osteoporosis.
- Secondary osteoporosis is caused by unspecified diseases and drugs affecting bone metabolism.

With the progressive aging of the population, osteoporosis has become a global socioeconomic and medical problem[39,44,45]. Statistics show that nearly one-third of women and one-fifth of men in the world are suffering or will suffer from osteoporosis[44].

Current treatment for osteoporosis involves the oral or intravenous administration of high doses of anti-resorptive drugs, which are therapeutic agent able to interfere with the resorptive activity to prevent further deterioration. Anti-resorptive drugs commonly used are small molecules, such as bisphosphonates and strontium salts, and human monoclonal antibody, such as denosumab[44–46]. However, the large use of these type of drugs due to the systemic administration can lead a side effect that limit their application and curative effects. Thus, it is necessary to develop more effective strategies for osteoporosis.

Recently, promising alternatives for the treatment of this metabolic dysfunction have emerged. These are based on materials with high osteogenic and osteoconductive activity, such as calcium phosphate bioceramics and hydrogel scaffolds[39,45]. In particular, ion doping of these scaffolds with elements or metals like strontium, zinc, iron and magnesium can promote osteoblast activity and at the same time suppress the osteoclast's action[11,45].

1.2.2. Bone infections

Bone infections are referred to bacterial infection in which bone lesions destroy bone tissue. In addition to traumatic or infective accidents, it can also occur after scaffold implantations[47]. Indeed, post-operative bone infection is one of the main problems that can lead to implant failure and include osteomyelitis (OM) and prosthetic joint infections[47–50]. OM, which can be classified as acute or chronic, is the inflammation of bone tissue caused by bacterial infection, including infections of the bone marrow, bone cortex, and surrounding soft tissue. The types of infections are blood-borne, post-traumatic and adjacent infections[51]. *Staphylococcus aureus*, a gram-positive bacteria strain, is the major responsible for skeletal infections[52]. This bacteria strain can form biofilm, which is the most problematic resistance mechanism of bacteria. The biofilm formation cycle is a complex process that can be described in 5 phases[53] (Figure 5):

i) Reversible attachment: bacteria approaching the surface.
ii) Irreversible attachment: bacteria interact with each other and adhere to the surface.
iii) Extracellular matrix formation: resident bacteria produce the extracellular polymeric substances.
iv) Biofilm maturation: bacteria communicate the presence of each other by releasing signaling molecules, stimulating the formation of microcolony and the biofilm maturation.
v) Dispersal or detachment: bacteria leave the biofilm and return to planktonic life, starting a new cycle of biofilm formation.

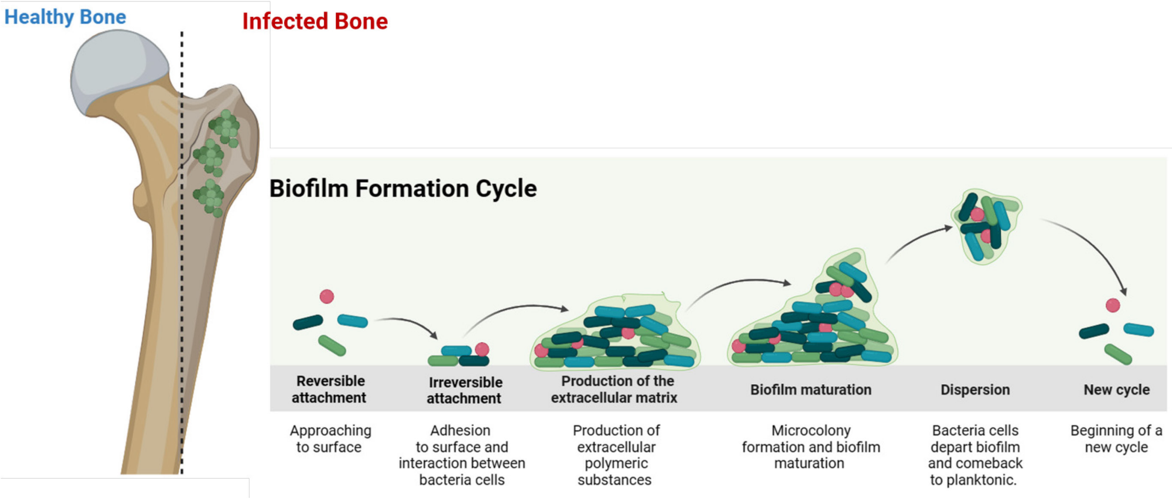

***Figure 5**. Comparison between healthy and infected bone and the biofilm formation cycle*

Another biofilm-forming bacteria strain on orthopaedic implants and devices is *Escherichia coli,* a gram-negative bacteria strain[53].

The current treatment of OM involves the administration of antibiotics by oral and intravenous ways for long periods and surgical removal of infected/necrotic bone; adequate bone removal can leave a massive bone defect where the antibiotic concentration is low, thus the bone will require to be filled[54]. Moreover, the biofilm formation provides a physical and impermeable barrier to immune cells and therapeutic agents, preventing the antibiotics actions. As a result, the dosage of antibiotics required to treat these bacteria is up to 1000 times higher than for planktonic bacteria[55]. Furthermore, bacterial infections and host inflammation can cause bone resorption of surrounding tissue[52,55]. Although systemic antibiotics are widely used and are the most important and effective methods of treating bone infections, they cannot target the surgical site, and determining the appropriate dosage remains sensitive[47,50]. In addition, high doses of antibiotics can lead to antimicrobial resistance, which is one of the most global public health issue that may be accelerated by the overuse of antibiotics worldwide[56–58].

Therefore, there is a critical need to develop an effective approach to not only prevent and treat bone infections but also to avoid antimicrobial resistance. The ideal bone substitute biomaterial in this type of application should be able to stimulate the bone formation (as calcium phosphate-based scaffold), prevent the biofilm formation and locally deliver antimicrobial ions (such as silver) and and/or antibiotics drugs[55].

1.2.3. Bone tumours

Bone tumours involve the invasion of tumours into bone tissue and can be divided into:

- primary tumours, namely developing by bone cells[59]
- secondary tumours, which develops elsewhere in the body (e.g., prostate, breast, lungs, kidneys) and spread to bone tissue at a later stage[59].

Osteosarcoma (OS)

Osteosarcoma (OS), a primary bone sarcoma, is a malignant tumour of mesenchymal origin characterised by the production of osteoid by the neoplastic cells[60,61]. Affecting mainly children and adolescents, OS is the most common malignant bone cancer and accounts for 8.9% of cancer-related deaths[62–64]. Current treatments for OS include systemic chemotherapy and surgical resection[65]. Surgery is the primary treatment for OS and consists of removal of the tumour mass, but the removal of the entire limb is often necessary[66]. Therefore, the regeneration of bone structure for aesthetic and functional activities and prevention of cancer recurrence are the main concerns after tumour mass resection[67].

Survival has been improved by advances in destructive systemic chemotherapy. The backbone of OS treatment include methotrexate (MTX) and doxorubicin (Dox)[68,69]. Since the introduction of chemotherapy for the treatment of OS in the late 1970s, patients diagnosed with OS receive neo-adjuvant treatment followed by postoperative adjuvant therapy with a chemotherapy cocktail, as high-dose of MTX or by combining Dox and cisplatin, with or without high-dose of MTX[70].

Choosing and using chemotherapeutic agents for OS is still controversial and may suffer from complications due to chemotherapeutic toxicity[71]. In recent years, novel treatment approaches have been proposed that use a drug delivery system to prevent side effects and improve treatment efficacy. Indeed, local delivery of anticancer agents from a medicated scaffold can improve the local concentrations with more efficient tumour killing, reducing drug resistance and limited systemic effects[59,65], while allowing healthy bone to regenerate after diseased tissue has been eradicated.

Bone metastasis (BM)

Bone tissue is a common site of metastasis for several types of solid tumours, such as breast and prostate cancer and accounts for a significant proportion of mortality in affected patients[72]. Metastasis is a multi-step process involving loss of intracellular cohesion, cell migration, angiogenesis, accessing the systemic circulation, surviving in the circulation, evading the local immune response, and growing in distant organs[59,72–74]. The invasion and adherence of cancer cells to the bone disrupts the homeostatic balance between bone formation and resorption. In particular, the formation of bone metastases is the result of a complex network of molecular events, with the establishment of a vicious cycle according to which cancer cells in the bone site induce RANKL production by osteoblasts, with a surge in bone resorption due to an increase in osteoclast formation[74,75] (Figure 6).

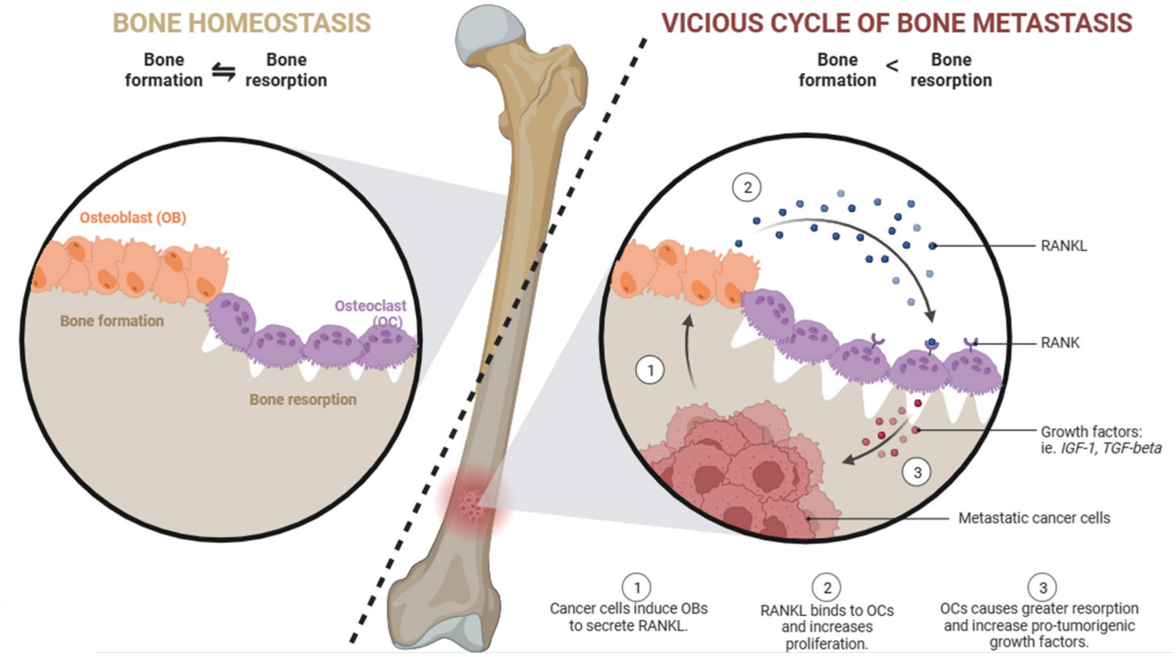

Figure 6. *Comparison between bone homeostasis and osteoporotic vicious cycle of bone metastasis.*

Bone metastasis (BM) is treated similarly to OS, including surgical removal of tumour bone and systemic neoadjuvant or adjuvant chemotherapy[59,74]. The choice of the anticancer drug for the treatment of BM depends on several factors such as local/spread cancer, the presence of extra-skeletal metastasis, and histological features of bone cancer[73].

Currently, in spite of various pharmacological therapies that have been proposed so far, the average healing rate of fracture on metastasis is extremely low and there are no approaches capable of achieving effective bone tissue regeneration. Furthermore, considering that a common surgical approach in bone cancer is the resection of damaged bone parts, the use of scaffolds able to sustain bone regeneration is highly desired. This goal is made more difficult considering that bone scaffolds should be able to promote tissue regeneration even under impairing conditions given by cancer. In this respect, the development of biomaterials implemented with specific bioactive molecules would represent an important integrated treatment in the approach to these patients and will establish the basis for the application of regenerative materials in cancer management.

1.3. Scaffold in bone tissue regeneration

The overall bone complexity, from a chemical and structural point of view, is the main responsible factor for the outstanding mechanical performance of bone and its self-repair ability[4,76]. Indeed, if massive bone defects occur, whether due to metabolic dysfunction, disease, or traumatic cause, the physiological bone healing process needs to be supported by a solid 3D scaffold, acting as a physical and instructive guide for cells to promote bone regeneration[77–80].

The design and development of biomimetic bone scaffolds must be inspired by the complex physiological bone composition and structure[4]. Some properties demanded for ideal bone scaffolds include *biocompatibility*, which is the ability of a biomaterial to function in vivo without eliciting any adverse side effects, *bioactivity*, which is the additional ability of a biomaterial to chemically bond with the surrounding tissue and to participate in specific biologically-relevant phenomena (e.g. ion-exchange) and *bioresorbability*, that is the ultimate ability of the implanted material to be resorbed over time, by active participation to the physiological turnover reactions, favoring the formation of new tissue[9,81–83].

More specifically, scaffolds should exhibit *osteoinductivity* and *osteoconductivity*, both stimulating the osteointegration of the scaffold, which consists in a direct bone-scaffold interaction essential to ensure the mechanical stability and also the in-growth of blood vessels[9,81]. In this respect, a leading concept guiding the scaffold development is the achievement of high mimicry with targeted bony tissues[84], aiming to achieve a physiological cell response while preventing adverse foreign body reactions.

Therefore, an ideal bone scaffold should be endowed with several physico-chemical features, including chemical composition mimicking both the natural bone ECM and mineral phase, open and interconnected porosity capable of promoting neo-vascularization, tissue in-growth, nutrient and oxygen supply, nano-structured surface topography positively driving adhesion, proliferation, and differentiation of cells, adequate mechanical properties able to sustain the biomechanical loads (bone mechano-trasduction), towards the effective regeneration of the tissue[81] (Table II and Figure 7).

***Table II**. Ideal features of scaffolds for bone regeneration, with respective proposed strategies to improve them.*

Properties	Proposed improving strategies
Open and interconnected porosity	• Traditional techniques for the fabrication of 3D-porous device (sacrificial template, direct foaming) • Low-temperature self-hardening methods • Biomimetic and biomorphic synthesis • 3D-printing technology
Mechanical properties	• Reinforced scaffold by compression, using fibers or dual setting system
Bio-functionality	• Biomimetic and biomorphic synthesis • Surface topography modifications
Bioactivity	• Biomimetic and biomorphic synthesis • Ion-doping ceramic-based scaffold • Ceramic-based composites

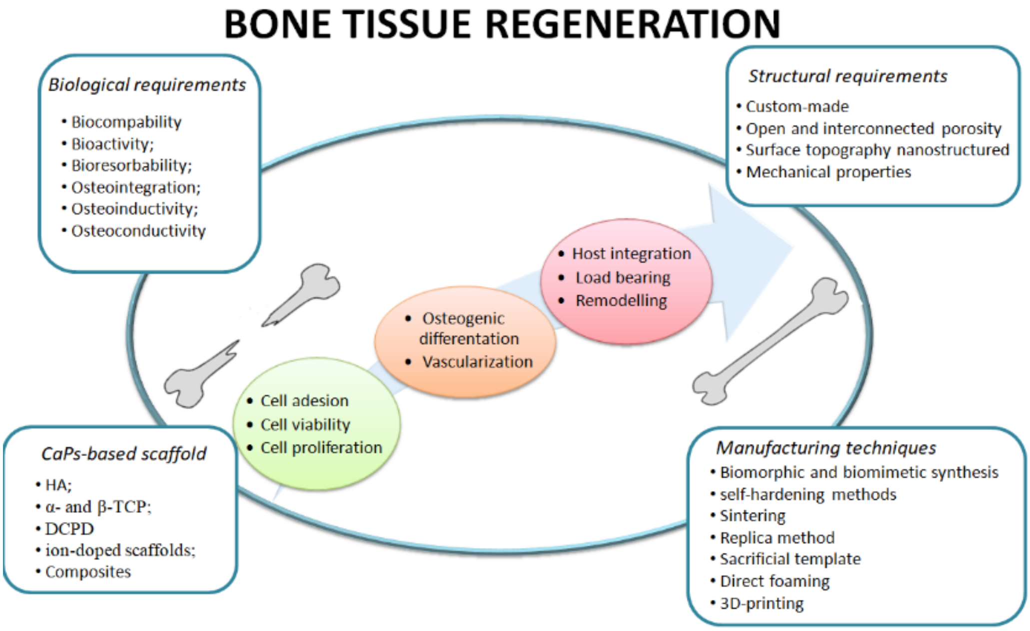

***Figure 7**. Flowchart of biological and structural requirements underlying the ideal scaffold for bone tissue regeneration[4].*

Several studies have been carried out on the research of biomaterials such as metals, natural or synthetic polymers, ceramics, and composites, which can match these characteristics[85–92]. Particularly, bioceramic-based scaffolds are widely used in numerous biomedical applications, due to their positive interaction with human tissue. Bioceramic-based materials can be classified as bioactive and bioinert. Ceramics considered as bioinert include alumina and zirconia; they show high chemical stability in vivo as well as high mechanical strength, however, they have not osteogenic properties[93]. Conversely, bioactive ceramics such as calcium phosphates (CaPs), silicates, bioactive glass, and titanium oxide can interact with cells, thus able to promote and stimulate bone regeneration[86–92,94] (Figure 8).

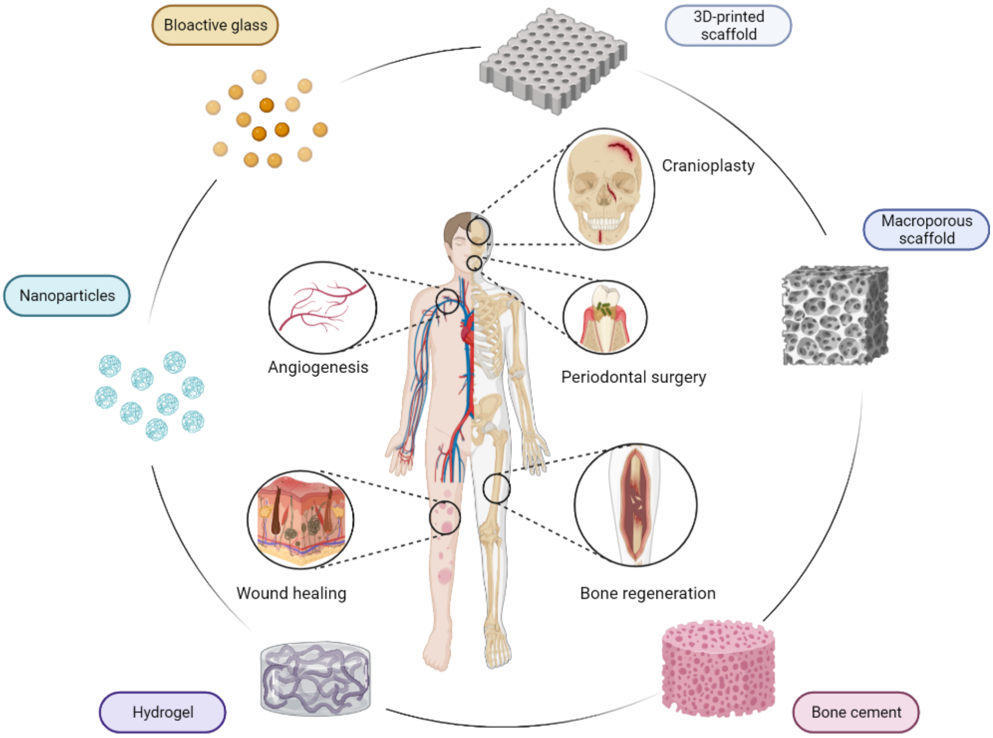

***Figure 8**. Bioceramics applications*

The mechanical properties of scaffolds play a significant role in bone tissue engineering. Relevant mechanical properties of bone include Young's modulus, toughness, shear modulus, tensile strength, fatigue, and compressive strength[95]. The mechanical strength of ceramics mainly relies on their chemical composition, grain size, porosity extent, and internal structural defects[96,97]. Several approaches have been reported to increase the mechanical performance and load transfer efficiency between the scaffold and surrounding bone tissue, mainly related to stronger interfacial bonding of the coating layer to the substrate[95].

Bioceramics typically exhibit higher compressive than tensile strength, but they are also intrinsically brittle, leading to sudden failure during handling and fixation[98]. In this respect, a critical challenge is related to the optimization of toughening mechanisms for ceramics[99,100]. However, developing an ideal bone substitute is difficult due to the varying mechanical properties and chemical, morphological, and structural characteristics of the site of bone regeneration, such as load-bearing bones, joints, skull, and spine.

1.4. Calcium phosphates

Calcium phosphates (CaPs) are a family of materials that form the inorganic component of hard tissues in vertebrates. They occur naturally as vertebrate bones, mammalian teeth, and fish scales, or in milk and blood as the main source of calcium[101]. In medicine, CaPs find a wide range of different applications throughout the body including dental implants, percutaneous devices, periodontal treatment, bone defect treatment, fracture treatment, total joint replacement, orthopedics, cranial-maxillofacial reconstruction, otolaryngology, spinal surgery and nanomedicine as drug delivery systems and as theranostic agent[97,102–107]. This is possible due to their excellent biological properties such as high biocompatibility, bioactivity, lack of toxicity or inflammatory and immune responses, osteoconductivity, osteoinductivity, and bioresorbability[82,101]. In particular, the high biocompatibility of CaPs is due to their chemical and structural similarity to the mineral phase of bone, which allows the body to recognize them as endogenous material[82,108–110]. Furthermore, the physicochemical properties of CaPs, such as crystalline phases, particle size, morphology, crystallinity, porosity, density, composition, Ca/P atomic ratio, or pH stability range, are functionally related and can be tailored by modifying the synthesis parameters. In particular, different morphologies, chemical compositions, or structures can be obtained by preparing different CaPs phases[101] (Figure 9).

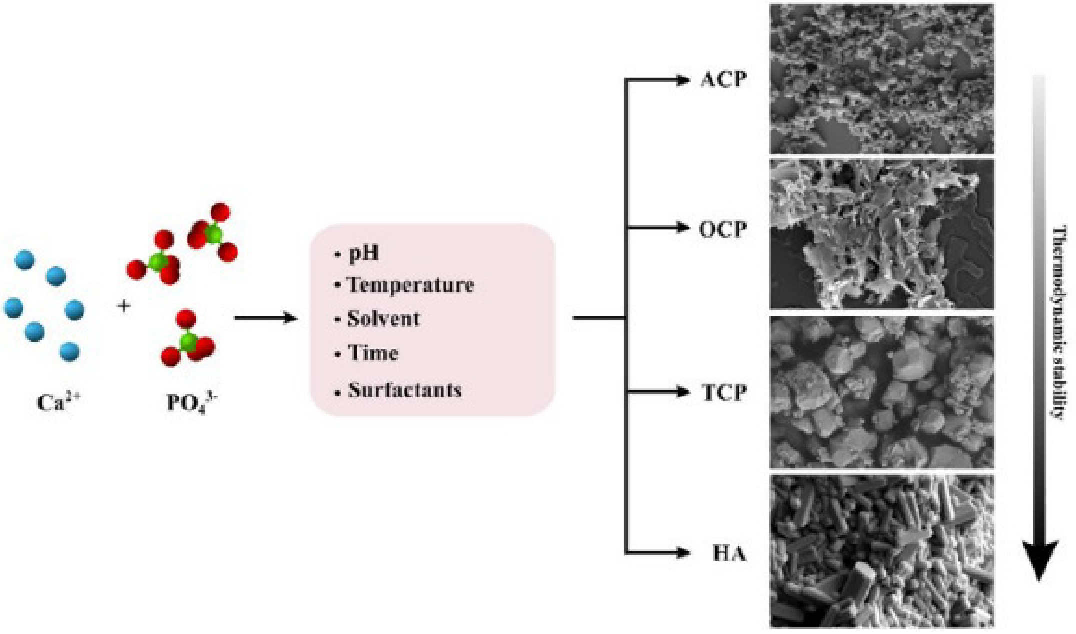

***Figure 9**. Principal synthesis parameters that influence the characteristics of calcium phosphates as well as the formation of different crystal phases (ACP: amorphous calcium phosphate, OCP: octacalcium phosphate, TCP: tricalcium phosphate, HA: hydroxyapatite, respectively)*[101,111]

The chemical composition of CaPs relies on multiple ions, including calcium (Ca^{2+}), orthophosphate (PO_4^{3-}), metaphosphate (PO_3^{-}), pyrophosphate ($P_2O_7^{4-}$) and hydroxide (OH^{-}) [12,82,97] (Table III).

Table III. Some CaP materials: name, abbreviation, chemical formula, Ca/P ratio, and solubility [82,97].

Name	*Abbreviation*	*Chemical formula*	*Ca/P ratio*	*Solubility at 25°C, mg/L*	*pH stability range*
Amorphous calcium phosphate	ACP	$Ca_xH_y(PO_4)_z \cdot nH2O$, n= 3–4.5, 15%–20% H_2O	1.18-2.20	-[a]	~ 5.0-12.0[b]
Hydroxyapatite	HA	$Ca_{10}(PO_4)_6(OH)_2$	1.67	~ 0.3	9.5-12.0
Calcium-deficient hydroxyapatite	CDHA	$Ca_{10-x}(PO_4)_{6-x}(HPO_4$ or $CO_3)_x(OH$ or ½ $CO_3)_{2-x}$	1.5-1.67	~ 9.4	6.5-9.5
Dicalcium phosphate anhydrous (monetite)	DCPA	$CaHPO_4$	1	~ 48	2.0-5.5 (>80°C)
Dicalcium phosphate dihydrate (brushite)	DCPD	$CaHPO_4 \cdot 2H_2O$	1	~ 88	2.0-6.0
Tetracalcium phosphate	TTCP	$Ca_4(PO_4)_2O$	2	~ 0.7	Precipitated from aqueous solution only at T>300°C
α-Tricalcium phosphate	α-TCP	$\alpha\text{-}Ca_3(PO_4)_2$	1.5	~ 2.5	Precipitated from aqueous solution only at T>1125°C
β-Tricalcium phosphate	β-TCP	$\beta\text{-} Ca_3(PO_4)_2$	1.5	~ 0.5	Precipitated from aqueous solution only at T>800°C

The solubility of CaPs compounds strongly influences their behavior *in vivo* [97].

The solid-state phase diagram of CaPs phases is shown in the following figure (Figure 10)[112]. The shaded area shows the region of biphasic-CaP formation; it can be prepared by mechanical mixing of HA and β-TCP or by precipitation method[82].

The complexity of the solid-state phase diagram of CaPs arises from the fact that calcium phosphate compounds can exhibit a wide range of compositions, crystal structures, and properties depending on factors such as temperature, pressure, and the presence of impurities. Additionally, the presence of different hydration states and the ability of some phases to undergo phase transformations further contribute to the complexity of the CaP phase diagram[112].

---

[a] Cannot be measured precisely[82]. However, the comparative solubility in acidic buffer decreases in the following order: ACP >> α-TCP >> β-TCP > CDHA >> HA[82]

[b] Always metastable. The composition of precipatated depends on the composition and the pH of electrolyte solution[82].

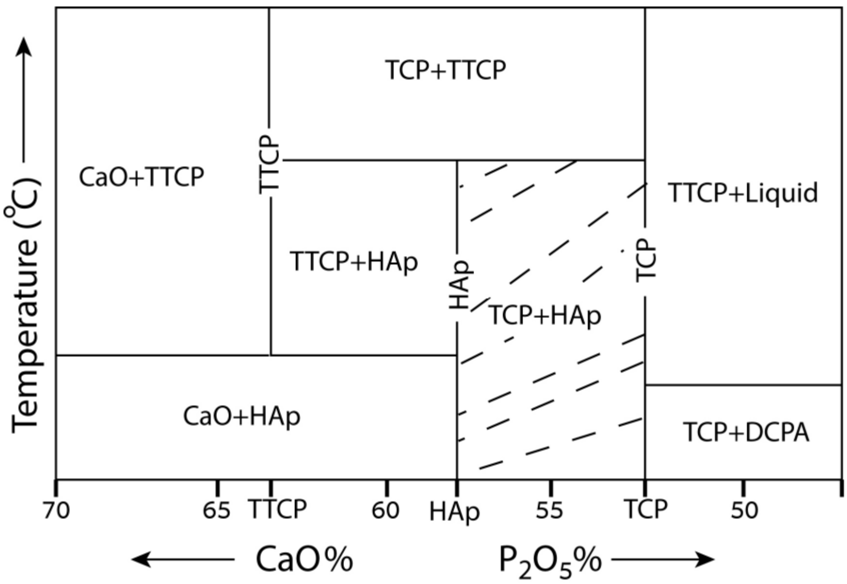

Figure 10. *Equilibrium phase diagram of different CaPs. The shaded region shows the phases of interest for biphasic-CaP formation*[82,112].

1.4.1. Amorphous calcium phosphate (ACP)

Amorphous calcium phosphate (ACP) is a special class of CaPs with variable chemical composition but similar glass-like physical properties in which there is neither translational nor orientational long-range ordering of the atomic positions[82]. ACP is a non-crystalline CaP phase ($Ca_xH_y(PO_4)_z·nH2O$, n= 3–4.5, 15%–20% H_2O), with Ca/P molar ratio ranging from 1.18 and 2.20 and represents the mineral precursor for bone and tooth formation in vertebrates[82]. It is characterized by excellent bioactivity, osteoconductivity, high cell adhesion, and tailorable biodegradation. Moreover, it is a non-crystalline phase and is more soluble than the crystalline CaPs, releasing a higher amount of calcium and phosphate ions in a short period. This latter property has been exploited in the dental field, leading to the development of ion-releasing oral care products containing ACP that trigger enamel and dentin remineralisation, restoring the mineral loss caused by caries[82,101,113,114]. The ability of ACP to release calcium, phosphate, and other ions in an aqueous environment is thought to contribute towards their osteoinduction. However, the rapid ions release can cause perturbations in the local pH and negatively impact cell attachment/proliferation in the short term and viability in the long term[82,101].

Commonly, ACP is obtained by wet precipitation in an aqueous environment and it is considered a transient precursor phase during the precipitation of other CaPs in aqueous systems. The degree of ACP amorphization increases as the concentration of calcium and phosphate ions and/or the pH of the electrolyte solution are increased[82]. A continuous gentle agitation of as precipitated ACP in the mother solution, especially at elevated temperatures, results in a slow recrystallization and formation of more crystalline CaPs, such as HA, due to the high structural similarity in the short-range order of ACP with HA. It was proposed that the basic structural unit of precipitated ACP is a 9.5 Å diameter, roughly spherical cluster of ions with the composition of $Ca_9(PO_4)_6$, so in the presence of water or moisture, it rearranges spontaneously to form a crystalline lattice[82]. Many factors such as pH, temperature, humidity, and the presence of ions/additives affect the crystallization process[101,115,116]. The main application of this CaP phase regards the biomedical field, in which it has found application as bone repair material in self-setting injectable cement, in the preparation of coatings on metallic or polymeric bone implants and as a drug delivery platform[101,115,116].

1.4.2. Hydroxyapatite (HA) and calcium-deficient hydroxyapatite (CDHA)

Apatite represents a large class of mineral phases exploited in several applications in different fields. The general composition of apatites is $M_{10}(XO_4)_6Z_5$, where M is a bivalent cation, XO_4 is a trivalent anion and Z is a monovalent anion[117,118]. Changing ion type, several apatites are obtained with different properties[117] and the ratio M/X is used to recognize each apatite[5,118].

Among CaPs, hydroxyapatite (HA) is particularly promising for bone tissue regeneration (BTR) due to its very close composition with natural apatite. Stoichiometric HA ($Ca_{10}(PO_4)_6(OH)_2$ with Ca/P ratio of 1.667) is the most stable and least soluble CaP. Stoichiometric structures can have both monoclinic and hexagonal crystal systems, but in biological environments, they take on a hexagonal[12]. In this crystal system, space group $P6_3/m$, calcium ions are present in two crystallographically different symmetry sites, 4f for Ca(I) and 6h for Ca(II). The Ca(I) ions are identified in columns along the three-fold axes of the structure at ¼, ¾, ¼ and ¾, ¼, and ½ positions; each Ca (I) ion is nine-coordinated with oxygen atoms. The Ca(II) ions form equilateral triangles at z= ¼ and z=¾, on the 6_3 axis of the structure; Ca (II) ions are seven-coordinated, with six O atoms and one OH^- ion (Figure 11a)[82,118–120].

Stoichiometric HA exhibits high stability at physiological pH, limiting its long-term resorption[12]. Therefore, various recent research has been focused on increasing the solubility and osteogenic activity of HA by ionic doping (figure 11b)[121,122]. The implications of ionic doping on the physico-chemical HA properties will be fully explained in paragraph 1.4.5.

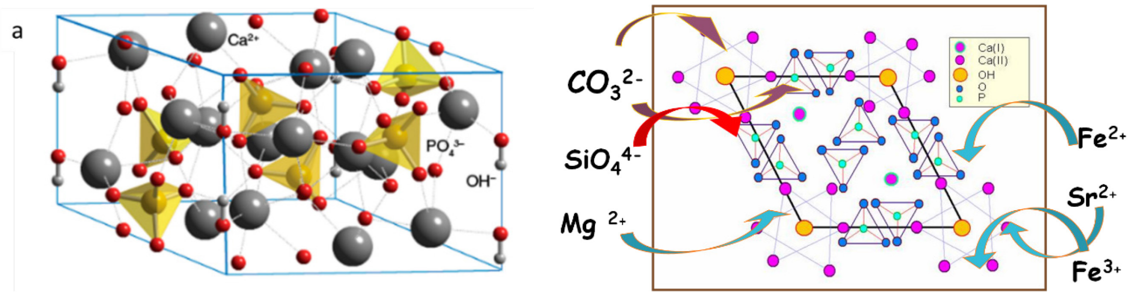

Figure 11. *Crystal structure of a) stoichiometric and b) some possible ionic substitution in the hydroxyapatite lattice hydroxyapatite*[13,82,119,120]

HA is characterized by several properties, including superior bioactivity, osteoconductivity, non-toxicity, non-immunogenicity, and biocompatibility in comparison to other CaP phases[82,101]. Another important feature for HA refer to its pH-dependent water solubility: it is stable in alkaline solutions, poorly soluble at neutrality and soluble at acidic pH[101,123,124]. Therefore, pH sensitivity can be exploited for pH-triggered drug delivery applications, where a drug-associated to HA is released only when the material encounters an acidic environment, as in the cases of inflammatory regions or endosomes and lysosomes after cellular uptake[125]. Furthermore, it has also been demonstrated that HA nanocrystal size and morphology can significantly affect its biocompatibility, bioactivity, and cell and tissue penetration capability[82,101]. Methods to synthesize stoichiometric and ion-doped nanocrystalline HA are listed in the following table (table IV)[126,127]:

Table IV*. Methods of hydroxyapatite synthesis*[127]

Method	Synthesis condition	HA characteristics
Precipitation	- Precipitation - Simple setup - Temperature ranging from RT to 80°C.	- Preferentially rod-like morphology - High production of pure product.
Hydrothermal	- Dissolution-precipitation - Inside a reactor - Temperature ranging from 100 to 250°C. - Pressure ranging from 1 to 50 atm.	- Versatility of morphology (from rod- to plate-like)

Sol-gel	- Hydrolysis-condensation - Temperature ranging from RT to 80°C.	- Finest HA nanoparticles (up to 20-50 nm)
Biomimetic deposition	- Nucleation growth (via SBF) - Temperature 37°C	- Applied to make bone-like nanocrystals apatite layer
Microwave	- Dissolution-precipitation - Inside a microwave oven - Temperature ranging from 100 to 250°C. - Pressure ranging from 1 to 50 atm	- Smaller particle size - Good purity - Closer size distribution

The high tunability of this material for its use in several kinds of applications has led to the increase of interest in the study of this material. Nanocrystalline ion-doped apatites are of great interest for medical application[127], in particular in nanomedicine. However, free nanoparticles are not as useful for bone regeneration as they would be if developed as 3D solid scaffold [127] (explained in section 1.5).

1.4.3. Dicalcium phosphate dihydrate (DCPD)

Dicalcium phosphate dehydrate (DCPD), also known as brushite, is one of the most easily synthetized CaP and can be converted into other CaPs (CDHA at pH>7, or OCP at pH≈6-7 and DCPA at pH<6). Brushite is biocompatible, biodegradable, and osteoconductive[82] and can be prepared by neutralization of phosphoric acid with calcium hydroxide at pH 3-4 at room temperature, by double decomposition between calcium and phosphate containing solutions in slightly acidic media, by conversion of calcium phosphate salts, in acidic media, or by reaction of calcium salts such as calcium carbonate in acidic orthophosphate solutions[82]. *In vivo* studies showed that DCPD converts into HA or it is degraded and replaced by bone[128–130]. Brushite in medicine is used as intermediate for tooth remineralization and in CaPs paste/cement[14,82,129–131].

1.4.4. Tricalcium Phosphate (TCP)

The notable interest in tricalcium phosphate (TCP) comes from the combination of its solubility and low Ca/P ratio, particularly interesting to obtain apatite crystals in aqueous environment[12]. There are two polymorphs of TCP: the high-temperature α-TCP and the low-temperature β-TCP[132]. The β-TCP polymorph is stable at room temperature, while a transformation into α-TCP occurs for temperatures higher than 1125°C. Besides a similar chemical composition, the TCP polymorphs have different crystalline structures (orthorhombic symmetry for α-TCP and rhombohedral space group R3c for β-TCP, figure 12), density, and solubility, thus resulting also in different biological performance[82].

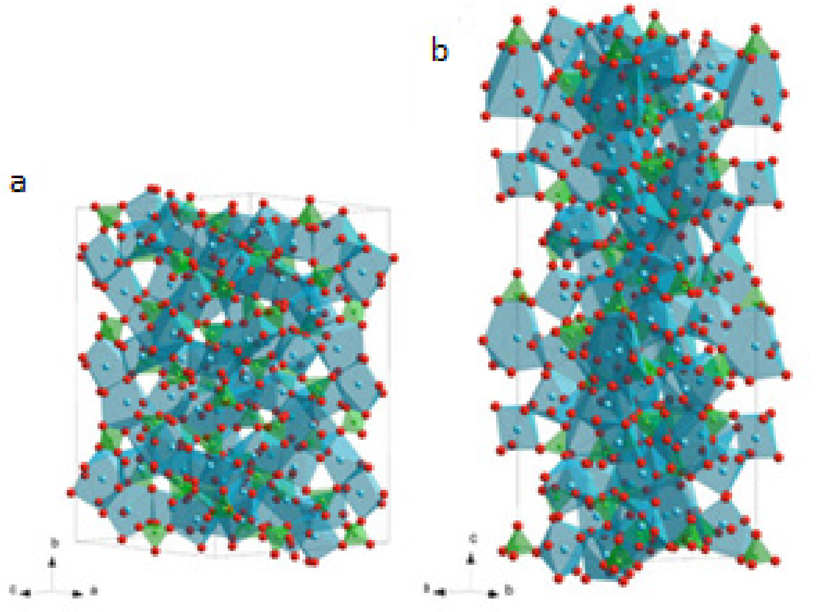

***Figure 12**. (a) Unit cell of orthorhombic α-TCP; (b) Unit cell of rhombohedral R3c β-TCP* [133]

The α-TCP phase is more soluble than β-TCP and can be easily hydrolyzed in calcium-deficient hydroxyapatite (Reaction 1).

$$3\ Ca_3(PO_4)_2 + H_2O \rightarrow Ca_9(HPO_4)(PO_4)_5OH \qquad \text{(Reaction 1)}$$

In addition, several ions can be introduced in the structure of TCP (Mg^{2+}, Sr^{2+}, Zn^{2+}, Si^{2+}, etc.), opening different thermodynamic scenarios in terms of polymorph stabilization, e.g. silicon was reported to stabilize α-TCP, while magnesium ions stabilize β-TCP [82,132].

Due to its high solubility, TCP has been used for the preparation of biphasic CaP scaffolds, able to conjugate the osteogenic properties of HA and the resorption behavior of TCP[134,135].

1.4.5. Ion-doped CaP bioceramics

Calcium phosphates, especially HA, are capable of hosting a variety of foreign ions, involving the formation of atomic defects but with limited modification of the overall crystal structure[121]. As biological apatites forming the inorganic part of bone are characterized by nanocrystallinity, poor crystal ordering and multiple ion doping, for decades various approaches were proposed to tune biological properties of CaPs to obtain novel biomaterials with multifunctional abilities including antibacterial and magnetic properties[11–15,136–143].

Some of the most studied substituting ions in bioceramics, with related biological role, are listed in Table V.

Table V. *Doping ions in calcium phosphate bioceramics, with related bio-functional ability*[2]

Ion	*Biological effects*	*Reference*
Si^{4+}	Induction of the biomimetic precipitation of HA	11,13–15,89,138,139,141–143
Sr^{2+}	Osteogenic activity	11,13–15,138,139
	Anti-osteoporotic agent	
	Enhancement of mechanical properties	
Mg^{2+}	Enhancement of bone growth	11,13–15,56,138,139,144
	Induction of angiogenesis	
	Antibacterial agent	
Zn^{2+}	Stimulation of osteoblastic activity	14,56,129,138,139
	Inhibition of bone resorption	
	Antibacterial agent	
Ag^{+}	Antibacterial agent	136–139,145–147
Mn^{2+}	Regulation of osteoblastic differentiation	138,139
	Control of bone resorption	
	Promotion of cell adhesion	
	Promotion of the synthesis of extracellular matrix proteins	
Cu^{2+}	Antibacterial agent	138,139
Co^{2+}	Neo-vascularization promotion	138,139
	High cell proliferation	
	Osteogenic activity	
$Fe^{2+/3+}$	Antibacterial agent	11,139,140,148,149
	Super-paramagnetism	
	Promotion of bone formation	
	Osteoinductivity	
F^{-}	Shrinkage of HA crystal lattice	138,150–154
	Decreasing solubilization and increasing the stability of HA	
	Induction of biomineralization	
	Osteogenic activity	
	Antibacterial agent	

Magnesium

Magnesium is considered the main ion capable of replacing Ca^{2+} in biological apatite, in an amount close to 1 wt.% [144]. Mg^{2+} ions play a key role in bone metabolism, taking part in the biochemical reaction beyond bone formation, while also controlling bone growth and metabolism [11,13,129,139,155].

Magnesium phosphates are also associated with higher dissolution rate than calcium phosphates[156]. Mg^{2+} has been shown to inhibit the formation of crystalline minerals such as hydroxyapatite, whereas more soluble phases like brushite are minimally affected by the presence of magnesium[157–159]. Specifically, it was observed in basic solutions that HA precipitation is inhibited by Mg substitution for Ca higher than 10% and amorphous calcium phosphate (ACP) or whitlockite, the Mg polymorph of β-tricalcium phosphate, forms[160,161]. The incorporation of magnesium was also associated with increased protein adsorption and cell adhesion on the surface of bioceramics[11,13]. Furthermore, an intrinsic antibacterial activity was also described for Mg-HA [56,138].

Strontium

Strontium (Sr^{2+}) is a natural component of bones and teeth and has affinity with Ca^{2+} ions, thus representing a calcium-like entity within cells, acting along similar biochemical and cellular pathways[138,162]. Strontium salts can delay the activation of calcium sensing receptors, inhibit the osteoclast maturation and activity, thus reducing bone resorption, and promote the differentiation and proliferation and collagen and non-collagen protein synthesis of osteoblast, promoting the bone formation[44,46,129,163–167]. Moreover, strontium ions can interfere with the communication between osteoclast and osteoblast by inhibiting the expression of RANKL[44]. In this context, the addition of strontium in bioceramics is promising for local treatment of bone affected by metabolic diseases such as osteoporosis[46,129,163–167] (chapter 1.2.1). Several approaches can be implemented to obtain Sr-doped bioceramics, including the addition of strontium salts in wet synthesis processes[144,168] or Sr-doped inorganic reactants involved during solid-state reactions at high temperature[167,169]. The incorporation of strontium ions replacing Ca^{2+} into the crystal lattice of calcium phosphates generally induces deformations in the crystal lattice, due to its higher ionic radius in respect to calcium[167,170]. This affects the physicochemical properties of CaPs, for instance, it was observed that Sr^{2+} ions stabilize the β-TCP polymorph, during thermal synthesis reactions[167]. Furthermore, various previous studies reported a mechanical reinforcement ascribed to strontium doping, possibly due to the enhancement of interatomic bond strength in the CaP crystal with respect to calcium [165,171,172].

Silicon

Silicon exhibits a key role in the physiological formation of bone and cartilage tissues, especially thanks to its intrinsic capacity to act both as cross-linker in ECM and to favor the precipitation of HA and bone mineralization[90,141]. It was reported the favoured formation of apatite in physiological fluid thus facilitating the chemical interaction into living bone structure following implantation [89,90,94]. The following steps explain the formation of apatite on the surface of silica-based bioceramics:

- Rapid exchange of Ca^{2+} with H^+ or H_3O^+ from body fluid solution results in hydrolysis of silica groups which creates silanol, according to $Si\text{-}O\text{-}Ca^+ + H^+ \rightarrow Si\text{-}OH^+Ca^{2+}(aq)$
- Loss of soluble silica in the form of $Si(OH)_4$ to the body fluid, resulting from breaking of Si-O-Si bonds and formation of silanol (Si-OH) at glass solution interface: $Si\text{-}O\text{-}Si + H_2O \rightarrow 2Si\text{-}OH$
- Condensation and polymerization of SiO_2-rich layer on the surface short in alkalis and alkaline-earth cations: $Si\text{-}OH+HO\text{-}Si \rightarrow Si\text{-}O\text{-}Si+H_2O$
- Migration of Ca_2^+ and PO_4^{3-} groups to the surface via SiO_2-rich layer forming a $CaO\text{-}P_2O_5$-rich film by incorporation of soluble calcium and phosphates from solution.
- The crystallization of amorphous $CaO\text{-}P_2O_5$-rich film by the addition of OH^- and CO_3^{2-} anions from body fluid forms a mixed hydroxyl, carbonated apatite layer.
- Adsorption and desorption of biological growth factors on the carbonated apatite layer to activate stem cells.
- The action of macrophages to remove debris from the site allowing cells to occupy their space.
- Attachment of stem cells on the bioactive surface and its differentiation to form osteoblasts.

- Generation of ECM by the osteoblast to form new bone and its crystallization in the living composite structure[90].

When silicon is employed in synthesizing bioceramics, specifically tricalcium phosphate (TCPs), that are typically acquired through high-temperature treatments, it can promote the development of α-TCP polymorph over β-TCP. Bioceramics containing silicon exhibit remarkable bioactivity, including Bioglasses (Na-Ca-P-Si), wollastonite ($CaSiO_3$), and Si-doped bioceramics (e.g. Si-HA and Si-TCP)[89–92,141,173].

The pivotal role of Si-containing bioceramics such as silicon-doped HA in BTE was confirmed by *in vivo* studies revealing the enhanced formation of collagen fibrils after 6 weeks at the bone/Si-HA interface and after 12 weeks with the bone/HA interface[141,142]. In addition, the enhanced formation of mature osteoclasts from mononuclear precursor cells was observed[141], thus showing the potential of silicon to favor the complex bone regeneration cascade by stimulating the various cell lines involved in new bone formation and remodeling. Long-term *in vivo* studies also reported the significantly higher bioresorbability of Si-doped HA scaffolds, compared to pure HA scaffolds, as only a few residues of the doped scaffold were observed at one year upon implantation, while non-doped HA scaffolds remained unchanged even after five years from implantation[143].

Silver

As mentioned previously, antimicrobial resistance is a global public health problem that may be accelerated by the overuse of antibiotics worldwide[56–58]. Therefore, developing drug-free solutions to replace systemic and intensive antibiotics administration combined with therapeutically effective biomaterials is an active research area[56]. Most of these solutions are based on the functionalization of biomaterials with antimicrobial elements such as silver or heavy metal nanoparticles[174,175]. Nevertheless, it is difficult to define and apply the correct dosage and distribution of antimicrobial metal nanoparticles, as these materials can have cytotoxic and genotoxic effects on healthy cells if overdosed[56,145]. Specifically, although silver ions are not toxic to mammals at low concentrations, they can cause argyria, a skin disorder, and cytotoxicity at high concentration[145,176,177]. Proposed mechanisms of action against bacteria include silver ions interfering with bacterial cell integrity, or binding to enzymes and proteins within bacteria or by generating reactive oxygen species (ROS), damaging the cell and its essential functions, resulting in bacterial death[174,176]. Stoichiometric hydroxyapatite has limited antibacterial resistance compared to ion-doped apatites, which have previously shown improved biomimetic and antibacterial properties, also about co-substitution with carbonate ions[56]. Several studies have attempted to improve the antibacterial properties of hydroxyapatite by incorporating of Ag^+ ions to replace Ca^{2+} [178,179]. The incorporation of silver ions into bioceramics, as a replacing element for calcium, is possible due to similar ionic radius[136]. The substitution of calcium by Ag^+ ions takes place preferentially in the Ca(I) site of the HA crystal lattice and its leads to an increase in the lattice parameters linearly with the total amount of silver [178,180]. However, although it is possible to obtain monophasic silver-doped hydroxyapatite[136,138] this is not straightforward, as silver tends to crystallize as silver oxides or phosphates[176–178], rather than entering the apatite lattice.

Iron

The incorporation of iron ions into bioceramics has been widely studied in recent decades, together with its neighbouring transition elements from the 4th period of periodic table (Mn, Co, Ni, Zn)[121], with the purpose to generate new bioceramics with magnetic properties. Indeed, super-paramagnetic iron oxide nanoparticles (SPIONs) are widely approved magnetic biomaterials (usually composed of magnetite Fe_3O_4 or maghemite γ-Fe_2O_3) as contrast agent in magnetic resonance imaging application for cancer diagnosis or hyperthermia-based cancer treatments. Nevertheless, their iron-oxide core causes also long-term cytotoxicity[140,148,181], therefore intensive effort is today dedicated to develop iron-doped magnetic ceramics preserving good biocompatibility and bioactivity.

In this respect, iron-doped calcium phosphate bone cement for magnetic hyperthermia were obtained, exhibiting improved osteoconductive and antibacterial properties [139,149,182–184]. A new concept of magnetic CaP was obtained by synthesizing apatite nanocrystals doped with $Fe^{2+/3+}$ ions[140,148], so as to generate intrinsic superparamagnetic ability, caused by specific positioning of Fe^{2+} and Fe^{3+} ions in the crystal lattice and in the outer hydrated layer of the apatite. Such a new phase exhibited magnetization ability similar to iron oxides, but excellent biocompatibility and enhanced osteogenic ability [185].

Fluorine

Fluorine ions take part in several biochemical processes, becoming particularly important for oral care application, neuro-modulation and bone structure[138]. Fluorine promotes the osteoblast proliferation and inhibits the osteoclast activation and differentiation; moreover, when present in low concentration it can enhance in vivo bone formation[138,152,153].

The substitution of OH^- groups of apatite with F^- ions accelerated the crystallization process, increased the stability of the crystals while decreasing their solubility[138,150]. The incorporation of fluorine also affected the crystal morphology, towards flattened hexagonal rod-like shapes [150]. Fluorine-doped HA exhibited also an antibacterial behaviour, inhibiting the adhesion and proliferation of bacteria typically detected in oral environment[138,153,154].

1.5. Calcium-phosphate scaffolds in bone tissue regeneration

As aforementioned in section 1.3, development the ideal bone scaffold is challenging. Indeed, in the development of bone scaffold, it is essential to assess the comprehensive characteristics of the bone defect site, including mechanical properties, composition and pore network, to reflect the site's requirements for regeneration.

Several scaffolds have been developed for the regeneration of various bone regions over the last two decades[186–191]. Macroporous sintered scaffolds are commonly used in cranioplasty and maxillofacial surgery, bone cement in minimally invasive surgery such as vertebroplasty and spinal fusion or as bone filler or joint replacement, biomorphic scaffold in the regeneration of load bearing bone, biomineralized collagen/hydroxyapatite scaffold for osteochondral regeneration and 3D printed scaffold for the regeneration of bone defects with complex morphology[186–191]. Calcium-phosphate based scaffolds used in the regeneration of different bone regions are summarized in the following figure (Figure 13).

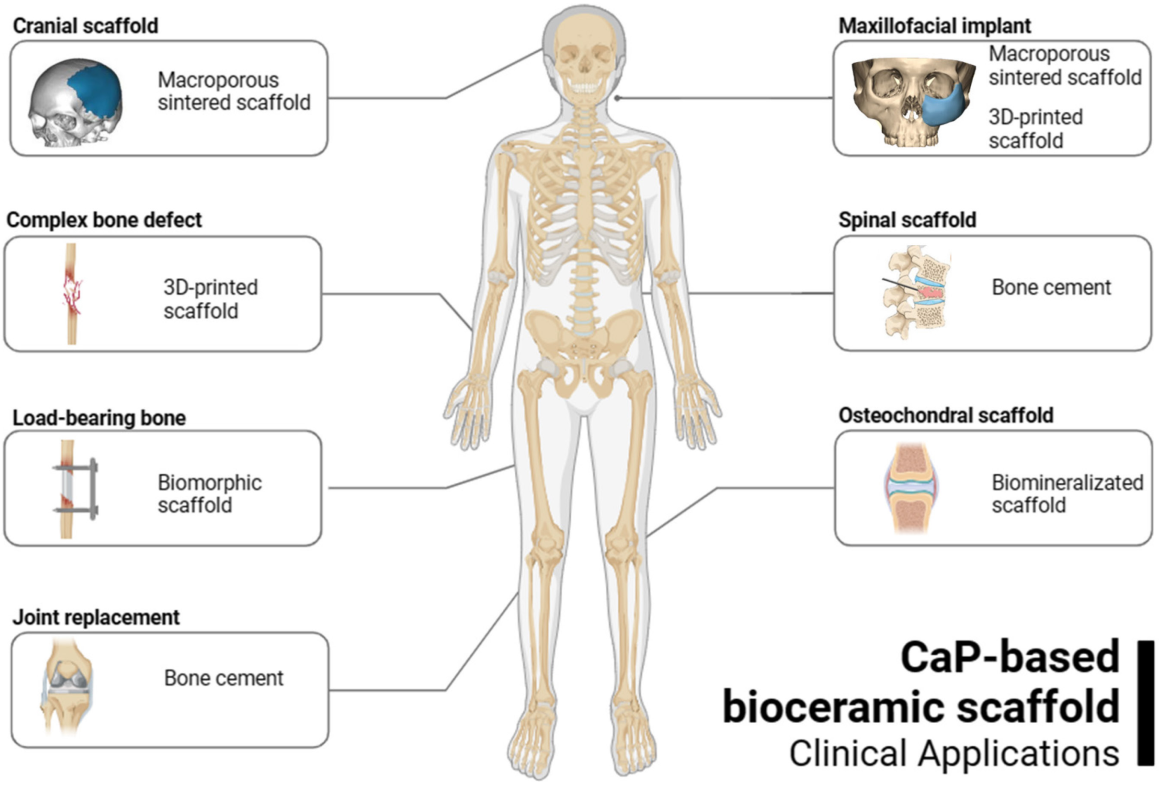

Figure 13. Calcium-phosphate scaffold for the regeneration of different bone regions

Tissue replacement and regeneration involve the development of three-dimensional porous scaffolds able to provide adequate space for bone cells and their communication without losing their mechanical environment[17]. Indeed, the biological events occurring upon implantation of a scaffold for BTR are strongly influenced by pore size distribution[4,17]. One of the main targets in the design of biomimetic CaP ceramic scaffolds is the ability to create a micro-environment stimulating cell differentiation into osteoblasts and to stimulate cell chemotaxis and new bone matrix deposition[13,191]. The morphological properties of scaffolds in terms of pore volume and size are important at both macroscopic and microscopic level. It was reported that osteointegration and angiogenesis can be favoured by interconnected macroporosity (100–600 µm) with channel-like microporosity[4,13]. An increase in pore size is generally associated with an increase in permeability and new bone ingrowth, while small pores are more suitable for soft tissue ingrowth. Over the past two decades, several technologies have been developed for the manufacturing of highly porous bioceramic-based scaffold for BTR[11–13,191–193].

Although HA-based scaffold has many advantages in terms of bioactivity and bioavailability, it is limited by fragility, typical of ceramic materials, poor mechanical strength and thus inability to withstand severe load-bearing condition[194]. One of the most common ways to confer mechanical properties of CaPs materials is via densification processes obtained through high-temperature sintering processes[194]. Even though densification usually results in scaffolds with superior mechanical strength, the properties of CaPs materials in terms of crystallinity, grain size, porosity and composition vary significantly upon sintering. High crystallinity, low porosity and small grain size tend to give higher stiffness, compressive strength and toughness but hamper tissue growth and binding of bone-resorbing cells[194].

The following sections describe the primary processing methods for porous scaffolds: partial sintering, the replica method, sacrificial templates, direct foaming, low-temperature self-hardening techniques, biomorphic and biomimetic synthesis and 3D printing technology.

1.5.1. Processing routes to macroporous ceramics

The development of materials with tailored porosity has been matter of intense research in the last decades, particularly in the case of composite scaffolds for bone tissue regeneration, because of the crucial role of porosity into the structure to guide and facilitate the cell proliferation and neovascularization[195].

One of the first reported approach to tune the porosity of ceramics was the **partial sintering** process: the pore size distribution is mainly affected by powder particle size and sintering temperature, as higher sintering temperatures induce a significant decrease in intergranular porosity [196,197].

A great research effort has been also devoted to the preparation of macroporous bioceramic scaffolds, leading to the establishment of various techniques, including template-assisted techniques (replica and sacrificial template) and template-free (direct foaming) (Figure 14)[195,198].

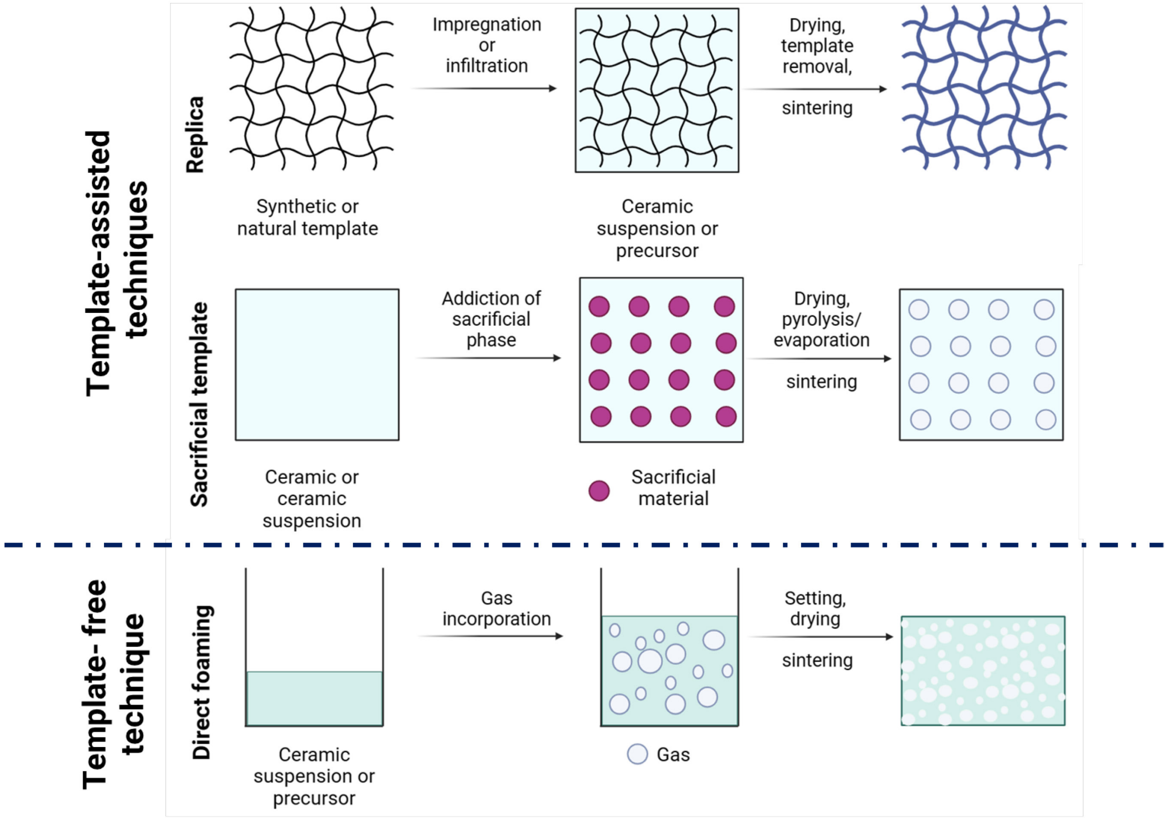

Figure 14. Schematic processing methods used for the fabrication of porous bioceramics; **(a)** template-assisted technique: replica; **(b)** template-assisted technique: sacrificial template; **(c)** template-free technique: direct foaming[195,199].

These methods generally involve the preparation of slurries, intended as aqueous suspensions of dispersed powders. Then, the slurries are properly manipulated, dried and thermally consolidated.

The **replica** method is a template-assisted technique based on the impregnation of a polymeric sponge with defined porous structure and pore size into the ceramic slurry in order to produce microporous structures exhibiting the original sponge morphology[199–202].

The templates used in this technique can be either synthetic or natural polymers (e.g., polyurethane and cellulose, respectively). The macroporous scaffolds obtained with this method can reach an anisotropic porosity ranging from 40% to 95% and are characterized by a cross-linked structure with highly interconnected pores ranging in size from 200 µm to 3 mm[195].

The **sacrificial template method** involves the homogeneous dispersion of sacrificial phases into a continuous matrix of ceramic particles or ceramic precursors, followed by drying and sintering. A wide variety of sacrificial materials can be used as pore-forming agents, including natural polymers (e.g., gelatine, potato starch, cotton), synthetic polymers (e.g., polymer beads, organic fibers, polyethylene), inorganic (e.g. NaCl, K_2SO_4). The removal of sacrificial materials from the matrix can be obtained by thermal treatments or chemical process. This method leads to porosity ranging from 20% to 90%, with average pore diameter 1-700 µm [195,201,203].

Template-free foaming techniques are particularly promising due to the absence of massive amounts of organic phases to be eliminated during the thermal consolidation[13,195]. Direct foaming represents an easy, cheap and fast way to prepare macroporous bioceramics with open porosity from 40% to 97% and pore size 10µm-1mm, by incorporating gas bubbles into ceramic slurries, followed by drying and sintering [193,201,202]. The total porosity volume is related to the amount of gas bubbles incorporated during the foaming process, whereas the pore size depends on the stability of the poured foam before drying [195,199].

The sacrificial template approach also includes freeze-casting method, based on the controlled freezing of liquid-based ceramic slurries[13]. The freezing of the liquid, generally water, induces the formation of anisotropic ice structures, intended as fugitive materials, during the subsequent freeze-drying process [204]. The efficacy of the process is affected by several parameters, including the viscosity of the slurry, the solvent, the freezing control in space and time [13,204]. Typical structures obtained by freeze casting methods showed well-defined pore connectivity along with directional and completely open porosity such as a lamellar morphology after sintering[201]. The channel-like anisotropic porosity obtained by freeze-casting method may lead to scaffolds with channels similar to cortical bone, particularly useful for long-bone applications[13].

1.5.2. Low-temperature self-hardening ceramics

The possibility to obtain bioactive ceramics through low-temperature self-hardening processes has been widely explored in the form of bone cement for injectable orthopaedic applications, including spinal fusion, vertebroplasty and kyphoplasty [88,127,189,205,206]

Calcium phosphate cements (CPC) were discovered by Brown and Chow in the 1980s[102,110,207], overcoming the drawbacks of polymethyl-methacrylate (PMMA) cements in terms of exothermic polymerization hardening and chemical composition. In this respect, CPCs exhibit bioactivity, bioresorbability and a physiological hardening at 37°C, also allowing the incorporation of biomolecules[102]. The main drawback of CPCs hampering their clinical applications is related to their poor mechanical performance, which limits their applicability to a moderate- or non-load-bearing situation [4,208].

CPCs can be classified by several parameters, including the number of components in the solid phase, the type of setting reaction and the type of end product (Table VI) [102,126].

Table VI. *Classification of CPC*

	Apatitic CPC		*Brushitic CPC*
	Single Component	*Multiple Components*	
Reactives	α-TCP	TTCP + DCPA/DCPD	β-TCP + MCPM/MCPA
Reaction type	Hydrolysis	Acid-Base	
Reaction	$3\alpha - Ca_3(PO_4)_2 + H_2O \rightarrow$ $Ca_9(HPO_4)(PO_4)_5(\mathrm{OH})$	$Ca_4(PO_4)_2O + 2CaHPO_4$ $\rightarrow Ca_{10}(PO_4)_6(\mathrm{OH})$	$\beta - Ca_3(PO_4)_2 + Ca(H_2PO_4)_2 \cdot H_2O$ $+7H_2O \rightarrow 4CaHPO_4 \cdot 2H_2O$

Many different CPCs formulations have been developed, which can be divided into two groups based on the type of end-product: brushite (DCPD) and apatite (HA or CDHA) cements. Both brushite and apatite CPCs are produced upon mixing one or more CaPs powders with aqueous solutions, which induces the dissolution of the initial CaPs; this is followed by precipitation into crystals of DCPD, HA, or CDHA depending on the compositions of the powders and the setting reactions that take place[126,209]. During precipitation, new apatitic crystals grow and their physical entanglement causes the hardening or setting at body temperature[4] . Therefore, the recrystallization process forms a network of intertwining elongated particles that can assume different shapes including needle-like morphology, favoured by small particle size, with higher surface area and supersaturation degree. On the contrary, a larger plate is favoured when the particles are larger (Figure 15)[127].

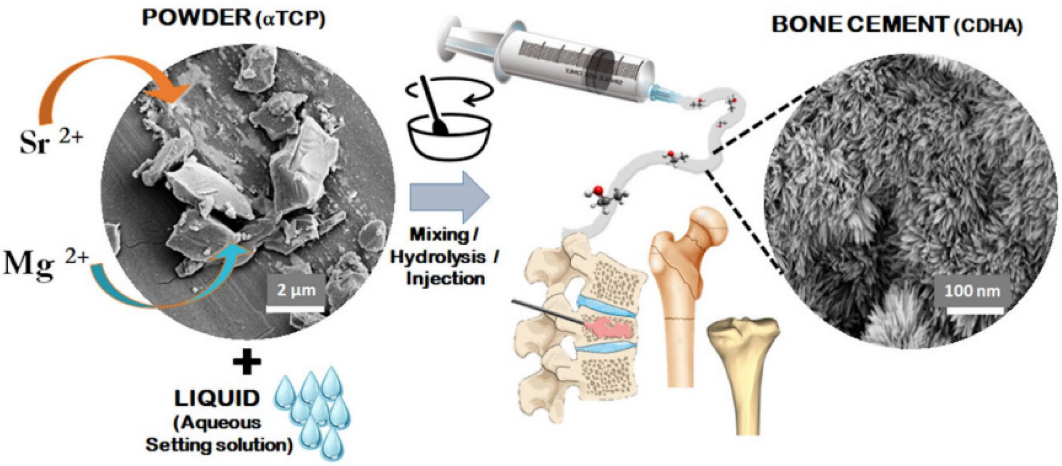

***Figure 15.** Scheme showing the mechanism of formation of apatitic bone cements and their applicability in bone regeneration[127].*

Apatitic CPCs can be obtained by mixing single or multi-components with aqueous solutions that undergo hydrolysis or acid–base reactions, respectively. In the first case, the end product is calcium-deficient hydroxyapatite (CDHA) and in the latter, it is stoichiometric HA or brushite[102,205]. Some examples are as follows:

Hydrolysis of metastable α-TCP:

$$3\ \alpha - Ca_3(PO_4)_2 + H_2O \rightarrow Ca_9(HPO_4)(PO_4)_5OH \qquad \textit{(Reaction 2)}$$

Acid–base reaction between tetra-calcium phosphate, TTCP (basic) and dicalcium phosphate anhydrous, DCPA (acidic):

$$Ca_4(PO_4)_2O + CaHPO_4 \rightarrow Ca_5(PO_4)_3OH \qquad \textit{(Reaction 3)}$$

Brushite CPC obtained by an acid–base reaction between TCP (almost neutral) and monocalcium phosphate monohydrate, MCPM (acidic):

$$\beta - Ca_3(PO_4)_2 + Ca(H_2PO_4)_2 \cdot H_2O + 7H_2O \rightarrow 4CaHPO_4 \cdot 2H_2O \qquad \textit{(Reaction 4)}$$

The approach based on the α-TCP hydrolysis is particularly interesting because it allows processing a single component that can be obtained by solid-state reactions, thus giving rise to pure apatitic bone cement[127]. Moreover, since the setting reaction takes place under in vivo conditions with a dissolution-precipitation process, without changings in terms of temperature and pH, leads to a precipitated calcium-deficient hydroxyapatite with an interconnected microporosity, which is chemically and structurally similar to biological apatites[210]. As mentioned in the section 1.4.4. foreign ions can be introduced in the structure of α-TCP during its synthesis, thus affecting its reactivity with water and the hydrolysis kinetics, but also the formation of ion- doped apatite upon setting, potentially affecting the biologic and mechanical performance of the set cement[4,127,167].

Two of the most important parameters that play a key role in the final CPC features are the liquid-to-powder ratio (LPR) and the particle size of the starting powder [97,102]. The LPR influences setting time, injectability, cohesion, mechanical properties and the porosity of harder CPC. The setting time is the "*time required from the start of powdered agent and liquid agent blending until hardening of the cement*", according to ISO/DIS 18531 for CaPs[88] and influences the clinical applicability of both apatite and brushite cements as well as their injectability[88] .

Both particle size and the LPR influence the final surface morphology of the brushite or apatite crystals and the total porosity of the final scaffolds, which affects the mechanical performance and the resorbability of scaffolds and therefore the overall bioactivity (Table VII) [97,102]. The reduction in the particle size of CaPs increases the surface area, thus affecting the reaction kinetics and yielding small needle-like crystals rather than large plate-like crystals as observed when larger CaP precursor particles are used[126]. Moreover, the porosity is also attributed to the amount of liquid phase used. Thus, by increasing the LPR, the amount of liquid phase decreases and the porosity increases. This effect of the LPR explains the difference between brushite and apatite cement in terms of microstructure porosity: the water consumption during the setting reaction of brushite cement is larger than that of the apatite, which leads to the formation of a larger crystal size and makes the total porosity smaller and average pore size greater than those of the apatitic cements[97].

***Table VII**. Effect of particle size and liquid-to-powder ratio on the crystals' morphology and pore distribution*

	Particle Size		**Liquid-to-Powder Ratio**	
	Fine Particles	*Coarse Particles*	*Low L/P*	*High L/P*
Final crystal morphology	Needle-like crystals	Plate-like crystals	Low inter-aggregate distance	High inter-aggregate distance
Pore size distribution	Fine	Coarse	Fine	Coarse

In general, the typical porosity of CPC ranges between nano- and micrometre size, allowing the flow of physiological fluids within the microstructure of the cement[207]- One of the advantages of CPC is the room-temperature self-hardening mechanism, which, combined with the intrinsic porosity, allows the incorporation of drugs, biologically active molecules and cells, obtaining drug delivery materials[102,211,212].

1.5.3. Biomorphic transformation

Bone mechano-transduction process is a biological phenomenon that is able to effectively translate the external mechanical stimuli exerted on the skeletal system into bio-electric signals, that can instruct bone cells to activate and sustain the continuous bone remodelling and self-repair upon damage[17,213]. Therefore, its activation is very important when it comes to regenerating the load-bearing bone parts. However, the reproduction of the complex biomechanical ability of bone tissue is quite a challenge. To date, it prevented the achievement of scaffold which are effective in healing load-bearing bone defect[17,213].

The exceptional mechanical performance of the bones is mainly due to their structure, hierarchically organized from the nano- to the macro- scale and the interaction that takes place at all levels of this organization. For this reason, long bone regeneration should be assisted by a scaffold with similar bone composition and structural complexity[13,214]. The conventional production methods do not produce inorganic and mechanically resistant scaffolds with bioactivity and hierarchical pore organization. The expression of chemical biomimesis in scaffolding for long bone regeneration is made difficult by the reduced mechanical strength of apatitic-based materials[13,214]. A valid approach to obtain bioceramic scaffolding with a complex structural hierarchy is based on biomorphic transformations of natural structures that mimic the morphology and microstructure of the target tissue [209,215].

Since 1970s, biomorphic transformations from natural sources have been proposed for the fabrication of bioceramic scaffolds due to their 3D highly interconnected porous architecture, including the replica of the porous microstructure of $CaCO_3$-based corals which are impossible to create artificially, replica of marine sponges, soft vegetal structures and fruits and wood-template bioceramics [209,216–218].

The approach of wood biotransformation is particularly interesting as many ligneous species exhibit a porous and hierarchically organized structure very close to that of cortical and cancellous bone. The transformation of wood generally involves pyrolysis followed by a hydrothermal treatment; in particular, a complex multi-step strategy to convert rattan wood structures into biomimetic HA scaffolds was proposed[219,220]. Especially, several subsequent and strictly controlled reactions are required, including: i) *pyrolysis* of wood to produce carbon template: ii) *carburization*, calcium infiltration to transform carbon in CaC_2; iii) *oxidation* process that leads to CaO formation; iv) *carbonation* by hydrothermal process or by heterogeneous processes carried out at supercritical conditions and high pressure and finally v) *phosphorylation* through hydrothermal process generating biomimetic, hierarchically organized scaffolds made of ion-doped HA (Figure 16).

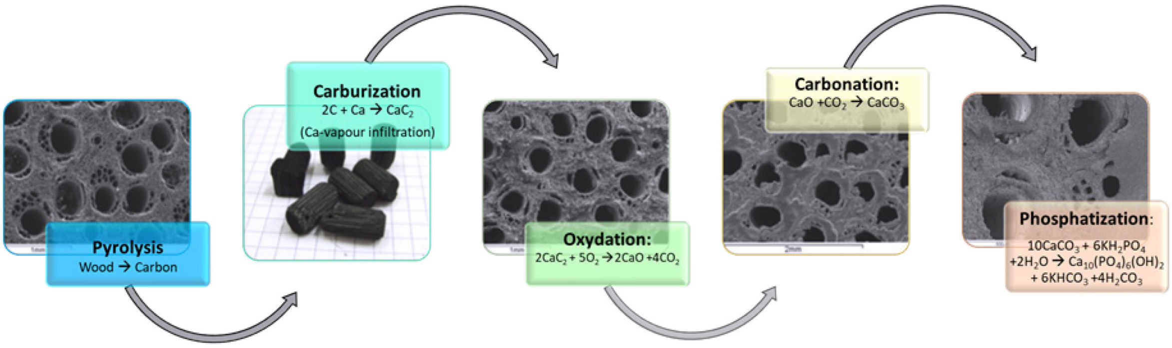

Figure 16. Multi-step transformation process of natural wood into biomorphic HA scaffold[13,214].

Biomorphic apatite scaffolds derived from rattan wood showed the ability to completely regenerate metatarsal bone defect in sheep, showing the complete bio-resorption of the scaffold which allowed the well-organized bone with mechanical properties to reproduce the original bone tissue[17,188]. The regeneration of load-bearing segmental bone is among the most relevant challenges considered in orthopaedics. Therefore, this result confirms that the heterogeneous chemical reactions are a promising approach to transform natural structures into 3D nanostructured apatitic scaffolds, recapitulating the major properties relevant for the inducement of bone regeneration in terms of composition, porosity, structure and mechanics[17] (figure 16).

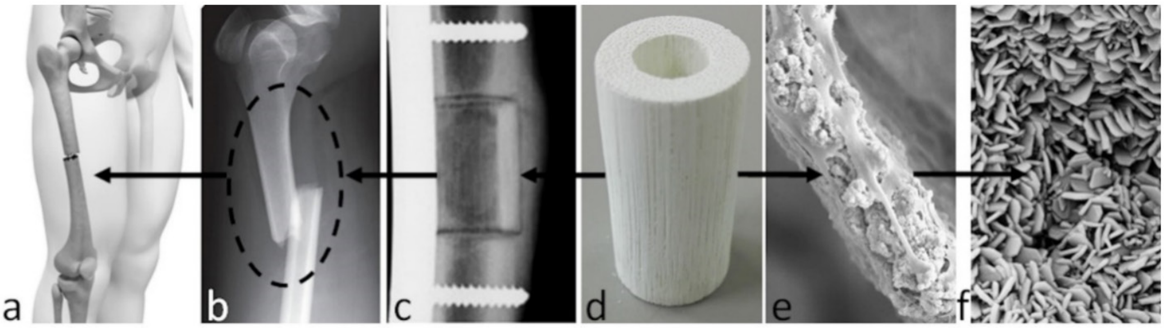

Figure 17. Biomorphic scaffolds for long bone regeneration and their application in long bone defects: (a) example of implantation site; (b) critical size defect; (c) radiography of implanted scaffold; (d) bone scaffold from wood; (e) scaffold–cell interaction, 250×; (f) scaffold nanostructure, 25,000×[127].

1.5.4. Biomineralization process

In the early of 2000s, a new approach for bone scaffolding was created through a bio-inspired manufacturing method with the objective of creating a 3D construct that closely imitates the physicochemical, morphological, and structural characteristics of hard human tissue [27,118,221].

As mentioned in section 1.1, biomineralization process is a complex phenomenon in which natural organisms generate a nanostructured hybrid inorganic/organic construct, characterized by inorganic nanocrystals grown on self-assembling bioorganic structure acting as a template and substrate guiding and controlling heterogeneous nucleation process[127]. In particular, mammalian hard tissue is formed by a biomineralization process, in which collagen-based components act as a template for the heterogeneous nucleation of ion-substituted HA through chemical, physical, morphological and structural control mechanisms[7,13].

It is possible to reproduce this process in the laboratory exactly as it occurs in nature. These bio-inspired mineralization processes involved the use of biopolymers, particularly type-I collagen fibrils, dispersed in an aqueous solution of ions generally involved in bone formation processes, the amount of which can determine the extent of the mineral phase in the biocomposite[17,118,127]. It is interesting to note that in these hybrid construct, the mineral phase is not simply embedded but heterogeneously nucleated on a bio-organic matrix. This more closely mimics the ultrastructural features of bone tissue[17]. In this context, fibrous hybrid materials may also have the potential to mimic the different mineral compositions found in multifunctional tissue, such as osteochondral or periodontium[17,127,222] (figure 17).

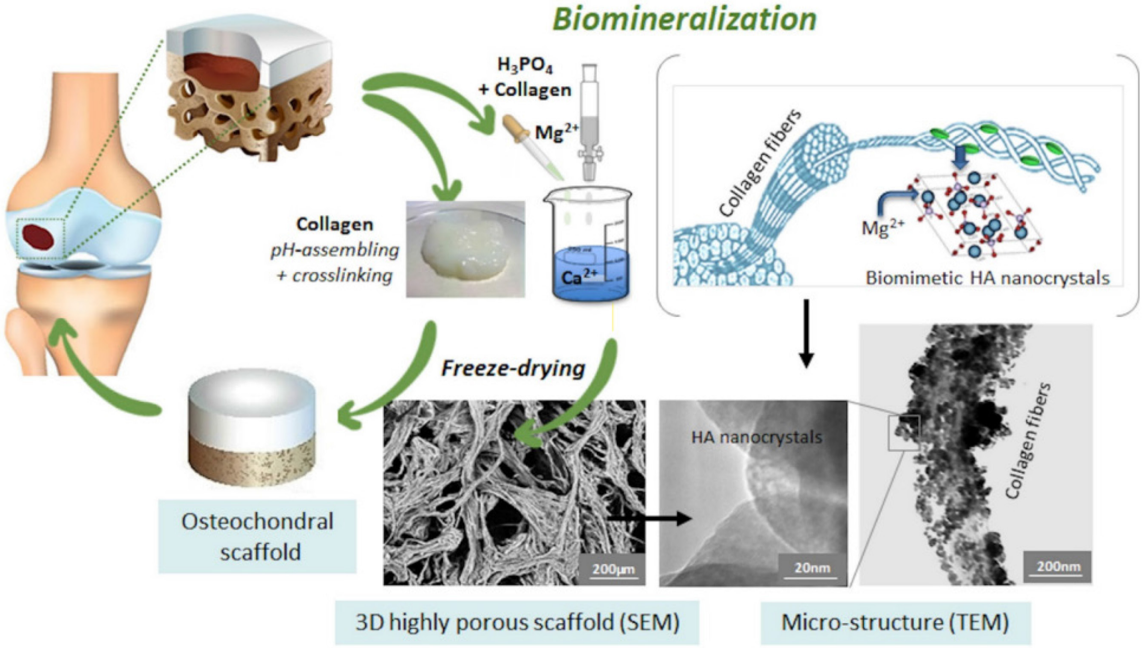

Figure 18.*Scheme of the bioinspired mineralisation process to develop osteochondral scaffolds*[127].

Therefore, this approach should address a relevant clinical need related to osteochondral defect repair[223,224], using a 3D biomimetic scaffold that simultaneously exhibits bioactive composition, porous fibrous structure and good malleability, capable of mimicking the different osteochondral regions, namely bone, tidemark and articular cartilage[17]. Bio-inspired hybrid materials have excellent capabilities in bone defect regeneration and offer the possibility of developing new promising alternatives for osteochondral defect regeneration[225]. An *in vivo* study of collagen/apatite hybrids in sheep demonstrated that the different layers of the scaffold induced specific cell differentiation into osteoblasts (in the osseous region) and chondrocytes (in the cartilaginous region) with the formation of osteochondral tissue with an ordered histoarchitecture[226], confirming the regenerative capacity enhanced by the high mimicry of osteochondral regions. Several clinical trials have also used hybrid HA/collagen osteochondral scaffolds. A striking aspect of the biomimetic approach, which has also been confirmed by clinical studies, is the achievement of devices that are able to modulate the behaviour of the cells solely by means of physicochemical and structural features, without the use of additional growth factors. However, these hybrid fibrous structures generally lack the mechanical properties that would allow them to be used in load-bearing areas, so technological advances are highly desired and expected in the coming decades, with a view to reducing recourse to invasive metallic joint reconstruction prostheses, which are currently the only solution available to patients suffering from osteochondral disease[5].

1.5.5. 3D-printing technique

Three-dimensional (3D) printing represents an additive manufacturing (AM) technique (also known as rapid prototyping) to produce complex-shape devices with complex geometry and design flexibility from 3D model schemes[227–231]. A wide range of materials has been employed with 3D-printing techniques, including metals, polymers, ceramics and composites[229,230].

Different 3D printing methods have been proposed[228–234]. Extrusion-based techniques consist on the deposition of ink to create designed structures, by forcing the ink through a nozzle[232] as a melt, in Fused Deposition Modelling (FDM), or viscous suspensions, in Direct Ink Writing (DIW), to form lines that solidify onto a build plate[234].

DIW represents an easy manufacturing technique which allows creating a wide range of structures, from solid monolithic part to high complex porous scaffolds and composite materials[232]. The use of pastes also allows for shape retention owing to the high solid loading and viscoelastic properties. The use of high viscous inks requires larger diameter nozzles compared to the conventional inkjet printing ink, it can therefore be used successfully to print extremely viscous pastes HA-based [232].

3D-printing technology finds a wide range of biomedical applications: craniofacial implants, dental models, prosthetic parts, scaffold for tissue regenerations (bone and skin), organ printing, tumour therapy and tissue model for drug discovery[227,228,235]. In this kinds of applications printable materials are formulated from biomaterials and bio-inspired materials to achieve patient-specific scaffolds with high structural complexity[227–230]. Moreover, printable biomaterials should be biocompatible and bioactive and should have good degradation kinetics, appropriated mechanical properties, give desirable cellular responses and exhibit tissue biomimicry [229,234].

Bioceramic powders, natural or synthetic hydrogels, polymers and their composites have been used as raw materials to formulate inks for 3D printing. Bioceramics commonly printed are calcium phosphate-based bioceramics (HA, TCP and biphasic CaPs), calcium silicate-based bioceramics and bioactive glasses[229,235]. Moreover, the precise tuning of the macro- and micro-porosity permitted by the 3D-printing technology not only allows the fabrication of scaffolds with hierarchical porosity but also leads to the controlled release of biomolecules or drug loaded in the scaffold matrix or adsorbed on the scaffold surface[186,229,236]. 3D-printed bioceramics include: *i)* sintered 3D-printed bioceramics, *ii)* non-sintered 3D-printed bioceramics and *iii)* composites with polymers[229].

In the first case, bioceramic scaffolds are printed and sintered, removing the organic phases and improving the mechanical properties of the structure[229]. In the presence of biologically active ions, like magnesium or strontium, in addition to an improvement of mechanical properties it was also reported an increase in biological performance in vivo[237]. Another study described biphasic CaP scaffolds (HA:β-TCP with a weight ratio 60:40) coated with calcium peroxide and polycaprolactone (PCL) in order to promote bone growth with greater proliferation of osteoblasts under hypoxic conditions, following the release of oxygen dependent on the concentration of calcium peroxide in the PCL coating[238].

In non-sintered 3D-printed bioceramics, a small amount of organic solvent are used as a binder for bioceramic powders and are not removed after printing[229]. Sun et al developed porous 3D scaffold of biodegradable CaP loaded with antibiotics for the regeneration of the bone tissue of the jaw, achieving a controlled drug release. This scaffold was based on HA or biphasic mixture of CaP (β-TCP and HA with weight ratio of 1:1) cross-linked with sodium alginate in the presence of the drug, the paste is then extruded by the 3D printer. By modulating the degree and the time of cross-linking it is possible to control the drug release kinetics. *In vitro* studies show low cytotoxicity and good cell adhesion and proliferation on the scaffold surface[186].

Bioceramic/polymer composite are synthesized to combine the bioactivity and osteoconductivity of bioceramics with the handling performance of polymers [229]. For example, the presence of strontium-doped HA nanoparticles in 3D printed PCL scaffolds leads to a significant increase in cell proliferation and bone regeneration, thanks to the simultaneous release of calcium and strontium ions, associated to an improvement in mechanical properties as related to the inorganic phase content[239]. HA nanoparticles were also used as external coating for 3D-printed polymer scaffolds, in order to enhance cell proliferation and differentiation while also strengthening the scaffold [240].

Recently, 4D printing approaches have been developed which, in addition to three-dimensional spatial control, introduces the concept of temporal control, i.e., active smart materials responsive and mechanically converted into other shapes via external stimuli. This technique enables the production of smart 3D scaffolds responding to external stimuli, such as changes in pH and temperature or when subjected to magnetism or light radiation of adequate energy [228,241].

1.6. Enhancing the biological performance of bioceramics

The *biofunctionalization* can be defined as the modification of a material to achieve improved biological function and/or stimulus, whether permanent or temporary. The biofunctionality of scaffolds for regenerative medicine has been considered to play a key role for effective tissue regeneration[242,243]. Several parameters can be tuned, including surface energy and roughness, Ca/P ratio, solubility, particle size and crystallinity, in order to improve the biological events beyond the interaction with biological environment, e.g. protein adsorption, cell attachment, cell proliferation and cell differentiation[135,244,245] (Table VIII).

Table VIII. *Effects of structural size, morphology and roughness surface of CaP biomaterials on cellular behaviour*[4,246]

Surface structure	***Parameters (size, morphology, roughness)***	***Biological function***	
		Enhance	***Decrease***
Micro/nano size (CaPs)	Microgroove width: From 20-40 um to 60-100 um	Cell number inside the pattern	Cell alignment and orientation
	Micrigroove depth From 3 um to 5.5 um		Cell adhesion force
	Microgroove depth pattern: from nano-hybrid to micro-hybrid	Cell adhesion, proliferation, osteogenesis	
Micro/nano Morphology (CaP)	Micro-morphology: Plate-like and net-like	Cell attachment expansion	
	Nano-morphology Plate-like and wire-like	osteogenesis	
Micro/nano Roughness (CaP)	Micro roughness Ra from 1 um to 2 um	Cell attachment Osteogenesis	
	Nano-roughness Ra from 5,3 nm to 9,8 nm	Focal adhesion Osteogenesis	

The architecture of biomimetic scaffolds greatly affects the chance to obtain a suitable microenvironment for bone regeneration. The presence of a diffuse macroporosity favours cell adhesion, cell proliferation and vascular growth. In turn, the surface micro-architecture enhances protein adsorption[135] and specific nano-topography could directly modulate the osteogenic differentiation, producing a favourable osteoimmune microenvironment[244]. Among the various microstructures, microgrooves have strong effects in the regulation of cell orientation and adhesion[246,247]. The width of the micro-channels controls the orientation while the depth regulates the adhesion strength of the cells, which decreases as the depth of the groove increases[246]. Micro-nano-hybrid structures (micropattern-nanorod-hybrid structure) showed higher cell adhesion, proliferation and alkaline phosphatase protein (ALP) activity than a single-scale structure (including nanorods and micropatterns)[246,248].

Surface roughness also plays a crucial role in cellular behaviour[246,249,250]. It was demonstrated that specifically designed roughness can enhance osteogenesis thanks to modulated concentration of calcium ions and osteocalcin in the grooves [250].

Another important parameter in cell behaviour modulation is the chemistry of the surface. The crystallinity of nanometric bioceramics, i.e. ACP and HA, was observed to affect the cell attachment efficiency, proliferation and differentiation of bone marrow-derived mesenchymal stem/stromal cells (BMSCs) [245]. Nano-HA allows a better adhesion, proliferation and differentiation of BMSCs into osteoblasts than ACP. The chemical approach of creating functional groups on the surface of the scaffolds is also promising to improve cell adhesion and osteogenic differentiation [244,246]. For example, functional groups such as $-COOH$ and $-NH_2$ improve the protein adsorption thanks to the formation of hydrogen bonds linking proteins, finally resulting in improved cell adhesion[244].

1.7. Calcium phosphate as drug-delivery system

Drugs are substances used for the prevention, treatment, or alleviation of disease and for the correction or repair of the consequences of disease. All drugs, whatever they are, have three important parameters that must be considered: the *dose* to be administered, the *time* between doses and the *total period* of use[55]. Regardless of the delivery system (oral or intravenous), drugs enter the bloodstream before reaching the target tissue/organ. Along the way, other processes may take place (e.g., biotransformation into another compound or elimination of the drug) which may lead to variations in drug concentration. The typical routes of drug administration and the corresponding plasma concentration profile as a function of time are shown in the next figure (Figure 16)[55].

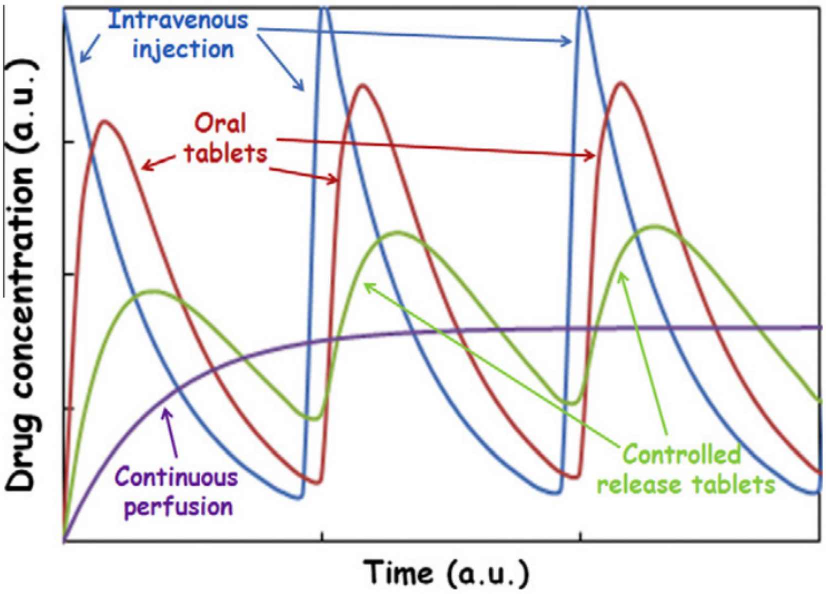

Figure 19. *Plot of drug concentration vs time for the most common drug administration way*[55].

Drugs with ideal pharmacokinetic behaviour should maintain the minimum effective concentration in blood without reaching toxic level[55]. In fact, current therapy for the treatment of bone disorders and diseases, such as infections and tumour, involves the surgical removal of the affected bone and the systemic administration of high drug doses to achieve an effective drug concentration in bone tissue. However, the high drug concentration in the blood can induce serious side effects in other organs and tissues[40,251,252]. Therefore, the controlled drug delivery is an essential tool to improve current therapy[55]. Particularly, the development of devices that can combine the bone defect regeneration and, at the same time, deliver the effective drug dose to the bone disorder site, without reaching toxic levels in the blood, is an active research area[40]. Hence, in the last decades, different drug delivery systems have been developed for bone affected by metabolic dysfunction (e.g. osteoporosis) or disease (bone infections, bone cancer), including hydroxyapatite nanoparticles (HA-NPs) and medicated scaffolds based on calcium phosphate[59,251–253].

The possibility of incorporating additional functions such as antimicrobial or antitumoral properties into osteoconductive and osteoinductive biomimetic apatite scaffolds can be seen as an ingenious way of tailoring bone repair biomaterials to the needs of the patient[50].

Therefore, in this Ph.D. Thesis is reported the research work aimed to develop bioactive apatitic-based scaffolds able to deliver ions and drugs locally, aimed to develop new therapies for the treatment of bone disorders and disease by combining the regenerative ability of calcium phosphate-based bone scaffold and the drugs clinically used (a schematic representation is shown in Figure 20).

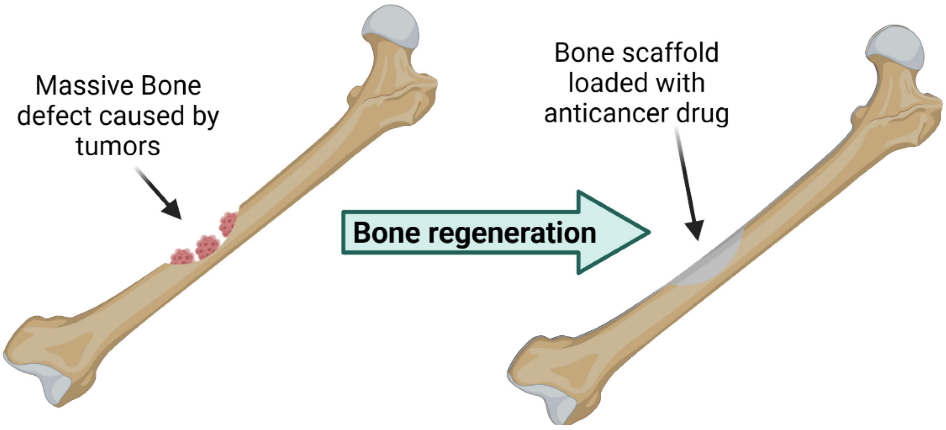

Figure 20. *Schematic representation of bone healing process by applying a device able to combine the bone defect regeneration and deliver an effective drug dose.*

Different apatitic-based bone scaffold was developed as delivery system in this research activity, and include:

- Macroporous sintered scaffolds, which are characterized by open and interconnected macroporosity commonly used in the reconstruction of cranial and craniofacial bone defects.
- Strontium-doped apatitic bone cement, which are characterized by microporosity and are commonly used as bone filler and in spinal surgery.

- Biomorphic scaffolds (b.Bone™ bone substitute, *Greenbone Ortho S.p.A.*), which are characterized by canicular and hierarchical pore structure that mimic the osteon 3D architecture and are commonly used in the regeneration of load-bearing bone.

Apatitic-based bone scaffolds were functionalizing with different types of drugs ranging from antimicrobial (tetracycline) to anti-tumoral (doxorubicin, methotrexate, and everolimus and denosumab), characterized by different physicochemical properties, such as hydrophilicity/hydrophobicity and size. Moreover, the mechanisms governing the drug release, crucial for the clinical application in the local drug administration, have been investigated.

1.7.1. Drugs of interest

Antibiotics

As aforementioned in section 1.1.2., one of the major problems associated with the implantation of scaffolds is postoperative infection, particularly the formation of bacterial biofilms on the surface of the implants which usually leads to implant failure[48–50]. Although the use of systemic administration of antibiotics is widespread, it cannot be targeted to the surgical site and the determination of appropriate dosages remains sensitive[50]. Moreover, antimicrobial resistance is a global public health problem that may be accelerated by the overuse of antibiotics worldwide[56–58].

It is therefore particularly attractive to be able to transfer some antimicrobial functions (antibiotics and antimicrobial ions) directly to the implanted biomaterials[50].

Tetracyclines are a family of antibiotics discovered in the 1940s. They are widely used as a broad-spectrum antibiotics, active against a wide range of gram-negative and gram-positive microorganisms[50,254]. Tetracycline (TC, molecular weight 444,44 $gmol^{-1}$, figure 21a) prevent growth of bacteria by reversibly interaction with the ribosome to inhibit bacteria protein synthesis and display a reversible bacteriostatic effect (figure 21b)[254–257].

TC molecules consist of a linear fused tetracyclic nucleus to which a variety of functional groups are attached and the retention of the linear fused tetracycle is one of the most important features of tetracycline for antibacterial activity[254]. TC is high soluble amphoteric drug, characterized by an pH-sensitive behaviour and photosensitivity[258]. Moreover, TC is a strong chelating agent and both pharmacokinetics and antibacterial activity are influenced by the chelation of metal ions[254]. In particular, a pH-sensitive behaviour just mentioned of TC was previously observed[259], specially three different forms exist in function of pH: *cationic*, at pH < 3.3, *zwitterionic*, at pH 3.3–7.7 and *anionic* at pH > 7.7; when pH reaches above 7.0, about 25% of TC exists in the anionic form[48], showing high affinity of TC with calcium ions [48,253,260].

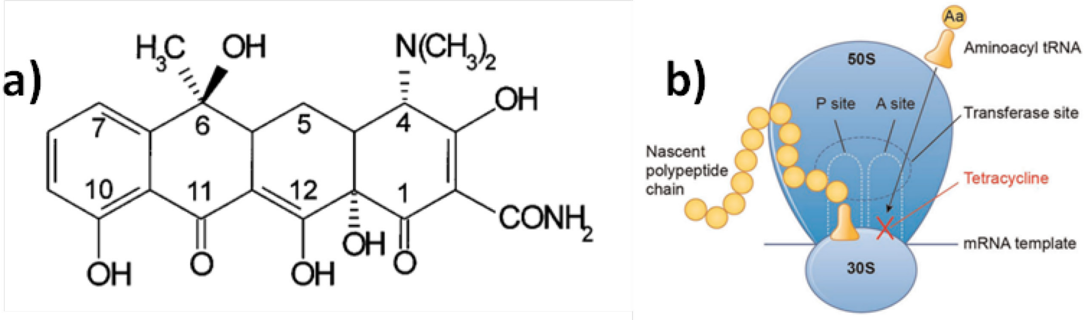

Figure 21. a) *Molecular structure of tetracycline* [256] *and* ***b)*** *its mechanism of action*[257]

Anticancer drugs

The *Associazione Italiana per la Ricerca contro il Cancro* (*AIRC*) estimates that about 350 new cases of primary bone cancer are diagnosed each year in Italy, while metastases from other cancers, such as breast or prostate cancer, are much more common, with an incidence of about 35,000 new cases per year (estimated by the *Associazione Italiana Oncologia Medica*, *AIOM*)[261].

Doxorubicin (Dox, molecular weight 543,53 $gmol^{-1}$) is widely used in cancer chemotherapy due to its broad spectrum of antitumor activity[262] against cancers of the hard tissue sarcoma[263], bladder, breast, stomach, lung, ovaries, thyroid, soft tissue sarcoma, multiple myeloma, and Hodgkin's lymphom[264]. Its chemical structure consist in anthracycline antibiotic with three planar and aromatic hydroxyanthraquinone rings (Figure 22a)[262] and it’s characterized by high solubility at acidic pH and an isoelectric point at about pH 8[265]. Dox acts by two mechanisms: *i)* by intercalating into and within DNA and interfering with the topoisomerase II-mediated DNA repair mechanism and *ii)* by releasing free radicals that cause damage to cell membranes, DNA and proteins (figure 22b)[266]. The significant side effects related to cardiac function and liver toxicity are a major problem associated with Dox administration.

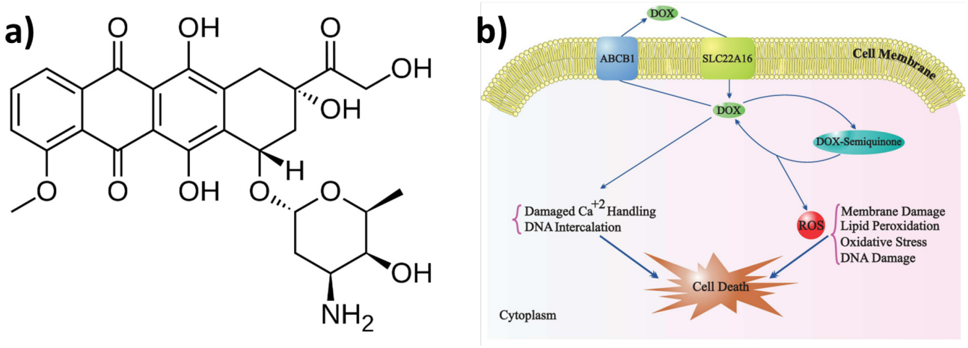

Figure 22. a) Molecular structure of Doxorubicin and b) its mechanism of action[266]

Methotrexate (MTX, molecular weight 454,44 gmol^{-1} figure 22a) is an antimetabolite drug, a competitive antagonist for folic acid. It is thought to affect cancer by competitive inhibition of dihydrofolate reductase (DHFR), an enzyme ultimately participating in DNA synthesis. In particular, it is widely used in the treatment of osteosarcoma[68], rheumatoid arthritis (figure 22b)[267], psoriasis and is useful in inflammatory bowel disease, multiple sclerosis and other connective tissue disease and transplantation thanks to its beneficial anti-inflammatory and immunomodulatory activity[268]. MTX is poor soluble in water due to the presence of glutamic acid moiety in its chemical structure[269]

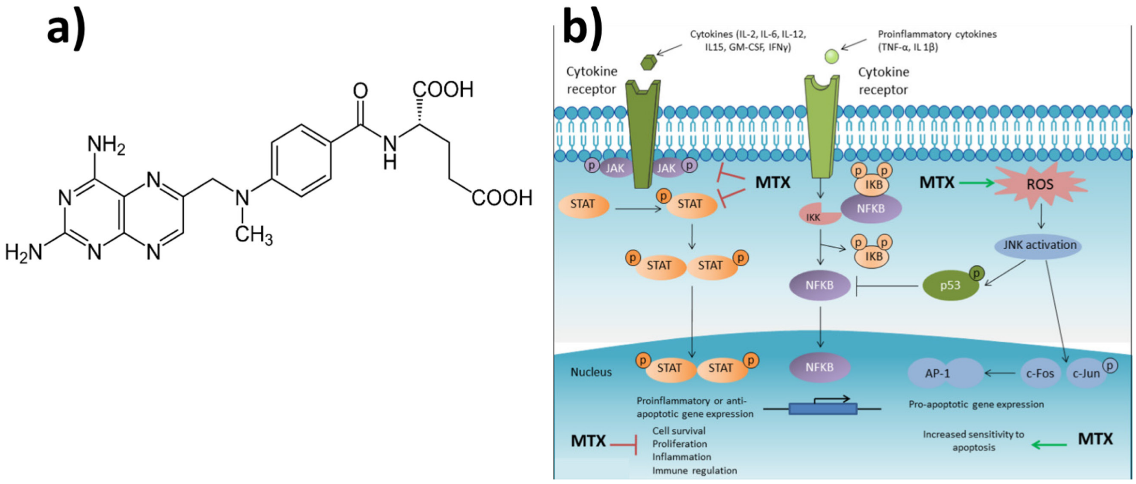

Figure 23. a) Molecular structure of methotrexate and b) its mechanism of action against rheumatoid arthritis[268]

Everolimus (Ev, molecular weight 958,22 gmol^{-1}, Figure 23a) has potent anti-proliferative and immunosuppressive properties[270]. Everolimus is an orally administered analogue of rapamycin that can inhibit the human kinase mammalian target of rapamycin (mTOR)[271] and it is widely used in the treatment of solid tumors such as breast cancer, metastatic renal cell carcinoma and metastatic pancreatic neuroendocrine tumors (figure 23b)[271]. The mTOR is an enzyme that act as central regulator of cell proliferation, growth and survival and the upregulation of proteins that regulate mTOR has been reported in several cancers[270,272]. The association between deregulation of the mTOR pathway and cancer has led to considerable interest in the development of mTOR-target cancer therapies, namely everolimus[272]. The molecular structure of Ev consist of a macrocycle lactone and is not soluble in water and highly soluble in organic solvent such as DMSO[270].

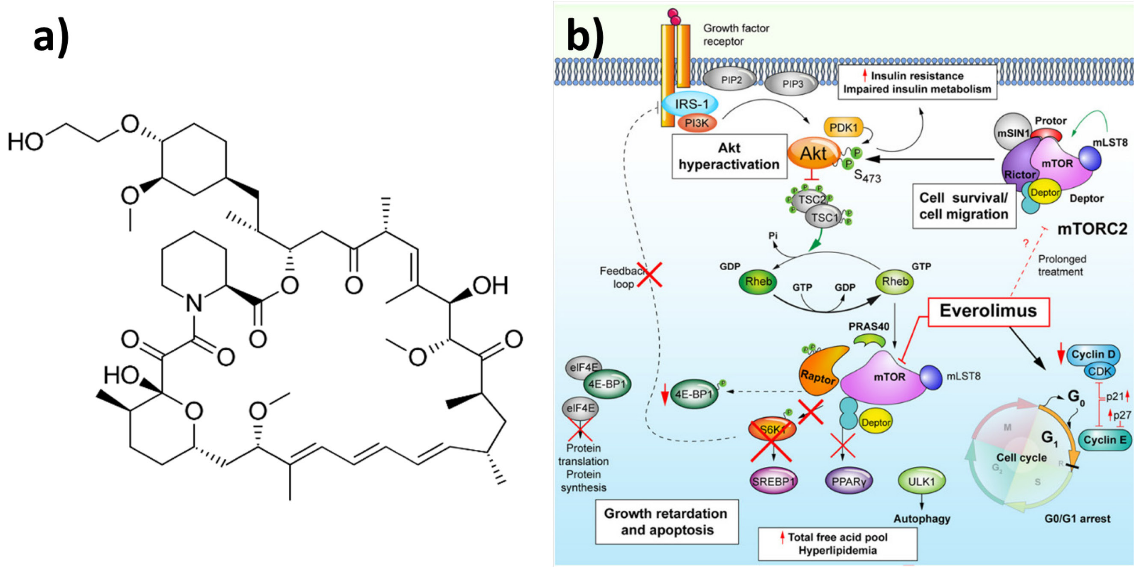

***Figure 24**. **a)** Molecular structure of Everolimus and **b)** its mechanism of action of inhibition of mTOR signalling patway*[272]

Antibodies

Antibodies are large glycoproteins belonging to the immunoglobulin (Ig) superfamily whose role in the immune system is to recognize, neutralize and mount an immune response to foreign antigens[273]. Their basic structure is composed of two heavy and two light chains arranged in the shape of a *Y*. At each end of the *Y* lies the Fragment Antigen Binding (Fab) part of the antibody, which is responsible for recognizing the specific antigen[273,274]. In immunotherapy based on monoclonal antibodies, the antibodies can directly target tumor cells while promoting the induction of a durable immune response against the tumour[273]. IgG is the most often form used in antibody therapy[273,274].

Denosumab (Den, molecular weight about 147 kDa) is a monoclonal antibody with high-selectivity for RANKL, thus revealing anti-RANKL function[275–277]. Denosumab is able to inhibit the RANK/RANKL signaling pathway that is essential for osteoclast activation, functions and survival[275]. As aforementioned, Den was proposed for the treatment of bone metabolic dysfunction, such osteoporosis (figure 24a) and bone destruction due to rheumatoid arthritis[275] or metastatic cancer (figure 24b)[275,277,278].

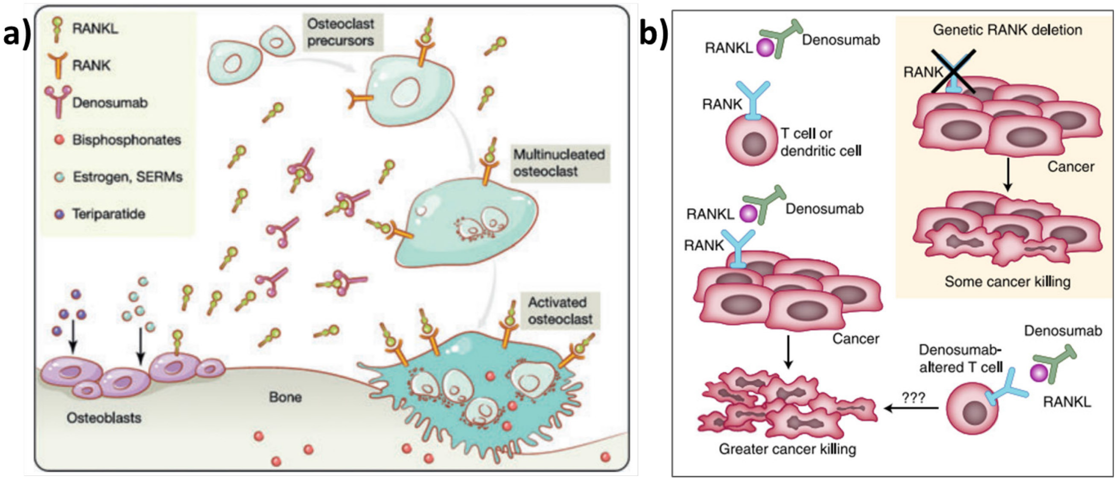

*Figure 25. **a)** Mechanism of action of denosumab for the osteoporosis treatment[276] and **b)** proposed mechanism of denosumab for the cancer treatment[277]*

1.7.2. Factors influencing the drug loading and release.

Factors influencing drug loading and release from calcium phosphate based scaffolds can be attributed to (i) the CaP scaffold characteristics, (ii) the physicochemical interaction between drug and carrier and (iii) the environmental conditions for loading and releasing the therapeutic agent or active pharmaceutical ingredients (API)[107,211,212].

Drug carrier properties are important not only for bone regeneration but also for adsorbing and delivering drugs. Reported properties include composition and microstructural characteristics such as crystallinity, porosity, morphology, specific surface area (SSA), grain boundaries and particle size[211,212]

In particular:

- The rate at which the drug is released is expected to vary directly with the solubility of the final CaP phase. For example, apatitic materials have shown more sustained drug release than brushitic one.

- The region between adjacent grains of different orientation is a preferred zone for drug adsorption due to its higher chemical reactivity. As a result, highly crystalline samples are more likely to adsorb lower amount of drug than poorly crystalline samples, which have more reactive surfaces with more heterogeneous and unstable ionic groups. In addition, low crystallinity materials have an irregular surface, resulting in higher drug affinity as surface defects create an active binding site.
- The crystal morphology affects the drug loading, plate-like HA crystals can adsorb more anticancer drug than needle-like particles.
- High SSA is expected to absorb higher amount of drug (linear relationship).
- Porosity, pore size and pore interconnectivity are the characteristics of the pore network. For drug delivery, it is challenging to fully control all these features. The amount of drug adsorbed is directly related to the overall porosity: increasing the internal void volume greatly increases the surface area available for drug adsorption. Both the kinetics of drug adsorption and the amount of drug loaded are influenced by pore size and interconnectivity. The nanometric nature of the pores, which can produce increased tortuosity, becomes a key factor in controlling drug diffusion. For example, if pores have a size comparable to that of a drug molecule, the effect of the pore size is more intense than when the pores are significantly larger than the drug molecules, in which case the latter can freely diffuse out of the pores and the release is controlled more by diffusion than by the structural factors. The relationship between drug molecule and pore size is therefore closely related to the drug transport mechanism. Proper matching of the pore size to the drug makes it possible to establish a non-Fickian diffusion-driven regime at the molecular scale, where suitably sized pores allow the release of a single molecule at a time, resulting in concentration-independent zero-order kinetics. Conversely, a Fickian diffusion regime and bursting effect can occur if the pore size greatly exceeds the dimensions of the drug molecule.

Concerning the drug, the chemical nature has an influence on the chemical interaction with the scaffold. These interactions usually have a retardation effect on drug release in a manner that is generally proportional to the intensity of the specific chemical interaction. In cement, not only the chemical nature, but also the drug dimension has an effect on the drug release kinetics[211,212]. Small molecule usually induces a delay in setting reaction and a consequent increase in the release rate during the first hours. Another important effect relies on the ability of the drug to induce physicochemical changes in the final cement, such as porosity, crystallinity and specific surface area[211,212,279]. This is particularly true for the drugs containing counterion, which can induce an increase in the final porosity and/or act as a nucleation centre for cement precipitation, thus reducing the crystallinity of the final product and accelerating release [211,212].

The interaction type that occur between drug and scaffold depends on the chemistry of both carrier and drug and on the properties of the loading solution. Either physisorption or chemisorption of the drug may occur, depending on the nature of the drug/carrier interaction (Figure 26).

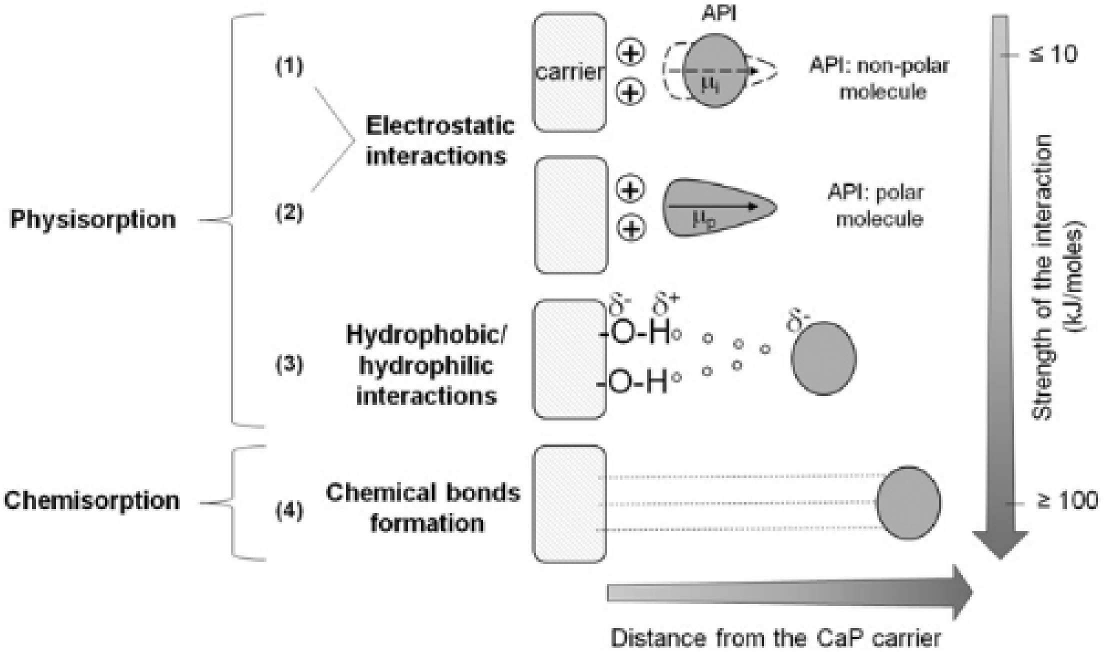

***Figure* 26**. *Different type of interaction between active pharmaceutic ingredients (API) and the CaP carrier surface: physical interactions via electrostatic (1,2) or hydrophobic/hydrophilic (3) interactions and chemical interaction (4) via new bond formation (--) between API and CaP surface* [211]

The drug adsorption through physical interactions take place when the drug molecules are adsorbed on the CaP surface via weak non-covalent interaction (H-bond, hydrophilic/hydrophobic interaction, Van der Waals and electrostatic forces) while drug chemisorption happens when new chemical bond is formed between the drug molecule and carrier[211,212]. Therefore, the adsorption depends on the degree of affinity between drug and carrier in each medium. This latter plays a key role by modulating both charge state of the carrier and the isoelectric point of drug. Electrostatic interactions are subordinated to the electric charges of drug and the caP surface, which themselves depend on the surrounding liquid medium. Additionally, any modification of carrier or active substance resulting in charges modification can change the adsorption profile and the drug release[211].

HA crystallites in the hexagonal system have plane *a* and *c* positively and negatively charged respectively. Therefore, acidic proteins and negative charged drug tends to adsorb on *a* plane, whereas basic proteins and positively charged drug tends to adsorb on *c* plane[211] (Figure 27).

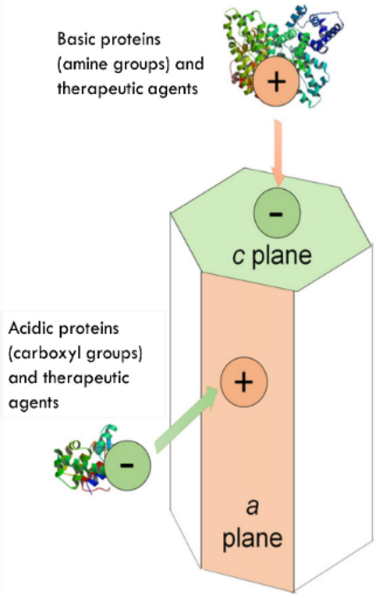

Figure 27. *Scheme of crystalline HA and its interaction with therapeutics*[211]

Several parameters influence the drug loading, such as temperature, pressure, drug physico-chemistry and if scaffold is immersed in drug solution become important even the concentration of the drug, the pH, the ionic strength and the contact time[211,212,279].

The drug release kinetic depends on several parameters (Figure 28). In particular, the properties of the liquid medium have an important effect on drug release mechanism and kinetics, for example the pH: in acidic environment, the release rate of drug from CaP is higher than basic one, due to the higher solubility of CaP in low pH environment. In general, release experiments can be performed using various experimental set-ups. Differences include: (i) volume of medium, (ii) agitation of medium, (iii) renewal or not of medium around the sample, (iv) how frequently and how this renewal is made (partial or total change at predetermined time points or continuous flow, in open or closed loop) [211,212,279].

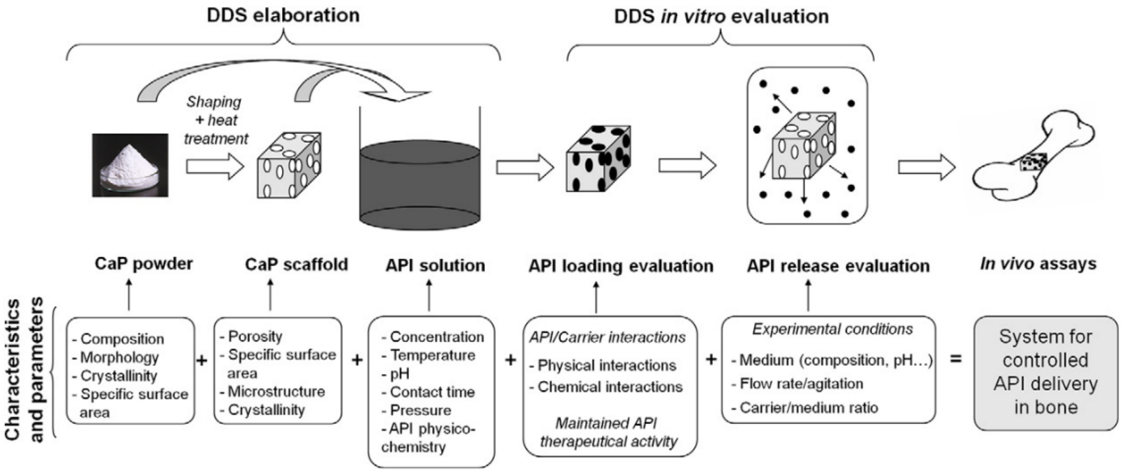

Figure 28. *Parameters controlling the release of drug from Calcium Phosphate-based drug delivery system*[211]

The mechanisms governing both drug loading and release processes can be determinate by various equations and semi-empirical mathematical models. The most commonly kinetic equation used to quantitatively interpret the reaction orders are: the zeroth, first and second orders (Figure 29).

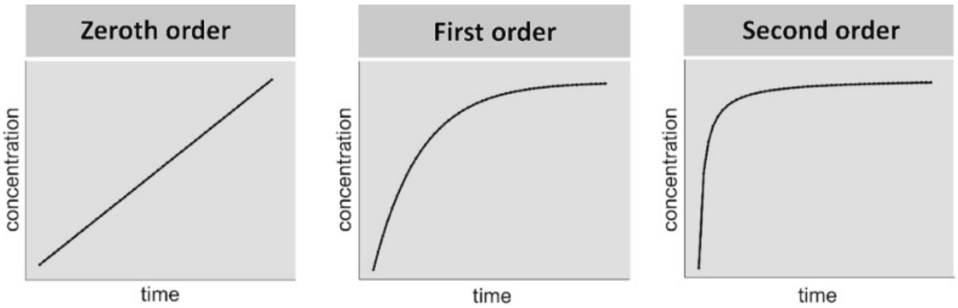

Figure 29. *Schematic illustration of the drug release profiles corresponding to the zeroth, the first and the second order of the reaction of release*[212]

1.7.3. Release mechanisms

The variety of sustained delivery systems (tablets, suppositories, patches, gels, microemulsions and solutions) depends largely on the route of administration, the main ones being oral, injectable, inhalable, transmucosal, transdermal and implantable. However, regardless of the delivery system and route considered, in vivo drug release is usually characterised by different steps. One of the most important is to establish the correct release kinetics according to the desired clinical effect[280].

Basically, drug delivery from matrices is governed by:

- Physical processes, which may include matrix erosion and swelling.
- Physicochemical processes, which may include matrix erosion, drug dissolution, drug transport (by diffusion and convection), interaction of the drug with the matrix structure and osmotic pressure[102,211,280].
- System parameters may include the initial drug distribution and concentration within the matrix, matrix geometry (cylindrical, spherical, etc.) and matrix size distribution (figure 30) [212,280].

Of course, the importance played by all these mechanisms in determining release kinetics is not always the same and it depends on the particular matrix considered[280].

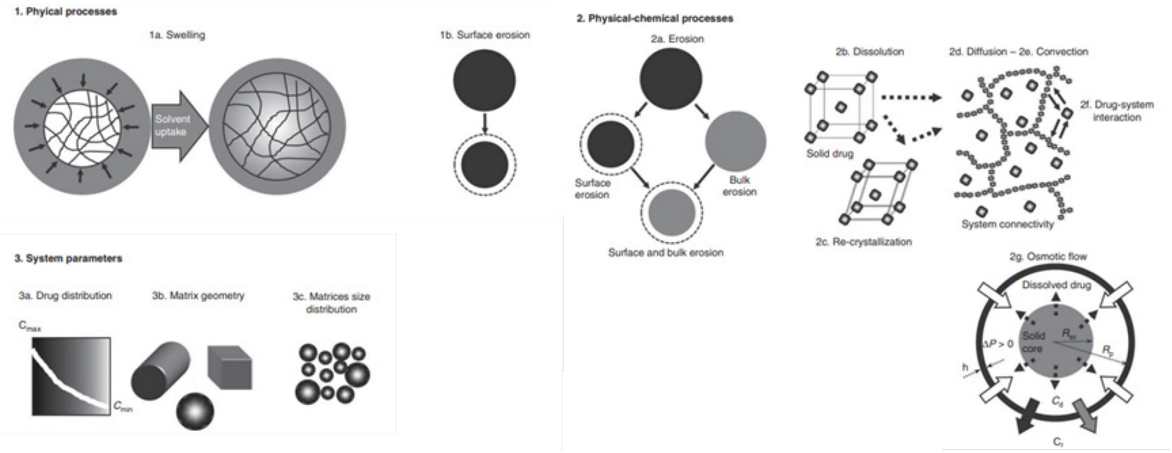

__Figure 30.__ The main phenomena affecting drug delivery from a matrix are physical (swelling and, in some cases, erosion), physico-chemical (erosion, dissolution, recrystallization, diffusion, convection, interaction of the drug with system structure, osmotic pressure) and system parameters (initial drug concentration distribution, matrix shape, matrix size distribution and osmosis)[280].

1.7.4. Mathematical model

Over the past decades mathematical modelling of diffusional and release processes has been used to design a number of simple and complex drug delivery systems and devices and to predict the overall release behaviour[281,282]. A model can be defined as an artificial representation of a phenomenon aimed at describing events that cannot be directly observed and at emulating how something behaves[280]. In particular, model-building process consists of defining the phenomenon to be studied, expressing it in mathematical terms, fitting experimental data and predicting experimental behaviour under different conditions from those considered in data fitting[280].

Kinetic equations

Zero-order kinetic

The zero-order kinetic equation is applicable when the drug dissolution is only a function of time and proceeds independently of the drug concentration at any given time point.[212]. Dissolution is a kinetic process and, therefore, the rate of dissolution reflects the amount of drug that is dissolved in a given time and can be described as follows:

$$\frac{dC}{dt} = \frac{DS}{Vl}(C_s - C) \qquad (Eq.\ 1)$$

Where *dC/dt* is the speed of dissolution, *D* is the diffusion coefficient of solute in the solution, *S* is the solute area exposed, *l* is the thickness of the diffusion layer, *Cs* is the solid solubility, *C* is the solute concentration into the solution on time *t* and *V* is the volume of solution[283].

The zero-order kinetics can be also described in terms of both.

- fraction of drug (f_i) dissolved during the time *t:*

$$f_i = K_0 t \qquad (Eq.\ 2)$$

- and concentration (C_t) at the time *t:*

$$C_t = C_0 + K_0 t \qquad (Eq.\ 3)$$

K_0 is the Zero-order constant and C_0 is the initial concentration of therapeutic agent released (generally $C_0=0$)[212,283].

First-order kinetic

The first order kinetics describes the drug adsorption/release. Here, the reaction's rate linearly depends on the drug concentration (eq. 4):

$$\frac{dC}{dt} = -km \qquad (Eq.\ 4)$$

Where *dC/dt* is the speed of reaction, *k* is the first order constant and *m* is the amount of adsorbed/released drug[212,283].

The integrated form from time *t=0* to a generic time *t* is (eq. 5):

$$log(m_0 - m_t) = log(m_0) - kt \qquad (Eq. 5)$$

m_0 is the initial drug amount dispersed in the matrix and m_t is the drug concentration released at the given time *t*.

Second-order kinetic

The second order kinetics involves the dependence of drug release/adsorption rate on the squared value of drug concentration (eq. 6 and eq. 7) [212]:

$$\frac{dm}{dt} = -km^2 \qquad (Eq. 6)$$

The integrated form is:

$$\frac{1}{(m_0 - m_t)} = \frac{1}{m_0} - kt \qquad (Eq. 7)$$

All the above-reported equation are of limited use for real and three-dimensional cases where the complexity and variety of environmental variables must be taken into account for the investigated systems to be modelled correctly[212]. Therefore, a series of empirical and semi-empirical models have been proposed for the application on drug-release system able to provide a more realistic interpretation on the release kinetics and mechanisms[212].

Semi-empirical model

Higuchi model

The Higuchi model is one of the most commonly used mathematical equation to describe the drug dissolution rate from a matrix system and it was first proposed in the 1960s[212,283]. Higuchi proposed models that consider a low concentration of therapeutic agent in the matrix, where the solubility and release takes place through the matrix porosity[283]. Only in systems where the following requirements and boundary conditions are met can this model be correctly applied:

- The matrix contains an initial drug concentration higher than the drug solubility.
- The diffusion is unidirectional.

- The thickness of the dosage form is larger than the size of the drug molecule.
- The matrix swelling or dissolution is negligible.
- The drug diffusivity is constant.
- The perfect sink condition are attained in the release environment [212].

The Higuchi equation is given as follow (eq. 8)

$$\chi_i = \sqrt{\frac{D\varepsilon}{\tau}(2C - \varepsilon C_s)C_s t} \qquad (Eq. 8)$$

Where χ_i is the fraction of the released drug by the time *t* by area unit, *D* is the diffusion coefficient in the matrix medium, ε is the matrix porosity, τ is the tortuosity factor, *C* is the initial drug amount and C_s is the drug solubility in the matrix medium[283].

The Higuchi model can be linearized by reporting the fraction of the dissolved drug as function of the square root of time (eq. 9):

$$\chi_i = K_H \sqrt{t} \qquad (Eq. 9)$$

Korsmeyer-Peppas (Power law) model

The Power law, known also as the Korsmeyer-Peppas model (KP-model), is a more comprehensive semi-empirical model for describing drug release from polymeric matrix or monolithic system that establishes the exponential relationship between the release and the time[212,283] (eq. 10)

$$f_i = \frac{M_i}{M_\infty} = Kt^n \qquad (Eq. 10)$$

Where f_i is the amount of drug released, M_∞ is the amount of drug at the equilibrium state, M_i is the amount of drug released over time *t*, *K* is the constant of incorporation of structural modification and geometrical characteristics of the system and *n* is the exponent of release, related to the drug release mechanism, in function of time *t*.

In addition, when the drug release process is characterized an abrupt increase of initial drug release (burst effect), the equation 10 become (eq. 11):

$$f_i = \frac{M_i}{M_\infty} = Kt^n + b \qquad (Eq. 11)$$

Where *b* is the burst effect

Depending on the *n* value that better matches to the release profile of the therapeutic agent in a matrix system, a classification can be made according to the type of behaviour observed:

- Fickian model (case I)
- Non-Fickian models (case II, Anomalous case and Super case II).

The release mechanism by Fickian diffusion is the mechanism by which drug diffusion through the drug delivery system matrix is solely determined by the diffusion process in the medium fluid; whereas in the anomalous transport (non-Fickian diffusion process) the drug delivery is due to both Fickian diffusion and other mechanisms contributing to drug release (e.g., matrix swelling and/or erosion) [283,284].

In the following table (Table IX) are listed the *n* value for cylindrical shaped samples and relative release kinetic and mechanisms[283,284]:

***Table IX**. Interpretation of the Korsmeyer-Peppas exponent for cylindrical samples*

***n* exponent value**	**Release regime**	**Release kinetics and mechanisms**
0 < n < 0,45	Hindered Fickian diffusion	Representative of system characterized by diffusive regime with hampered release.
n = 0,45	Fickian diffusion (case I)	Representative of first-order kinetic where diffusion is the main release mechanism, and the rate linearly depends on the drug concentration
0,45 < n < 0,89	Anomalous transport	Characteristic of those case where in addition to diffusion, other mechanisms contribute to the drug release (e.g., matrix erosion, presence of tortuous Porosity).
n = 0.89	Non-Fickian transport (case II)	Corresponds to a zeroth order kinetic in which release proceeds independently of the drug concentration at any given time point
n > 0,89	Super case II	Extreme form of transport that usually occurs when modification in the matrix take place (gradient drug concentration in the matrix).

In this work, the KP-model was applied to drug release kinetic profiles from ceramic matrices.

Weibull model

The Weibull model is a distribution function with the property to describe the phenomena and process associated to a finite time. It is based on a function proposed originally by Weibull (1951) and Langenbucher (1972) adapted the function to describe the drug release curves[283,284]. The equation is expressed in terms of the drug fraction accumulated (*m*) in the solution on time *t*:

$$m = 1 - e^{\left[\frac{-(t-T)^{b}}{a}\right]} \qquad (Eq. 12)$$

Or

$$m = 1 - e^{-(t-T)^{b}/a} \qquad (Eq. 13)$$

The scale parameter (*a*) defines the timescale of the process. The localization parameter (*T*) represents the latency time of the release process, many times being zero. The form parameter (*b*) characterizes the type of curve:

- b=0: exponential
- b>1: sigmoid, with ascendant curvature delimited by an inflection point.
- b>1: parabolic, displaying high initial slope and a consistent exponential character.

This model is considered more useful for comparing the drug release profile of matrix systems[283,284]. The aforementioned equation is an empirical model lacking kinetic foundation; therefore, it primarily describes the properties of dissolution kinetics of the drug rather than allowing for interference. Furthermore, the model does not prescribe an intrinsic dissolution factor parameter for the drug and therefore cannot describe any kind of in vitro/in vivo correlation[283–285].

Hill model

The Hill equation or model is a three-parameter equation of a nonlinear relationship between two variables, *x* and *y*[286]*:*

$$y = \frac{y_{max}X^{\alpha}}{C^{\alpha}+X^{\alpha}} \qquad (Eq. 14)$$

The three parameters are: *y*, *c* and the coefficient *α.*

In pharmacology, the Hill equation was proposed by Wagner as a model for describing the relationship between drug concentration and effect. Furthermore, the equation has been recognised as a valuable tool for characterising the pharmacological activity of drugs in a quantitative way. It has been extensively employed when the relationship between drug concentration and effect is non-linear and saturable [286].

Hill conducted experiments in the early 1900s on the general setting of physico-chemical equilibria. There is a significant connection between Hill's equation and the laws of equilibrium reactions. When dealing with a single equilibrium reaction in a liquid phase between two molecules, *L* and *M* and their combinationcombination *LM*, Hill's equation is applicable[286]:

$$L + M \rightleftharpoons LM \qquad \textit{(Reaction 5)}$$

Derived from the law of mass action of Waage and Guldberg, the dissociation equilibrium constant K_D is defined as:

$$K_D = \frac{[L][M]}{[LM]} \qquad (Eq. 15)$$

Where *[L]*, *[M]* and *[LM]* are the molar concentrations of the three species[286].

In equilibrium concentration, it is possible to define *T* as the entire concentration of *L* molecule and *y* as the ratio of *L* which have reacted:

$$T = [L] + [LM] \qquad (Eq. 16)$$

$$y = \frac{[LM]}{[LM]+[L]} \qquad (Eq. 17)$$

Substituting *[LM]* by this expression from Eq. 15:

$$y = \frac{[M]}{K_D+[M]} \qquad (Eq. 18)$$

This is a Hill equation derived from Eq. 14 with two parameters $c=K_D^{1/2}$ and $\alpha=1$; in this way, the *C* parameter of Hill equation is directly related to K_D, constant of the law of mass action[286]. Indeed, these two parameters have a physical meaning beyond their formal one: α represents the number of binding patterns between *M* and *L* and *c* is related to K_D, which represent the *M* concentration for which $y=0,5$ (i.e. $y_{max/2}$) and so it is an expression of affinity[286].

The Hill model is also used for modelling drug release processes that involve two different mechanisms: diffusion and chemical reaction[287]. In this case, the Hill equation is given by:

$$\frac{M_t}{M_0} = \left(\frac{M_t}{M_0}\right)_{lag} + \frac{(M_t/M_0)_{max}}{1+(t_{1/2}/t)^H} \qquad (Eq.\ 19)$$

Where (M_t/M_0) is the cumulative amount of released drug at time t, $(M_t/M_0)_{lag}$ is the amount of drug released in the lag time, $(M_t/M_0)_{max}$ is the maximum amount of drug released, $t_{1/2}$ in the time in which (M_t/M_0) reaches $(M_t/M_0)_{max/2}$, H (previously named α) is the Hill coefficient that give the slope of the sigmoidal curve at $t_{1/2}$ [287].

For drug release kinetics, which follows a sigmoidal pathway, can be classified into three phases, namely lag phase, burst phase and saturation phase. The length of the initial phase (lag phase) depends on the strength of interaction between the drug and matrix. This is followed by a diffusion step which involves the drug getting released out of the pores. The absence of lag phase suggest the absence of strong interaction between the drug and the scaffold[287].

REFERENCES

1. Dapporto, M. Development of new bioactive and porous apatitic scaffolds for the regeneration of load-bearing bones. *Univ. degli Stud. di Bol.* (2016).
2. Clarke, B. Normal bone anatomy and physiology. *Clin. J. Am. Soc. Nephrol.* **3 Suppl 3**, 131–139 (2008).
3. Bartl, R. & Bartl, C. Bone disorders: Biology, diagnosis, prevention, therapy. *Bone Disord. Biol. Diagnosis, Prev. Ther.* 1–602 (2017) doi:10.1007/978-3-319-29182-6.
4. Tavoni, M., Dapporto, M., Tampieri, A. & Sprio, S. Bioactive Calcium Phosphate-Based Composites for Bone Regeneration. *J. Compos. Sci.* **5**, 227 (2021).
5. Campodoni, E. Design and development of bio-hybrid multifunctional materials for regenerative medicine. *Univeristà degli Stud. di Parma* (2018).
6. Katsimbri, P. The biology of normal bone remodelling. *Eur. J. Cancer Care (Engl).* **26**, 1–5 (2017).
7. Kielty, C. M. & Grant, M. E. The Collagen Family: Structure, Assembly, and Organization in the Extracellular Matrix. *Connect. Tissue Its Heritable Disord.* 159–221 (2003) doi:10.1002/0471221929.ch2.
8. Armiento, A. R., Hatt, L. P., Sanchez Rosenberg, G., Thompson, K. & Stoddart, M. J. Functional Biomaterials for Bone Regeneration: A Lesson in Complex Biology. *Adv. Funct. Mater.* **1909874**, 1–41 (2020).
9. Jodati, H., Bengi, Y. & Evis, Z. A review of bioceramic porous scaffolds for hard tissue applications : Effects of structural features. **46**, 15725–15739 (2020).
10. No, Y. J. *et al.* Effect of baghdadite substitution on the physicochemical properties of brushite cements. *Materials (Basel).* **12**, 1–15 (2019).
11. Tampieri, A. *et al.* Hydroxyapatite: From nanocrystals to hybrid nanocomposites for regenerative medicine. in *Handbook of Bioceramics and Biocomposites* 119–144 (Springer International Publishing, 2016). doi:10.1007/978-3-319-12460-5_6.
12. Jeong, J., Kim, J. H., Shim, J. H., Hwang, N. S. & Heo, C. Y. Bioactive calcium phosphate materials and applications in bone regeneration. *Biomater. Res.* **23**, 1–11 (2019).
13. Sprio, S. *et al. Composite biomedical foams for engineering bone tissue*. *Biomedical Foams for Tissue Engineering Applications* (2014). doi:10.1533/9780857097033.2.249.
14. Barrère, F., van Blitterswijk, C. A. & de Groot, K. Bone regeneration: Molecular and cellular interactions with calcium phosphate ceramics. *Int. J. Nanomedicine* **1**, 317–332 (2006).
15. Sprio, S. *et al.* Biomimesis and biomorphic transformations: New concepts applied

to bone regeneration. *J. Biotechnol.* **156**, 347–355 (2011).

16. Rho, J. Y., Kuhn-Spearing, L. & Zioupos, P. Mechanical properties and the hierarchical structure of bone. *Med. Eng. Phys.* **20**, 92–102 (1998).

17. Pupilli, F. *et al.* Design Strategies and Biomimetic Approaches for Calcium Phosphate Scaffolds in Bone Tissue Regeneration. (2022).

18. Porter, J. R., Ruckh, T. T. & Popat, K. C. Bone tissue engineering: A review in bone biomimetics and drug delivery strategies. *Biotechnol. Prog.* **25**, 1539–1560 (2009).

19. Reznikov, N., Shahar, R. & Weiner, S. Bone hierarchical structure in three dimensions. *Acta Biomater.* **10**, 3815–3826 (2014).

20. Marotti, G., Muglia, M. A. & Palumbo, C. Structure and function of lamellar bone. *Clin. Rheumatol.* **13 Suppl 1**, 63–68 (1994).

21. Fratzl, P. & Weinkamer, R. Nature's hierarchical materials. *Prog. Mater. Sci.* **52**, 1263–1334 (2007).

22. Glimcher, M. J. Mechanism of calcification: Role of collagen fibrils and collagen-phosphoprotein complexes in vitro and in vivo. *Anat. Rec.* **224**, 139–153 (1989).

23. Wang, Y. *et al.* Water-mediated structuring of bone apatite. *Nat. Mater.* **12**, 1144–1153 (2013).

24. Rey, C., Miquel, J. L., Facchini, L., Legrand, A. P. & Glimcher, M. J. Hydroxyl groups in bone mineral. *Bone* **16**, 583–586 (1995).

25. Roach, H. I. Why does bone matrix contain non-collagenous proteins? The possible roles of osteocalcin, osteonectin, osteopontin and bone sialoprotein in bone mineralisation and resorption. *Cell Biology International* vol. 18 617–628 (1994).

26. Scaglione, S. *et al.* Order versus Disorder: In vivo bone formation within osteoconductive scaffolds. *Sci. Rep.* **2**, 1–6 (2012).

27. Sprio, S., Sandri, M., Panseri, S., Cunha, C. & Tampieri, A. Hybrid scaffolds for tissue regeneration: Chemotaxis and physical confinement as sources of biomimesis. *J. Nanomater.* **2012**, (2012).

28. Yu, L. & Wei, M. Biomineralization of collagen-based materials for hard tissue repair. *Int. J. Mol. Sci.* **22**, 1–17 (2021).

29. Tseng, Y. H., Mou, C. Y. & Chan, J. C. C. Solid-state NMR study of the transformation of octacalcium phosphate to hydroxyapatite: A mechanistic model for central dark line formation. *J. Am. Chem. Soc.* **128**, 6909–6918 (2006).

30. Robin, M. *et al.* Insights into OCP identification and quantification in the context of apatite biomineralization. *CrystEngComm* **22**, 2728–2742 (2020).

31. Hamai, R., Tsuchiya, K. & Suzuki, O. Adsorption of serum albumin onto octacalcium phosphate in supersaturated solutions regarding calcium phosphate phases.

Materials (Basel). **12**, (2019).

32. Moriishi, T. *et al.* Osteocalcin is necessary for the alignment of apatite crystallites, but not glucose metabolism, testosterone synthesis, or muscle mass. *PLoS Genet.* **16**, 1–29 (2020).
33. Simon, P. *et al.* First evidence of octacalcium phosphate@osteocalcin nanocomplex as skeletal bone component directing collagen triple–helix nanofibril mineralization. *Sci. Rep.* **8**, 1–17 (2018).
34. Nudelman, F. *et al.* The role of collagen in bone apatite formation in the presence of hydroxyapatite nucleation inhibitors. *Nat. Mater.* **9**, 1004–1009 (2010).
35. Seeman, E. Bone modeling and remodeling. *Crit. Rev. Eukaryot. Gene Expr.* **19**, 219–233 (2009).
36. Parfitt, A. M. The cellular basis of bone remodeling: The quantum concept reexamined in light of recent advances in the cell biology of bone. *Calcif. Tissue Int.* **36**, (1984).
37. Raggatt, L. J. & Partridge, N. C. Cellular and molecular mechanisms of bone remodeling. *J. Biol. Chem.* **285**, 25103–25108 (2010).
38. Vascular-supply-and-circulation @ www.britannica.com.
39. Lei, C. *et al.* Advances in materials-based therapeutic strategies against osteoporosis. *Biomaterials* **296**, 122066 (2023).
40. Chindamo, G. *et al.* Bone diseases: Current approach and future perspectives in drug delivery systems for bone targeted therapeutics. *Nanomaterials* **10**, (2020).
41. Bean, A. C. Basic Science Concepts in Musculoskeletal Regenerative Medicine. in *Regenerative Medicine for Spine and Joint Pain* (eds. Cooper, G., Herrera, J., Kirkbride, J. & Perlman, Z.) 5–27 (Springer International Publishing, 2020). doi:10.1007/978-3-030-42771-9_2.
42. Sommerfeldt, D. & Rubin, C. Biology of bone and how it orchestrates the form and function of the skeleton. *Eur. Spine J.* **10**, 86–95 (2001).
43. Li, J. J., Ebied, M., Xu, J. & Zreiqat, H. Current Approaches to Bone Tissue Engineering: The Interface between Biology and Engineering. *Adv. Healthc. Mater.* **7**, 1–8 (2018).
44. Wang, H. *et al.* Mechanistic advances in osteoporosis and anti-osteoporosis therapies. *MedComm* **4**, 1–26 (2023).
45. Patel, D. & Wairkar, S. Bone regeneration in osteoporosis: opportunities and challenges. *Drug Deliv. Transl. Res.* **13**, 419–432 (2023).
46. Marie, P. J. Strontium as therapy for osteoporosis. *Curr. Opin. Pharmacol.* **5**, 633–636 (2005).
47. Shuaishuai, W. *et al.* Implantable biomedical materials for treatment of bone

infection. *Front. Bioeng. Biotechnol.* **11**, 1–19 (2023).

48. Dapporto, M. *et al.* Strontium-doped apatitic bone cements with tunable antibacterial and antibiofilm ability. *Front. Bioeng. Biotechnol.* **10**, 1–17 (2022).

49. Li, B. & Webster, T. J. Bacteria antibiotic resistance: New challenges and opportunities for implant-associated orthopedic infections. *J. Orthop. Res.* **36**, 22–32 (2018).

50. Cazalbou, S., Bertrand, G. & Drouet, C. Tetracycline-loaded biomimetic apatite: An adsorption study. *J. Phys. Chem. B* **119**, 3014–3024 (2015).

51. Zeng, M. *et al.* Diagnosis and treatment of chronic osteomyelitis based on nanomaterials. *World J. Orthop.* **14**, 42–54 (2023).

52. Masters, E. A. *et al.* Skeletal infections: microbial pathogenesis, immunity and clinical management. *Nat. Rev. Microbiol.* **20**, 385–400 (2022).

53. Muhammad, M. H. *et al.* Beyond Risk: Bacterial Biofilms and Their Regulating Approaches. *Front. Microbiol.* **11**, 1–20 (2020).

54. Alegrete, N., Sousa, S. R., Peleteiro, B., Monteiro, F. J. & Gutierres, M. Local Antibiotic Delivery Ceramic Bone Substitutes for the Treatment of Infected Bone Cavities and Bone Regeneration: A Systematic Review on What We Have Learned from Animal Models. *Materials (Basel).* **16**, (2023).

55. Vallet-Regí, M. & Arcos, D. Bioceramics for drug delivery. *Acta Mater.* **61**, 890–911 (2013).

56. Sprio, S. *et al.* Surface Phenomena Enhancing the Antibacterial and Osteogenic Ability of Nanocrystalline Hydroxyapatite, Activated by Multiple-Ion Doping. *ACS Biomater. Sci. Eng.* **5**, 5947–5959 (2019).

57. Hutchings, M., Truman, A. & Wilkinson, B. Antibiotics: past, present and future. *Curr. Opin. Microbiol.* **51**, 72–80 (2019).

58. Ahmad, M. & Khan, A. U. Global economic impact of antibiotic resistance: A review. *J. Glob. Antimicrob. Resist.* **19**, 313–316 (2019).

59. Liao, J., Han, R., Wu, Y. & Qian, Z. Review of a new bone tumor therapy strategy based on bifunctional biomaterials. *Bone Res.* **9**, (2021).

60. Lindsey, B. A., Markel, J. E. & Kleinerman, E. S. Osteosarcoma Overview. *Rheumatol. Ther.* **4**, 25–43 (2017).

61. Pilavaki, P., Gahanbani Ardakani, A., Gikas, P. & Constantinidou, A. Osteosarcoma: Current Concepts and Evolutions in Management Principles. *J. Clin. Med.* **12**, (2023).

62. Jackson, T. M., Bittman, M. & Granowetter, L. Pediatric Malignant Bone Tumors: A Review and Update on Current Challenges, and Emerging Drug Targets. *Curr. Probl. Pediatr. Adolesc. Health Care* **46**, 213–228 (2016).

63. Belayneh, R., Fourman, M. S., Bhogal, S. & Weiss, K. R. Update on Osteosarcoma. *Curr. Oncol. Rep.* **23**, 71 (2021).

64. Ottaviani, G. & Jaffe, N. The epidemiology of osteosarcoma. *Cancer Treat. Res.* **152**, 3–13 (2009).

65. Jafari, F. *et al.* Osteosarcoma: A comprehensive review of management and treatment strategies. *Ann. Diagn. Pathol.* **49**, 151654 (2020).

66. Beaury, M. W., Kelly-Beaury, M. L., Sharp, G. & Cottrell, J. A. A Review of Osteosarcoma Therapeutics. *J. Cancer Treat. Diagnosis* **2**, 21–29 (2018).

67. Bischoff, I. *et al.* In vitro evaluation of a biomaterial-based anticancer drug delivery system as an alternative to conventional post-surgery bone cancer treatment. *Mater. Sci. Eng. C. Mater. Biol. Appl.* **93**, 115–124 (2018).

68. Xu, M., Xu, S. F. & Yu, X. C. Clinical analysis of osteosarcoma patients treated with high-dose methotrexate-free neoadjuvant chemotherapy. *Curr. Oncol.* **21**, 678–684 (2014).

69. Beaury, M. W., Kelly-Beaury, M. L., Sharp, G. & Cottrell, J. A. A Review of Osteosarcoma Therapeutics. *J. Cancer Treat. Diagnosis* **2**, 21–29 (2018).

70. Bishop, M. W., Janeway, K. A. & Gorlick, R. Future directions in the treatment of osteosarcoma. *Curr. Opin. Pediatr.* **28**, 26–33 (2016).

71. Janeway, K. A. & Grier, H. E. Sequelae of osteosarcoma medical therapy: a review of rare acute toxicities and late effects. *Lancet. Oncol.* **11**, 670–678 (2010).

72. Song, M. K., Park, S. I. & Cho, S. W. Circulating biomarkers for diagnosis and therapeutic monitoring in bone metastasis. *J. Bone Miner. Metab.* **41**, 337–344 (2023).

73. Macedo, F. *et al.* Bone metastases: An overview. *Oncol. Rev.* **11**, (2017).

74. Ban, J., Fock, V., Aryee, D. N. T. & Kovar, H. Mechanisms, diagnosis and treatment of bone metastases. *Cells* **10**, 1–30 (2021).

75. Esposito, M., Guise, T. & Kang, Y. The biology of bone metastasis. *Cold Spring Harb. Perspect. Med.* **8**, 1–16 (2018).

76. Kang, J. *et al.* Anisotropy characteristics of microstructures for bone substitutes and porous implants with application of additive manufacturing in orthopaedic. *Mater. Des.* **191**, 108608 (2020).

77. Oryan, A., Alidadi, S., Moshiri, A. & Maffulli, N. Bone regenerative medicine: Classic options, novel strategies, and future directions. *J. Orthop. Surg. Res.* **9**, 1–27 (2014).

78. Vaish, A., Murrell, W. & Vaishya, R. History of regenerative medicine in the field of orthopedics. *J. Arthrosc. Surg. Sport. Med.* **0**, 1–5 (2020).

79. Berthiaume, F., Maguire, T. J. & Yarmush, M. L. Tissue Engineering and Regenerative

Medicine: History, Progress, and Challenges. *Annu. Rev. Chem. Biomol. Eng.* **2**, 403–430 (2011).

80. Cooper, G., Herrera, J., Kirkbride, J. & Perlman, Z. Introduction to Regenerative Medicine. in *Regenerative Medicine for Spine and Joint Pain* (eds. Cooper, G., Herrera, J., Kirkbride, J. & Perlman, Z.) 1–4 (Springer International Publishing, 2020). doi:10.1007/978-3-030-42771-9_1.

81. Pereira, H. F. *et al.* Scaffolds and coatings for bone regeneration. *J. Mater. Sci. Mater. Med.* (2020) doi:10.1007/s10856-020-06364-y.

82. Eliaz, N. & Metoki, N. Calcium phosphate bioceramics: A review of their history, structure, properties, coating technologies and biomedical applications. *Materials (Basel).* **10**, (2017).

83. Williams, D. F. On the mechanisms of biocompatibility. *Biomaterials* **29**, 2941–2953 (2008).

84. Polo-Corrales, L., Latorre-Esteves, M. & Ramirez-Vick, J. E. Scaffold design for bone regeneration. *Journal of Nanoscience and Nanotechnology* vol. 14 15–56 (2014).

85. Burdușel, A.-C. Bioactive composites for bone regeneration. *Biomed. Eng. Int.* **1**, 9–15 (2019).

86. Fernandez de Grado, G. *et al.* Bone substitutes: a review of their characteristics, clinical use, and perspectives for large bone defects management. *J. Tissue Eng.* **9**, (2018).

87. Shue, L., Yufeng, Z. & Mony, U. Biomaterials for periodontal regeneration A review of ceramics and polymers Biomaterials for periodontal regeneration A review of ceramics and polymers. **2535**, (2012).

88. Yousefi, A.-M. A review of calcium phosphate cements and acrylic bone cements as injectable materials for bone repair and implant fixation. *J. Appl. Biomater. Funct. Mater.* **17**, 228080001987259 (2019).

89. Gul, H., Khan, M. & Khan, A. S. *3 - Bioceramics: types and clinical applications*. *Handbook of Ionic Substituted Hydroxyapatites* (Elsevier Ltd, 2020). doi:10.1016/B978-0-08-102834-6.00003-3.

90. Venkatraman, S. K. & Swamiappan, S. Review on calcium- and magnesium-based silicates for bone tissue engineering applications. *J. Biomed. Mater. Res. - Part A* 1546–1562 (2020) doi:10.1002/jbm.a.36925.

91. Lei, Q. *et al.* Sol–Gel-Based Advanced Porous Silica Materials for Biomedical Applications. *Adv. Funct. Mater.* **1909539**, 1–28 (2020).

92. Arcos, D. & Vallet-Regí, M. Sol-gel silica-based biomaterials and bone tissue regeneration. *Acta Biomater.* **6**, 2874–2888 (2010).

93. Yamamuro, T. Bioceramics. in *Biomechanics and Biomaterials in Orthopedics* (ed.

Poitout, D. G.) 22–33 (Springer London, 2004). doi:10.1007/978-1-4471-3774-0_3.

94. Li, X., Wang, J., Joiner, A. & Chang, J. The remineralisation of enamel: A review of the literature. *J. Dent.* **42**, S12–S20 (2014).

95. Prasadh, S. & Wong, R. C. W. Unraveling the mechanical strength of biomaterials used as a bone scaffold in oral and maxillofacial defects. *Oral Sci. Int.* **15**, 48–55 (2018).

96. Doremus R H. Review Bioceramics. *J. Mater. Sci.* **27**, 285–297 (1992).

97. Kucko, N. W., Herber, R.-P., Leeuwenburgh, S. C. G. & Jansen, J. A. Calcium Phosphate Bioceramics and Cements. *Princ. Regen. Med.* 591–611 (2019) doi:10.1016/b978-0-12-809880-6.00034-5.

98. Roseti, L. *et al.* Scaffolds for Bone Tissue Engineering: State of the art and new perspectives. *Mater. Sci. Eng. C* **78**, 1246–1262 (2017).

99. Peroglio, M. *et al.* Toughening of bio-ceramics scaffolds by polymer coating. *J. Eur. Ceram. Soc.* **27**, 2679–2685 (2007).

100. Steinbrech, R. W. Toughening mechanisms for ceramic materials. *J. Eur. Ceram. Soc.* **10**, 131–142 (1992).

101. Carella, F. Synthesis and Characterization of Nanostructured Calcium Phosphate Matrices for Biomedical and Environmental Applications. *Univerista degli Stud. di Parma* (2022).

102. Ginebra, M. P., Canal, C., Espanol, M., Pastorino, D. & Montufar, E. B. Calcium phosphate cements as drug delivery materials. *Adv. Drug Deliv. Rev.* **64**, 1090–1110 (2012).

103. Iafisco, M. *et al.* Superparamagnetic iron-doped nanocrystalline apatite as a delivery system for doxorubicin. *J. Mater. Chem. B* **4**, 57–70 (2016).

104. Szcześ, A., Hołysz, L. & Chibowski, E. Synthesis of hydroxyapatite for biomedical applications. *Adv. Colloid Interface Sci.* **249**, 321–330 (2017).

105. Dorozhkin, S. V. Bioceramics of calcium orthophosphates. *Biomaterials* **31**, 1465–1485 (2010).

106. Dorozhkin, S. V. & Epple, M. Biological and medical significance of calcium phosphates. *Angew. Chemie - Int. Ed.* **41**, 3130–3146 (2002).

107. Uskoković, V. Mechanism of formation governs the mechanism of release of antibiotics from calcium phosphate nanopowders and cements in a drug-dependent manner. *J. Mater. Chem. B* **7**, 3982–3992 (2019).

108. Surmenev, R. A., Surmeneva, M. A. & Ivanova, A. A. Significance of calcium phosphate coatings for the enhancement of new bone osteogenesis - A review. *Acta Biomater.* **10**, 557–579 (2014).

109. Low, K. L. *et al.* Calcium phosphate-based composites as injectable bone substitute materials. *J. Biomed. Mater. Res. - Part B Appl. Biomater.* **94**, 273–286 (2010).

110. Zhang, J., Liu, W., Schnitzler, V., Tancret, F. & Bouler, J. M. Calcium phosphate cements for bone substitution: Chemistry, handling and mechanical properties. *Acta Biomater.* **10**, 1035–1049 (2014).

111. Francesca Carella, Lorenzo Degli Esposti, Alessio Adamiano, MIchele Iafisco, . The Use of Calcium Phosphates in Cosmetics, State of the Art and Future Perspectives. *Materials (Basel).* **4**, (2021).

112. Manjubala, I., Sastry, T. P. & Kumar, R. V. S. Bone in-growth induced by biphasic calcium phosphate ceramic in femoral defect of dogs. *J. Biomater. Appl.* **19**, 341–360 (2005).

113. Cochrane, N. J., Cai, F., Huq, N. L., Burrow, M. F. & Reynolds, E. C. Critical review in oral biology & medicine: New approaches to enhanced remineralization of tooth enamel. *J. Dent. Res.* **89**, 1187–1197 (2010).

114. Zhao, J., Liu, Y., Sun, W. Bin & Zhang, H. Amorphous calcium phosphate and its application in dentistry. *Chem. Cent. J.* **5**, 1–7 (2011).

115. Dorozhkin, S. V. Amorphous calcium (ortho)phosphates. *Acta Biomater.* **6**, 4457–4475 (2010).

116. Combes, C. & Rey, C. Amorphous calcium phosphates: Synthesis, properties and uses in biomaterials. *Acta Biomater.* **6**, 3362–3378 (2010).

117. Hughes, J. M. & Rakovan, J. F. Structurally robust, chemically diverse: Apatite and apatite supergroup minerals. *Elements* **11**, 165–170 (2015).

118. Campodoni, E. Design and development of bio-hybrid multifunctional materials for regenerative medicine. *Univeristà di Parma* (2018).

119. Ran, J. *et al.* Comparisons among Mg, Zn, Sr, and Si doped nano-hydroxyapatite/chitosan composites for load-bearing bone tissue engineering applications. *Mater. Chem. Front.* **1**, 900–910 (2017).

120. Rangavittal, N., Landa-Cánovas, A. R., González-Calbet, J. M. & Vallet-Regí, M. Structural study and stability of hydroxyapatite and β-tricalcium phosphate: Two important bioceramics. *J. Biomed. Mater. Res.* **51**, 660–668 (2000).

121. Uskoković, V. Ion-doped hydroxyapatite: An impasse or the road to follow? *Ceram. Int.* **46**, 11443–11465 (2020).

122. Graziani, G., Boi, M. & Bianchi, M. A review on ionic substitutions in hydroxyapatite thin films: Towards complete biomimetism. *Coatings* **8**, (2018).

123. Lelli, M. *et al.* Hydroxyapatite nanocrystals as a smart, pH sensitive, delivery system for kiteplatin. *Dalt. Trans.* **45**, 13187–13195 (2016).

124. Bharath, G. *et al.* Mesoporous hydroxyapatite nanoplate arrays as pH-sensitive drug carrier for cancer therapy. *Mater. Res. Express* **6**, (2019).

125. Degli Esposti, L., Carella, F., Adamiano, A., Tampieri, A. & Iafisco, M. Calcium phosphate-based nanosystems for advanced targeted nanomedicine. *Drug Dev. Ind. Pharm.* **44**, 1223–1238 (2018).

126. Ginebra, M. P., Espanol, M., Maazouz, Y., Bergez, V. & Pastorino, D. Bioceramics and bone healing. *EFORT Open Rev.* **3**, 173–183 (2018).

127. Ruffini, A. *et al.* Nature-inspired unconventional approaches to develop 3d bioceramic scaffolds with enhanced regenerative ability. *Biomedicines* **9**, (2021).

128. Theiss, F. *et al.* Biocompatibility and resorption of a brushite calcium phosphate cement. *Biomaterials* **26**, 4383–4394 (2005).

129. Pina, S. & Ferreira, J. M. F. Brushite-forming Mg-, Zn- and Sr-substituted bone cements for clinical applications. *Materials (Basel).* **3**, 519–535 (2010).

130. Cabrejos-Azama, J. *et al.* Magnesium substitution in brushite cements for enhanced bone tissue regeneration. *Mater. Sci. Eng. C* **43**, 403–410 (2014).

131. Huan, Z. & Chang, J. Novel bioactive composite bone cements based on the β-tricalcium phosphate-monocalcium phosphate monohydrate composite cement system. *Acta Biomater.* **5**, 1253–1264 (2009).

132. Carrodeguas, R. G. & De Aza, S. α-Tricalcium phosphate: Synthesis, properties and biomedical applications. *Acta Biomater.* **7**, 3536–3546 (2011).

133. Goto, T. & Katsui, H. Chemical vapor deposition of ca-p-o film coating. *Interface Oral Heal. Sci. 2014 Innov. Res. Biosis-Abiosis Intell. Interface* 103–115 (2015) doi:10.1007/978-4-431-55192-8_9/FIGURES/12.

134. Lobo, S. E. & Livingston Arinzeh, T. Biphasic Calcium Phosphate Ceramics for Bone Regeneration and Tissue Engineering Applications. *Materials (Basel).* **3**, 815–826 (2010).

135. Maji, K. & Mondal, S. Calcium Phosphate Biomaterials for Bone Tissue Engineering: Properties and Relevance in Bone Repair. in *Racing for the Surface: Antimicrobial and Interface Tissue Engineering* (eds. Li, B., Moriarty, T. F., Webster, T. & Xing, M.) 535–555 (Springer International Publishing, 2020). doi:10.1007/978-3-030-34471-9_20.

136. Lim, P. N., Teo, E. Y., Ho, B., Tay, B. Y. & Thian, E. S. Effect of silver content on the antibacterial and bioactive properties of silver-substituted hydroxyapatite. *J. Biomed. Mater. Res. - Part A* **101 A**, 2456–2464 (2013).

137. Gopi, D., Shinyjoy, E. & Kavitha, L. Synthesis and spectral characterization of silver/magnesium co-substituted hydroxyapatite for biomedical applications. *Spectrochim. Acta - Part A Mol. Biomol. Spectrosc.* **127**, 286–291 (2014).

138. Shi, H. *et al.* Hydroxyapatite based materials for bone tissue engineering: A brief and comprehensive introduction. *Crystals* **11**, 1–18 (2021).

139. Hurle, K., Oliveira, J. M., Reis, R. L., Pina, S. & Goetz-Neunhoeffer, F. Ion-doped Brushite Cements for Bone Regeneration. *Acta Biomater.* **123**, 51–71 (2021).

140. Iannotti, V. *et al.* Fe-Doping-Induced Magnetism in Nano-Hydroxyapatites. *Inorg. Chem.* **56**, 4446–4458 (2017).

141. Pietak, A. M., Reid, J. W., Stott, M. J. & Sayer, M. Silicon substitution in the calcium phosphate bioceramics. *Biomaterials* **28**, 4023–4032 (2007).

142. Patel, N. *et al. A comparative study on the in vivo behavior of hydroxyapatite and silicon substituted hydroxyapatite granules*.

143. Mastrogiacomo, M. *et al.* Reconstruction of extensive long bone defects in sheep using resorbable bioceramics based on silicon stabilized tricalcium phosphate. *Tissue Eng.* **12**, 1261–1273 (2006).

144. Iafisco, M., Ruffini, A., Adamiano, A., Sprio, S. & Tampieri, A. Biomimetic magnesium-carbonate-apatite nanocrystals endowed with strontium ions as anti-osteoporotic trigger. *Mater. Sci. Eng. C* **35**, 212–219 (2014).

145. Stanić, V. *et al.* Synthesis of antimicrobial monophase silver-doped hydroxyapatite nanopowders for bone tissue engineering. *Appl. Surf. Sci.* **257**, 4510–4518 (2011).

146. Jadalannagari, S., Deshmukh, K., Ramanan, S. R. & Kowshik, M. Antimicrobial activity of hemocompatible silver doped hydroxyapatite nanoparticles synthesized by modified sol–gel technique. *Appl. Nanosci.* **4**, 133–141 (2014).

147. Gokcekaya, O., Ueda, K., Narushima, T. & Ergun, C. Synthesis and characterization of Ag-containing calcium phosphates with various Ca/P ratios. *Mater. Sci. Eng. C* **53**, 111–119 (2015).

148. Tampieri, A. *et al.* Intrinsic magnetism and hyperthermia in bioactive Fe-doped hydroxyapatite. *Acta Biomater.* **8**, 843–851 (2012).

149. Uskoković, V. *et al.* Gold is for the mistress, silver for the maid: Enhanced mechanical properties, osteoinduction and antibacterial activity due to iron doping of tricalcium phosphate bone cements. *Mater. Sci. Eng. C* **94**, 798–810 (2019).

150. Degli Esposti, L. *et al.* Combined Effect of Citrate and Fluoride Ions on Hydroxyapatite Nanoparticles. *Cryst. Growth Des.* **20**, 3163–3172 (2020).

151. Degli Esposti, L., Markovic, S. & Ignjatovic, N. phosphate combined with citrate and fluoride. *J. Mater. Chem. B* **10**, (2021).

152. Yin, X. *et al.* Solubility, Mechanical and Biological Properties of Fluoridated Hydroxyapatite/Calcium Silicate Gradient Coatings for Orthopedic and Dental Applications. *J. Therm. Spray Technol.* **29**, 471–488 (2020).

153. Wang, L. *et al.* Polyetheretherketone/nano-fluorohydroxyapatite composite with antimicrobial activity and osseointegration properties. *Biomaterials* **35**, 6758–6775 (2014).

154. Ge, X. *et al.* Antibacterial coatings of fluoridated hydroxyapatite for percutaneous implants. *J. Biomed. Mater. Res. - Part A* **95 A**, 588–599 (2010).

155. Nabiyouni, M., Ren, Y. & Bhaduri, S. B. Magnesium substitution in the structure of orthopedic nanoparticles: A comparison between amorphous magnesium phosphates, calcium magnesium phosphates, and hydroxyapatites. *Mater. Sci. Eng. C* **52**, 11–17 (2015).

156. Klammert, U., Ignatius, A., Wolfram, U., Reuther, T. & Gbureck, U. In vivo degradation of low temperature calcium and magnesium phosphate ceramics in a heterotopic model. *Acta Biomater.* **7**, 3469–3475 (2011).

157. Salimi, M. H., Heughebaert, J. C. & Nancollas, G. H. Crystal Growth of Calcium Phosphates in the Presence of Magnesium Ions. *Langmuir* **1**, 119–122 (1985).

158. Cao, X. & Harris, W. Carbonate and magnesium interactive effect on calcium phosphate precipitation. *Environ. Sci. Technol.* **42**, 436–442 (2008).

159. Wang, L. & Nancollas, G. H. Calcium orthophosphates: Crystallization and Dissolution. *Chem. Rev.* **108**, 4628–4669 (2008).

160. Diallo-Garcia, S. *et al.* Influence of magnesium substitution on the basic properties of hydroxyapatites. *J. Phys. Chem. C* **115**, 24317–24327 (2011).

161. Cao, X., Harris, W. G., Josan, M. S. & Nair, V. D. Inhibition of calcium phosphate precipitation under environmentally-relevant conditions. *Sci. Total Environ.* **383**, 205–215 (2007).

162. Pors Nielsen, S. The biological role of strontium. *Bone* **35**, 583–588 (2004).

163. Pina, S., Torres, P. M., Goetz-Neunhoeffer, F., Neubauer, J. & Ferreira, J. M. F. Newly developed Sr-substituted α-TCP bone cements. *Acta Biomater.* **6**, 928–935 (2010).

164. Bianchi, M. *et al.* Strontium doped calcium phosphate coatings on poly(etheretherketone) (PEEK) by pulsed electron deposition. *Surf. Coatings Technol.* **319**, 191–199 (2017).

165. Guo, D., Xu, K., Zhao, X. & Han, Y. Development of a strontium-containing hydroxyapatite bone cement. *Biomaterials* **26**, 4073–4083 (2005).

166. Montesi, M., Panseri, S., Dapporto, M., Tampieri, A. & Sprio, S. Sr-substituted bone cements direct mesenchymal stem cells, osteoblasts and osteoclasts fate. (2017) doi:10.1371/journal.pone.0172100.

167. Sprio, S. *et al.* Novel Osteointegrative Sr-Substituted Apatitic Cements Enriched with Alginate. *Materials (Basel).* **9**, 763 (2016).

168. Landi, E. *et al.* Sr-substituted hydroxyapatites for osteoporotic bone replacement. *Acta Biomater.* **3**, 961–969 (2007).

169. Dapporto, M., Gardini, D., Tampieri, A. & Sprio, S. Nanostructured Strontium-Doped Calcium Phosphate Cements: A Multifactorial Design. *Appl. Sci.* **11**, 2075 (2021).

170. Jegou Saint-Jean, S., Camiré, C. L., Nevsten, P., Hansen, S. & Ginebra, M. P. Study of the reactivity and in vitro bioactivity of Sr-substituted α-TCP cements. *J. Mater. Sci. Mater. Med.* **16**, 993–1001 (2005).

171. Frasnelli, M. *et al.* Synthesis and characterization of strontium-substituted hydroxyapatite nanoparticles for bone regeneration. *Mater. Sci. Eng. C* **71**, 653–662 (2017).

172. Wang, Q. *et al.* Experimental and simulation studies of strontium/fluoride-codoped hydroxyapatite nanoparticles with osteogenic and antibacterial activities. *Colloids Surfaces B Biointerfaces* **182**, 110359 (2019).

173. Sepantafar, M., Mohammadi, H., Maheronnaghsh, R., Tayebi, L. & Baharvand, H. Single phased silicate-containing calcium phosphate bioceramics: Promising biomaterials for periodontal repair. *Ceram. Int.* **44**, 11003–11012 (2018).

174. Lim, P. N., Chang, L. & Thian, E. S. Development of nanosized silver-substituted apatite for biomedical applications: A review. *Nanomedicine Nanotechnology, Biol. Med.* **11**, 1331–1344 (2015).

175. Rajendran, A., Barik, R. C., Natarajan, D., Kiran, M. S. & Pattanayak, D. K. Synthesis, phase stability of hydroxyapatite-silver composite with antimicrobial activity and cytocompatability. *Ceram. Int.* **40**, 10831–10838 (2014).

176. Akter, M. *et al.* A systematic review on silver nanoparticles-induced cytotoxicity: Physicochemical properties and perspectives. *J. Adv. Res.* **9**, 1–16 (2018).

177. Hanawa, T. *et al.* Cytotoxicities of oxides, phosphates and sulphides of metals. *Biomaterials* **13**, 20–24 (1992).

178. Rameshbabu, N. *et al.* Antibacterial nanosized silver substituted hydroxyapatite : Synthesis and characterization. **10**, (2006).

179. Ciobanu, C. S. *et al.* Synthesis and antimicrobial activity of silver-doped hydroxyapatite nanoparticles. *Biomed Res. Int.* **2013**, (2013).

180. Badrour, L., Sadel, A., Zahir, M., Kimakh, L. & El Hajbi, A. Synthesis and physical and chemical characterization of Ca10-xAgx(PO4)6(OH) 2-x□x apatites. *Ann. Chim. Sci. des Mater.* **23**, 61–64 (1998).

181. Ito, A., Shinkai, M., Honda, H. & Kobayashi, T. Medical application of functionalized magnetic nanoparticles. *J. Biosci. Bioeng.* **100**, 1–11 (2005).

182. Manchón, A. *et al.* A new iron calcium phosphate material to improve the osteoconductive properties of a biodegradable ceramic: A study in rabbit calvaria.

Biomed. Mater. **10**, (2015).

183. Perez, R. A., Patel, K. D. & Kim, H. W. Novel magnetic nanocomposite injectables: Calcium phosphate cements impregnated with ultrafine magnetic nanoparticles for bone regeneration. *RSC Adv.* **5**, 13411–13419 (2015).
184. Xu, C. *et al.* Magnetic Hyperthermia Ablation of Tumors Using Injectable Fe3O4/Calcium Phosphate Cement. *ACS Appl. Mater. Interfaces* **7**, 13866–13875 (2015).
185. Panseri, S. *et al.* Intrinsically superparamagnetic Fe-hydroxyapatite nanoparticles positively influence osteoblast-like cell behaviour. *J. Nanobiotechnology* **10**, 1 (2012).
186. Sun, H. *et al.* 3D printing of calcium phosphate scaffolds with controlled release of antibacterial functions for jaw bone repair. *Mater. Des.* **189**, 108540 (2020).
187. Finceramica. CustomBone. Date accessed: 08/10/2023 https://www.finceramica.it/en/prodotti_servizi/neurochirurgia/custombone_sostituto_osseo_su_misura.
188. Kon, E. *et al.* Bone Regeneration in Load-Bearing Segmental Defects, Guided by Biomorphic, Hierarchically Structured Apatitic Scaffold. *Front. Bioeng. Biotechnol.* **9**, 1–16 (2021).
189. Lewis, G. Injectable bone cements for use in vertebroplasty and kyphoplasty: State-of-the-art review. *J. Biomed. Mater. Res. - Part B Appl. Biomater.* **76**, 456–468 (2006).
190. Sprio, S., Fricia, M., Maddalena, G. F., Nataloni, A. & Tampieri, A. Osteointegration in cranial bone reconstruction: A goal to achieve. *J. Appl. Biomater. Funct. Mater.* **14**, e470–e476 (2016).
191. Abbasi, N., Hamlet, S., Love, R. M. & Nguyen, N. T. Porous scaffolds for bone regeneration. *J. Sci. Adv. Mater. Devices* **5**, 1–9 (2020).
192. Sprio, S., Ruffini, A., Dapporto, M. & Tampieri, A. *New biomimetic strategies for regeneration of load-bearing bones*. *Bio-Inspired Regenerative Medicine: Materials, Processes and Clinical Applications* vol. 6 (2016).
193. Dapporto, M., Sprio, S., Fabbi, C., Figallo, E. & Tampieri, A. A novel route for the synthesis of macroporous bioceramics for bone regeneration. *J. Eur. Ceram. Soc.* **36**, 2383–2388 (2016).
194. Vivanco, J., Araneda, A. & Ploeg, H. L. Effect of Sintering Temperature on Microstructural Properties of Bioceramic Bone Scaffolds. *Ceram. Trans.* **237**, 101–109 (2012).
195. Studart, A. R., Gonzenbach, U. T., Tervoort, E. & Gauckler, L. J. Processing routes to macroporous ceramics: A review. *J. Am. Ceram. Soc.* **89**, 1771–1789 (2006).
196. Champion, E. Sintering of calcium phosphate bioceramics. *Acta Biomater.* **9**, 5855–

5875 (2013).

197. Eom, J. H., Kim, Y. W. & Raju, S. Processing and properties of macroporous silicon carbide ceramics: A review. *J. Asian Ceram. Soc.* **1**, 220–242 (2013).

198. Ohji, T. & Fukushima, M. Macro-porous ceramics: processing and properties. *Int. Mater. Rev.* **57**, 115–131 (2012).

199. Kim, I. J., Park, J. G., Han, Y. H., Kim, S. Y. & Shackelford, J. F. Wet foam stability from colloidal suspension to porous ceramics: A review. *J. Korean Ceram. Soc.* **56**, 211–232 (2019).

200. Liverani, L. *Porous Biomaterials and Scaffolds for Tissue Engineering*. *Encyclopedia of Biomedical Engineering* vol. 1 (Elsevier, 2019).

201. Babaie, E. & Bhaduri, S. B. Fabrication Aspects of Porous Biomaterials in Orthopedic Applications: A Review. *ACS Biomater. Sci. Eng.* **4**, 1–39 (2018).

202. Mabrouk, M., Beherei, H. H. & Das, D. B. Recent progress in the fabrication techniques of 3D scaffolds for tissue engineering. *Mater. Sci. Eng. C* **110**, 110716 (2020).

203. Han, Y. H. *et al.* Spark plasma sintered bioceramics–from transparent hydroxyapatite to graphene nanocomposites: a review. *Adv. Appl. Ceram.* **119**, 57–74 (2020).

204. Deville, S. Freeze-casting of porous ceramics: A review of current achievements and issues. *Adv. Eng. Mater.* **10**, 155–169 (2008).

205. Ginebra, M. P. *Cements as bone repair materials*. *Bone Repair Biomaterials* (Woodhead Publishing Limited, 2009). doi:10.1533/9781845696610.2.271.

206. Şahin, E. Calcium Phosphate Bone Cements. *Cem. Based Mater.* (2018) doi:10.5772/intechopen.74607.

207. O'Neill, R. *et al.* Critical review: Injectability of calcium phosphate pastes and cements. *Acta Biomater.* **50**, 1–19 (2017).

208. Canal, C. & Ginebra, M. P. Review article Fibre-reinforced calcium phosphate cements : A review. *J. Mech. Behav. Biomed. Mater.* **4**, 1658–1671 (2011).

209. Bigi, A. & Boanini, E. Functionalized biomimetic calcium phosphates for bone tissue repair. *J. Appl. Biomater. Funct. Mater.* **15**, e313–e325 (2017).

210. Ginebra, M. P., Traykova, T. & Planell, J. A. Calcium phosphate cements as bone drug delivery systems: A review. *J. Control. Release* **113**, 102–110 (2006).

211. Parent, M., Baradari, H., Champion, E., Damia, C. & Viana-Trecant, M. Design of calcium phosphate ceramics for drug delivery applications in bone diseases: A review of the parameters affecting the loading and release of the therapeutic substance. *J. Control. Release* **252**, 1–17 (2017).

212. Fosca, M., Rau, J. V. & Uskoković, V. Factors influencing the drug release from

calcium phosphate cements. *Bioact. Mater.* **7**, 341–363 (2022).

213. Lyons, J. G., Plantz, M. A., Hsu, W. K., Hsu, E. L. & Minardi, S. Nanostructured Biomaterials for Bone Regeneration. *Front. Bioeng. Biotechnol.* **8**, 1–28 (2020).

214. Tampieri, A. *et al.* From wood to bone: Multi-step process to convert wood hierarchical structures into biomimetic hydroxyapatite scaffolds for bone tissue engineering. *J. Mater. Chem.* **19**, 4973–4980 (2009).

215. Sprio, S. *et al.* Bio-inspired assembling/mineralization process as a flexible approach to develop new smart scaffolds for the regeneration of complex anatomical regions. *J. Eur. Ceram. Soc.* **36**, 2857–2867 (2016).

216. Vincent, J. F. V., Bogatyreva, O. A., Bogatyrev, N. R., Bowyer, A. & Pahl, A. K. Biomimetics: Its practice and theory. *J. R. Soc. Interface* **3**, 471–482 (2006).

217. White RA, Weber JN, W. E. Replamineform: a new process for preparing porous ceramic, metal, and polymer prosthetic materials. *Science (80-.).* **176**, 922–924 (1972).

218. Baino, F. & Ferraris, M. Learning from Nature: Using bioinspired approaches and natural materials to make porous bioceramics. *Int. J. Appl. Ceram. Technol.* **14**, 507–520 (2017).

219. Tampieri, A. *et al.* Heterogeneous chemistry in the 3-D state: An original approach to generate bioactive, mechanically-competent bone scaffolds. *Biomater. Sci.* **7**, 307–321 (2019).

220. Sprio, S. *et al.* Hierarchical porosity inherited by natural sources affects the mechanical and biological behaviour of bone scaffolds. *J. Eur. Ceram. Soc.* **40**, 1717–1727 (2020).

221. Tampieri, A. *et al.* Biologically inspired synthesis of bone-like composite: Self-assembled collagen fibers/hydroxyapatite nanocrystals. *J. Biomed. Mater. Res. - Part A* **67**, 618–625 (2003).

222. Krishnakumar, G. S. *et al.* Evaluation of different crosslinking agents on hybrid biomimetic collagen-hydroxyapatite composites for regenerative medicine. *Int. J. Biol. Macromol.* **106**, 739–748 (2018).

223. Mano, J. F. *et al.* Natural origin biodegradable systems in tissue engineering and regenerative medicine: present status and some moving trends. *J. R. Soc. Interface* **4**, 999–1030 (2007).

224. Jiang, C. C. *et al.* Repair of porcine articular cartilage defect with a biphasic osteochondral composite. *J. Orthop. Res.* **25**, 1277–1290 (2007).

225. Langer, R. & Vacanti, J. P. Tissue engineering. *Science (80-.).* **260**, (1993).

226. Kon, E. *et al.* Orderly osteochondral regeneration in a sheep model using a novel nano-composite multilayered biomaterial. *J. Orthop. Res.* **28**, 116–124 (2010).

227. Guvendiren, M., Molde, J., Soares, R. M. D. & Kohn, J. Designing Biomaterials for 3D Printing. *ACS Biomater. Sci. Eng.* **2**, 1679–1693 (2016).

228. Hart, L. R. *et al. 3D and 4D printing of biomaterials and biocomposites, bioinspired composites, and related transformers*. *3D and 4D Printing of Polymer Nanocomposite Materials: Processes, Applications, and Challenges* (Elsevier Inc., 2019). doi:10.1016/B978-0-12-816805-9.00015-6.

229. Wang, C. *et al.* 3D printing of bone tissue engineering scaffolds. *Bioact. Mater.* **5**, 82–91 (2020).

230. Ngo, T. D., Kashani, A., Imbalzano, G., Nguyen, K. T. Q. & Hui, D. Additive manufacturing (3D printing): A review of materials, methods, applications and challenges. *Compos. Part B Eng.* **143**, 172–196 (2018).

231. Bose, S., Robertson, S. F. & Bandyopadhyay, A. Surface modification of biomaterials and biomedical devices using additive manufacturing. *Acta Biomater.* **66**, 6–22 (2018).

232. Chen, Z. *et al.* 3D printing of ceramics: A review. *J. Eur. Ceram. Soc.* **39**, 661–687 (2019).

233. Ghorbani, F., Li, D., Ni, S., Zhou, Y. & Yu, B. 3D printing of acellular scaffolds for bone defect regeneration: A review. *Mater. Today Commun.* **22**, (2020).

234. Sinha, S. K. *Additive manufacturing (AM) of medical devices and scaffolds for tissue engineering based on 3D and 4D printing*. *3D and 4D Printing of Polymer Nanocomposite Materials: Processes, Applications, and Challenges* (Elsevier Inc., 2019). doi:10.1016/B978-0-12-816805-9.00005-3.

235. Ma, H., Feng, C., Chang, J. & Wu, C. 3D-printed bioceramic scaffolds: From bone tissue engineering to tumor therapy. *Acta Biomater.* **79**, 37–59 (2018).

236. Akkineni, A. R. *et al.* 3D plotting of growth factor loaded calcium phosphate cement scaffolds. *Acta Biomater.* **27**, 264–274 (2015).

237. Tarafder, S., Dernell, W. S., Bandyopadhyay, A. & Bose, S. SrO- and MgO-doped microwave sintered 3D printed tricalcium phosphate scaffolds: Mechanical properties and in vivo osteogenesis in a rabbit model. *J. Biomed. Mater. Res. - Part B Appl. Biomater.* **103**, 679–690 (2015).

238. Touri, M. *et al.* Oxygen-Releasing Scaffolds for Accelerated Bone Regeneration. *ACS Biomater. Sci. Eng.* **6**, 2985–2994 (2020).

239. Liu, D. *et al.* 3D printed PCL/SrHA scaffold for enhanced bone regeneration. *Chem. Eng. J.* **362**, 269–279 (2019).

240. Mondal, S. *et al.* Hydroxyapatite nano bioceramics optimized 3D printed poly lactic acid scaffold for bone tissue engineering application. *Ceram. Int.* **46**, 3443–3455 (2020).

241. Alshahrani, H. A. Review of 4D printing materials and reinforced composites: Behaviors, applications and challenges. *J. Sci. Adv. Mater. Devices* **6**, 167–185 (2021).

242. Pina, S. *et al.* Scaffolding strategies for tissue engineering and regenerative medicine applications. *Materials* vol. 12 1824 (2019).

243. Stevens, M. M. Biomaterials for bone tissue engineering. *Mater. Today* **11**, 18–25 (2008).

244. Zhu, L., Luo, D. & Liu, Y. Effect of the nano/microscale structure of biomaterial scaffolds on bone regeneration. *Int. J. Oral Sci.* **12**, 1–15 (2020).

245. Hu, Q. *et al.* Effect of crystallinity of calcium phosphate nanoparticles on adhesion, proliferation, and differentiation of bone marrow mesenchymal stem cells. *J. Mater. Chem.* **17**, 4690–4698 (2007).

246. Xiao, D. *et al.* The role of calcium phosphate surface structure in osteogenesis and the mechanisms involved. *Acta Biomater.* **106**, 22–33 (2020).

247. Holthaus, M. G., Stolle, J., Treccani, L. & Rezwan, K. Orientation of human osteoblasts on hydroxyapatite-based microchannels. *Acta Biomater.* **8**, 394–403 (2012).

248. Zhao, C. *et al.* The role of the micro-pattern and nano-topography of hydroxyapatite bioceramics on stimulating osteogenic differentiation of mesenchymal stem cells. *Acta Biomater.* **73**, 509–521 (2018).

249. Costa, D. O. *et al.* The differential regulation of osteoblast and osteoclast activity bysurface topography of hydroxyapatite coatings. *Biomaterials* **34**, 7215–7226 (2013).

250. Zan, X., Sitasuwan, P., Feng, S. & Wang, Q. Effect of Roughness on in Situ Biomineralized CaP-Collagen Coating on the Osteogenesis of Mesenchymal Stem Cells. *Langmuir* **32**, 1808–1817 (2016).

251. Grigore, M. E. Drug Delivery Systems in Hard Tissue Engineering. *SF J. Biotechnol. Biomed. Eng.* **1**, 1001–1006 (2018).

252. Ke Ren, A. D. Drug Delivery Strategies for Treating Osteoporosis. *Orthop. Muscular Syst.* **s2**, 8–11 (2014).

253. Ratier, A., Freche, M., Lacout, J. L. & Rodriguez, F. Behaviour of an injectable calcium phosphate cement with added tetracycline. *Int. J. Pharm.* **274**, 261–268 (2004).

254. Chopra, I. & Roberts, M. Tetracycline Antibiotics: Mode of Action, Applications, Molecular Biology, and Epidemiology of Bacterial Resistance. *Microbiol. Mol. Biol. Rev.* **65**, 232–260 (2001).

255. Roberts, M. C. Tetracycline resistance determinants: Mechanisms of action, regulation of expression, genetic mobility, and distribution. *FEMS Microbiol. Rev.* **19**, 1–24 (1996).

256. Schnappinger, M. D. & Hillen, W. Tetracyclines: antibiotic action, uptake, and resistance mechanisms. *Arch Microbiol* **165**, 359–369 (1996).

257. Graber, E. M. Treating acne with the tetracycline class of antibiotics: A review. *Dermatological Rev.* **2**, 321–330 (2021).

258. Sehumagher, G. E. Tetracycline tableau: chemistry, pharmacy & pharmacology. *Am. J. Hosp. Pharm.* **20**, 580–586 (1963).

259. Gopal, G., Alex, S. A., Chandrasekaran, N. & Mukherjee, A. A review on tetracycline removal from aqueous systems by advanced treatment techniques. *RSC Adv.* **10**, 27081–27095 (2020).

260. Ratier, A. *et al.* Setting characteristics and mechanical behaviour of a calcium phosphate bone cement containing tetracycline. *Biomaterials* **22**, 897–901 (2001).

261. Tumore ossa: sintomi, prevenzione, cause, diagnosi. https://www.airc.it/cancro/informazioni-tumori/guida-ai-tumori/tumore-alle-ossa.

262. Rodríguez-Ruiz, I. *et al.* PH-responsive delivery of doxorubicin from citrate-apatite nanocrystals with tailored carbonate content. *Langmuir* **29**, 8213–8221 (2013).

263. Kamba, S. A., Ismail, M., Hussein-Al-Ali, S. H., Ibrahim, T. A. T. & Zakaria, Z. A. B. In vitro delivery and controlled release of doxorubicin for targeting osteosarcoma bone cancer. *Molecules* **18**, 10580–10598 (2013).

264. Rivankar, S. An overview of doxorubicin formulations in cancer therapy. *J. Cancer Res. Ther.* **10**, 853–858 (2014).

265. Nikravan, G., Haddadi-Asl, V. & Salami-Kalajahi, M. Stimuli-responsive DOX release behavior of cross-linked poly(acrylic acid) nanoparticles. *e-Polymers* **19**, 203–214 (2019).

266. Faraji, A., Manshadi, H. R. D., Mobaraki, M., Zare, M. & Houshmand, M. Association of ABCB1 and SLC22A16 gene polymorphisms with incidence of doxorubicin-induced febrile neutropenia: A survey of iranian breast cancer patients. *PLoS One* **11**, 1–10 (2016).

267. Almeida, A. *et al.* Methotrexate promotes recovery of arthritis-induced alveolar bone loss and modifies the composition of the oral-gut microbiota. *Anaerobe* **75**, (2022).

268. Bedoui, Y. *et al.* Methotrexate an old drug with new tricks. *Int. J. Mol. Sci.* **20**, (2019).

269. Mukesh, U., Kulkarni, V., Tushar, R. & Murthy, R. S. R. Methotrexate loaded self stabilized calcium phosphate nanoparticles: A novel inorganic carrier for intracellular drug delivery. *J. Biomed. Nanotechnol.* **5**, 99–105 (2009).

270. FDA. Clinical Pharmacology and Biopharmaceutics Review. *Fda* 1–5 (2009).

271. de Wit, D. *et al.* Everolimus pharmacokinetics and its exposure–toxicity relationship

in patients with thyroid cancer. *Cancer Chemother. Pharmacol.* **78**, 63–71 (2016).

272. Saran, U., Foti, M. & Dufour, J. F. Cellular and molecular effects of the mTOR inhibitor everolimus. *Clin. Sci.* **129**, 895–914 (2015).

273. Zahavi, D. & Weiner, L. Monoclonal Antibodies in Cancer Therapy. *Antibodies* **9**, 34 (2020).

274. Weiner, L. M., Surana, R. & Wang, S. Monoclonal antibodies: versatile platforms for cancer immunotherapy. *Nat. Rev. Immunol.* **10**, 317–327 (2010).

275. Pageau, S. C. Denosumab. *MAbs* **1**, 210–215 (2009).

276. Hanley, D. A., Adachi, J. D., Bell, A. & Brown, V. Denosumab: Mechanism of action and clinical outcomes. *Int. J. Clin. Pract.* **66**, 1139–1146 (2012).

277. Iqbal, J., Sun, L., Mechanick, J. I. & Zaidi, M. Anti-cancer actions of Denosumab. *Curr. Osteoporos. Rep.* **9**, 173–176 (2011).

278. Brown, J. E. & Coleman, R. E. Denosumab in patients with cancer-a surgical strike against the osteoclast. *Nat. Rev. Clin. Oncol.* **9**, 110–118 (2012).

279. Ginebra, M. P., Canal, C., Espanol, M., Pastorino, D. & Montufar, E. B. Calcium phosphate cements as drug delivery materials. *Adv. Drug Deliv. Rev.* **64**, 1090–1110 (2012).

280. Grassi, M. & Grassi, G. Application of mathematical modeling in sustained release delivery systems. *Expert Opin. Drug Deliv.* **11**, 1299–1321 (2014).

281. Peppas, N. A. & Narasimhan, B. Mathematical models in drug delivery: How modeling has shaped the way we design new drug delivery systems. *J. Control. Release* **190**, 75–81 (2014).

282. Trucillo, P. Drug Carriers: A Review on the Most Used Mathematical Models for Drug Release. *Processes* **10**, 1094 (2022).

283. Bruschi, M. L. Mathematical models of drug release. in *Strategies to Modify the Drug Release from Pharmaceutical Systems* 63–86 (Elsevier, 2015). doi:10.1016/B978-0-08-100092-2.00005-9.

284. Paarakh, M. P., Jose, P. A. N. I., Setty, C. M. & Peter, G. V. Release Kinetics – Concepts and Applications. *Int. J. Pharm. Res. Technol.* **8**, 12–20 (2019).

285. Papadopoulou, V., Kosmidis, K., Vlachou, M. & Macheras, P. On the use of the Weibull function for the discernment of drug release mechanisms. *Int. J. Pharm.* **309**, 44–50 (2006).

286. Goutelle, S. *et al.* The Hill equation: A review of its capabilities in pharmacological modelling. *Fundam. Clin. Pharmacol.* **22**, 633–648 (2008).

287. Mandal, S. S., Jose, D. & Bhattacharyya, A. J. Role of surface chemistry in modulating drug release kinetics in titania nanotubes. *Mater. Chem. Phys.* **147**, 247–253 (2014).

CHAPTER 2 – MATERIALS AND ANALYTIC METHODS

2.1. Materials

The list of reagents, drugs and scaffolds used in this Ph.D. research is briefly reported:

Reagents: calcium carbonate ($CaCO_3$, ≥99.0% pure), calcium phosphate dibasic anhydrous ($CaHPO_4$, ≥98.0% pure), calcium chloride dihydrate ($CaCl_2 \cdot 2H_2O$, ≥99.0% pure), calcium hydroxide ($Ca(OH)_2$, ≥95.0% pure), 4-(2-hydroxyethyl)-1-piperazineethanesulfonic acid (HEPES, $C_8H_{18}N_2O_4S$, ≥99.0% pure), hydrochloric acid (HCl, 37% pure), magnesium chloride dihydrate ($MgCl_2 \cdot 2H2O$, ≥99.0% pure), nitric acid (HNO_3; 65% pure), orthophosphoric acid (H_3PO_4 85% pure), potassium chloride (KCl ≥99.5% pure), sodium carbonate monobasic ($NaHCO_3$, ≥99.7% pure), sodium citrate tribasic dihydrate ($Na_3(C_6H_5O_7) \cdot 2H_2O$, ≥99.0% pure (named thereafter $Na_3(Cit)$), sodium hydroxide (NaOH, ≥98.0% pure), sodium phosphate dibasic dihydrate ($Na_2HPO_4 \cdot 2H_2O$, ≥99.0% pure), strontium chloride dihydrate ($SrCl_2 \cdot 2H_2O$, ≥99.0% pure), strontium carbonate ($SrCO_3$, ≥98% pure), commercial hydroxyapatite ($Ca_{10}(PO_4)_6(OH)_2$, ≥95% pure), sodium alginate (Alginic Acid Sodium Salt from Brown Algae), sodium acetate (CH_3CO_2Na ≥99% pure), dimethyl sulfoxide (DMSO, C_2H_6OS, ≥99.5% pure), ethanol (C_2H_6O, ≥99.8% pure) were purchased from Sigma Aldrich (St. Luis, MO, USA) and used without further purification. Dolapix CA (Zschimmer and Schwartz, Germany), Olympicon A (Olimpia Tensioattivi, Italy) and W53 (Zschimmer and Schwartz, Germany).

All the solutions were prepared with ultrapure water (18.2 MΩ × cm, 25 °C, arium© pro, Sartorius).

Drugs: tetracycline hydrochloride (TC, $C_{22}H_{24}N_2O_8 \cdot HCl$, ≥95% pure), doxorubicin hydrochloride (Dox, $C_{27}H_{29}NO_{11} \cdot HCl$, 98-102% (HPLC)), methotrexate (MTX, $C_{20}H_{22}N_8O_5 \cdot xH2O$, ≥98% pure (HPLC)), everolimus (Ev, $C_{53}H_{83}NO_{14}$, ≥95% pure (HPLC)), were purchased from Sigma Aldrich (St. Luis, MO, USA) and Xgeva (injectable form of Denosumab, Den, $C_{6404}H_{9912}N_{1724}O_{2004}S_{50}$ 1,7 mL, 70 mg/mL) was purchased from Amgen S.r.l. (Italy).

All the solutions were prepared with ultrapure water (18.2 MΩ × cm, 25 °C, arium© pro, Sartorius) or in DMSO.

Scaffolds: b.bone™ Bone Substitute scaffolds were supplied by *Greenbone® Ortho S.p.A.* (Italy) as a partner of *DINAMICA Project*.

2.2. Analytics methods

The principles of the analytical techniques and the sample preparation routes are briefly reported, according to previous works and doctoral thesis[1-4].

2.2.1. X-Ray Diffraction (XRD)

Powder X-ray Diffraction (PXRD) is a non-destructive analytical technique used to identity phases in crystalline materials. The material is finely ground and homogenised and the average composition of the bulk phase is analysed. The PXRD patterns of the samples were recorded using Cu Kα radiation ($\lambda = 1.54178$ Å) generated at 40 kV and 40 mA as the X-ray source on a D8 Advance diffractometer (Bruker, Karlsruhe, Germany) equipped with a Lynx eye position sensitive detector. Spectra were recorded with a step size (2θ) of 0.02 and a counting time of 0.5 s in the 2θ range from 10 to 80°.

References used: hydroxyapatite #09-0432, αTCP #29-0359 and βTCP #09-0169.

2.2.2. Fourier-Transformation Infrared Spectroscopy (FTIR)

To characterise the vibrational structure of the samples, assess the presence of functional groups and study variations in local order, Fourier transform infrared (FT-IR) spectrometry was used. The FT-IR analyses were performed on a Nicolet iS5 spectrometer (Thermo Fisher Scientific Inc., Waltham, MA, USA) with a resolution of 2cm^{-1}, using an accumulation of 32 scans covering the range 4000 to 400 cm^{-1}, with a diamond ATR accessory model iD7.

2.2.3. Inductively Coupled Plasma Optical Emission Spectroscopy (ICP-OES)

Inductively coupled plasma optical emission spectroscopy (ICP-OES) was used to determine the elemental composition of the samples. Elemental quantification (Ca, P, Sr…) was performed by Agilent 5100 ICP-OES spectrometer (Agilent Technologies, Santa Clara, CA, USA). Samples were prepared by dissolving 10 mg of sample powder in 50 mL of 2 wt% HNO_3 solution. Standard solutions of the analysed element, obtained by dilution of certified 1000 ppm standards (Sigma Aldrich, St. Luis, MO, USA), were used to construct a concentration/emission calibration curve in the concentration range 1 - 100 ppm.

2.2.4. Scanning Electron Microscopy (SEM)

The micromorphology of the samples was assessed by secondary electron imaging using scanning electron microscopy (SEM). SEM micrographs and EDS spectra were obtained using a field emission microscope (FESEM, mod. ΣIGMA, ZEISS NTS GmbH, Oberkochen, Germany). A 4.00 kV operating voltage was used. Carbon tape or carbon adhesive was used to fix the samples on aluminium stubs. Energy Dispersive X-Ray Spectrometry (Oxford Scientific, OXFORD INCA Energy 350 X-Max 50, Oxford, United Kingdom) associated with Scanning Electron Microscopy (SEM) (Zeiss, EVO MA10-HR “dual gun”, Oberkochen, Germany) at 20 kV, was used to investigate the percentage of the elements.

2.2.5. Specific surface area measurement and porosimetry

The specific surface area (SSA) of the powdered samples was measured by N_2 adsorption using the Brunauer-Emmett-Taller (BET) method. The BET N_2 adsorption method was performed using a Surfer instrument (Thermo Fisher Scientific Inc, Waltham, MA, USA). Prior to measurement, the crystalline samples were pre-treated at 200°C for 1 hour under vacuum.

2.2.6. Gillmore Needle Apparatus

Gillmore Needle Apparatus are used to determinate the initial and final setting times of bone cements and, according to standard ASTM C266-99. The apparatus consists of two horizontal arms which carry two weighted steel needles precisely machined to meet the requirement. The initial needle 2.12 mm dia., weighs 113 g, and the final needle 1.06 mm dia., weighs 453,6 g.

2.2.7. Dynamic light scattering (DLS) and Z potential

The hydrodynamic diameter and polydispersity index of nanoparticulate samples were determined using dynamic light scattering (DLS). A Zetasizer Nano analyzer (Malvern, UK) was used to measure nanoparticle size. DLS measurements were performed using the refractive index of hydroxyapatite (1.63) for the nanoparticles and the refractive index of water (1.33) and viscosity (0.887 cP) for the solvent as working parameters with backscatter detection (λ = 630 nm; θ = 173°). The concentration of the nanoparticles ranged from 0,1 and 0,5 mg/mL and double-distilled water was used as a solvent. The results are reported as the Z-average of three measurements of at least 10 runs for 10 s at 25 °C of the hydrodynamic diameters and relative polydispersity indices.

2.2.8. UV-Visible spectrophotometer

The absorption kinetics and the release profiles of different types of drugs were investigated by UV-visible spectroscopy (LAMBDA™ 750 UV/Vis/NIR spectrophotometer from PerkinElmer). For each drug release experiment, a calibration curve Absorbance vs concentration was collected by measuring standard solutions obtained from the dilution of the mother solution, considering the molar extinction coefficient of each drug.

2.2.9. High-Performance Liquid Chromatography

The quantification of Den by High-Performance Liquid Chromatography (HPLC) was carried out using a 1260 Infinity II LC System (Agilent Technologies, Santa Clara, USA). Analyses were performed adopting the method reported by Ferriera Probelli R. et al[5]. with modifications using an Agilent Eclipse Plus C4 column (100 mm × 2.1 mm, 3.5 µm, Agilent Technologies, Santa Clara, USA). The mobile phase was a mixture of 75:25% v/v of an aqueous solution of 30 mM Na_2SO_4 and ACN with TFA (0.05% v/v). The sample was eluted at a flow rate of 1.0 $mL\ min^{-1}$, the temperature was set at 25°C and the wavelength for denosumab detection was fixed at 214 nm. The elution time of Den was 10.4 min.

REFERENCES

1. Dapporto, M. Development of new bioactive and porous apatitic scaffolds for the regeneration of load-bearing bones. *Università degli Studi di Boogna.* (2016).
2. Campodoni, E. Design and development of bio-hybrid multifunctional materials for regenerative medicine. *Univeristà degli Studi di Parma* (2018).
3. Degli Esposti, L. Tailoring calcium phosphate nanoparticles for biomedical applications: a functional by design approach. *Univeristà degli Studi di Parma* (2018).
4. Carella, F. Synthesis and Characterization of Nanostructured Calcium Phosphate Matrices for Biomedical and Environmental Applications. *Univeristà degli Studi di Parma* (2022).
5. Ferreira Parobelli, R. et al. International Journal of Biological Macromolecules Quantitation of the monoclonal antibody Denosumab by bioassay and validated LC methods. *Int. J. Biol. Macromol*. **119**, 96–104 (2018).

CHAPTER 3 – DRUG RELEASE FROM MACROPOROUS SINTERED SCAFFOLD

This research activity has been supported by the Italian Ministry of Health in *Progetto Nazionale Finalizzato - GR-2016-02364704*, BIOBOS: "An in vitro and ex vivo model of biomimetic regenerative devices to treat bone metastases and soft tissue tumors".

Macroporous sintered scaffolds (MSS) are characterized by open and interconnected macroporosity commonly used in the reconstruction of cranial and craniofacial bone defects caused by trauma, tumor removal, autologous bone resorption and rejection of other prosthetic materials[1,2].

I focused my research activity on the development of MSS by direct foaming method, aiming to deliver tetracycline locally. As reported above, direct foaming guarantees about 80% of porosity by incorporating gas bubbles into ceramic slurries, followed by drying and sintering[3-8]. However, the sintering process is a thermal treatment that leads to the improvement of mechanical properties, but at the same time leads to an increase in crystallinity of HA and, therefore, a decrease in terms of chemical reactivity of scaffold surface[9]. This makes it more difficult to functionalise the surface with drugs and therefore achieve extended drug release over time[9].

3.1. Experimental methods

3.1.1. Macroporous sintered scaffold production

The preparation of MSS was carried out as previously reported[4,5]. Briefly, Commercial HA powder was calcined at 1000°C for 5 h and sieved below 150 µm. The powder was then dispersed in water using Dolapix CA at a weight ratio HA:H_2O:dispersant=73:23:4. The suspension was prepared in a 250 mL zirconia jar with zirconia balls (15 mm diameter) using a high-energy milling treatment, stirring for 30 minutes at 400 rpm (Pulverisette 6, Fritsch, Germany). Subsequently, 2% by weight of Olimpicon A and 0.7% by weight of W53 were added to the suspension as foaming agents about the amount of powder. After 5 minutes of rapid stirring at 400 rpm, the resulting foamed suspension was poured into paper moulds and dried for 2 days at room temperature to obtain stable ceramic foams (direct foaming process summarized in Figure 31). Finally, samples were sintered at 1250°C for 1h and cut into 1cm *x* 1cm *x* 0.5cm (l *x* w *x* h) parallelepipeds.

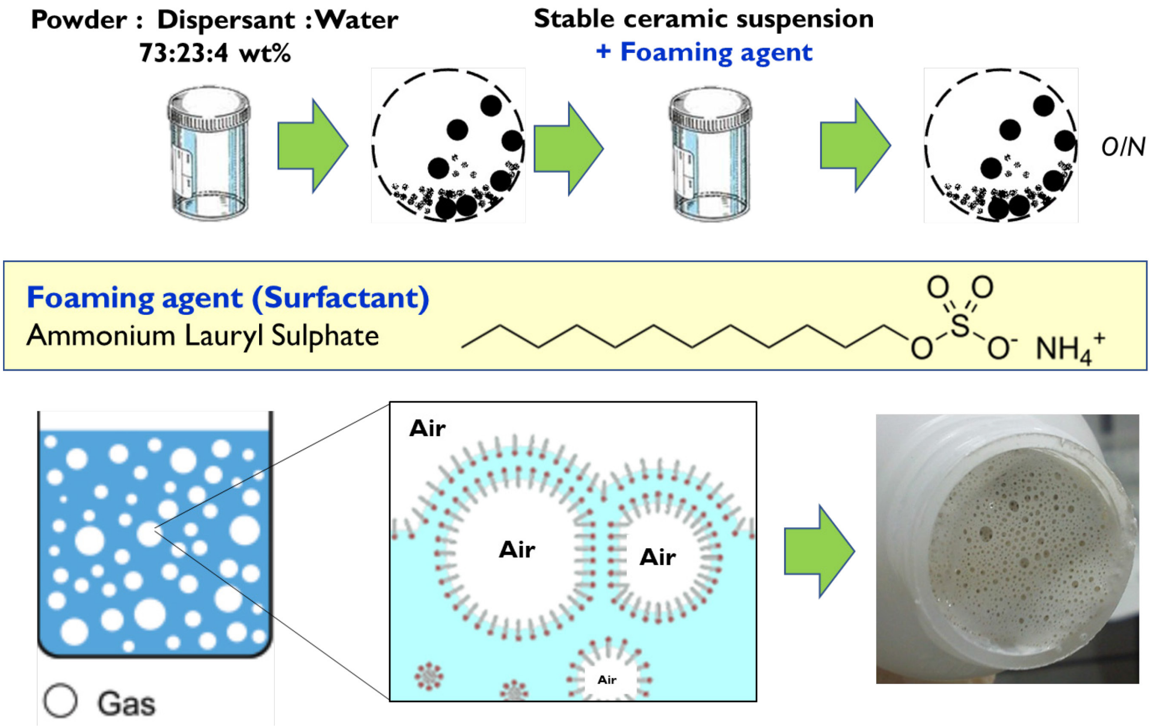

Figure 31.Schematic representation of direct foaming process.

3.1.2. Macroporous sintered scaffold for the delivery of tetracycline

Macroporous sintered scaffolds (MSSs) was functionalized with tetracycline as follow (schematized in figure 32): 100 µL of 1mg/mL of TC solution was added on scaffold surface using a pipet by depositing two drops of 50 µL. After solvent evaporation (1h at RT), TC-loaded MSSs were covered with:

i) A single layer of calcium chloride cross-linked sodium alginate, herein called **1-layer.**

ii) A double layer of calcium chloride cross-linked sodium alginate, herein called **2-layer.**

iii) A single thicker layer of calcium chloride cross-linked sodium alginate, herein called **1-thick-layer.**

by adding 1 mL of 5 wt.% sodium alginate solution on the TC-loaded MSS surface and cross-linked by dripping calcium chloride solution 1M.

As control, a drug-loaded and not coated MSS was developed too, herein called **0-layer**.

Tetracycline release experiments were conducted by immersing TC-loaded MMS in 5 mL of HEPES buffer solutions (0.01M, with KCl 0.01M, pH 7.4) in thermostatic stirrer in dark condition at 37°C up to 24h. At each time point, the 10% of solution was collected, renewed with the same volume. The collected samples were acidified with HCl 1M, to reach pH 1 and spectrophotometrically analysed by monitoring the optical density of TC at 355 nm (calibration curve between 0.05 and 50 µg/mL of TC, R^2=0.99).

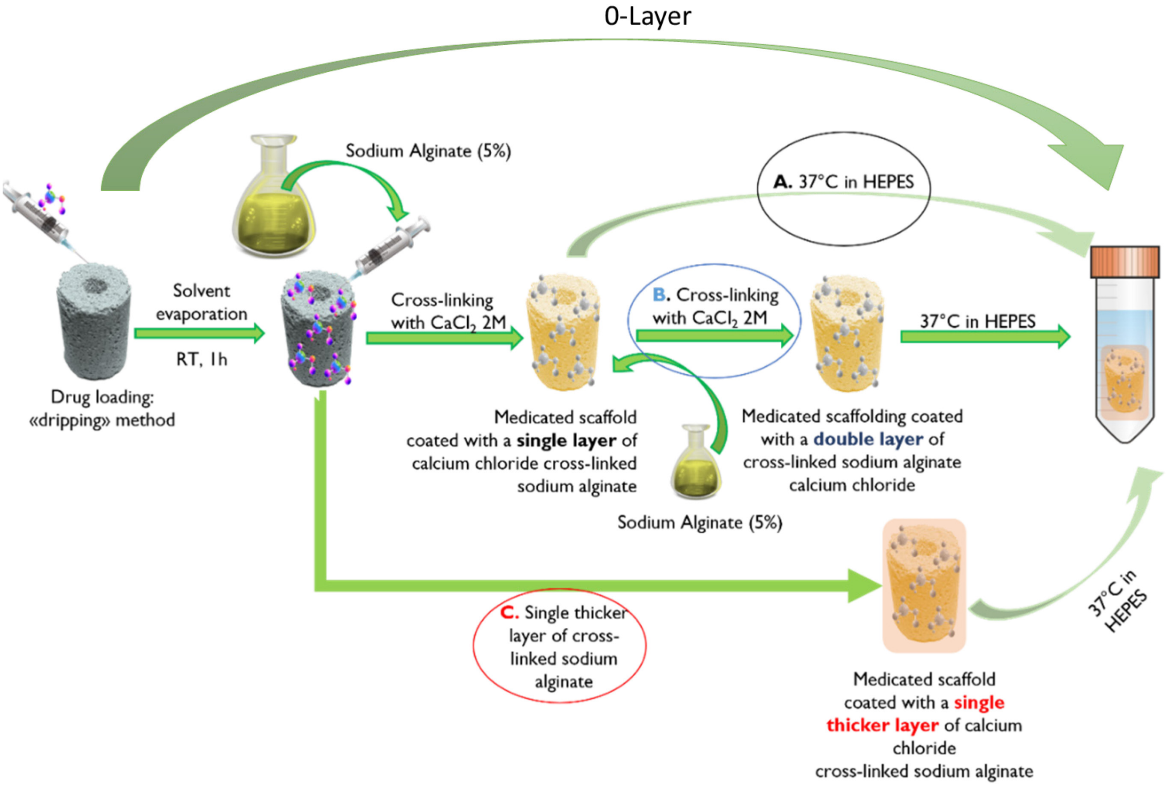

Figure 32. *Schematic representations of tetracycline loading macroporous sintered scaffold and drug release experiment*

3.2. Results and discussion

Commercial HA, calcined HA and sintered macroporous scaffold were found to consist of pure apatite phase from the XRD pattern, with increasing crystallinity in the thermally treated powder and samples attested by higher intensity in XRD peaks as well as the peak narrowing that puts in evidence peak splitting at higher diffraction, according to Bragg's law (Figure 33).

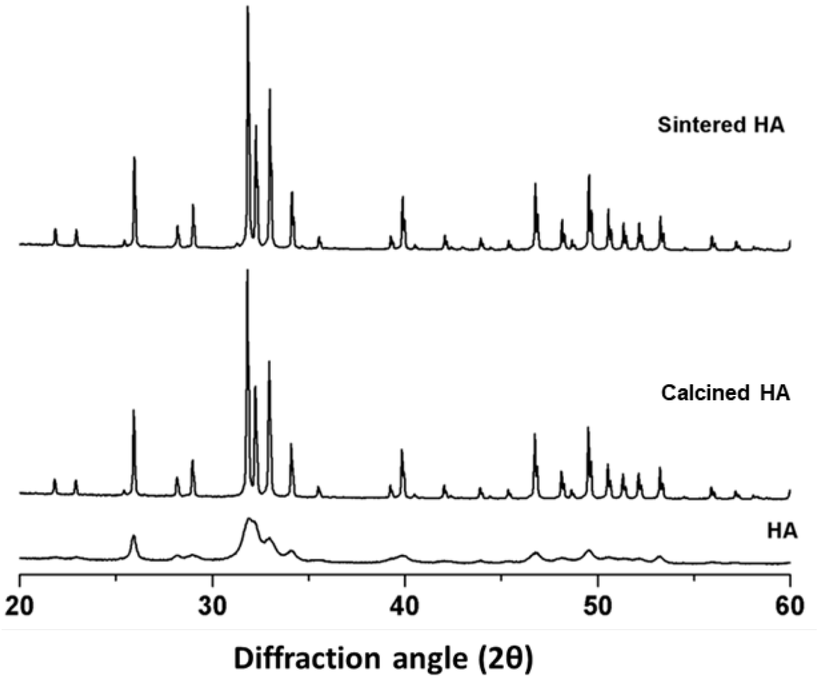

Figure 33. Diffraction profiles of hydroxyapatite (HA), calcined hydroxyapatite (calcined HA) and sintered macroporous sintered scaffold.

SEM analysis after thermal sintering treatment showed a high degree of porosity for MSS, with interconnected spherical pores (Figure 34a). In addition, a good degree of structural consolidation was observed at the coalescence level between the HA grains, interspersed with micrometric pores (Figure 34b).

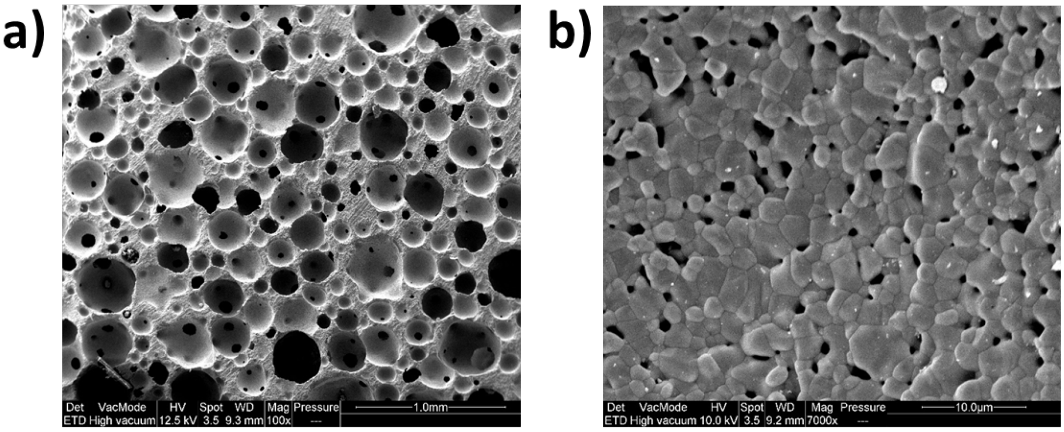

Figure 34. SEM images of macroporous sintered scaffold.

The overall porosity of the scaffolds, measured by Archimedes method, was 83.1±0.2 %, also confirmed by mercury porosimetry analysis (84%), which showed a bimodal distribution of pores, with an average diameter of 218 ± 8 µm and a modal diameter of 742 ± 2 µm (Figure 34).

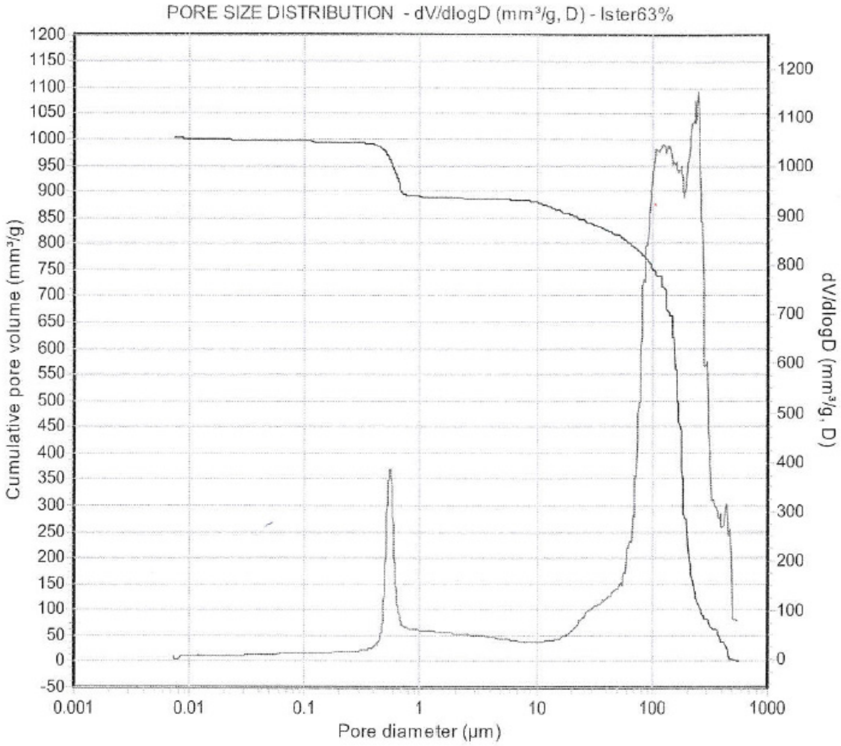

Figure 35. *Mercury porosimetry analysis on macroporous sintered scaffold*

Some physics characteristics of MSS, as compressive strength, Young's modulus, Weibull modulus and characteristic strength are reported on the following table (Table X), and was determined in our previous studies[5].

Table X. *Mechanical characterization of macroporous sintered scaffold*

	Number of specimens	Compressive strength (MPa)	Young's modulus (GPa)	Weibull modulus (m)	Characteristic strength (σ_c)
MSS	23	1.7 ± 0.4	0.8 ± 0.3	6.2	2.1

To understand the mechanism governing TC release from MMS, TC kinetic release profile was fitted with the Korsmeyer-Peppas (Eq. 10).

Firstly, the calibration curve of tetracycline in water (showed in Figure 35) was constructed by monitoring the optical density of TC in standard solution ranging from 0,5 and 50 µg/mL, which were prepared by dilution of mother solution (1 mg/mL).

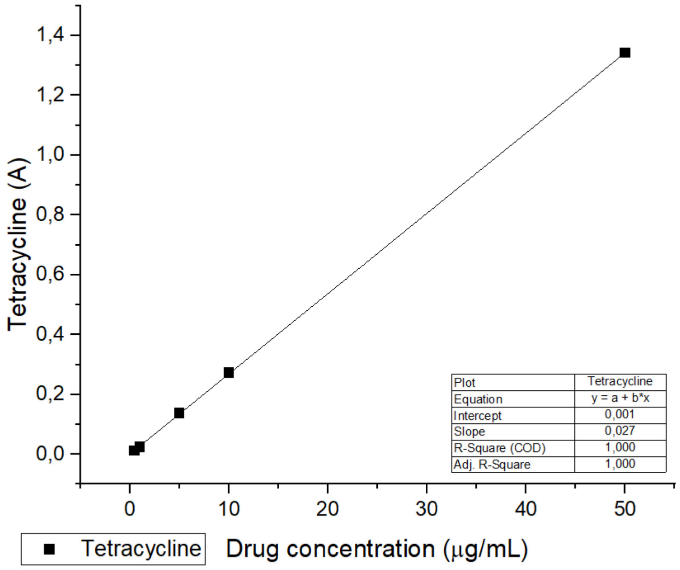

Figure 36*. Calibration curve of tetracycline in water*

Tetracycline kinetic release profiles from MSS samples are shown in Figure 36 and the result of the fitting with the mathematical models in the tables below (table XI).

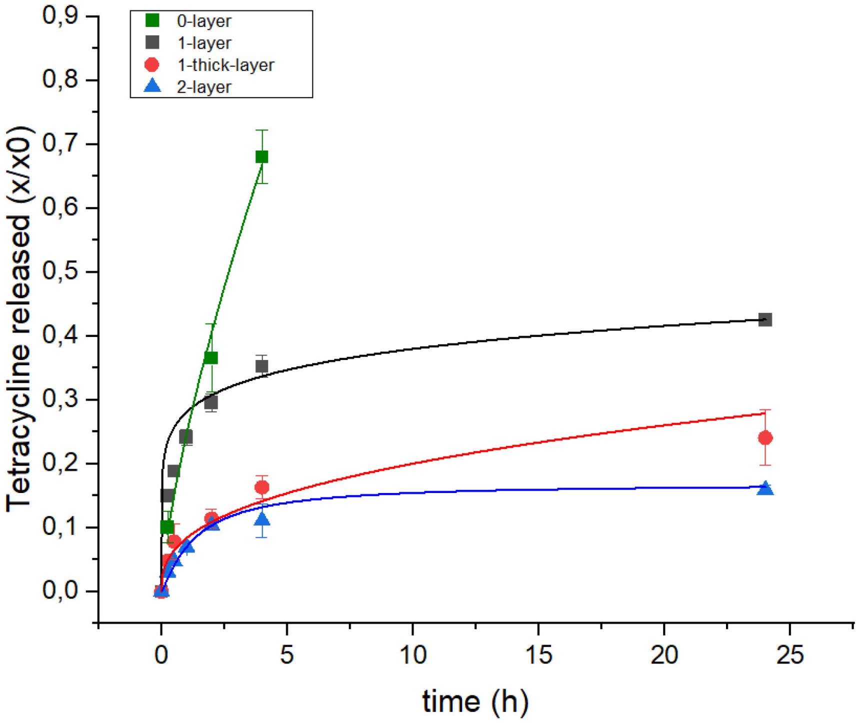

Figure 37. *Kinetic release profiles of tetracycline from un-coated MSS (green line) and MSS covered with a single layer of calcium chloride cross-linked sodium alginate (black line), double layer of calcium chloride cross-linked sodium alginate (blue line) and with a single thicker layer of calcium chloride cross-linked sodium alginate (red line).*

***Table XI. n** exponent value of Korsmeyer-Peppas model and relative release regime obtained by fitting the tetracycline release profiles.*

Samples	***n* value**	**Release regime**	***R*²**
0-layer	0.86 ± 0.19	Non-Fickian diffusion (Case II) (Zeroth-order kinetics)	0.96
1-layer	0.13 ± 0.01	Hindered Fickian Diffusion	0.99
1-thick-layer	0.34 ± 0.03	Hindered Fickian Diffusion	0.96
2-layer	0.45 ± 0.06	Fickian Diffusion (First-order kinetics)	0.99

The fitting with Korsmeyer-Peppas model (Eq. 10) evidenced a non-Fickian diffusion that correspond a zeroth-order kinetics for 0-layer samples, a hindered Fickian diffusion pattern for 1-layer and 1-thick-layer samples, while a first-order kinetics (therefore a Fickian diffusion) for the 2-layer sample (see Table IX). The findings imply that producing a single or multiple cross-linked sodium alginate layers could alter the release mechanism from non-Fickian diffusion to Fickian diffusion, consequently enabling a more consistent drug release over time.

3.3. Conclusions

In this work, the direct foaming method was implemented to prepare hydroxyapatite-based macroporous scaffolds with high open porosity (i.e., > 80 vol%). This process can also be considered as a reliable tool to customise the porosity and mechanical performance of scaffolds, potentially opening new personalised therapies for the regeneration of the skull and of load-bearing bone. The results demonstrate the ability to create multi-layers of sodium alginate, resulting in different tetracycline release mechanisms. In this respect, the release mechanism changed from 0-order to 1st-order kinetics moving from uncoated MSS to 2-layer samples. In coated samples, the coatings contain one or two cross-linked layers of sodium alginate, acting as polymeric barriers hampering the diffusion of tetracycline and resulting in diffusion rates strictly dependent on the drug concentration.

Further studies will be carried out to determine the effect of drug loading concentrations on release kinetics. In addition, *in-vitro* studies will be performed to evaluate bacteriostatic and bactericidal activity against two different bacterial strains: *Escherichia coli* and *Staphylococcus aureus*.

REFERENCES

1. Finceramica. CustomBone. Date accessed 08/10/2023 https://www.finceramica.it/en/prodotti_servizi/neurochirurgia/custombone_sostituto_osseo_su_misura
2. Sprio, S., Fricia, M., Maddalena, G. F., Nataloni, A. & Tampieri, A. Osteointegration in cranial bone reconstruction: A goal to achieve. *J. Appl. Biomater. Funct. Mater*. **14**, e470–e476 (2016).
3. Studart, A. R., Gonzenbach, U. T., Tervoort, E. & Gauckler, L. J. Processing routes to macroporous ceramics: A review. *J. Am. Ceram. Soc*. **89**, 1771–1789 (2006).
4. Dapporto, M. Development of new bioactive and porous apatitic scaffolds for the regeneration of load-bearing bones. *Univ. degli Stud. di Bol*. (2016).
5. Dapporto, M., Sprio, S., Fabbi, C., Figallo, E. & Tampieri, A. A novel route for the synthesis of macroporous bioceramics for bone regeneration. *J. Eur. Ceram. Soc*. **36**, 2383–2388 (2016).
6. Mabrouk, M., Beherei, H. H. & Das, D. B. Recent progress in the fabrication techniques of 3D scaffolds for tissue engineering. *Mater. Sci. Eng*. C **110**, 110716 (2020).
7. Roseti, L. et al. Scaffolds for Bone Tissue Engineering: State of the art and new perspectives. *Mater. Sci. Eng*. C **78**, 1246–1262 (2017).
8. Babaie, E. & Bhaduri, S. B. Fabrication Aspects of Porous Biomaterials in Orthopedic Applications: A Review. *ACS Biomater. Sci. Eng*. **4**, 1–39 (2018).
9. Parent, M., Baradari, H., Champion, E., Damia, C. & Viana-Trecant, M. Design of calcium phosphate ceramics for drug delivery applications in bone diseases: A review of the parameters affecting the loading and release of the therapeutic substance. *J. Control. Release* **252**, 1–17 (2017)

CHAPTER 4 – STRONTIUM-DOPED APATITIC BONE CEMENT: FROM BONE REGENERATION TO TREATMENT OF BONE DISEASES

This chapter reports on research activities aimed at developing new therapies for the treatment of bone disorders and diseases by functionalizing the strontium-doped apatitic bone cement with drugs (TC, Dox, MTX, Ev and Den).

As earlier introduced, bone cements are promising candidates for the regeneration of bone defects of complex morphology, thanks to their self-hardening properties, bioactive composition, and nanosized structure, which provide a high specific surface area for cell attachment and conductivity. Such properties also make CPCs interesting for functionalization with various biomolecules, to create multifunctional devices with enhanced therapeutic capabilities. In this context, strontium has been chosen as a doping ion in cement formulation because of its anti-osteoporotic activity. As explained in section 1.4.5, it can influence the activity of osteoblasts and osteoclasts by promoting bone formation and reducing bone resorption.

However, the optimization of bone cement necessarily includes the comprehension of the kinetics of the hydrolysis reaction leading to the HA formation and the rheological behavior of the slurries that should be injected.

Therefore, this chapter can be divided into two main sections: i) a first section reporting the study of the setting reaction of bone cement, and ii) a second part dealing with the development of strontium-doped apatitic bone cement as a drug delivery system for local administration of drug, by loading cement with different types of therapeutic agent (tetracycline, doxorubicin, methotrexate, everolimus and denosumab) using different approaches.

Part of the Chapter 4.2 has been published in Journal of Composite Science 2021, 5, 227 as “*Tavoni, M.; Dapporto, M.; Tampieri, A.; Sprio, S. - Bioactive Calcium Phosphate-Based Composites for Bone Regeneration*”. Part of the Chapter 4.2.1 has been published in Frontiers in Bioengineering and Biotechnology 2022, 10 as “*M. Dapporto, M. Tavoni, E. Restivo, F. Carella, G. Bruni, L. Mercatali, L. Visai, A. Tampieri, M. Iafisco, S. Sprio - Strontium-doped apatitic bone cements with tunable antibacterial and antibiofilm ability*”. Part of the Chapter 4.2.2 has been submitted in Bioactive materials as “*Lanzillotti C., Iaquinta M.R., Mosaico M., Patergnani S., Giorgi C., Sprio S., Dapporto M., Tavoni M., Tampieri A., Montesi M., Martini F., Mazzoni E. - Calcium phosphate cements for the treatment of bone tissue affected by osteosarcoma*”.

4.1. Hardening kinetics: a preliminary characterization

A mandatory task to develop scaffolds for bone tissue engineering applications is represented by the manipulation of bioceramic slurries. In this context, the rheology and self-hardening kinetics represent a powerful tool for the precise control of the final properties of the scaffolds, especially when self-hardening materials are considered.

Both physical parameters, such as the liquid/powder (L/P) ratio, and chemical parameters, such as the presence of setting accelerator salts or even doping ions, strongly influence the kinetics of the setting reaction[1-3]. In this study, the setting reaction of calcium phosphate pastes was preliminary monitored in terms of pH and phase composition over time. The inorganic composition of precursor powders involved αTCP and Sr-αTCP, while different liquid compositions and L/P ratios were used (see Table XII).

Table XII. *Slurries formulation was used in the study of the setting reaction.*

Powder	Liquid phase	Sr mol%	L/P	acronyms	Time (min)
αTCP	H_2O	-	10	**A10**	360
		-	5	**A5**	360
		-	1	**A1**	360
αTCP	5% Na_2HPO_4 (H_2O milli Q)	-	10	**ANaP10**	360
		-	5	**ANaP5**	360
		-	1	**ANaP1**	120
Sr-αTCP	5% Na_2HPO_4 (H_2O milli Q)	2	1	**SrANaP1**	180

Slurries made of αTCP or Sr-αTCP mixed with the aqueous solutions, eventually containing $Na_2HPO_4 \cdot 2H_2O$ (typical setting accelerator), were studied by continuous pH measurements and analyzed by ATR and XRD.

4.1.1. Experimental methods

Cement preparation

α-tricalcium phosphate (αTCP) was prepared by mixing calcium carbonate ($CaCO_3$), dicalcium phosphate dibasic anhydrous ($CaHPO_4$) while and Sr-doped α-tricalcium phosphate solid precursor (Sr-αTCP) was prepared by adding $SrCO_3$ to $CaCO_3$ and $CaHPO_4$, both followed by thermal treatment at 1400°C for 1 hour and rapid cooling, obtaining a final composition of αTCP and Sr-αTCP as Sr/(Ca+Sr) ≈ 2 mol%[4]. The powders were milled by planetary ball milling (Pulverisette 6 classic line, Fritsch, Germany) for 50 min at 400 rpm using a zirconia jar and 5 mm diameter grinding media. The liquid component was made of 10 mL of aqueous solution, eventually enriched with 5 wt% of $Na_2HPO_4 \cdot 2H_2O$. Finally, appropriate amounts of powder and liquid (i.e., liquid-to-powder ratio) were mixed to obtain the CPC and SrCPC cement (see Table XI).

After mixing powder and liquid, samples were characterized at specific time intervals: 30-120-240-360 min, except for ANaP1 and SrANaP1 for which characterization was performed every 30 min up to 2 h for ANaP1 and 30-120-180 min for SrANaP1. Samples were collected, lyophilized, ground, and analysed by XRD and ATR (Figure 38).

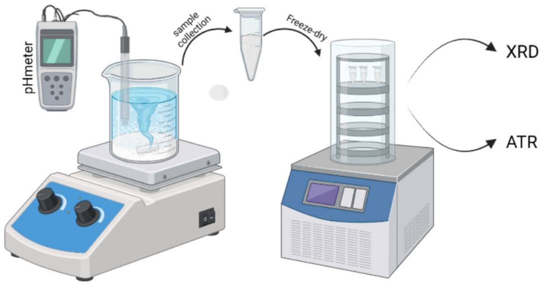

Figure 38. *Schematic representation of methods.*

4.1.2. Results and discussion

The XRD analysis of αTCP and Sr-αTCP inorganic precursor powders first confirmed the typical pattern of the αTCP phase (Figure 39).

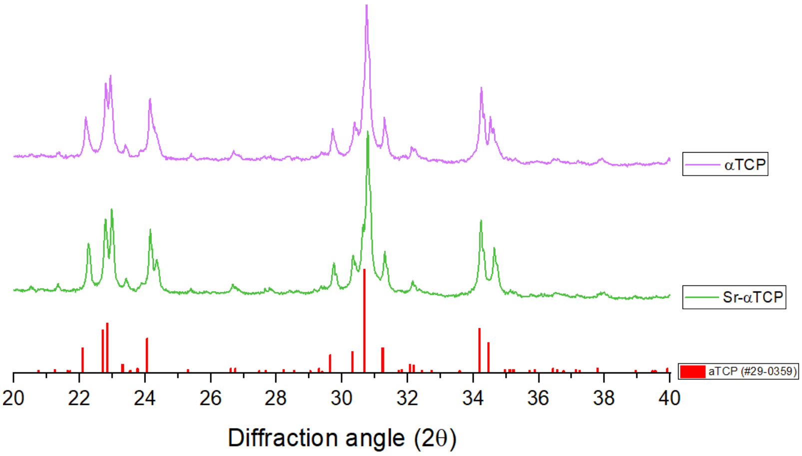

Figure 39. *XRD pattern of α-tricalcium phosphate (αTCP, purple line) and Strontium doped α-tricalcium phosphate (Sr-αTCP, green line)*

The chemical analysis of the Sr-αTCP phases confirmed the presence of strontium in amounts close to the nominal composition of the starting mixture (Table XIII).

Table XIII. *Chemical analysis and elemental composition of αTCP and Sr-αTCP*

	Sr nominal amount (mol%)	**Ca/P**	**(Ca+Sr)/P**	**Sr/(Ca+Sr) mol%**
αTCP	0	1.52 ± 0.01	-	-
Sr- αTCP	2	1.45 ± 0.03	1.49 ± 0.01	2.00 ± 0.06

Upon mixing powder and liquid phases, significant pH variations of the samples were observed, especially when setting accelerator salts were also present (Figure 40).

The lower L/P was associated to faster pH variations and faster hardening kinetics over time. Then, the presence of setting accelerator salts (sodium phosphate) was firstly associated with an increase in pH (i.e., a more basic environment), an acceleration of the hydrolysis reactions of αTCP to CDHA (reaction 2, paragraph 1.5.2), followed by a descent lasting directly proportional to the LP ratio.

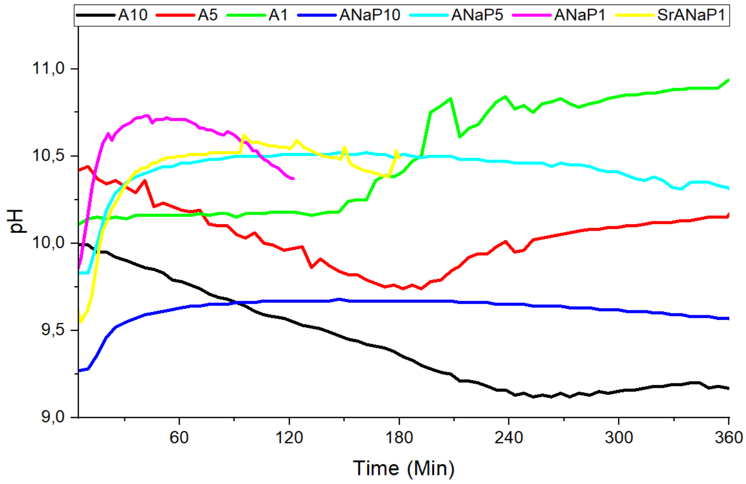

***Figure 40**. pH profile of αTCP samples in water suspension with L/P 10 (**A10, black line**), L/P5 (**A5, red line**), L/P1 (**A1, green line**), αTCP samples in water suspension enriched with 5% of sodium phosphate with L/P10 (**ANaP10, blue line**), L/P5 (**ANaP5, light blue line**) and L/P1 (**ANaP1, purple line**) and Sr- α-TCP in water suspension enriched with 5% of sodium phosphate wit L/P 1 (**SrANaP1**, **yellow line**)*

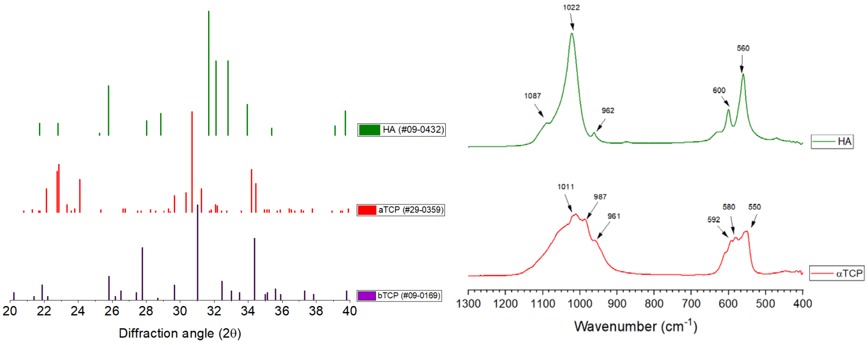

***Figure 41**. **a)** Reference diffraction pattern of hydroxyapatite (#09-0432, green line), αTCP (#29-0359, red line), and βTCP (#09-0169, violet line), **b)** Reference ATR spectra of commercial HA (green line) and αTCP (red line)*

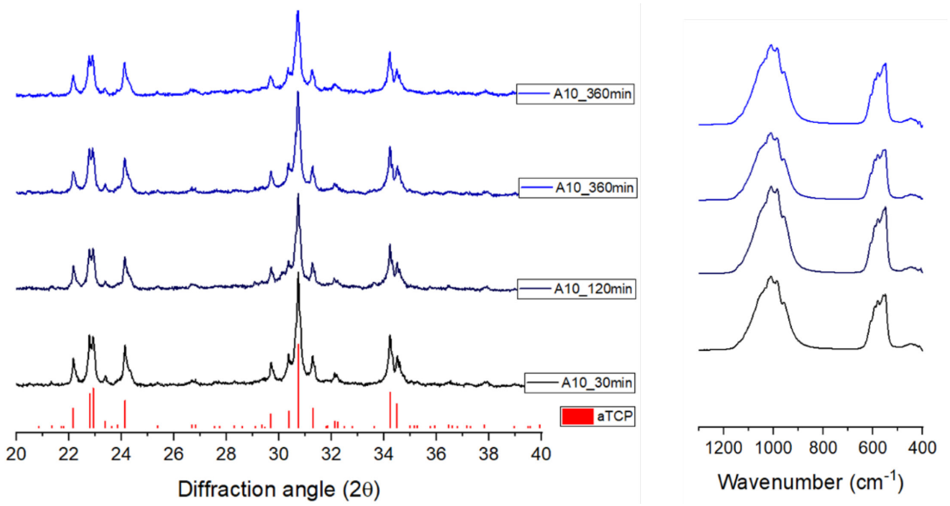

*Figure 42. a) Diffraction profile and b) ATR spectra of α-TCP samples with L/P = 10 (**A10**) at different time points: 30 min (Black line), 120 min (navy line), 240 min (blue line) 360 min (light blue line)*

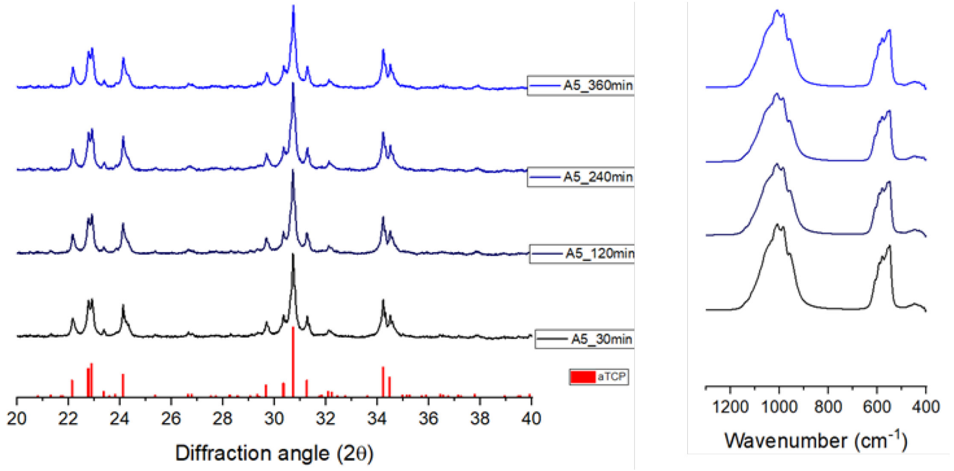

*Figure 43. a) Diffraction profile and b) ATR spectra of α-TCP samples with L/P = 5 (**A5**) at different time points: 30 min (Black line), 120 min (navy line), 240 min (blue line) 360 min (light blue line)*

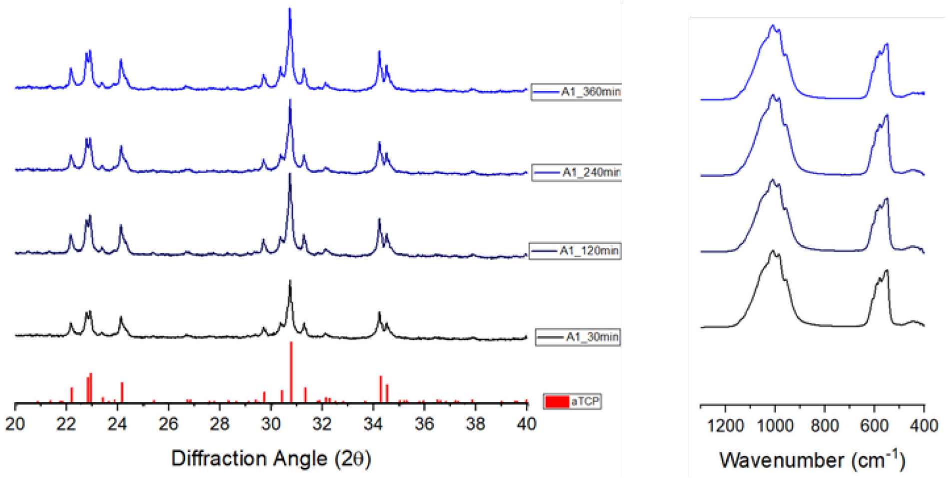

*Figure 44. a) Diffraction profile and b) ATR of α-TCP samples with L/P = 1 (**A1**) at different time points: 30 min (Black line), 120 min (navy line), 240 min (blue line) 360 min (light blue line)*

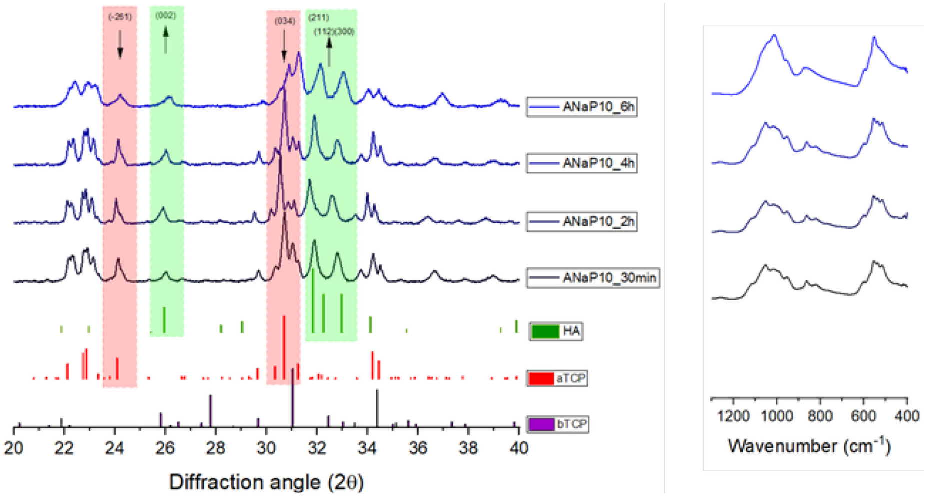

***Figure 45**. **a)** Diffraction profile and **b)** ATR of αTCP samples with 5wt% of NaP at L/P = 10 (**ANaP10**) at different time point: 30 min (Black line), 120 min (navy line), 240 min (blue line) 360 min (light blue line)*

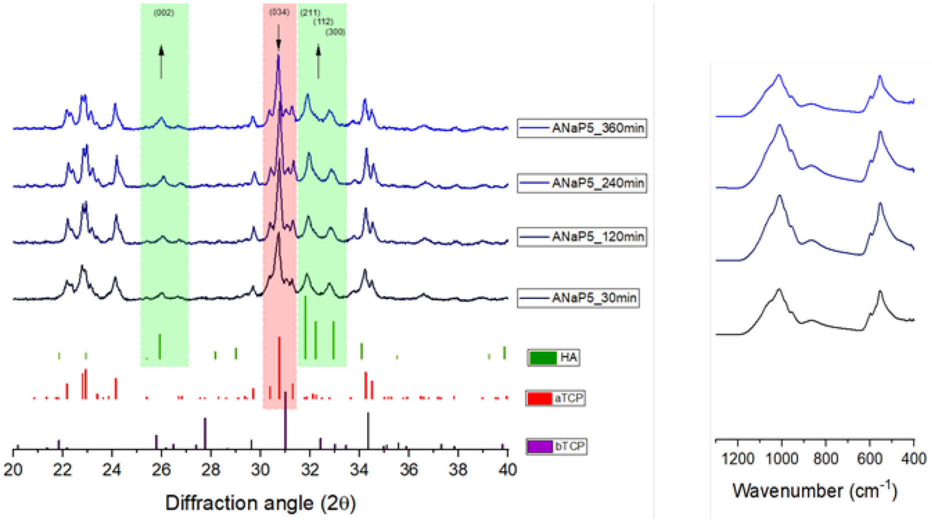

***Figure 46. a)** Diffraction profile and **b)** ATR of αTCP samples with 5wt% of NaP at L/P = 5 (**ANaP5**) at different time points: 30 min (Black line), 120 min (navy line), 240 min (blue line) 360 min (light blue line)*

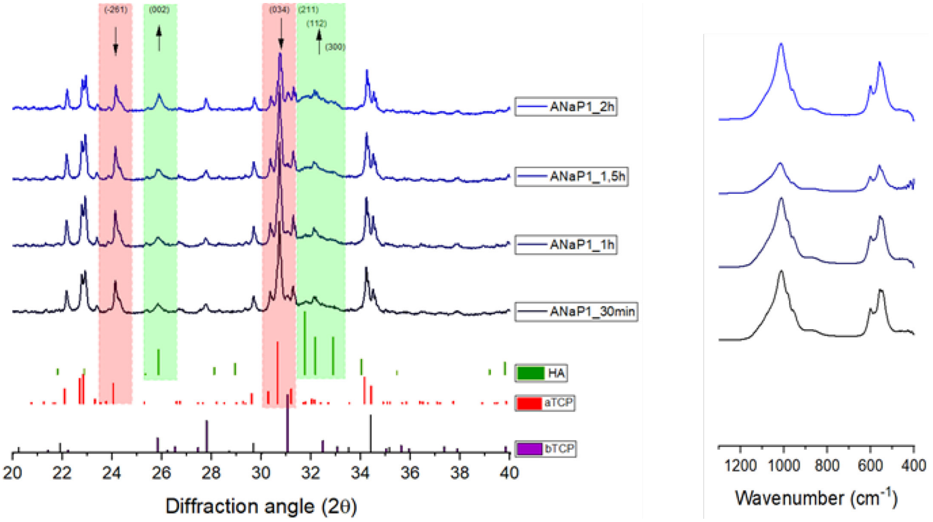

***Figure 47. a)** Diffraction profile and **b)** ATR of αTCP samples with 5wt% of NaP L/P = 10 (**ANaP1**) at different time points: 30 min (Black line), 120 min (navy line), 240 min (blue line) 360 min (light blue line)*

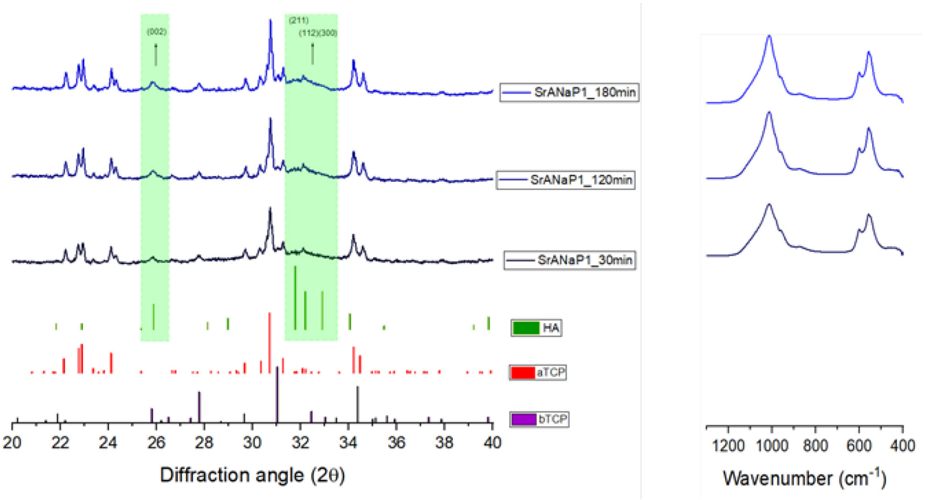

***Figure 48**. **a)** Diffraction profile and **b)** ATR of Sr-αTCP samples with L/P = 1 (**SrANaP1**) at different time points: 30 min (Black line), 120 min (navy line), 240 min (blue line) 360 min (light blue line)*

Comparing the pH profiles (Figure 40) of the A group and the ANaP group samples it is possible to observe how the presence of both $Na_2HPO_4 \cdot 2H_2O$ and strontium doping ion, as well as the L/P ratio, influences the kinetics of the hydrolysis reaction of αTCP into HA.

It can be hypothesized that for both ***A*** and ***ANaP*** groups (**A10**, **A5**, **A1**, **ANaP10**, **ANaP5**, **ANaP1**, SrANaP1) the addition of αTCP powder leads to the basification of the system due to the dissociation of TCP, as shown in the following reaction (reaction 6):

$$Ca_3(PO_4)_2 \xrightarrow{H_2O} 3Ca^{2+} + 2PO_4^{3-} \qquad (Reaction\ 6)$$

The pH profiles of ***A*** samples (**A10**, **A5,** and **A1**) show an intermediate behavior of **A5** compared to **A10** and **A1**. **A5** shows a minimum pH value around 180 min and then rises again until 420 min. In **A10** the acidification of the system was around 250 minutes and no re-basification was observed. Probably due to the high concentration of αTCP, a continuous alkalinization was observed in **A1**. During the first two hours, due to the presence of PO_4^{3-} ions in the solution that establish an acid-base equilibrium with water forming OH^- and HPO_4^{2-} ions, the increase of the pH was slow and constant. HPO_4^{2-} anion established an acid-base equilibrium with the water, with the formation of the initial anion and the conjugated acid $H_2PO_4^-$. In **A10**, where the powder concentration is lower, the trend is exactly the opposite. Based on XRD, all the ***A*** group samples at each time-point are made by a pure low crystalline αTCP, which means that the hydrolysis reaction has not yet taken place after 6 hours (phases quantification of the samples Figure 49, Table XIV). This is also confirmed by the ATR spectra which show the characteristic bands of αTCP for all ***A*** samples at each time point.

Comparing the pH profiles of ***ANaP*** samples (**ANaP10**, **ANaP5**, **ANaP1**) with those of the ***A*** group, it was observed a more stable pH profile, most probably due to the presence of Na_2HPO_4, which dissociates in water according to the following reaction (reaction 7):

$$Na_2HPO_4 \xrightarrow{H_2O} 2Na^+ + HPO_4^{2-} \qquad \textit{(Reaction 7)}$$

The mono-hydrogen phosphate ions, which is the conjugated base of a polyprotic acid, is a buffer and undergoes into acid-base balance with water according to the following equilibria (reaction 8 and 9)

$$HPO_4^{2-} + H_2O \rightleftharpoons H_2PO_4^- + OH^- \qquad \textit{(Reaction 8)}$$

$$HPO_4^{2-} + H_2O \rightleftharpoons PO_4^{3-} + H_3O^+ \qquad \textit{(Reaction 9)}$$

The acidic constant dissociation of HPO_4^{2-} is very low, about 10^{-13}, thus the equilibria described from Reaction 8 are favoured over Reaction 9. This can be the reason why the solution enriched with Na_2HPO_4 showed a constant pH profile even 7 h after the addition of αTCP. Moreover, the pH profiles of ANaP samples are lower than the A one (buffer effect).

In all ***ANaP*** samples, the pH increases with the addition of the powder to the aqueous solution enriched with 5wt% of sodium phosphate salt and remains stable. Compared to **ANaP10** and **ANaP5**, the pH curve of **ANaP1** appears compressed due to the lower LP ratio (lower the LP ratio, shorter setting time), reaching the maximum pH (10.8) around 40 minutes. In **ANaP5**, the maximum pH is higher than the **A5** sample, but the fluctuations are strongly attenuated, in fact, the pH profile is much more linear. For the **ANaP1** sample, only 120 minutes of tests were performed, particularly due to the faster hardening. Such a comparable high viscosity was obtained also in other sample (e.g., **ANaP5**), but only after 6h.

The low L/P, associated with the presence of Na_2HPO_4 in an aqueous solution, led to a significant change in pH behavior. It is therefore reasonable that what is observed in the case of **ANaP1** at close to 120 minutes is the same behavior that can also be seen in the other ***ANaP*** samples, but at much longer times, even more than 420 minutes. Indeed, this acidification is appreciable at 360 minutes for **ANaP10** and 300 for **ANaP5** samples. These pH behaviors suggest the HA formation. This hypothesis is confirmed by a semi-quantitative analysis of powders, as shown in Figures 45, 46, and 47 (**ANaP10**, **ANaP5,** and **ANaP1** respectively). In this group, a decrease in the intensity of the αTCP peaks is observed (2θ = 24.1 and 30.7, corresponding to (-261) and (034) reflections respectively), while the HA peaks increase at 2θ = 25.8, 31.7, 32.3 and 32.9, corresponding to (002), (211), (112) and (300) reflections respectively. This phase evolution suggests that the presence of sodium phosphate in the setting solution may interfere with the hydrolysis reaction of αTCP to HA. In addition, βTCP is present in all samples of this group, suggesting that the conversion to HA is via the formation of the beta-polymorph (phase quantifications of the samples are summarized in Figure 49 and Tables XIV and XV). The formation of HA is also confirmed by ATR analysis. In each sample of ***ANaP*** group is observed evolution of characteristics bands of αTCP into HA bands, even in **ANaP10** where the speed hydrolysis reaction of αTCP into HA is lower than **ANaP5** and **ANaP1**.

In this work, the effect of Sr^{2+} ions on the kinetic of the hydrolysis reaction was also evaluated. The pH profile of **SrANaP1** is quite like that of **ANaP1** but with a prolonged time. Also, in the case of **SrANaP1** samples, the XRD pattern and ATR spectra showed the formation of HA, especially in the case of XRD, which showed a decrease in the intensity of the αTCP peaks and an increase in the HA peaks, in particular the HA peak at 2θ = 25.8, corresponding to (002) reflections. Comparing the phase composition of the 2h samples (Figure 49, Table XII), the formation of HA is about 14% for **SrANaP1** (which is comparable to **ANaP10** and **ANaP5** samples, which are composed of 12 and 13% of HA respectively) and 23% for **ANaP1**. These results confirm that the presence of strontium ions in powder formulation slows down the hydrolysis reaction into HA.

Phase identification (Figure 42-48) and quantification (Figure 49, Table XIII) for each sample were carried out by XRD analysis using X'Pert High Score software. In particular, phase quantification was evaluated based on the reference intensity ratio (RIR) of each crystalline phase. The RIR method is the comparison of the intensity of one or more peaks of a phase with the intensity of a peak of a standard (usually the reflection of corundum 113) in a 50:50 mixture by weight[5].

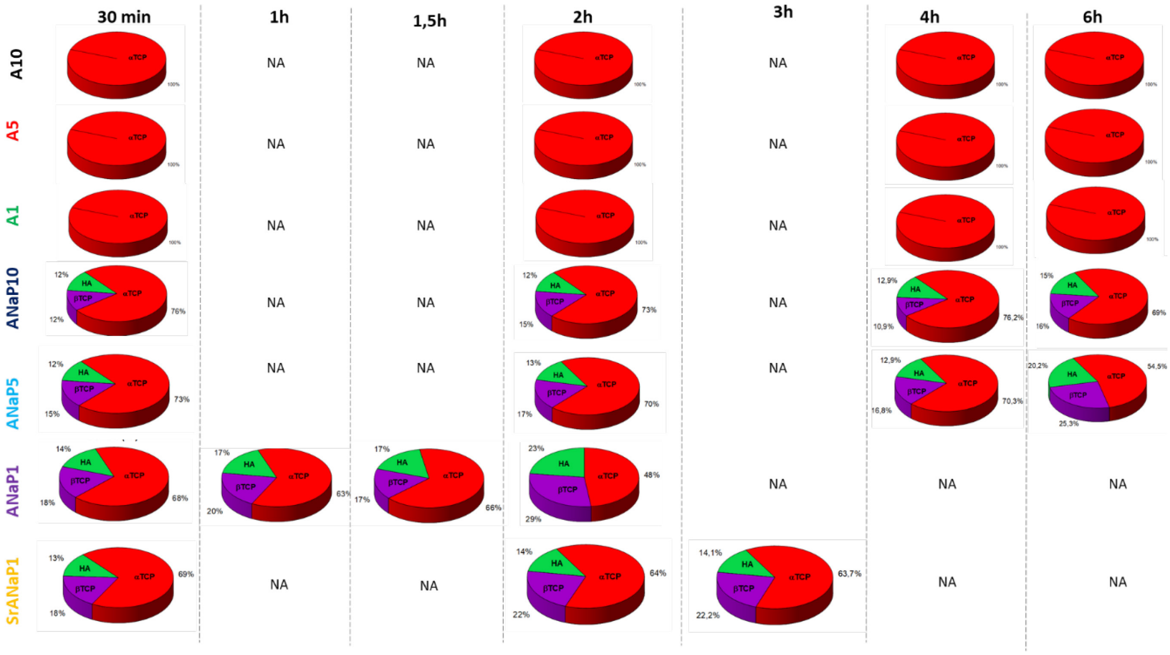

Figure 49. Phase quantification of A, ANaP, and SrANaP groups: ***A10****,* ***A5****,* ***A1****,* ***ANaP10,*** *and* ***ANaP5*** *at time-point of 30 min, 2h, 4h, 6h,* ***ANaP1*** *at the time point of 30min, 1h, 1,5h and 2h and* ***SrANaP1*** *at time 30 min, 2h and 3h.*

Table XIV. Phase quantification of ***A10****,* ***A5****,* ***A1****,* ***ANaP10****,* ***ANaP5****,* ***ANaP1*** *and* ***SrANaP1*** *at each time point.*

	30 min	60 min	90 min	120 min	180 min	240 min	360 min
A10	100% αTCP		-	100% αTCP	-	100% αTCP	100% αTCP
A5	100% αTCP	-	-	100% αTCP	-	100% αTCP	100% αTCP
A1	100% αTCP	-	-	100% αTCP	-	100% αTCP	100% αTCP
ANaP10	12% HA 12% βTCP 76% αTCP	-	-	12% HA 15% βTCP 73% αTCP	-	12.9% HA 10.9% βTCP 76.2% αTCP	15% HA 16% βTCP 69% αTCP
ANaP5	12% HA 15% βTCP 73% αTCP	-	-	13% HA 17% βTCP 70% αTCP	-	12.9% HA 16.8% βTCP 70.3% αTCP	20.2% HA 25.3% βTCP 54.5% αTCP
ANaP1	14% HA 18% βTCP 68% αTCP	17% HA 20% βTCP 63% αTCP	17% HA 17% βTCP 66% αTCP	23% HA 29% βTCP 48% αTCP	-	-	-
SrANaP1	13% HA 18% βTCP 69% αTCP	-	-	14% HA 22% βTCP 64% αTCP	14.1% HA 22.2% βTCP 63.7% αTCP	-	-

Table XV. Summary of effect on the final phase composition of L/P ratio and presence of NaP and strontium doping ion

Samples	Water	5% NaP in water
A10-ANaP10	No HA was observed over 6h	15% of HA in 6h
A5-ANaP5	No HA was observed over 6h	20,2% of HA in 6h
A1-ANaP1	No HA was observed over 6h	23% of HA in 2h
SrANaP1	-	14% of HA in 3h

4.1.3. Conclusions

In this research activity, α-tricalcium phosphate phases were successfully synthesized by solid state reactions at high temperatures. In particular, the physicochemical behaviour of pastes obtained upon mixing the powders with different amounts and compositions of aqueous solutions was investigated. It was observed that L/P, in addition to setting accelerator salts and the presence of foreign ions, played a major role in the kinetic of the hydrolysis reaction of αTCP into HA.

This research represents only a preliminary step of wider activity, to correlate the physicochemical features with the rheological behavior of pastes, towards precise modeling of the viscosity, manipulation, and extrudability of self-hardening calcium phosphate pastes and cement, which are also important in 3D-printing applications.

References

1. Ginebra, M. P., Driessens, F. C. M. & Planell, J. A. Effect of the particle size on the micro and nanostructural features of a calcium phosphate cement: A kinetic analysis. *Biomaterials* **25**, 3453–3462 (2004).
2. Ambard, A. J. & Mueninghoff, L. Calcium phosphate cement: Review of mechanical and biological properties. *J. Prosthodont*. **15**, 321–328 (2006).
3. Raymond, S. et al. Accelerated hardening of nanotextured 3D-plotted self-setting calcium phosphate inks. *Acta Biomater*. **75**, 451–462 (2018).
4. Dapporto, M., Gardini, D., Tampieri, A. & Sprio, S Nanostructured Strontium-Doped Calcium Phosphate Cements: A Multifactorial Design. *Appl. Sci*. **11**, 2075 (2021).
5. Huang, Q., Wang, C., & Shan, Q. Quantitative Deviation of Nanocrystals Using the RIR Method in X-ray Diffraction (XRD). *Nanomaterials* **12**, (2022)

4.2. Drug release from strontium-doped apatitic bone cement

As mentioned in section 1.5.2, one of the main advantages of CPC is the room-temperature self-hardening mechanism allowing the incorporation of therapeutic agents and bioactive molecules[1–3].

The cement matrix has pores that allow the surrounding physiological fluids to permeate it. The release of drugs is primarily caused by diffusion through the fluid that fills the pores (see Figure 50a). Since the microstructure of the material through which diffusion occurs is closely related to the process of diffusion itself, a successful model must take the material's microstructure into account[3]. When cement resorption is relevant, increasing the porosity can enhance the solubilized drug's mobility and surface area in contact with the release medium, resulting in accelerated drug release (Figure 50b). Conversely, in most bioactive materials, an apatitic layer forms in vivo on the surface of the CPC, which may obstruct drug release, consequently inducing a membrane effect (Figure 50c).

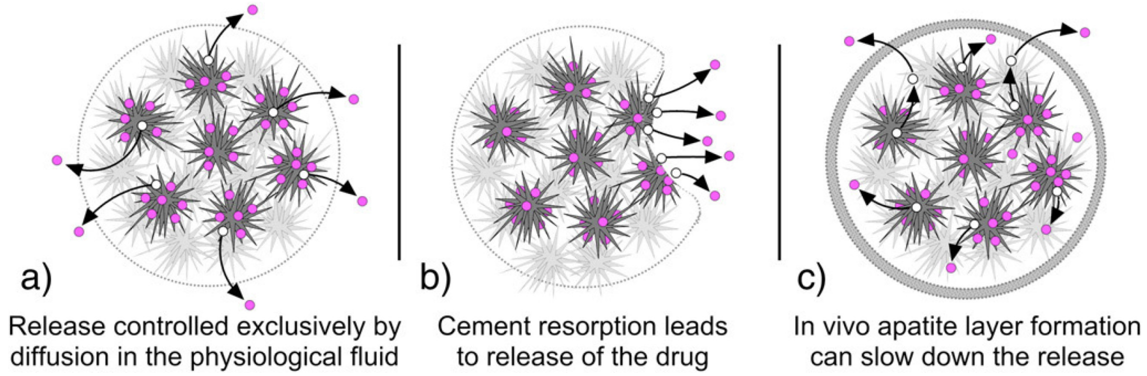

Figure 50. *Drug release from cement may include* ***a)*** *controlled drug release by drug diffusion through liquid permeating the cement,* ***b)*** *the former controls the release of the drug and* ***c)*** *an apatite layer may be formed on the surface of the cement after implantation, preventing diffusion of the drug into the surrounding tissue[3].*

The incorporation of therapeutic agents in CPCs can be achieved in different ways: by dissolving the drug in the liquid phase or by a combination with the powder phase of the CPC mixing setting[3] (Figure 51a, b). Another possible approach is the superficial adsorption of drugs on the CPC surface incubating cement in a drug solution, but in this case is not possible to obtain injectable drug-loaded cement (Figure 51c, d). Additionally, the kinetic release of drugs depends on the functionalization, microstructure, and resorbability of the CPC matrix[1-3].

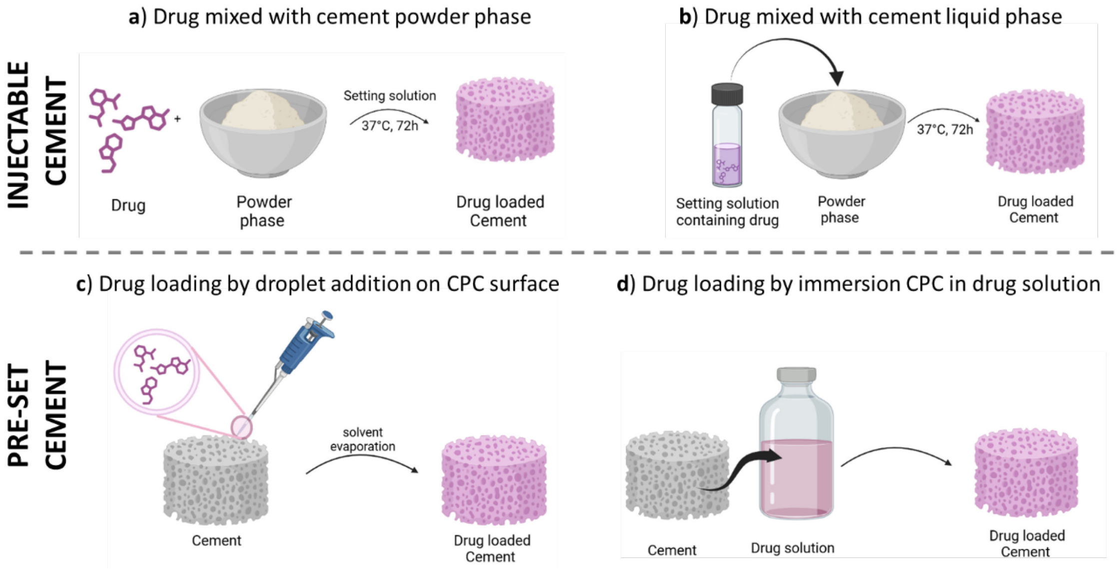

***Figure 51**. Different ways for the incorporation of drugs or biologically active molecules in Bone Cement (CPC).*

This Ph.D. thesis aimed to produce injectable strontium-doped apatitic bone cement, thus, to achieve a sustained drug release essential for the clinical application, the drug loading was made by mixing the drug in the cement powder phase or liquid phase. It is important to consider that the dissolution of the drug in the liquid phase can lead changes pH or ionic strength of the liquid phase, which can provoke the precipitation of the drug that was initially dissolved[3]. Furthermore, this research activity optimized another approach to modulate the kinetics release of TC, Dox, and Den, by mixing drug-loaded hydroxyapatite nanoparticles with the cement powder phase.

4.2.1. Strontium-doped apatitic bone cement with tuneable antibacterial and antibiofilm ability

This research activity has been supported by the *Italian Ministry of Health* in *Progetto Nazionale Finalizzato - GR-2016-02364704*, BIOBOS: “An in vitro and ex vivo model of biomimetic regenerative devices to treat bone metastases and soft tissue tumors”.

As previously reported, postoperative infection, particularly the formation of bacterial biofilms on the surface of implants, is one of the major problems associated with the implantation of scaffolds for bone regeneration. Therefore, in this work, an apatitic bone cement functionalized with tetracycline was developed.

Here, a self-hardening paste based on strontium-substituted HA by using Sr-doped α-tricalcium phosphate powders ($\alpha(Sr, Ca)_3(PO_4)_2$: Sr-αTCP) as unique solid precursor[4,5] was synthetized. Strontium was chosen as a doping ion because of its ability to enhance stem cell proliferation and modulate osteoblast and osteoclast cell fate in vitro. The aim was to re-equilibrate the natural bone turnover in the osteoporosis scenario, as reported in previous work[6].

Before mixing with the liquid component, the precursor powder was added with tetracycline (TC) or TC-loaded HA nanoparticles, suitably synthesized to achieve modulation of TC release. The incorporation of unfunctionalized HA-NPs into CPCs has been previously investigated, resulting in higher dynamic viscosity and final compressive strength of the cement[7]. Here, the TC adsorption process on HA-NPs was optimized and the TC release profile from SrCPC functionalized with free TC or TC-loaded HA-NPs was investigated under physiological conditions. Furthermore, the effect of TC functionalization on the overall microstructure and mechanical properties of the cement was evaluated.

The microbiological evaluation of TC-loaded CPCs was carried out by Elisa Restivo of the Molecular Medicine Department, Center for Health Technologies, UdR INSTM of the University of Pavia, Prof. Giovanna Bruni of Department of Chemistry, Physical Chemistry Section, Center for Colloid and Surfaces Science, University of Pavia, and Prof. Livia Visai of

---

Part of this Chapter 4.2.1 has been published in Frontiers in Bioengineering and Biotechnology 2022, 10 as “*M. Dapporto, M. Tavoni, E. Restivo, F. Carella, G. Bruni, L. Mercatali, L. Visai, A. Tampieri, M. Iafisco, S. Sprio - Strontium-doped apatitic bone cements with tunable antibacterial and antibiofilm ability*”.

Medicina Clinica-Specialistica, UOR5 Laboratorio di Nanotecnologie, ICS Maugeri, IRCCS.IRCCS Two reference infectious bacterial strains, *Escherichia coli,* and *Staphylococcus aureus* were used to evaluate the antibacterial activity of TC-loaded CPCs. In addition, TC-loaded CPCs were tested against bacterial biofilms to evaluate their ability to inhibit biofilm formation and/or disrupt preformed biofilms. Physicochemical mechanisms inherent in the chemical composition and multi-scale structure of the cured bone graft substitute, which may influence the drug release profile and antibacterial properties, were also *investigated and* discussed.

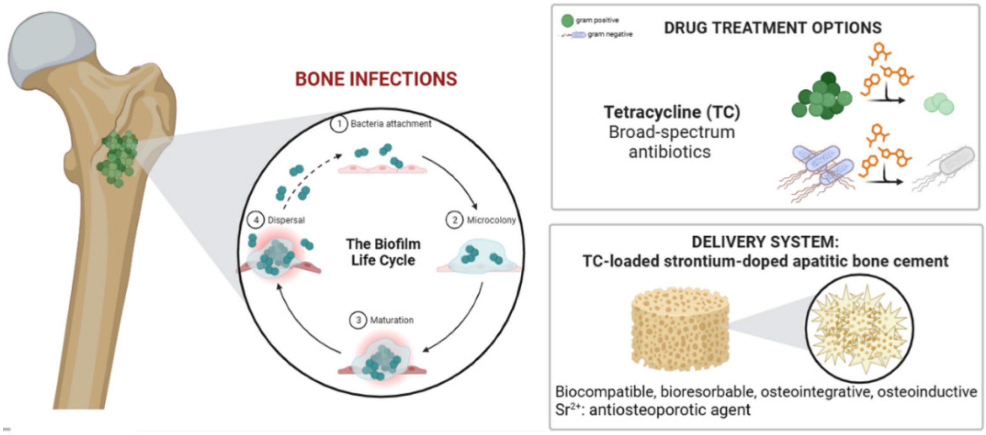

Figure 52. *Biofilm cycle and proposed treatment for bone infections*

Materials and methods

Synthesis of hydroxyapatite nanoparticles stabilized with acetate (NPs)

Hydroxyapatite nanoparticles (NPs) were synthesized as follows: a solution of H_3PO_4 (0.21 M) was dropped into a solution of $Ca(CH_3COO)_2$ (0.35 M) maintaining pH=10 by addition of NH_4OH. This mixture was stirred at room temperature overnight, then followed by powder sedimentation (2 hours) and washing with ultrapure water by multiple centrifuges at 10000 rpm per 5 minutes. Finally, NPs were freeze-dried under a vacuum (3 mbar) overnight.

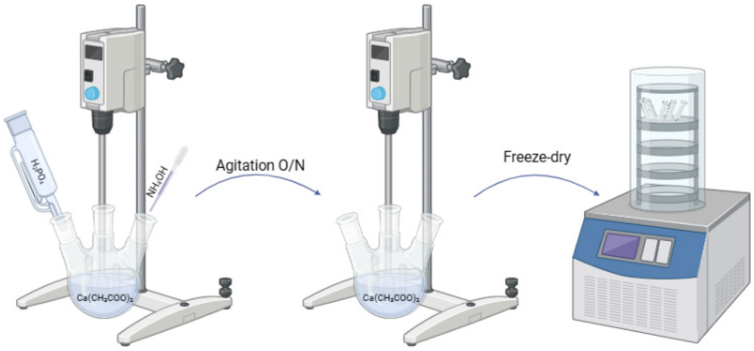

Figure 53. *Schematic representation of the experimental setup for the synthesis of acetate-stabilized hydroxyapatite nanoparticles. Created with BioRender.com*

Functionalization of CaPAc with TC

Firstly, HEPES buffer solutions (0.01M, with KCl 0.01M, pH 7.4) containing different amounts of tetracycline hydrochloride (TC) were prepared in dark conditions, to prevent the photodegradation of the drug under UV radiation. The titration of TC in HEPES was carried out by monitoring the optical density at 355 nm UV-vis spectrophotometry (calibration curve between 0.5 and 50 µg/mL of TC, R^2=1). Subsequently, the adsorption kinetics of TC on NPs (hereinafter referred to as NP-TC) were studied by dispersing 20 mg of NPs in 5 mL of TC solutions (1 mg/mL), in a thermostatic stirrer at 37°C up to 24 hours. At each time point, the supernatant was obtained after centrifuging the suspensions at 12000 rpm for 2 minutes, then analyzed by UV spectroscopy and completely refreshed. In this way, the adequate incubation time to maximize the TC adsorption on NPs was found. Then, the adsorption of increasing amounts of TC was also explored (0.1 and 1 mg/mL), with the same solid/liquid ratio and temperature used to determine the adsorption kinetic. This protocol was used to determine the optimal incubation time and TC concentration to optimize the drug loading. TC-free NP solutions were also prepared and analyzed as a control sample.

Preparation of TC-loaded calcium phosphate cements

Sr-αTCP powder precursor of SrCPC was synthesized as reported in section 4.2.1.

Preliminary experiments were carried out to evaluate the effect of dry addition of increasing amounts of NPs, in the range of 0-30 wt% concerning the Sr-αTCP precursor, on the setting times and injectability of SrCPC. In this way, the maximum amount of NPs capable of avoiding significant variations in the setting times and viscosity of the SrCPC was identified. Then, the same amount of NP-TC was dry-mixed with SrCPC in different amounts before mixing with the liquid component to prepare NP_TC loaded cement (hereafter coded as SrCPC-NPs_TC). The powder and liquid components were mixed with L/P ratio of 0.6 using a high-energy planetary shear mixer (Thinky Mixer ARE-500, Thinky, Japan) at 1000 rpm for 90 seconds. The liquid component of the paste was made of aqueous solutions of disodium hydrogen phosphate dihydrate, 5 wt%, and sodium alginate, 2 wt% (Figure 54). The effect of NP addition was tested by also preparing control TC-loaded SrCPC samples without TC_NPs cement (hereafter coded as SrCPC-TC) by dry mixing TC to the Sr-αTCP precursor in the same amount as used for NPs_TC (Figure 55).

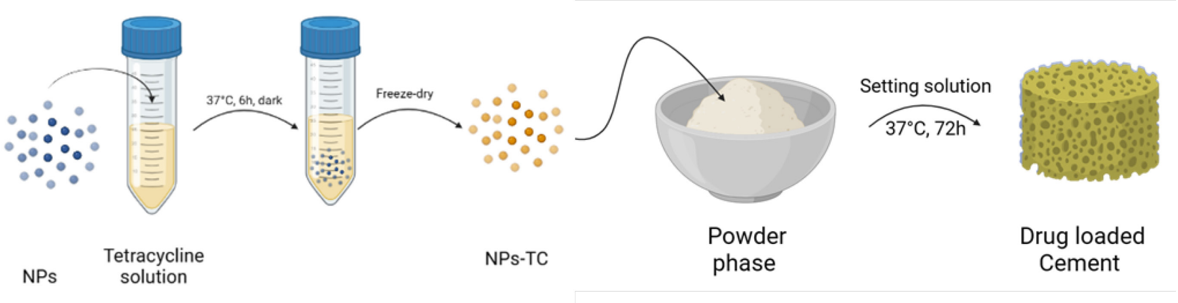

Figure 54. *Schematic representation of the preparation of tetracycline doped hydroxyapatite nanoparticles and cement containing tetracycline doped hydroxyapatite nanoparticles. Created with BioRender.com*

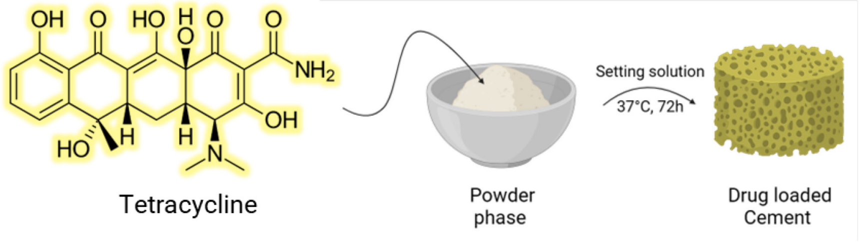

Figure 55. *Schematic representation of the preparation of cement loaded with tetracycline. Created with BioRender.com*

Physico-chemical characterization

In addition to the characterizations reported in Chapter 2, the compressive strength of cements was evaluated in this research activity. The compressive strength of cement was evaluated by testing cylindrical specimens (n. Five samples; diameter = 8 mm; height = 17 mm) obtained after hardening in Teflon moulds for 30 min and then immersed in HEPES solution at 37°C for 7 days. The tests were performed in displacement control at 1 mm/min by a universal testing machine (Zwick Roell Z050).

Bacterial strains and Bacterial biofilm culture conditions

The microorganisms used were *Escherichia coli* ATCC 25922 (*E. coli*) and S*taphylococcus aureus* ATCC 25923 (*S. aureus*), kindly obtained from the laboratory of Prof. R. Migliavacca (*Department of Clinical-Surgical Diagnostic and Pediatric Sciences, Unit of Microbiology and Clinical Microbiology*, University of Pavia, Italy). Bacteria were grown in 10 mL of appropriate medium, overnight, under aerobic conditions at 37°C using a shaker incubator (VDRL Stirrer 711/CT, Asal Srl, Italy). *E. coli* was inoculated in Luria Bertani broth (LB) (ForMediumTM, UK) whereas *S. aureus* was in TSB (Tryptic Soy Broth) (ForMediumTM, UK).

The number of bacterial cells/ml of both cultures was determined by comparing the optical density (OD600) of the sample with a standard curve relating OD600 to cell number 8-10.

Evaluation of antibacterial and antibiofilm activity of scaffolds

The antimicrobial activity of SrCPC-TC and SrCPC_NP-TC formulation was tested on cylindrical specimens (diameter = 10 mm; height = 3 mm), previously sterilized with a dose of 25 kGy gamma rays. No reduction in antibiotic release capacity of sterilized samples was observed in comparison with unsterilized ions-doped apatitic bone cement (data not shown). The antimicrobial activity was performed on all the cylindrical specimens with both bacterial strains.

The viability was estimated through the quantitative 3-(4,5-dimethylthiazol-2-yl)-2,5-diphenyltetrazolium bromide (MTT) colorimetric assay (Sigma-Aldrich, St. Louis, SM, United States). This test measures dehydrogenase activity as an indicator of the bacterial metabolic state. MTT solution (5 mg/mL), dissolved in sterile PBS (0.134 M NaCl, 20 mM Na_2HPO_4, 20 mM NaH_2PO_4), was used as a stock solution and the working concentration was 0.5 mg/mL. The test was performed for 3 h at 37°C. Upon the presence of viable bacteria, reduction of the MTT salt results in purple insoluble formazan granules that are dissolved in acidified 2-propanol (0.04 N HCl). The colorimetric reaction was analyzed at CLARIOstar (BMG Labtech, Ortenberg, Germany) at 570 nm wavelength with 630 nm as the reference wavelength. Results were normalized to bacterial cells cultured with LB medium of Tissue Culture Plate (TCP = Control). All the viability experiments were carried out in triplicate and repeated 2 times.

Direct and indirect contact experiment with planktonic bacteria

Sterile scaffolds were washed twice in sterile ddH2O. Two types of assays were performed in planktonic conditions: direct and indirect contact.

Direct contact conditions

600 µl of $1*10^4$ bacteria were incubated for 6h, 24h, and 48h, at 37°C, onto the cements, using a tissue culture plate as control (Ctrl). The viability has been assessed either on the supernatant of planktonic bacteria kindly removed from the scaffolds (analysis 1); or on the bacteria adherent onto the scaffold's surface (analysis 2). In particular:

- Analysis 1): 600 µL of the bacterial supernatants were added with 60 µL of MTT and incubated for 3 h at 37°C.
- Analysis 2): After removal of planktonic bacteria the SrCPC scaffolds were washed twice in PBS 1X and transferred into a 15 ml tube with 600 µL of PBS 1X. The tubes were vortexed to allow the detachment of bacteria. Aliquots of 100 µL were transferred into a 96-well plate and the viability was determined as previously described. Furthermore, after this treatment, the scaffolds were incubated on agar plates to confirm the absence of live bacterial cells for each strain.

Indirect contact conditions

LB (0.5 ml) medium was incubated with each scaffold placed at the bottom of a 24-well sterile culture plate (Euroclone S.p.A, Italy), overnight at 37°C to allow release of ions and tetracycline. No pH changes in the LB medium were observed.

Two-fold serial dilutions of the overnight solutions were performed starting from a volume of 100 µl of solution. 100 µl of 1*104 bacteria were inoculated and incubated for 24 h at 37°C. The viability was determined by MTT assay as previously described.

Antibiofilm experiment

Sterile scaffolds were washed twice in sterile ddH2O. The assays were performed for both bacterial strains in two types of conditions: pre-biofilm and post-biofilm.

Pre-biofilm culture conditions

Overnight cultures of *E. coli* and *S. aureus* were diluted to $1*10^7$/sample in LB containing 0.5% glucose for *E. coli* and 0.25% for *S. aureus*[11]. Aliquots of 600 µl of the diluted bacterial suspensions were directly seeded onto the scaffolds contained in 24-well culture plates (Euroclone S. p.a, Italy) and incubated for 24 h at 37°C. After the incubation time, the scaffolds were washed twice with PBS 1X and transferred into a 15 ml tube with 600 µl of PBS 1X. The tubes were vortexed to allow the detachment and resuspension of biofilm. Aliquots of 100 µl were transferred into a 96-well plate to evaluate cell viability with MTT assay as previously described.

Post-biofilm culture conditions

Firstly, the TC and ions released from the nude scaffolds in LB medium were performed in sterile conditions as previously described (indirect contact experiment). Afterward, to allow the formation of a biofilm of both bacterial strains, 200 µl of 1*107 bacteria (cultured overnight) were diluted in glucose-containing LB, directly plated in 96-well flat-bottomed sterile polystyrene microplates (Euroclone S. p.a, Italy) and incubated for 24 h at 37°C. After overnight incubation, the supernatant, containing planktonic bacteria, was carefully removed from the preformed bacterial biofilms. Two-fold serial dilutions of LB medium containing the released TC and ions from the nude scaffolds were added to the preformed biofilms for 24 h at 37°C. After the incubation time, each biofilm was washed twice with sterile PBS 1X and resuspended to detect cell viability by MTT assay as previously described.

SEM of the scaffold with bacteria biofilm

Bacteria were diluted as described in the previous section. After 24 h of incubation at 37°C, in pre-and post-biofilm conditions, the planktonic bacteria were removed and the biofilms were washed carefully with PBS 1X and fixed with 2.5% (v/v) glutaraldehyde (Sigma-Aldrich, St. Louis, SM, United States) in 0.1 M Na-cacodylate buffer (Sigma-Aldrich, St. Louis, SM, United States) (pH 7.2), for 1 h at 4°C. After two washes with Na-cacodylate, to remove excess glutaraldehyde, *E. coli* biofilms were dehydrated just with two washes of 96% ethanol (Merck Life Science S. r.l, Milano, Italy) for 10 min whereas *S. aureus* biofilms were dehydrated using increasing concentrations of ethanol (25, 50%, 75%) for 5 min and two washes of 96% ethanol for 10 min. The samples were lyophilized for 3 h using a K-850 apparatus (Emitech Ltd., Ashford, UK) and placed on a mounting base. Finally, they were gold sputtered and images were acquired using a Zeiss EVO-MA10 scanning electron microscope (Carl Zeiss, Oberkochen, Germany), 20 kV acceleration voltage.

Statistical analysis of microbiological tests

All the statistical calculations were carried out by considering the mean of the results (in triplicate) obtained from two separate experiments. The analysis was carried out using GraphPad Prism 9 (GraphPad Inc, San Diego, CA, United States). Statistical analysis was performed using Student's unpaired, two-sided t-test (significance level of $p < 0.05$). In addition, a two-way analysis of variance (ANOVA), followed by Bonferroni's multiple comparisons test was performed.

Results and discussion

Physico-chemical and release properties of NP-TC and NP-TC loaded cements.

The XRD analysis of HA-NPs reveals the typical pattern of pure HA (hexagonal, space group P63/m, figure 56a), with marked peak broadening related to the small crystal size according to the synthesis temperature (T = 40° C)[12]. No other crystalline phases were detected. The average crystalline domain size, evaluated by Scherrer's formula ($\tau = \frac{K\lambda}{\beta cos\theta}$), was 13.4 ± 2.4 nm, thus confirming the nano-crystallinity of HA-NPs. The SSA of the HA-NPs was 160.05 m^2g. The FTIR-ATR spectrum (figure 56b) confirms the vibrational signatures of HA, particularly all vibration modes of PO_4^{3-}, including the characteristic bands for v1, v2, v3 and v4 stretching modes at 963, 472, 1040 and 560–600 cm^{-1}, respectively, were detected[9]. SEM analysis (figure 43c) confirms the nano-size and the needle-like morphology of HA-NPs, which is consistent with the high SSA value found by the BET method.

A preliminary set of experiments was carried out to determine the maximum extent of HA-NPs that could be added to SrCPCs without significant variations in setting times and injectability, keeping into account that an initial setting time of ~15–20 min is considered as suitable to meet the clinical practice requirements[14,15]. A slight decrease in the initial setting times was observed, associated with a marked increase in the final setting time, when raising the concentration of HA-NPs in the cement (Figure 56d). After the initial setting, the cements were analysed by XRD along 7 days, to quantify the extent of transformation into HA. We detected enhanced HA formation in the cements enriched with

HA-NPs (i.e., in the range 10–20 vol% more than the control, see Figure 56e), ascribable to the ability of HA-NPs to act as seeds for heterogeneous nucleation of HA[3,7,14], thus enhancing the dissolution/reprecipitation process. Interestingly, we detected an increasingly lower crystallinity of the HA phase forming the cement in samples containing HA-NPs, as attested by the increase of Full Width at Half Maximum (FWHM) of the HA (002) reflection (Figure 56f), which is inversely related to the crystalline domain size along the c axis of the HA lattice[16,17]. This finding suggests that the presence of HA-NPs, besides favoring the cement setting and phase transformation process, also represents a hindering factor for the crystal growth of the new HA phase, which can be beneficial to achieve higher bioactivity. The addition of 10wt% HA-NPs, with respect to Sr-αTCP amount, was finally selected as the optimal amount for the preparation of CPC formulations with performance compliant for clinical applications.

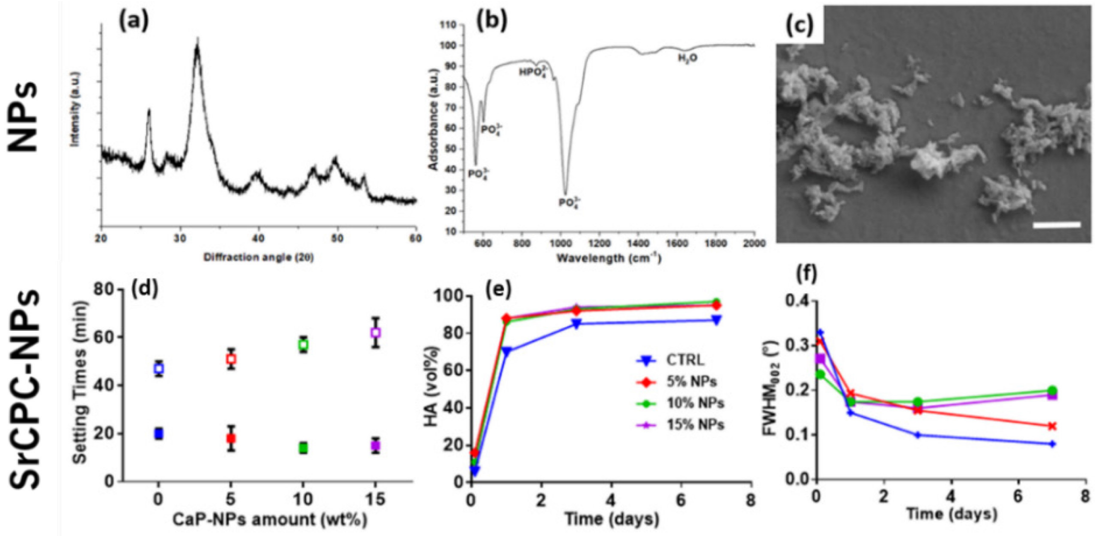

Figure 56. ***a)*** *X-ray diffraction pattern of HA-NPs;* ***b)*** *FTIR-ATR spectrum of HA-NPs;* ***c)*** *SEM micrograph of HA-NPs (scale bar = 500 nm. Effect of HA-NPs on SrCPC properties:* ***d)*** *Initial and final setting times;* ***e)*** *Phase transformation into HA up to 7 days;* ***f)*** *Full-Width at Half Maximum (FWHM) of the (002) peak up to 7 days.*

Experiments were carried out to optimize the adsorption of TC on HA-NPs (NP-TC). The adsorption kinetic of a TC solution on HA-NPs at incubation times up to 24 h evidenced the time of 6h as an adequate soaking time to achieve a quasi-equilibrium condition (Figure 57a). Then, given the optimal contact time of 6 h, the adsorption was evaluated at different TC model concentrations (Figure 57b). The adsorbed amount of TC on HA-NPs increased as a function of TC in solution, reaching a quantity of about 880.8 µg/m^2. Pristine HA-NPs exhibited slightly positive zeta potential, while a decrease in zeta potential was observed with increasing the TC concentration. In this respect, TC was reported as an amphoteric molecule with ionizable groups (i.e., a tricarbonyl amide group, a phenolic diketone group, and a dimethyl amino group) capable to undergo protonation or deprotonation reactions as a function of pH[18]. As described in the above section, a pH-sensitive behavior of TC was previously observed, three different forms exist in the function of pH: cationic, at $pH < 3.3$, zwitterionic, at pH 3.3–7.7 and anionic at $pH > 7.7$; when pH reaches above 7.0, about 25% of TC exists in the anionic form[19]. The rise of the negative surface with increasing the TC amount confirms such behavior as the pH was kept at 7.4 namely in the reported range for TC zwitterionic form, but also closely borderline with the anionic character of TC. The loading of TC on NPs was monitored by FTIR-ATR analysis (Figure 57c), highlighting vibrational peaks of TC at 1648–1582 cm^{-1} assigned to C=C stretching, aromatic C-H bending at 1458 cm^{-1} and CH_3 bending at 1357 cm^{-1} [20,21]. Aromatic in-plane and out-plane deformation peaks were detected in the range 1247–1000 cm^{-1} and 567–501 cm^{-1}, respectively, whereas the vibrational peak at 965 cm^{-1} was assigned to C-N stretching. The adsorption of TC on the surface of HA-NPs is attested especially by the increased intensity of the adsorption bands at 1640 and 1420 cm^{-1}, assigned to C=C stretching and aromatic C-H bending, respectively. Figure 44D shows that the TC release profiles from differently loaded HA-NPs feature a similar trend, reaching a plateau after 7 days. The sample loaded with 1 mg/mL TC solution (NP-TC1) exhibited an increased amount of released TC along the first 3 days and after 21 days (~80 wt%), in comparison with the sample loaded with 0.1 mg/mL (NP-TC 0.1). Such a long-term release profile suggested a stable linking of TC to the surface of HA-NPs, possibly facilitated by the presence of charged anionic groups (such as phosphate) on the apatite surface[22]. In our working conditions, the formation of electrostatic interactions between TC and the apatite surface can be hypothesized. The originated ammonium groups of TC are generally associated with low-affinity interactions to the surface of apatite. The adsorption of TC molecules on biomimetic apatite powders was previously investigated and modeled[23]. In this study, the coordination of TC with apatite exhibited a negative change in Gibbs free adsorption energy, in a range close to the limit between simple physisorption and chemisorption, ascribed to the absence of very high affinity charged end group on the TC molecules, thus excluding multilayer adsorption. Another recent computation study also described the bonding between TC and HA as weak coordination interactions including Van der Waals and hydrogen bonds[24].

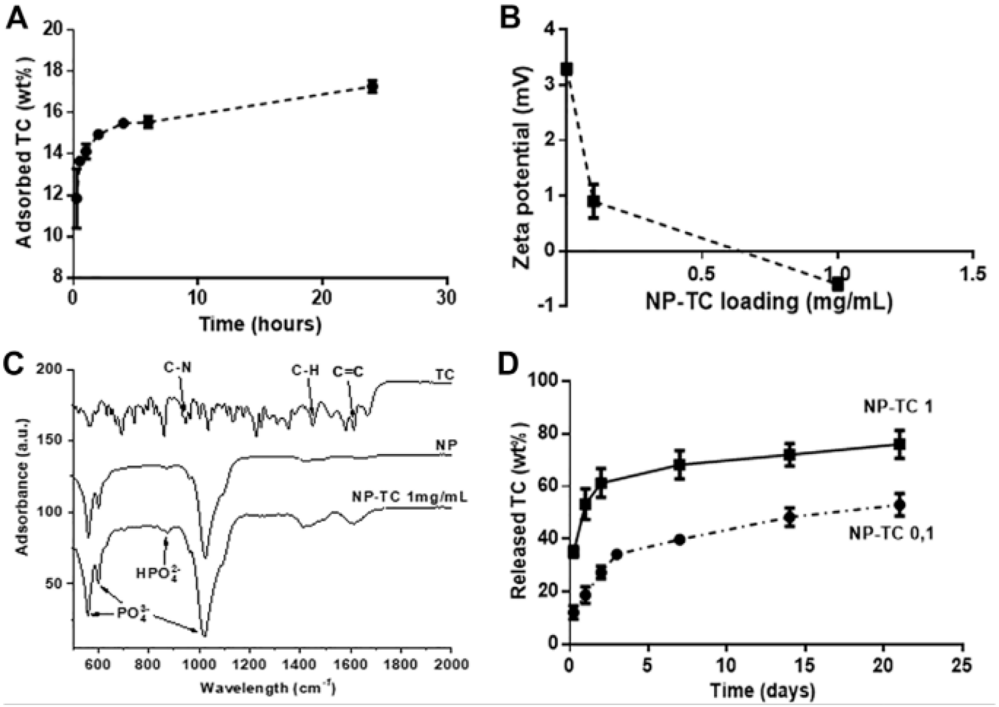

Figure 57. (A) TC adsorption kinetic on HA-NPs (TC concentration = 1 mg/mL); (B) Zeta Potential analysis of NP-TC; (C) FTIR-ATR spectra for TC, NP, and NP-TC 1 mg/mL; (D) Release profile of TC from NPs, functionalized with both 0.1 and 1 mg/mL TC concentration

The setting reaction of NP-TC1 loaded SrCPC (SrCPC_NP-TC1) was characterized by XRD (Figure 58a). At 2 h after mixing only the αTCP phase was detected, while at 72 h only the crystalline HA phase was observed, without any secondary phases. By comparing the XRD patterns of SrCPC_NP-TC1 and SrCPC-NP, we can conclude that the presence of linked TC did not affect the setting process and extent of phase transformation of the precursors into HA. The effect of NP-TC on the TC release from cements was investigated over 35 days by testing both SrCPC_TC and SrCPC_NP-TC1 cements (Figure 58b).

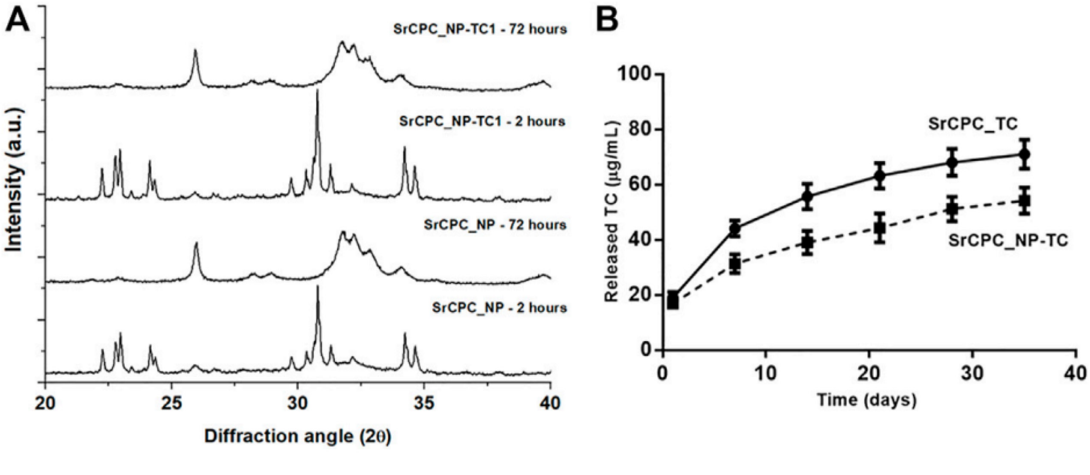

Figure 58 ***a)*** *XRD of cement with TC (SrCPC_NP-TC1) and without TC (SrCPC_NP) at 2 and 72 h upon mixing and maturation at 37°C;* ***b)*** *Release profile of TC from cement with NPs (SrCPC_NP-TC) and without NPs (SrCPC_TC)*

SrCPC_TC cement was obtained by mixing the precursor powder with free TC (i.e., not bound to any HA-NPs) in the same amount detected on NP-TC1 (≈19.2 mg). Interestingly, despite the same TC amount in both formulations, a significant decrease in TC release was exhibited by the SrCPC_NP-TC1 formulation, for each time point. This finding shows that, when linked to HA-NPs, the release profile of TC results further slackened. The mathematical interpretation of our results was also proposed, according to semiempirical models able to describe drug release from polymeric or monolithic systems, such as Korsmeyer-Peppas or power law model (paragraph 1.6.4., Eq. 10), according to table IX. The fitting of the empirical is reported in Table XV and Figure 59.

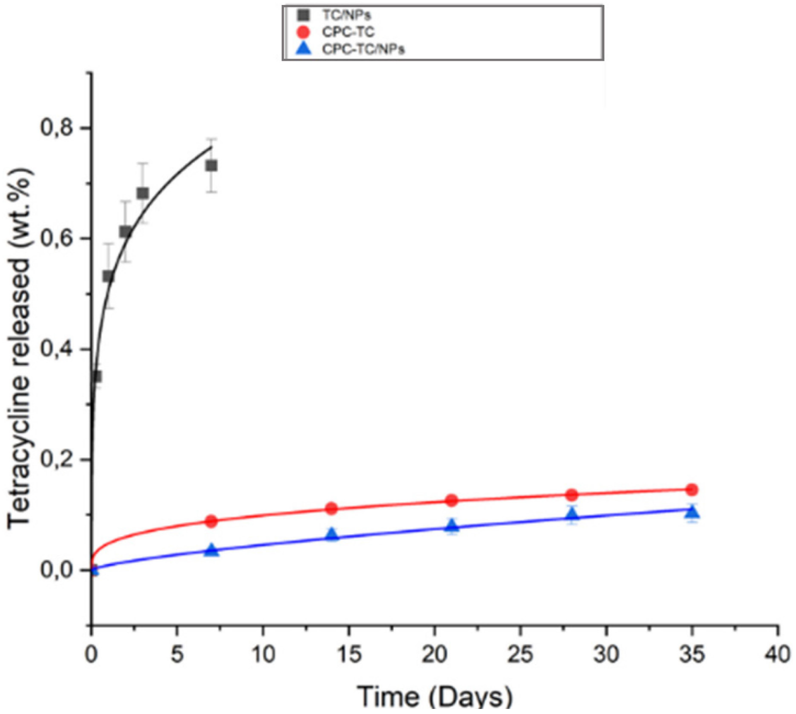

Figure 59. Kinetic release profiles of tetracycline from NP-TC (black line), SrCPC-TC (red line), and SrCPC-NP_TC (blue line) with respective fitting curves

Table XVI. n exponent value of the Korsmeyer-Peppas model and relative release regime obtained by fitting the tetracycline release profiles.

Samples	K-P model applied	*n* value	Release regime
TC/NPs	$f_i = \frac{M_i}{M_\infty} = Kt^n + b$	n = 0.229 ± 0.019	Diffusive regime with hampered release
SrCPC-TC	$f_i = \frac{M_i}{M_\infty} = Kt^n$	n = 0.312 ± 0.001	Diffusive regime with hampered release
SrCPC-TC/NPs	$f_i = \frac{M_i}{M_\infty} = Kt^n$	n = 0.704 ± 0.048	Anomalous transport

The lowest n coefficient was calculated for the NP-TC sample, exhibiting an initial burst release, thus involving the addition of a constant b value into the model, associated with Diffusive regime with hampered release. The same Fickian release regime was also associated with SrCPC-TC, based on the *n* coefficient. Interestingly, a significantly higher n coefficient was calculated for SrCPC-NP_TC, confirming that the addition of NP-TC led to a different, non-Fickian, release regime, named Anomalous transport. It was hypothesized that the mechanisms underlying this condition include a combination of TC diffusion and dissolution of NP-TC or cement matrix. The rate of degradation of SrCPCs can be considered much lower than the rate of drug release, so that, when the drug was simply mixed with the cement without the use of NPs, the drug release is mainly controlled by the process of diffusion through the cement matrix. It was reported that the presence of the drug in a SrCPC matrix can be generally ascribable to *i)* segregation of the drug in the liquid phase within the micropores of the material, *ii)* adsorption or chemical bound on the surface of the newly formed crystals, or *iii)* drug crystals or aggregates, in case of drug concentration higher than the drug solubility in the liquid phase. On this basis, we also hypothesized that the TC is mainly adsorbed on the crystal surface or entrapped, as individual, or aggregated molecules, within the nanopores or micro-voids existing between the entangled HA crystals. Then, this scenario is complicated by the addition of NP-TC, leading to a significant slackening in TC release, possibly due to a combination of SrCPC matrix dissolution and TC desorption from the NP surface.

Degradation tests of the bone cement were also performed for up to 35 days, in terms of calcium and strontium ions release, exhibiting higher calcium release for the TC-containing formulations (Figure 60A). The microstructure of cements was also investigated by SEM, exhibiting flaky to needle-like HA crystals, particularly after the addition of NPs (Figures 60 and 62). The compressive strength of cement formulations was also evaluated at 7 days after soaking in HEPES at 37°C, exhibiting a significant decrease only for the TC-containing formulations (Table XVI). It is possible to observe that the addition of NPs, free TC, and TC-functionalized NPs induces a reduction of compressive strength. On one side, the presence of NPs may also represent an obstacle hindering the grain interlocking phenomenon, typical of hardened CPC cements. On the other hand, the effect of the drugs on the mechanical performance of CPC was reported as difficult to predict, due to the possible chemical interaction of foreign molecules with the setting reaction[3]. Notwithstanding, the cement exhibits mechanical strength suitable for application addressing bone regeneration in non-load-bearing bone parts[25,26].

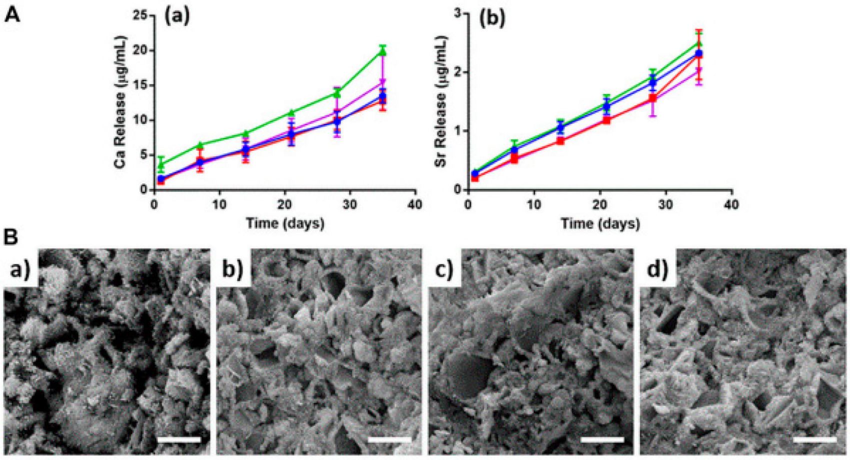

Figure 60. A) *Ion releases up to 35 days:* ***(a)*** *Calcium,* ***(b)*** *Strontium. SrCPC (blue), SrCPC_NP (red), SrCPC_TC (green), SrCPC_NP-TC (violet);* ***(B)*** *SEM micrographs of cements: CPC* ***(a)****, CPC_TC* ***(b)****, CPC_NP* ***(c)****, CPC_NP-TC* ***(d)****. Scale bar = 5 µm.*

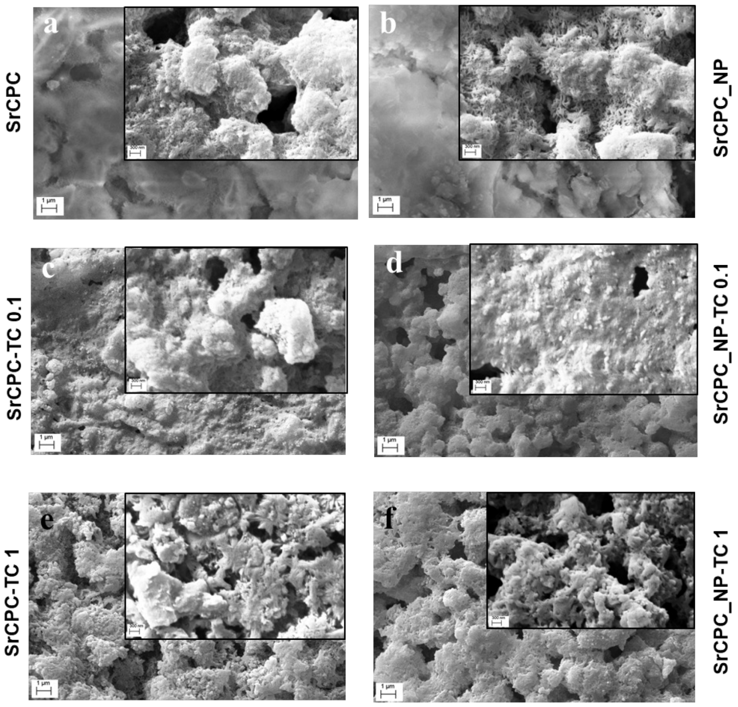

Figure 61*. SEM images of the scaffolds were performed at magnification 15KX (1 µm bar) and 50KX (insets, 300 nm bar), respectively. (a) SrCPC;* ***(b)*** *SrCPC_NP;* ***(c)*** *SrCPC_TC 0.1;* ***(d)*** *SrCPC_NP-TC 0.1;* ***(e)*** *SrCPC_TC 1;* ***(f)*** *SrCPC_NP-TC 1.*

Table XVII. *Compression strength of cements with and without NPs or TC, at 7 days after soaking in HEPES at 37°C.*

	SrCPC	**SrCPC_NP**	**SrCPC_TC**	**SrCPC_NP-TC**
Compressive strength (MPa)	13.0 ± 4.4	9.4 ± 0.8	7.5 ± 1.4	6.3 ± 0.5

In vitro microbiological evaluation of bone cements

Antimicrobial tests were carried out on antibiotic-containing cements (SrCPC_TC and SrCPC_NP-TC) using TC-free SrCPC_NP and SrCPC formulations as control samples. The following experiments were performed to evaluate the antibacterial properties of bone cement scaffolds either in planktonic or in biofilm conditions.

Effect of bone cements scaffolds on bacterial planktonic cultures viability

Bacterial viability was evaluated through the MTT colorimetric assay on planktonic cultures through direct contact (Figure 62) and indirect contact experimental setup (Figure 50). The direct contact tests were performed at 6 h, 24 h, and 48 h either on the supernatant, containing the planktonic bacteria (Analysis 1, Figure 62A) or on the bacteria adherent on the scaffold surface (Analysis 2, Figure 62B).

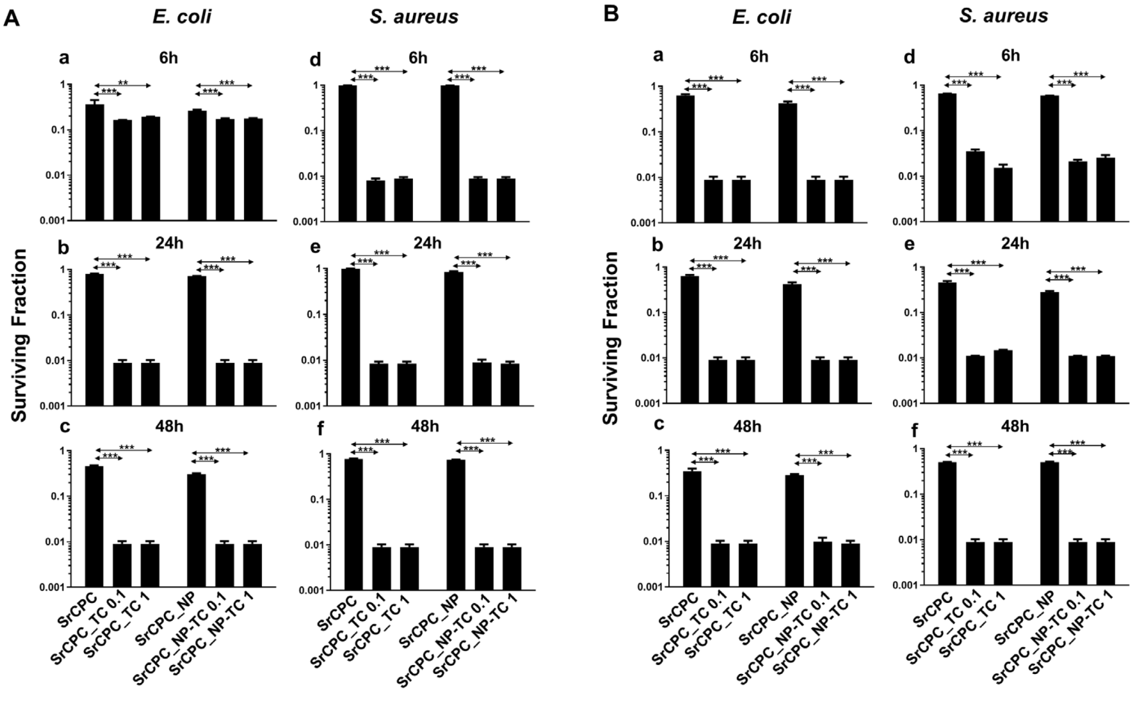

Figure 62. *Bacterial viability of* ***A)*** *planktonic culture and* ***b)*** *adherent bacteria to the scaffold.* ***a-c*** *for E.coli and d-f for S. aureus*

Both analyses of the direct test were important to be performed: analysis 1 allowed to determine whether the substances released from the scaffolds could contribute to reducing bacterial viability of both bacterial strains; analysis 2, being performed on adherent bacteria to the scaffolds, could indicate whether the surface itself holds anti-adhesive properties. Finally, by indirect tests, it was evaluated only the contribution of the released substances from the scaffolds on the bacterial viability. Regarding the direct contact test, the analyses performed on the bacterial supernatant removed from the scaffolds after time-dependent incubation (analysis 1) (Figure 62A) revealed that both types of cements, SrCPC_TC and SrCPC_NP-TC, loaded with two different concentrations of TC (0.1 mg/mL and 1 mg/mL) showed a two logs reduction of the viability of both Gram positive and Gram-negative bacteria after 6 h (Figure 62,b–f) in comparison to their controls (SrCPC and SrCPC_NP). Significantly different effects were also exerted by both SrCPC_TC and SrCPC_NP-TC on *E. coli* and *S. aureus* cells survival at 6 h (Figure 62A). TC is an antibiotic that inhibits bacterial protein synthesis by preventing the association of aminoacyl-tRNA with bacterial ribosomes. Therefore, to interact with the target, the antibiotic needs to cross one or more membranes depending on bacteria[27]. Gram-positive bacteria are characterized by the presence of a thick peptidoglycan layer associated with an inner cytoplasmic membrane; furthermore, the cell wall contains teichoic acids and lipoteichoic acids that are polysaccharides covalently attached to the peptidoglycan and inserted into the cytoplasmic membrane, respectively. Conversely, Gram-negative bacteria contain both a cytoplasmic and an outer membrane with a lipopolysaccharide (LPS), while a thin peptidoglycan layer is placed between the two membranes[28]. TC was reported to be less effective against Gram-negative than Gram-positive bacteria because of the presence of a second (outer) membrane[29,30]. In Gram-negative bacteria, TC indeed crosses the outer membrane through a cationic complex with Mg^{2+}, using specific porins (OmpF and OmpC). Later, the antibiotic is attracted towards cytoplasm across the outer membrane by Donnan membrane potential, causing the accumulation of TC-Mg^{2+} complex in the periplasmic space where the antibiotic molecules dissociate from Mg^{2+} [27,30]. Since the molecules at this stage are uncharged and lipophilic, they can diffuse through the inner membrane and accumulate in the cytoplasm. In Gram-positive instead, the uptake of tetracycline across the cytoplasmic membrane is energy-dependent and driven by the ΔpH component of the proton motive force. Within the cytoplasm, tetracycline molecules are likely to become chelated since the internal pH and divalent metal ion concentrations are higher than those outside the cell[27.] Indeed, it is probable that the active drug species which binds to the ribosome is a Mg^{2+}-tetracycline complex. The association of TC with the ribosome is reversible (at low concentration), explaining the bacteriostatic effects of these antibiotics.

However, at high concentration, this antibiotic can be a bactericidal agent[30]. The results of analysis 2 of the direct contact test related to the *E. coli* and *S. aureus* adhesion onto the scaffold surfaces are reported in Figure 49B. Both the antibiotic-containing scaffolds (SrCPC_TC and SrCPC_NP-TC) retained antibacterial properties at 6 h of incubation, showing two logs of viability reduction. The anti-adhesive ability of bone cement can be ascribed to the sustained release of TC, associated with the release of Ca^{2+}, PO_4^{3-} and Sr^{2+} ions showing relevant antibacterial effects, as previously observed[31-33]. Moreover, on SrCPC and SrCPC_NP the adhesion was reduced for *E. coli* after 48 h (Figure 49B,c) and for *S. aureus* after 24 h (Figure 49B,e–f). The reduced adhesion was probably due to the characteristics of the surface because it is known in the literature that properties such as surface charge density and roughness affect bacterial adhesion[30]. Surface charge involves van der Waals force and electrostatic interactions that are the major forces in bacterial adhesion onto material surfaces. Considering that bacteria are usually negatively charged, due to carboxyl groups, and amino and phosphate groups on their cell wall, more adhesion is often observed on positively charged surfaces. Another property that can influence adhesion is surface roughness. The higher is the degree of roughness, the more reduced will result in bacterial adhesion, because of the decreased contact area between bacteria and surface[34] as well as hydroxyapatite[35]. In Figure 62, the statistical analysis of TC loaded cements in comparison to their respective control. The statistics between SrCPC control compared to SrCPC_NP-TC cement and SrCPC-NP compared to SrCPC-TC were reported table XIV for both planktonic (A-B) and adherent bacteria (C-D). The analysis showed a significant difference in TC-loaded cements ($p < 0.05$). Moreover, there was a significant difference between SrCPC and SrCPC_NP controls after 24 h and 48 h of incubation with both planktonic bacteria (table XVII A–B) and after 6 h and 24 h of both bacterial adhesions (table XVII C–D).

Table XVIII. *Statistics of planktonic culture viability* ***(A-B)*** *and bacterial adhesion* ***(C-D).*** *ANOVA followed by Bonferroni's test was performed to compare SrCPC with SrCPC_NP scaffolds incubated through direct contact for 6h, 24h, and 48h with E. coli (A, C) and S. aureus (B, D). *p < 0.05, **p < 0.01 and ***p < 0.001. ns = not significant value*

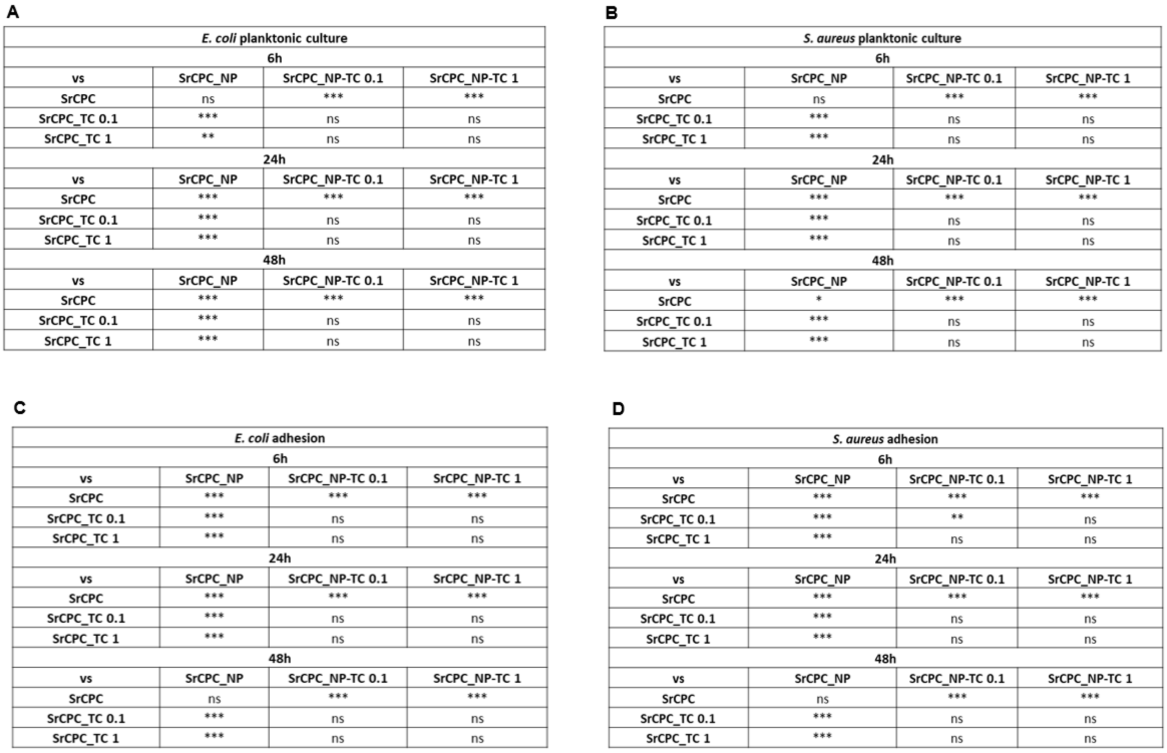

A

E. coli **planktonic culture**			
6h			
vs	**SrCPC_NP**	**SrCPC_NP-TC 0.1**	**SrCPC_NP-TC 1**
SrCPC	ns	***	***
SrCPC_TC 0.1	***	ns	ns
SrCPC_TC 1	**	ns	ns
24h			
vs	**SrCPC_NP**	**SrCPC_NP-TC 0.1**	**SrCPC_NP-TC 1**
SrCPC	***	***	***
SrCPC_TC 0.1	***	ns	ns
SrCPC_TC 1	***	ns	ns
48h			
vs	**SrCPC_NP**	**SrCPC_NP-TC 0.1**	**SrCPC_NP-TC 1**
SrCPC	***	***	***
SrCPC_TC 0.1	***	ns	ns
SrCPC_TC 1	***	ns	ns

B

S. aureus **planktonic culture**			
6h			
vs	**SrCPC_NP**	**SrCPC_NP-TC 0.1**	**SrCPC_NP-TC 1**
SrCPC	ns	***	***
SrCPC_TC 0.1	***	ns	ns
SrCPC_TC 1	***	ns	ns
24h			
vs	**SrCPC_NP**	**SrCPC_NP-TC 0.1**	**SrCPC_NP-TC 1**
SrCPC	***	***	***
SrCPC_TC 0.1	***	ns	ns
SrCPC_TC 1	***	ns	ns
48h			
vs	**SrCPC_NP**	**SrCPC_NP-TC 0.1**	**SrCPC_NP-TC 1**
SrCPC	*	***	***
SrCPC_TC 0.1	***	ns	ns
SrCPC_TC 1	***	ns	ns

C

E. coli **adhesion**			
6h			
vs	**SrCPC_NP**	**SrCPC_NP-TC 0.1**	**SrCPC_NP-TC 1**
SrCPC	***	***	***
SrCPC_TC 0.1	***	ns	ns
SrCPC_TC 1	***	ns	ns
24h			
vs	**SrCPC_NP**	**SrCPC_NP-TC 0.1**	**SrCPC_NP-TC 1**
SrCPC	***	***	***
SrCPC_TC 0.1	***	ns	ns
SrCPC_TC 1	***	ns	ns
48h			
vs	**SrCPC_NP**	**SrCPC_NP-TC 0.1**	**SrCPC_NP-TC 1**
SrCPC	ns	***	***
SrCPC_TC 0.1	***	ns	ns
SrCPC_TC 1	***	ns	ns

D

S. aureus **adhesion**			
6h			
vs	**SrCPC_NP**	**SrCPC_NP-TC 0.1**	**SrCPC_NP-TC 1**
SrCPC	***	***	***
SrCPC_TC 0.1	***	**	ns
SrCPC_TC 1	***	ns	ns
24h			
vs	**SrCPC_NP**	**SrCPC_NP-TC 0.1**	**SrCPC_NP-TC 1**
SrCPC	***	***	***
SrCPC_TC 0.1	***	ns	ns
SrCPC_TC 1	***	ns	ns
48h			
vs	**SrCPC_NP**	**SrCPC_NP-TC 0.1**	**SrCPC_NP-TC 1**
SrCPC	ns	***	***
SrCPC_TC 0.1	***	ns	ns
SrCPC_TC 1	***	ns	ns

The antibiotic solutions released from SrCPC_TC 1 and SrCPC_NP-TC 1 samples were tested to evaluate, as indirect contact, the viability of both bacterial strains in comparison to free TC concentrations. As expected, the solution released from both types of apatitic bone cement scaffolds showed an antibacterial effect on both Gram-negative and positive bacteria (Figure 63). In particular, the solution released from SrCPC_TC 1 showed a viability reduction of two logs against *E. coli* and this was more efficient in comparison to the free-added tetracycline (TC 1) at the same concentration (Figure 63a). Conversely, the SrCPC_NPTC 1 solutions were not as effective (ca. One log of reduction) as the free TC 1 (Figure 63b). No significant differences were detected against *S. aureus* by using SrCPC_TC and SrCPC_NP-TC (Figures 63c,d). In general, a reduction in viability of ca. One log for both samples was observed if compared to free TC (2 logs of reduction).

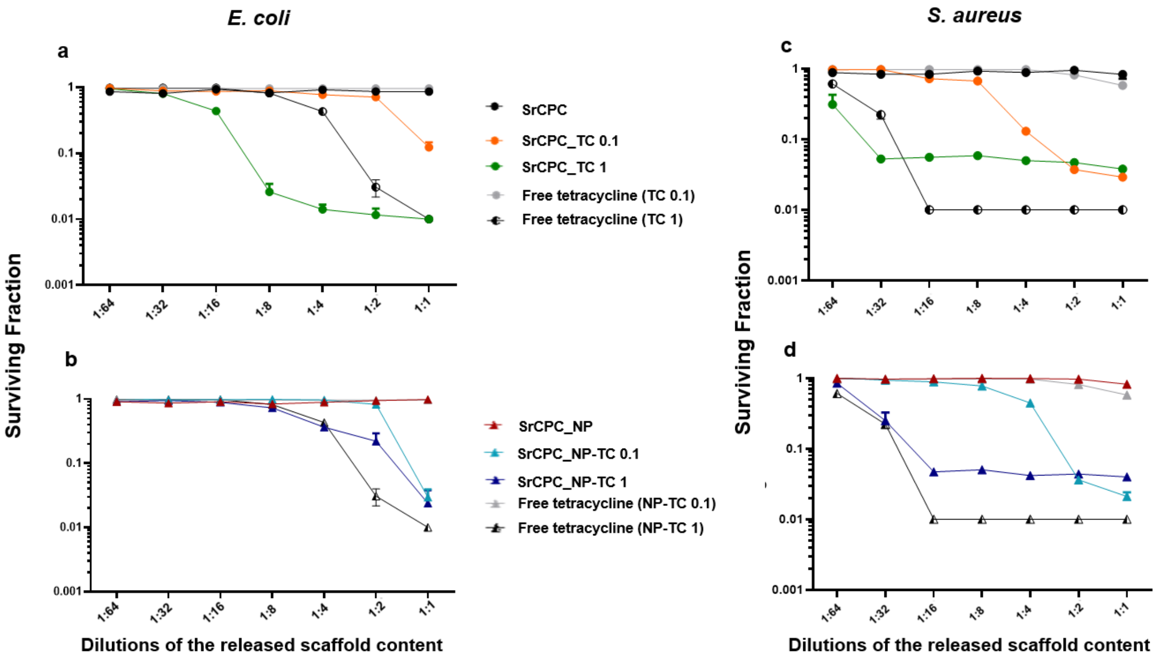

Figure 63. *Bacterial viability of planktonic cultures through indirect contact.* ***a-b)*** *E. coli and* ***c-d)*** *S. aureus*

Effect of bone cements scaffolds on biofilm formations

Given the promising results from planktonic and adherent bacteria, the ability of SrCPC scaffolds to prevent the formation of bacterial biofilms (pre-biofilm conditions) (Figure 64) or reduce the preformed biofilms (post-biofilm conditions) (Figure 65) was also investigated, as also previously reported[36-38].

In pre-biofilm conditions, the formation of both biofilms is prevented by SrCPC_TC and SrCPC_NP-TC at both concentrations when bacterial cells are directly seeded on the bone cement scaffolds and allowed to grow for 24 h at 37° C. SrCPC_TC and SrCPC_NP-TC scaffolds showed, in *E. coli*, one log of reduction in respect to their sample controls (Figure 64Aa). *S. aureus* biofilm formation was, instead, reduced by about half log from SrCPC_TC and SrCPC_NP-TC (Figures 64A,b).

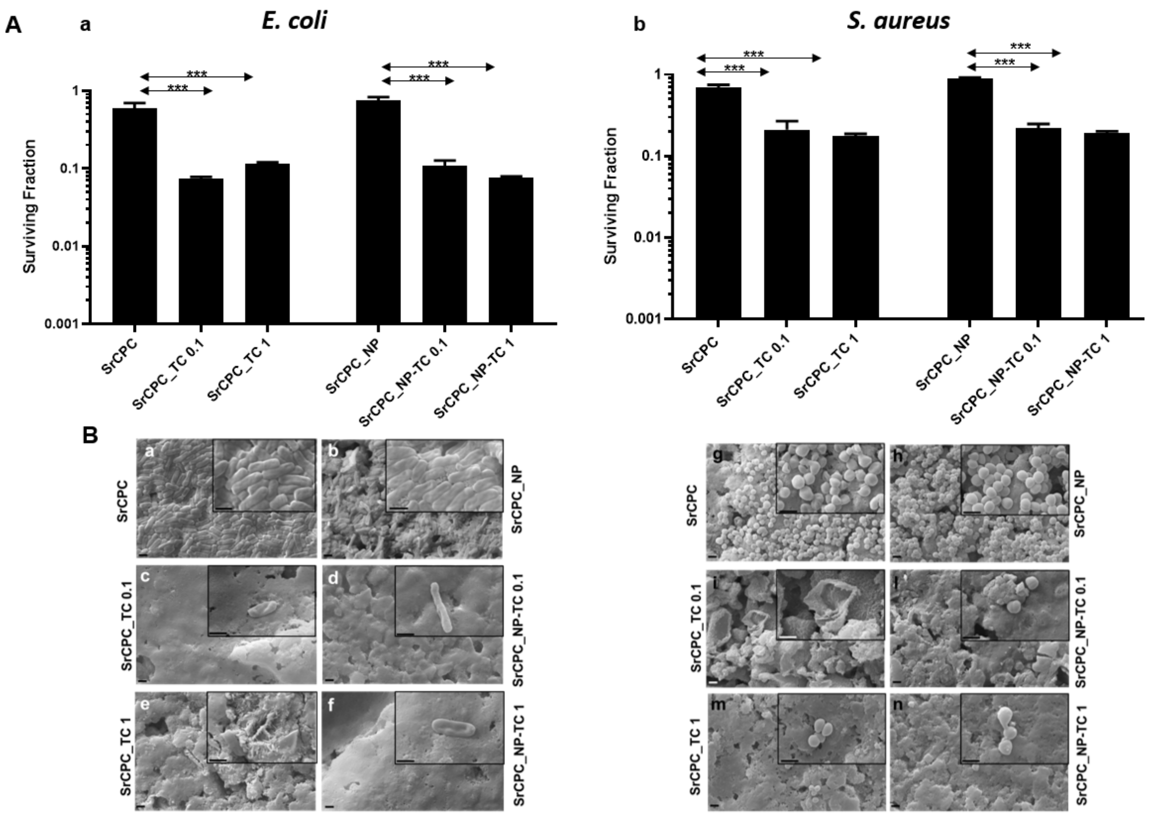

Figure 64. *Effect of the tested scaffolds on the formation of bacterial biofilms (Pre-biofilm condition).* ***A*** *– Viability of bacterial biofilms:* ***A, a)*** *E.Coli and* ***A,b*** *S.Aureus.* ***B)*** *SEM images of biofilm:* ***B, a-f)*** *E. coli (B,a-f) and* ***B, g-n*** *S. aureus.*

The statistical analysis of cement between bacterial biofilms is represented in Table XV. The analysis showed a significant difference between *S. aureus* TC-loaded cements compared to *E. coli* cement control ($p < 0.05$).

Table XIX. Comparison between bacterial biofilms. *ANOVA followed by Bonferroni's test was performed to compare the viability of E. coli and S. aureus biofilms formed on scaffolds (pre-biofilm conditions). *p < 0.05, **p < 0.01 and ***p < 0.001. ns = not significant value.*

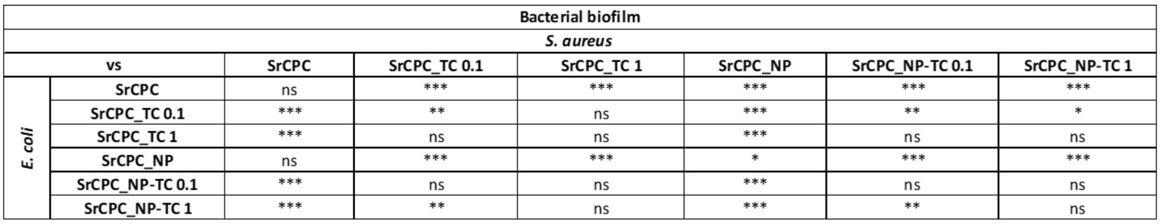

Bacterial biofilm							
		S. aureus					
vs		SrCPC	SrCPC_TC 0.1	SrCPC_TC 1	SrCPC_NP	SrCPC_NP-TC 0.1	SrCPC_NP-TC 1
E. coli	SrCPC	ns	***	***	***	***	***
	SrCPC_TC 0.1	***	**	ns	***	**	*
	SrCPC_TC 1	***	ns	ns	***	ns	ns
	SrCPC_NP	ns	***	***	*	***	***
	SrCPC_NP-TC 0.1	***	ns	ns	***	ns	ns
	SrCPC_NP-TC 1	***	**	ns	***	**	ns

In addition, SrCPC_NP and SrCPC_TC 0.1 cements were statistically significant in both bacterial biofilms ($p < 0.05$). This minor susceptibility of *S. aureus* biofilm to tetracycline-containing bone cements, concerning *E. coli* biofilm, could be explained by the resistance mechanisms that bacteria show against TC, as previously described. Moreover, the results on sample controls (SrCPC and SrCPC_NP) obtained from assessing the viability of biofilm in pre-biofilm conditions showed a small reduction of viability for both bacteria. These data demonstrated that the adhesion on bone cements was slightly hindered from scaffold surfaces, we attributed such an effect to surface nano-roughness. Although this property may contribute to decreased bacterial adhesion[34], the most anti-adhesive effect of SrCPC bone cements was due to the presence of tetracycline that reduced both biofilm formation of ca. One log. Data were supported by SEM observations showing *E. coli* and *S. aureus* biofilms formations on SrCPC and SrCPC_NP (Figure 65B); further study should be performed to measure their thickness. On the contrary, SrCPC_TC (Figures 65B,c,e, i,m) and SrCPC_NP-TC (Figures 65Bd,f,l,n) scaffolds, did not allow the formation of biofilms.

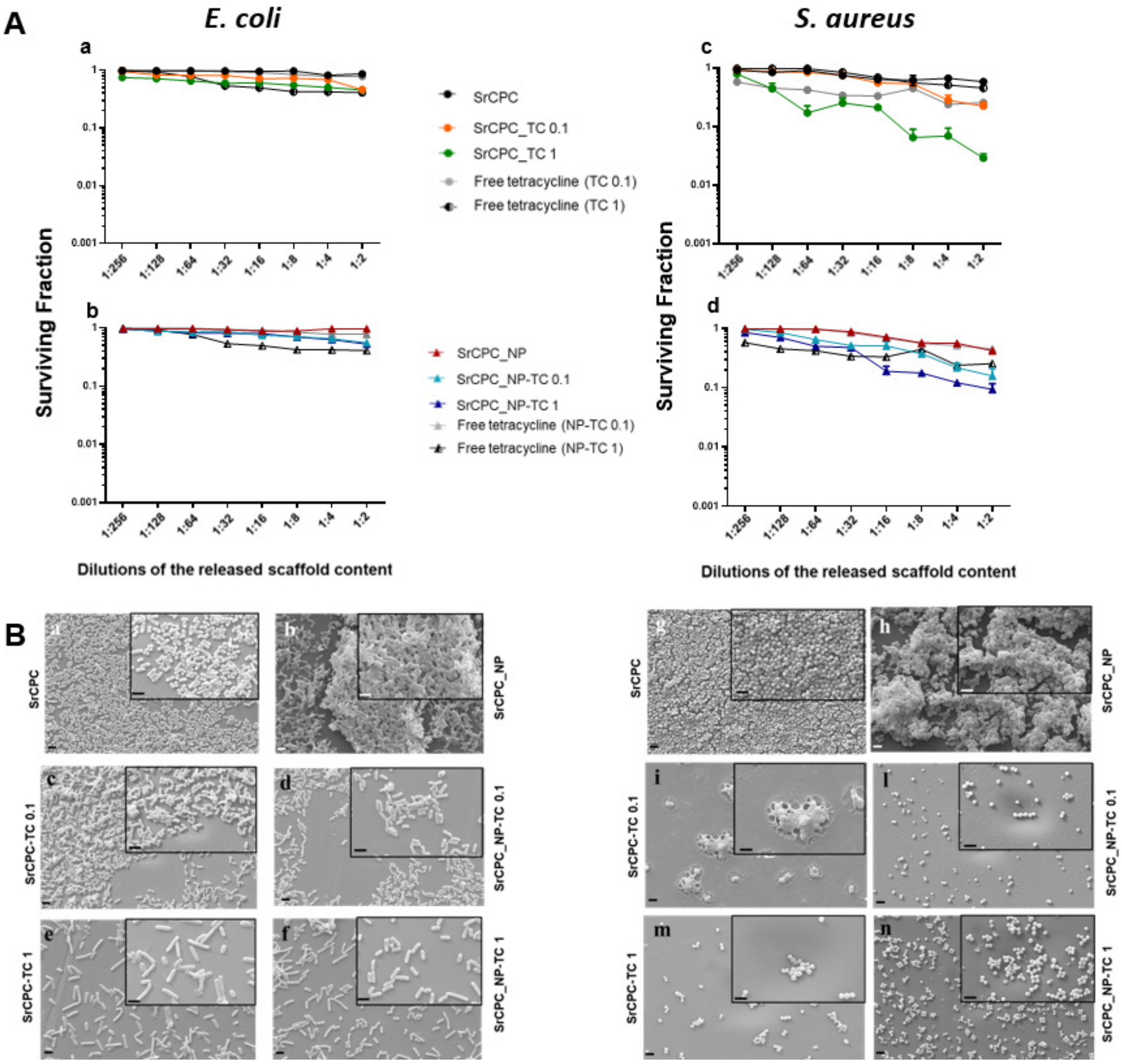

***Figure 65**. Effect of scaffold-released contents on bacterial-formed biofilms (post-biofilm condition). A - Viability of bacterial biofilms: a-b) E. coli and c-d) S. aureus (c-d). B - SEM images of bacteria in scaffold surface: a,g) SrCPC, b,h) SrCPC_NP, c, i) SrCPC-TC 0.1 mg/mL and e, m) 1 mg/mL, d, l) SrCPC_NP-TC 0.1 mg/mL and f, n) 1 mg/mL.*

In post-biofilm conditions, TC and ions released from the scaffolds after 24 h incubation at 37° C were tested in a dose-dependent manner against both bacterial-preformed biofilms

(Figure 65A). Free tetracycline was used as a positive control at the same concentrations released from the scaffolds. As illustrated in Figure 52A the solutions, particularly those incubated either with SrCPC_TC 1 or SrCPC_NP-TC 1, were more effective against *S. aureus* biofilms (Figures 65Ac,d) in comparison to *E. coli* (Figures 65Aa,b). The efficacy of tetracycline on Gram-positive bacteria[26] is due to the different mechanisms of diffusion, related to the different structures of cell walls between Gram-positive and negative bacteria[24]. These viability data are also supported by SEM images (Figure 65B).

Overall, our results showed that Sr-doped apatitic bone cements are capable of effective reduction of *E. coli* and *S. aureus* as evaluated in planktonic and biofilm conditions. Particularly, we showed that the release of TC, associated with the intrinsic physicochemical features of bone cement, such as the ability of multiple Ca^{2+}, PO_4^{3-} and Sr^{2+} ion release as well as the surface nanotexture can play a relevant role in limiting bacterial adhesion, viability and formation of bacterial biofilms. We established the conditions to load different amounts of TC on HA-NPs, which were incorporated and distributed throughout the whole volume of the hardened SrCPC cements, thus obtaining the ability to modulate the TC release process and to achieve a release profile sustained over weeks. Devices with regenerative properties associated with sustained long-term antibacterial effects, effective also in preventing biofilm formation, may have great clinical relevance thus overcoming the well-known problems related to systemic administration such as reduced drug availability at the target site, adverse side effects, and promising also to overcome the bacterial resistance to antibiotics. In respect to the ability of sustained drug delivery, the cement TC release process was modulated by a combination of factors: 1) desorption from NP surface modulated by dissolution processes involving the cement and the NPs themselves; 2) diffusion of TC through the nano/micro-pores network of the SrCPCs. Such a canaliculi network, spontaneously formed during the reprecipitation process yielding the cement hardening, was already shown to play a key role in new bone penetration and osteointegration during a previous in vivo test in rabbit femur defects[4]. The microbiological results obtained in the present work show that such features, together with a composition capable of releasing bioactive Ca^{2+}, PO_4^{3-} and Sr^{2+} ions and with a diffuse nanotexture providing high specific surface area, are all key aspects making apatitic bone cements promising as multifunctional devices. Indeed, nano-crystallinity associated with ion-release ability was previously shown as a relevant factor to exhibit osteogenic and antibacterial properties in apatitic nanoparticles[8,39]. In this paper, we show that such features are effective also when dealing with bone cements developed as 3D bodies, characterized by mechanical properties suitable to regenerate non-load-bearing bony defects, typical for instance in the case of tumoral bone resections. Indeed, the chemical similarity of TC with anthracycline (i.e., doxorubicin) indicates that our approach could be carried out also with anticancer drugs and potentially with many bioactive molecules, thus representing a promising solution to sustain bone regeneration also in case of bone cancer or other co-morbidities.

Conclusions

In the present work, injectable self-hardening CPCs partially substituted with Sr^{2+} ions and capable of sustained release of TC were developed. The modulation of the drug release profile was achieved by linking TC with appositely synthesized HA-NPs and mixing with the cement precursor powder before mixing with the liquid components.

This work illustrates the capability of hydroxyapatite nanoparticles in effectively modulating drug release. The presence of nanoparticles induced a significant change in the drug release kinetic, from a diffusive process to anomalous transport, thus moving to non-linear relationships between the expected displacement of molecules and time, possibly due to alterations in the microstructure of the cement matrix.

This study was carried out to evaluate the potential capacity of bone cement to contrast post-operative infectious complications. Extensive *in vitro* microbiological characterization demonstrated the intrinsic ability of our Sr-doped CPCs to contrast infections caused by *E. coli* and *S. aureus* bacteria. In addition, the TC-containing cements showed the ability to oppose the formation of biofilms.

Effective antibacterial character in the absence of antibiotic drugs was also shown, thus suggesting intrinsic compositional and textural features of the bone cement such as surface nano-roughness, possibly acting as intrinsic factors capable of hindering biofilm adhesion and organization. These results give a promising perspective regarding the fight against bacterial infections and the careful use of antibiotics, thus aiding in circumventing bacterial resistance phenomena, which are among the major threats after orthopedic surgeries.

REFERENCES

1. Parent, M., Baradari, H., Champion, E., Damia, C. & Viana-Trecant, M. Design of calcium phosphate ceramics for drug delivery applications in bone diseases: A review of the parameters affecting the loading and release of the therapeutic substance. *J. Control. Release* **252**, 1–17 (2017).
2. Fosca, M., Rau, J. V. & Uskoković, V. Factors influencing the drug release from calcium phosphate cements. *Bioact. Mater.* **7**, 341–363 (2022).
3. Ginebra, M. P., Canal, C., Espanol, M., Pastorino, D. & Montufar, E. B. Calcium phosphate cements as drug delivery materials. *Adv. Drug Deliv. Rev.* **64**, 1090–1110 (2012).
4. Sprio, S. *et al.* materials Novel Osteointegrative Sr-Substituted Apatitic Cements Enriched with Alginate. (2016) doi:10.3390/ma9090763.
5. Dapporto, M., Gardini, D., Tampieri, A. & Sprio, S. Nanostructured Strontium-Doped Calcium Phosphate Cements: A Multifactorial Design. (2021) doi:10.3390/app11052075.
6. Montesi, M., Panseri, S., Dapporto, M., Tampieri, A. & Sprio, S. Sr-substituted bone cements direct mesenchymal stem cells, osteoblasts and osteoclasts fate. (2017) doi: 10.1371/journal.pone.0172100.
7. Montufar, E. B., Maazouz, Y. & Ginebra, M. P. Relevance of the setting reaction to the injectability of tricalcium phosphate pastes. *Acta Biomater.* **9**, 6188–6198 (2013).
8. Sprio, S. *et al.* Enhancement of the Biological and Mechanical Performances of Sintered Hydroxyapatite by Multiple Ions Doping. *Front. Mater.* **7**, 1–18 (2020).
9. Bari, A. *et al.* Copper-containing mesoporous bioactive glass nanoparticles as multifunctional agent for bone regeneration. *Acta Biomater.* **55**, 493–504 (2017).
10. Villani, M. *et al.* Polyurethane-based coatings with promising antibacterial properties. *Materials (Basel).* **13**, 1–21 (2020).
11. Pallavicini, P. *et al.* Silver nanoparticles synthesized and coated with pectin: An ideal compromise for anti-bacterial and anti-biofilm action combined with wound-healing properties. *J. Colloid Interface Sci.* **498**, 271–281 (2017).
12. Sprio, S. *et al.* Surface Phenomena Enhancing the Antibacterial and Osteogenic Ability of Nanocrystalline Hydroxyapatite, Activated by Multiple-Ion Doping. *ACS Biomater. Sci. Eng.* **5**, 5947–5959 (2019).
13. Ahmed, Y. M. Z., El-Sheikh, S. M. & Zaki, Z. I. Changes in hydroxyapatite powder properties via heat treatment. *Bull. Mater. Sci.* **38**, 1807–1819 (2015).

14. Dricssens, F. C. M., Flanell, J. A., Boltong, M. G., Khairoun, I. & Ginebra, M. P. Osteotransductive bone cements. *Proc. Inst. Mech. Eng. Part H J. Eng. Med.* **212**, 427–435 (1998).

15. Bohner, M. Reactivity of calcium phosphate cements. *J. Mater. Chem.* **17**, 3980–3986 (2007).

16. Pleshko, N., Boskey, A. & Mendelsohn, R. Novel infrared spectroscopic method for the determination of crystallinity of hydroxyapatite minerals. *Biophys. J.* **60**, 786–793 (1991).

17. Poralan, G. M., Gambe, J. E., Alcantara, E. M. & Vequizo, R. M. X-ray diffraction and infrared spectroscopy analyses on the crystallinity of engineered biological hydroxyapatite for medical application. *IOP Conf. Ser. Mater. Sci. Eng.* **79**, (2015).

18. Chang, P. H., Li, Z., Jiang, W. T., Kuo, C. Y. & Jean, J. S. Adsorption of tetracycline on montmorillonite: influence of solution pH, temperature and ionic strength. *Desalin. Water Treat.* **55**, 1380–1392 (2015).

19. Gopal, G., Alex, S. A., Chandrasekaran, N. & Mukherjee, A. A review on tetracycline removal from aqueous systems by advanced treatment techniques. *RSC Adv.* **10**, 27081–27095 (2020).

20. Trivedi, M. K. *et al.* Spectroscopic Characterization of Chloramphenicol and Tetracycline: An Impact of Biofield Treatment To cite this version : HAL Id : hal-01376485 Pharmaceutica Spectroscopic Characterization of Chloramphenicol and Tetracycline : An Impact of Biofield Trea. **6**, 0–5 (2016).

21. Qayoom, I. *et al.* A biphasic nanohydroxyapatite/calcium sulphate carrier containing Rifampicin and Isoniazid for local delivery gives sustained and effective antibiotic release and prevents biofilm formation. *Sci. Rep.* **10**, 1–14 (2020).

22. Drouet, C., Gomez-Morales, J., Iafisco, M. & Sarda, S. *Calcium phosphate surface tailoring technologies for drug delivering and tissue engineering*. *Surface Tailoring of Inorganic Materials for Biomedical Applications* (2012). doi:10.2174/978160805462611201010043.

23. Cazalbou, S., Bertrand, G. & Drouet, C. Tetracycline-loaded biomimetic apatite: An adsorption study. *J. Phys. Chem. B* **119**, 3014–3024 (2015).

24. Song, J. *et al.* Sorption Studies of Tetracycline Antibiotics on Hydroxyapatite (001) Surface—A First-Principles Insight. *Materials (Basel).* **15**, (2022).

25. Keller, T. S., Carter, D. R., Hernandez, C. J. & Beaupre, G. S. The Influence of Bone Volume Fraction and Ash Fraction on Bone Strength and Modulus. *Bone* **29**, 74–78 (2001).

26. Keaveny, T. M., Morgan, E. F., Niebur, G. L. & Yeh, O. C. Biomechanics of trabecular bone. *Annu. Rev. Bioedical Eng.* 307–33 (2001).

27. Chopra, I. & Roberts, M. Tetracycline Antibiotics: Mode of Action, Applications, Molecular Biology and Epidemiology of Bacterial Resistance. *Microbiol. Mol. Biol. Rev.* **65**, 232–260 (2001).

28. Auer, G. K. & Weibel, D. B. Bacterial Cell Mechanics. *Biochemistry* **56**, 3710–3724 (2017).

29. Epand, R. M., Walker, C., Epand, R. F. & Magarvey, N. A. Molecular mechanisms of membrane targeting antibiotics. *Biochim. Biophys. Acta - Biomembr.* **1858**, 980–987 (2016).

30. Rusu, A. & Buta, E. L. The development of third-generation tetracycline antibiotics and new perspectives. *Pharmaceutics* **13**, (2021).

31. Sampath Kumar, T. S., Madhumathi, K., Rubaiya, Y. & Doble, M. Dual mode antibacterial activity of ion substituted calcium phosphate nanocarriers for bone infections. *Front. Bioeng. Biotechnol.* **3**, 1–10 (2015).

32. Baheiraei, N., Eyni, H., Bakhshi, B., Najafloo, R. & Rabiee, N. Effects of strontium ions with potential antibacterial activity on in vivo bone regeneration. *Sci. Rep.* **11**, 1–9 (2021).

33. Jiao, J., Zhang, S., Qu, X. & Yue, B. Recent Advances in Research on Antibacterial Metals and Alloys as Implant Materials. *Front. Cell. Infect. Microbiol.* **11**, 1–19 (2021).

34. Zheng, S. *et al.* Implication of Surface Properties, Bacterial Motility and Hydrodynamic Conditions on Bacterial Surface Sensing and Their Initial Adhesion. *Front. Bioeng. Biotechnol.* **9**, 1–22 (2021).

35. Maleki-Ghaleh, H. *et al.* Antibacterial and cellular behaviors of novel zinc-doped hydroxyapatite/graphene nanocomposite for bone tissue engineering. *Int. J. Mol. Sci.* **22**, (2021).

36. Balato, G. *et al.* Bacterial biofilm formation is variably inhibited by different formulations of antibiotic-loaded bone cement in vitro. *Knee Surgery, Sport. Traumatol. Arthrosc.* **27**, 1943–1952 (2019).

37. Cara, A., Ferry, T., Laurent, F. & Josse, J. Prophylactic Antibiofilm Activity of Antibiotic-Loaded Bone Cements against Gram-Negative Bacteria. *Antibiotics* **11**, (2022).

38. Jacquart, S. *et al.* Injectable bone cement containing carboxymethyl cellulose microparticles as a silver delivery system able to reduce implant-associated infection risk. *Acta Biomater.* **145**, 342–357 (2022).

39. Ballardini, A. *et al.* New hydroxyapatite nanophases with enhanced osteogenic and antibacterial activity. *J. Biomed. Mater. Res. Part A* **106**, 521–530 (2017).

4.2.2. Calcium phosphate cements enriched with strontium ion for the treatment of osteosarcoma.

This research activity was focused on the development of bone cements doped with doxorubicin (Dox) or methotrexate (MTX) for the treatment of bone affected by osteosarcoma. This work was supported by *Progetto Nazionale PRIN – 017 C8RYSS*, RE-GROWTH: "*Osteosarcoma and mesenchymal stem cells to assay innovative materials, bioactive injectable bone cements, with drug delivery ability, to contrast spine tumour recurrence and to enhance healthy bone regrowth*".

As previously reported, osteosarcoma (OS) is one of the most common bone cancers, affecting mainly children and adolescents[1,2]. The treatments of OS include systemic administration of high dose of drugs (MTX and Dox) and a surgical resection[3].

Apart from treating cancer cells without causing side effects to the patient, there is another important clinical need to consider in cancer therapy: regenerating new healthy bones after eradicating diseased tissue. As previously reported, apatitic bone cement is one of the best scaffolds for this clinical need.

Therefore, this research aims to combine the anticancer activity of doxorubicin and methotrexate with the well-established regenerative potential of calcium phosphate cements and may represent a valuable approach to osteosarcoma. The biological activity of these scaffolds against adipose-derived stem cells (hASCs) and a human osteosarcoma cell line (SAOS-2) was investigated by Dr. Carmen Lanzillotti, Dr. Maria Rosa Iaquinta, Dr. Raffaella De Pace and Dr. Maria Mosaico a of Laboratories of Cell Biology and Molecular Genetics, Department of Medical Sciences, University of Ferrara, Dr. Simone Patergnani and Dr. Carlotta Giorgi of Laboratories of Cell Signalling, Department of Medical Sciences, University of Ferrara, Dr. Martini Fernanda of Technological Laboratory for Advanced Therapy (LTTA), University of Ferrara, and Dr. Elisa Mazzoni of Department of Chemical, Pharmaceutical and Agricultural Sciences, University of Ferrara.

Part of the Chapter 4.3.2 has been submitted in Bioactive materials as "*Lanzillotti C., Iaquinta M.R., Mosaico M., Patergnani S., Giorgi C., Sprio S., Dapporto M., Tavoni M., Tampieri A., Montesi M., Martini F., Mazzoni E. - Calcium phosphate cements for the treatment of bone tissue affected by osteosarcoma*".

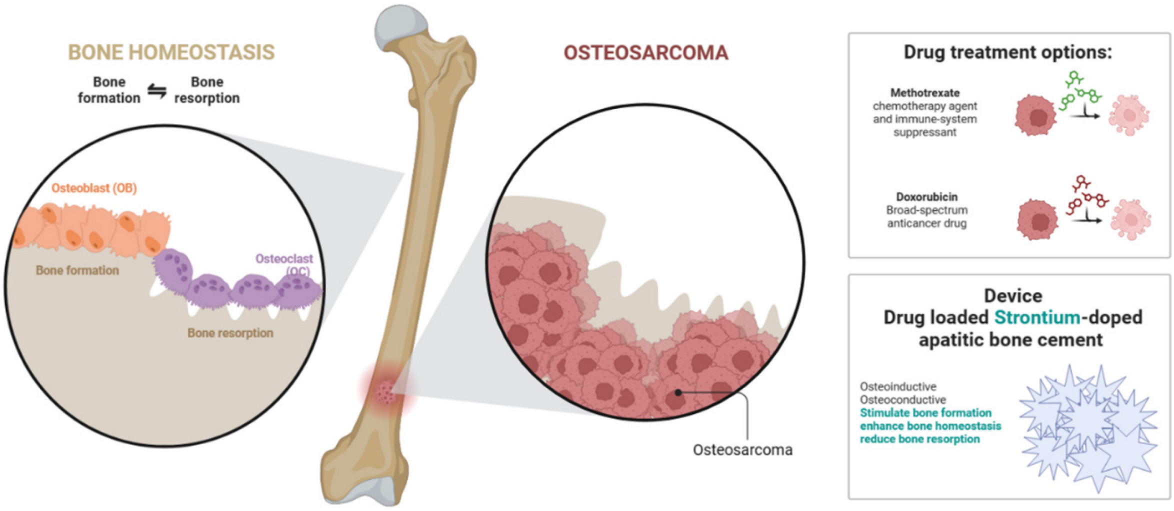

Figure 66. *Proposed treatment for osteosarcoma*

Experimental methods

Preparation of drug-loaded bone cements

The Sr-αTCP powder precursor of SrCPC was synthesized as reported in section 4.1.1.

The liquid component of the paste was prepared from aqueous solutions of disodium hydrogen phosphate dihydrate, 5 wt%, and sodium alginate, 2 wt%. The cements were prepared by mixing the powder and liquid phases by a liquid/powder (LP) ratio of 0.6. Cements were functionalized by mixing the drug with cement precursor before mixing with the cement liquid phase, as reported in table XIX (schematic representation in figure 67). Disc-shaped samples (diameter = 10 mm, height = 2 mm) were obtained for each sample.

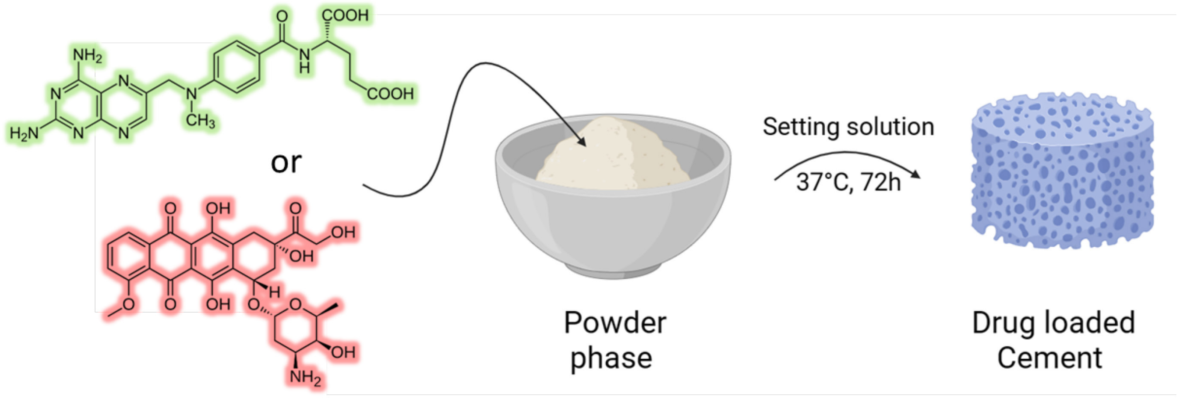

Figure 67*. Schematic representation drug (methotrexate or doxorubicin) loading bone cement process.*

Table XX. Cement formulation

	Sr-αTCP (g)	Drug (g)	Setting solution (g)
SrCPC	3	-	1.800
SrCPC-MTX	3	0.010	1.806
SrCPC-Dox	3	0.010	1.806

MTX and Dox release experiments were conducted by immersing drug-loaded SrCPC in 2 mL of HEPES buffer solutions (0.01M, with KCl 0.01M, pH 7.4) in a thermostatic stirrer in dark condition at 37°C up to 7 days. At each time point, the total solution was collected and renewed with equal volume. The collected samples were acidified with HCl 1M, to reach pH 1 and spectrophotometrically analyzed by monitoring the optical density of MTX and Dox at 306 and 480 nm, respectively (calibration curve between 0.1 and 50 µg/mL of MTX, R^2=0.999 and between 0.5 and 50 µg/mL of Dox, R^2=0.997). The physical mechanisms underlying drug release were further investigated and hypothesized based on the Korsmeyer-Peppas or power law model (paragraph 1.6.4., Eq. 10).

Before cell seeding, the scaffolds were sterilized with two washes of 70% ethanol (20 minutes each), PBS 1× (10 minutes each), and UV light (60 minutes on each side) and kept in 5 mL of medium at 37°C for 3 days under sterile conditions.

Cell cultures

The SAOS-eGFP engineered cells were derived from parental SAOS-2 cells engineered with green fluorescent protein (GFP)[4] SAOS-eGFP cell line were expanded in Dulbecco's Modified Eagle Medium F- 12 (DMEM/F12; Lonza, Milan, Italy) with 10% FBS and 1% of Geneticin (Invitrogen, Milan, Italy) and kept in a humidified atmosphere at 37°C with 5 % CO_2[5]. SAOS-eGFP cells were seeded with a concentration of 1.5 x 104 cells per well and grown on i) SrCPC-MTX, ii) SrCPC-Dox, and iii) drug-free SrCPC, as control, until the time of the analysis[5]. The compatibility and osteoinductivity of SrCPC scaffolds were evaluated using hASCs cultures at day 14. The hASCs used in this study were purchased (PT-5006, Lonza Milan, Italy) as cryopreserved frozen cells during the first passage. The company certified that hASCs are positive for surface markers CD13, CD29, CD44, CD73, CD90, CD105, and CD166, while being negative for other markers, such as CD14, CD31, and CD45.

Cells were expanded in MEM (Lonza, Milan, Italy) supplemented with 20% foetal bovine serum (FBS), antibiotics and maintained in a humidified atmosphere at 37°C with 5% CO_2[6,7]. The hASCs were seeded with a concentration of 1.5 x 104 cells per well and were grown on i) SrCPC scaffold and ii) the tissue culture polystyrene (TCPS) vessels, as control, until the analysis.

Scanning Electron Microscopy (SEM) analyses

Scanning electron microscope (SEM) analysis was carried out to investigate the structure of SrCPC, SrCPC-MTX, and SrCPC-DOX biomaterials and to analyze cell-cement interaction. To this purpose, SAOS-eGFP cells (1.5 x 10^4) were grown on SrCPC-MTX, SrCPC-DOX scaffolds, and drug-free SrCPC, as control, up to day 7, whereas hASCs (1.5 x 10^4) were grown on SrCPC scaffold up to day 14. After cell culture, scaffolds were washed with PBS 1x and fixed for 1 h by 2.5% glutaraldehyde and 4 h by 1% osmium solution in phosphate buffer. Samples were sputter-coated with gold and observed SEM (Cambridge United Kingdom, model Stereoscan S-360)[7,8]. The analysis was performed in triplicate for each experimental group.

Alamar Blue assay

The metabolic activity of SAOS-eGFP cells grown on SrCPC-MTX and SrCPC-DOX scaffolds was evaluated using the Alamar Blue assay (Invitrogen, Milan, Italy). Cells were incubated in a medium with 5% of Alamar Blue reagent for 3 hours at 37°C. A concentration of 1.6 x 105 cells and serial 1:2 dilutions were seeded to generate a calibration curve consisting of scalar concentration of SAOS-eGFP cells up to 5,000 cells. In addition, the metabolic activity rate of hASCs grown on the SrCPC scaffold and TCPS, as controls, was determined using the Alamar Blue assay at days 1, 2 and 7. Supernatant optical density was measured at a 570 nm wavelength and a 620 nm reference wavelength using a spectrophotometer (Thermo Electron Corporation, model Multiskan EX, Helsinki, Finland)[7,8]. The analysis was performed in triplicate. The analysis was performed in triplicate for each experimental group. Each experimental group was tested at different time points, i.e. on day 1, 2, and 7[9-11].

SAOS-eGFP cells fluorescence analysis

Digital images of SAOS-eGFP cells grown on drug-free SrCPC, SrCPC-MTX, and SrCPC-DOX scaffolds were obtained using a confocal microscope (LSM510; Carl Zeiss, Jena, Germany) with a 10 × 1.4 NA Plan- Apochromat oil-immersion objective and equipped with ZEN microscope imaging software (Zeiss Instruments). The SAOS-eGFP cells fluorescence intensity mean for each sample was evaluated using ImageJ software as previously reported Analysis was performed at day 7.

Caspase-3/7 activities

Caspase 3/7 activities were analyzed using the CellEvent™ Caspase-3/7 Green detection reagent (Life Technologies, cat: C10723) according to the manufacturer's instructions. Briefly, SAOS-2 cells (1×105 cells/well) were seeded in a 24-well plate on Sr-CPC, SrCPC-DOX, and SrCPC-MTX materials for 4 days. After in143cubation, cells were labeled with 5 uM CellEvent™ caspase-3/7 green detection reagent in PBS 1x and 5% FBS. Stained cells were observed under a fluorescence microscope using a 10 × 1.4 NA Plan- Apochromat oil-immersion objective and equipped with ZEN microscope imaging software (Zeiss Instruments). Digital Images were acquired in z-stacks at 8 µm. All experiments were performed independently in triplicate.

Enzyme-linked immunosorbent assay (ELISA) to semi-quantified caspase-3

Semi-quantification of cleaved caspase-3 protein was detected by using RayBio® CASP-3 (D175) ELISA Kit (RayBio® cat: PTE-CASP3-D175-T). This Sandwich ELISA is for measuring cleaved CASP-3 (Asp-175) as well as caspase-3 in human cell lysates. Briefly, SAOS-2 cells (1×105 cells/well) were seeded in a 24-well plate on SrCPC, SrCPC-DOX, and SrCPC-MTX biomaterials for 4 days. Absorbance of the developed chromophore was measured using a colorimetric ELISA reader (Thermo Electron Corporation, model Multiskan EX, Finland) at a wavelength (λ) of 450 nm. Total caspase 3 and activated/cleaved caspase-3 activity was measured as the ratio between activated and total caspase 3 calculated. The data was reports as OD median value and Standard deviation (SD). Experiments were performed in technical triplicate for each biological sample (n = 3).

Live/Dead Assay

Cytocompatibility of hASCs grown on scaffolds was assessed by live/dead dye and confocal laser scanning microscopy at day 3, 6 and 14. A live/dead Cell Double Staining Kit for mammalian cells (Calbiochem, Milan, Italy) was employed to analyze the viability of hASCs grown on biomaterials. Live/Dead assay was performed according to the manufacturer's instructions. Cell-permeable green fluorescent Cyto-dye (Ex. max.: 488 nm; Em. max.: 518 nm) was used to stain live cells, whereas propidium iodide (Ex. max.: 488 nm; Em. max.: 615 nm) was used to stain dead cells. Scaffolds were kept in saline solution during analysis with confocal microscope (LSM510; Carl Zeiss, Jena, Germany) using a 10 × 1.4 NA Plan-Apochromat oil-immersion objective and equipped with ZEN microscope imaging software (Zeiss Instruments). Digital Images were acquired in z-stacks at 0.5 µm. Moreover, Live/Dead assay was performed in cells grown on a glass slide in contact with the SrCPC scaffold and on TCPS, as control. Digital images were acquired at TE 200-E fluorescent microscope through ACT-1 software for DXM120F digital cameras (Nikon Instruments, Sesto Fiorentino, Italy) at 20X magnification and analysed using Image J software[12]. The analysis was performed in triplicate for each experimental group. Experiments were performed in technical triplicate for each biological sample (n = 3).

Cytoskeleton architecture

hASCs grown on SrCPC scaffolds were assessed by tetramethyl-rhodamine-iso-thio-cyanate (TRITC) conjugated-phalloidin (Sigma, Milan, Italy) to stain cytoskeleton filaments at day 14. The cells were washed with PBS 1X and fixed with formalin 10% for 10 minutes at room temperature. Afterwards, cell nuclei were marked with 0.5 mg/ml DAPI (Invitrogen, Milan, Italy) and images were acquired using a TE 200-E fluorescent microscope (10X and 20X magnification). Images were obtained through ACT-1 software for DXM120F digital cameras (Nikon Instruments, Sesto Fiorentino, Italy). Cell cytoskeleton analysis at 40X magnification was carried out with Olympus Xcellence multiple wavelength high-resolution fluorescence microscopy system (Olympus) and analyzed using Image J software[8,13]. The analysis was performed in triplicate for each experimental group.

Human Extracellular Matrix, Adhesion Molecules, and Osteogenesis RT^2 Profiler PCR Array

hASCs were grown on tested SrCPC scaffold and TCPS control up to day 14. At days 3, 6, and 14, RNA was isolated using the RNeasy Plus Micro Kit (Qiagen, Milan, Italy) following the provided protocol. RNA quality and quantity were evaluated using a Nanodrop spectrophotometer (ND-1000, Nanodrop Technologies, Wilmington, DE, USA), then reverse transcribed to cDNA using the RT^2 First Strand cDNA Kit as recommended (Qiagen, Milan, Italy)[8]. The analysis was performed in triplicate for each experimental group. The

Human Extracellular Matrix and Adhesion Molecules PCR Array (Qiagen, Milan, Italy, Catalog n. PAHS-013Z) were employed to analyze the genes modulated in hASCs grown on SrCPC scaffold at days 3, 6, and 14. RT2 Profiler PCR Array for Extracellular Matrix and Adhesion Molecules allowed to analysis the expression of 84 genes involved in cell-to-cell adhesion, cells to the extracellular matrix (ECM) adhesion, and 5 housekeeping genes. Analyses were carried out using the SYBR Green method on a CFX96 Touch™ PCR detection system (Bio-Rad, Milan, Italy)[6].

Alizarin Red Staining assay in hASCs grown on SrCPC scaffold.

The biological property of SrCPC scaffold was assessed in hASCs grown on (i) the biomaterial and (ii) TCPS, up to day 14 in basal culture medium constituted by αMEM (Lonza, Milan, Italy) supplemented with 20% fetal bovine serum (FBS) and antibiotics[6,7]. Alizarin Red staining was employed to detect the matrix mineralization in hASCs grown on the scaffold. HASCs grown on SrCPC scaffold and TCPS, for 14 days, were fixed in 4% neutral buffered formalin and stained with a 40 mM, pH 4.2 solution of Alizarin Red (Sigma-Aldrich) to analyse the mineral matrix deposition. After extensive washing, to remove unbound staining, pictures were taken using a standard light microscope (Nikon Eclipse TE 2000-E microscope, Nikon Instruments Spa, Sesto Fiorentino, Italy) equipped with a digital camera (DXM 1200F; Nikon Instruments Spa, Sesto Fiorentino, Italy). Afterwards, the mineralized substrates were dissolved using 20% methanol and 10% acetic acid in a water solution (Sigma-Aldrich, Milan, Italy), whereas the quantification was carried out, in triplicate, using a spectrophotometer (Thermo Electron Corp., model Multiskan EX, Vantaa, Finland) at a wavelength (λ) of 450 nm[14,16]. The analysis was performed in triplicate for each experimental group.

Osteocalcin protein expression

The ELISA test was carried out on day 14 to identify osteocalcin (OCN) protein expression in hASCs grown on the SrCPC scaffold and on TCPS (control group). Protein extraction was performed using a Cell Extraction Buffer (Thermo Fisher Scientific, Milan Italy) with 1 mM of phenylmethylsulphonyl fluoride (PMSF) and a protease inhibitor cocktail. Protein concentration was evaluated through the bicinchoninic acid (BCA) (Thermo Fisher Scientific, Milan Italy) according to the provided instructions. The OCN protein was quantified using the Human OCN Instant ELISA (Thermo Fisher Scientific, Milan, Italy) following the provided protocol[14]. The analysis was performed in triplicate for each experimental group.

Human Osteogenesis RT^2 Profiler PCR Array

The human Osteogenesis PCR Array (Qiagen, Milan, Italy, Catalog n. PAHS-026Z), performed in triplicate, was assessed to identify genes, which are involved in osteogenic pathways modulated by SrCPC scaffolds in hASCs at day 3, 6 and 14. RT2 Profiler PCR Array for human osteogenesis was employed in real-time to analyse the expression of 84 genes involved in skeletal development and bone mineral metabolism, as well as cell adhesion molecules. Analyses were carried out using the SYBR Green method on a CFX96 Touch™ PCR detection system (Bio-Rad, Milan, Italy)[6].

Statistical analysis

Statistical analyses of experiments, which were performed in triplicate, were carried out using GraphPad Prism 7.0 software for Windows. Data obtained from the AlamarBlue assay were analyzed with 2-way ANOVA and multiple comparison tests. t-test was used to analyze the OCN protein expression and matrix mineralization, whereas statistical analysis of fluorescence intensity mean was carried out using One-way ANOVA. The activated Caspase 3 expression levels measured by ELISA test were expressed in their media ± standard deviation. $p<0.05$ indicates that the difference is statistically significant. In terms of data analysis of Real-Time PCR, the fold change for each gene expression was calculated using the $2-\Delta\Delta CT$ method and then normalized by comparing these values with those of the housekeeping genes, which were used as controls. All reactions were performed in triplicate; twice fold up- or down-regulated expression (Log2 fold change (FC) > 1 or < -1) compared to controls was considered significant.

Results and discussion

Physico-chemical features of SrCPC, SrCPC-MTX, and SrCPC-Dox scaffolds

The phase composition of SrCPC was investigated before mixing the precursors and at 72 hours after mixing at 37°C, exhibiting the typical diffraction patterns of αTCP and apatite, respectively (figure 68).

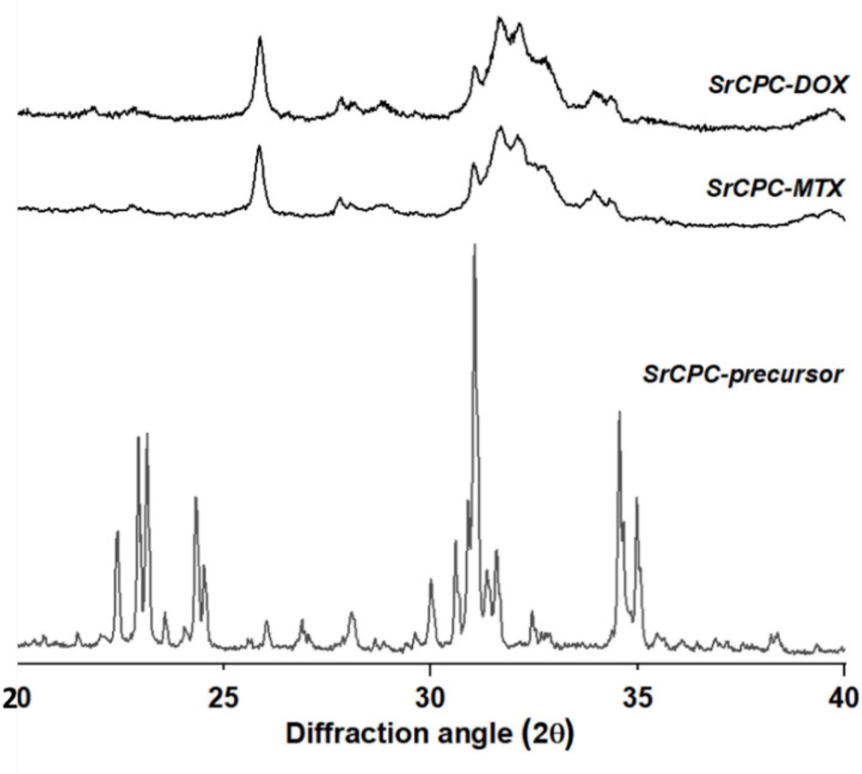

Figure 68. Diffraction patterns of SrCPC precursor before mixing with liquid component (control). SrCPC-MTX and SrCPC-Dox patterns are investigated at 72 hours after mixing.

Some physics characteristics of SrCPC, such as Young's modulus, porosity, and pore size are reported in the following table (Table XX), and were determined in previous studies[23-25]:

***Table XXI**. Young's modulus, porosity, and pore size of SrCPC*

	Young's modulus	Porosity	Porre size
SrCPC	2.3 ± 0.2 GPa	40 ± 5%	60%: 0.01-0.1 µm 40%: 0.5-1 µm

The drug release profile of SrCPC-MTX and SrCPC-Dox scaffolds was performed for up to 7 days and fitted with the Korsmeyer-Peppas model (Eq. 10).

Firstly, the calibration curves of MTX and Dox in HEPES acidified with HCl 1 M (pH 1) a (showed in Figure 69) were constructed by monitoring the optical density of MTX in standard solution ranging from 0.1 and 50 µg/mL, which were prepared by dilution of mother solution (100 µg/mL) and of Dox in standard solution ranging from 0,5 and 50 µg/mL mg/mL, which were prepared by dilution of mother solution (100 µg/mL).

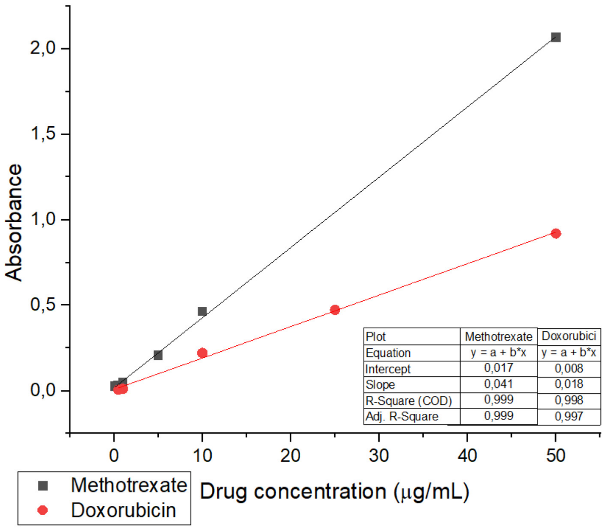

Plot	Methotrexate	Doxorubici
Equation	y = a + b*x	y = a + b*x
Intercept	0,017	0,008
Slope	0,041	0,018
R-Square (COD)	0,999	0,998
Adj. R-Square	0,999	0,997

***Figure 69**. Calibration curve of MTX (black line) and Dox (red line)*

MTX and Dox kinetic release profiles from SrCPC are shown in Figure 70 and the result of the fitting with the mathematical models in the tables below (table XXI)

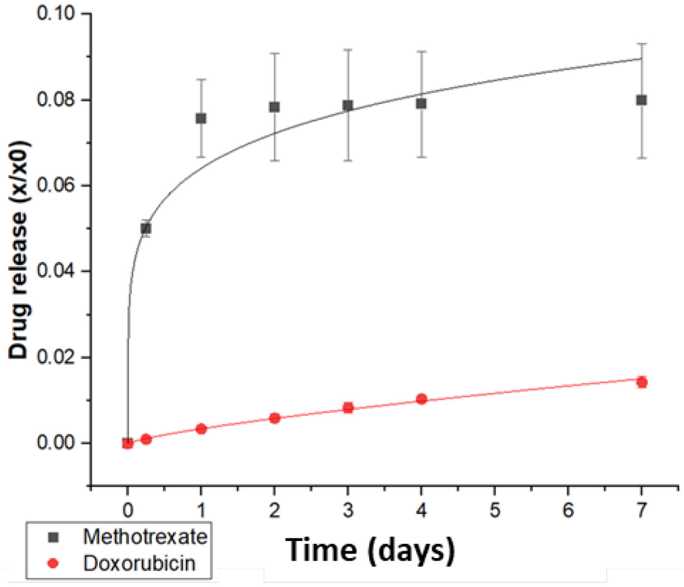

***Figure 70.** Kinetic release profiles of Methotrexate (black line) and Doxorubicin (red line) from bone cement.*

***Table XXII. n** exponent value of the Korsmeyer-Peppas model and relative release regime obtained by fitting the tetracycline release profiles.*

Korsmeyer-Peppas model	**Samples**	***n* value**	**Respective release regime**
$\boldsymbol{f_i = \frac{M_i}{M_\infty} = Kt^n}$	SrCPC-MTX	n = 0.172 ± 0.022	Diffusive regime with hampered release
	SrCPC-DOX	n = 0.755 ± 0.034	Anomalous transport

The SrCPC-MTX has been mathematically associated with a process defined as a diffusive regime with the hindered release, whereas for SrCPC-DOX the release mechanism is governed by anomalous transport, which is a combination of diffusion and other mechanism (such as swelling/erosion)[14]. This difference is due to several factors, including the chemical nature of the drug and its interaction with the superficial end-groups exposed by the material[15]. In particular, MTX contains a glutamic acid that can interact with the surface of nanocrystalline hydroxyapatite, in particular with the two carboxylate end-groups, resulting in binding to Ca^{2+} ions[15,16]. Conversely, Dox is characterized by an aromatic chemical structure with multiple functional groups and oxygen atoms. In the typical alkaline environment that occurs during the cement setting reaction, the Dox structure has hydrogen atoms attached to the –OH groups and positively charged amino groups ($-NH_3^+$). In this state, Dox has a high affinity for the apatite nanocrystals forming the cement matrix[17], thus resulting in a slower and different release kinetics.

The samples evidenced the typical microstructure of self-hardening apatitic bone cements featuring elongated interlocking nanocrystals (Figure 71a). Comparison between the SEM images shows that the loading with Dox (Figure 71b) or MTX (Figure 71c) does not affect the structural features of the scaffold.

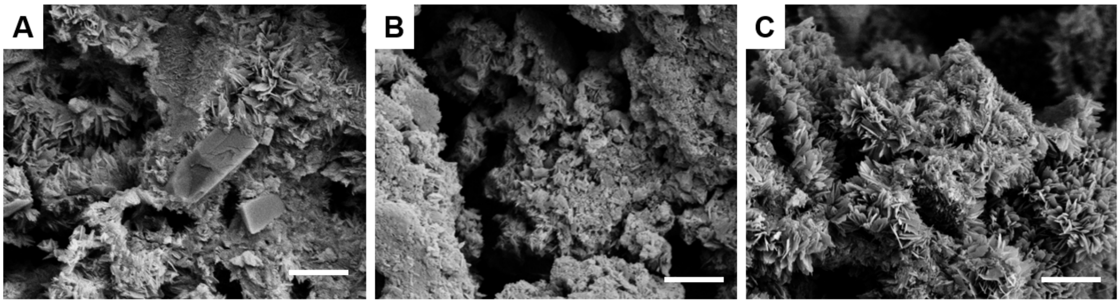

Figure 71. *SEM images of* ***A)*** *drug free SrCPC (control),* ***B)*** *SrCPC-Dox and* ***C)*** *SrCPC-MTX. Scale bar=1 µm*

Cytotoxic effects of SrCPC-MTX and SrCPC-DOX on SAOS-2 and SAOS-eGFP

The ability of SrCPC scaffolds factionalized with anticancer drugs methotrexate (SrCPC-MTX) and doxorubicin (SrCPC-DOX) to contrast OS cell proliferation was analysed in vitro in SAOS-eGFP cells, up to day 7. The effects of drug release were assessed in the engineered SAOS-eGFP cells grown on the biomaterials by evaluating cell number, fluorescence intensity rate and reduction in metabolic activity. The SEM analysis was used to investigate the cytotoxic effects of the functionalized cements on the SAOS-2 cells grown on them up to the 7th day.

At day 7, the SAOS-2 cells were well spread and completely covered the surface of the SrCPC scaffold, showing their natural morphology and the cytoplasmic extensions that connected them to the scaffold surface and to each other. In this study, SrCPC-MTX and SrCPC-DOX scaffolds were prepared to achieve release approximately 48,73 ± 14,15 µg/mL and 5,18 ± 0,42 µg/mL after 3 days, respectively. At day 7, SAOS-2 cells grew almost completely on SrCPC-MTX scaffold surface (Figure 72a). However, compared to SAOS-2 cells grown on the control, cells growing on the drug-loaded scaffolds showed an altered morphology. The cell culture exhibited an altered morphology as demonstrated by cell swelling and few cytoplasmic bridges between cells. In contrast, with SrCPC-Dox, there was no coverage of the scaffold surface by SAOS-2 cells. In this case, only a small number of cells with an altered morphology could be seen on the surface of the scaffold (Figure 72a). These results suggest that the SrCPC-MTX and SrCPC-Dox scaffolds have a cell killing effect on SAOS-2 cells when compared to the SrCPC scaffold.

Fluorescence intensity of SAOS-eGFP cells grown on SrCPC-DOX and SrCPC-MTX.

Fluorescence intensity analyses of SAOS-eGFP cells were performed to evaluate the anti-proliferative activity of the functionalized scaffolds. By evaluating the fluorescence intensity emitted by the engineered cell line on day 7, the effects of SrCPC-MTX and SrCPC-DOX scaffolds on the viability of SAOS-eGFP cells were investigated. The SrCPC scaffold was completely covered by SAOS-eGFP cells (Figure 72b), as shown in the digital images obtained using a confocal microscope. Indeed, the number of SAOS-eGFP cells decreased in SrCPC-MTX and cells were largely absent in SrCPC-DOX (Figure 72b), confirming the SEM analysis. The confocal microscopy data were confirmed by quantification of fluorescence intensity. The mean fluorescence intensity of SAOS-eGFP cells grown on the SrCPC scaffold was higher than that of cells grown on SrCPC-MTX ($p < 0.05$) and SrCPC-DOX ($p < 0.005$). Between the SrCPC-MTX and SrCPC-DOX groups (Figure 72c), there were no statistical differences.

Metabolic activity

The effects of SrCPC-MTX and SrCPC-DOX scaffolds on the metabolic activity of SAOS-2 cells were investigated using the Alamar Blue assay on days 1, 2 and 7, evaluating the fluorescence intensity emitted by the engineered cell line. Up to day 7, SAOS-2 cells grown on the control drug-free SrCPC showed increasing metabolic activity. Conversely, SAOS-2 cell numbers on SrCPC-MTX and SrCPC-DOX increased during the first two days, then decreased at day 7 (Figure 72d; $p>0.05$). At day 7, the number of SAOS-2 cells in MTX/DOX conjugated scaffolds was significantly reduced compared to the control ($p<0.005$ and $p<0.001$, respectively) (Figure 72d). The SrCPC-DOX material induced a complete cytotoxic effect. This was detected by the absence of cells on the material as shown by the Alamar blue assay (Figure 72d).

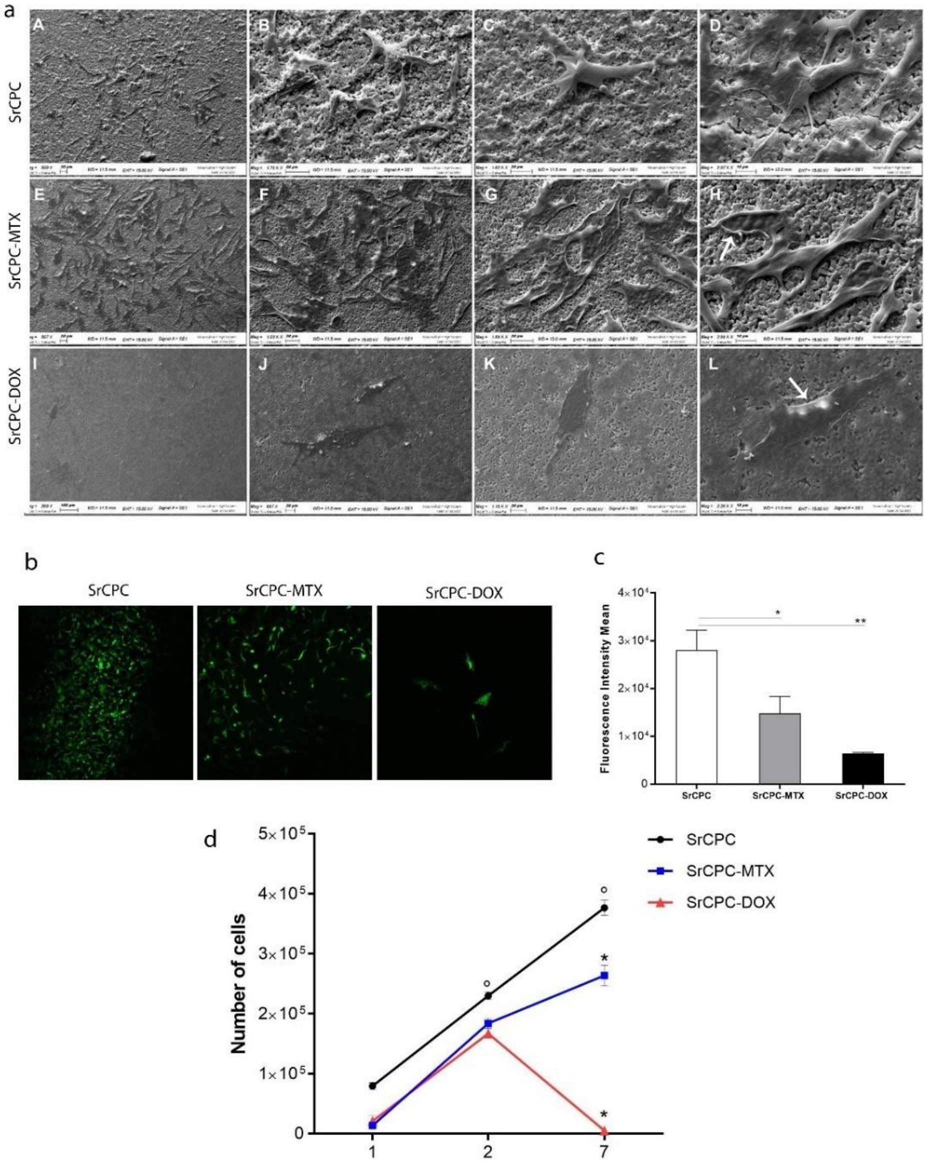

***Figure 72**. Cytotoxic effects of SrCPC-MTX and SrCPC-DOX on SAOS-eGFP. (a) SEM analysis. SrCPC scaffold, Scale bar: 20 µm, 500X, Scale bar: 20 µm, 1.79K X, Scale bar: 20 µm, 1.62K X, Scale bar: 10 µm, 3.07K X, respectively (A-D). SrCPC-MTX, Scale bar: 20 µm, 507X, Scale bar: 20 µm, 1.03K X, Scale bar: 20 µm, 1.69K X, Scale bar: 10 µm, 2.99K X, respectively (E-H). SrCPC-DOX scaffold. Scale bar: 100 µm, 268X, Scale bar: 20 µm, 687 X, Scale bar: 20 µm, 1.15K X, Scale bar: 10 µm, 2.26K X, respectively (I-L). (b) Confocal images of SAOS- eGFP cells on SrCPC, SrCPC-MTX, SrCPC-DOX, Scale bar: 100 µm. (c) fluorescence intensity of SAOS-eGFP cells. (d) number of SAOS-eGFP cells grown on SrCPC, SrCPC-MTX and SrCPC-Dox up to 7 days.*

Positive staining of Caspase-3/7 expression protein in SAOS-2 grown on SrCPC-DOX.

SAOS-2 cell cultures were grown on scaffolds for 4 days to gain insight into the putative mechanism of SrCPC-DOX and SrCPC-MTX induced cell death. In SAOS-2 cells grown on SrCPC-DOX scaffolds, activated caspase-3/7 expression proteins were visualised. Indeed, the SAOS-2 cells grown on SrCPC-DOX showed significantly higher levels of caspase-3/7-positive cells (green) compared to SrCPC-MTX. Caspase-3/7 protein expression was lower in SAOS-2 cells grown on unmedicated SrCPC compared to other experimental groups (Figure 73A).

Higher levels of activated Caspase 3 expression proteins in SAOS-2 grown on SrCPC-DOX and SrCPC-MTX

Quantification of cleaved caspase-3 protein shows the apoptotic process induced in SAOS-2 cells grown on SrCPC-DOX and SrCPC-MTX for 4 days (Figure 59B). The ELISA test revealed significantly higher levels of cleaved caspase-3 protein in the SAOS-2 culture grown on SrCPC-DOX, resulting in a significant increase in the expression of cleaved caspase-3 protein expressed as (mean ± SD) (0.705 ± 0.021) compared to the control of SrCPC (0.475 OD ± 0.021) ($p<0.05$) and TCPS (0.163 OD ± 0.014). Compared to the controls, i.e., SrCPC and TCPS, the material SrCPC-DOX showed a higher OD level (2.502 OD ±0.07 SD) (Figure 73B).

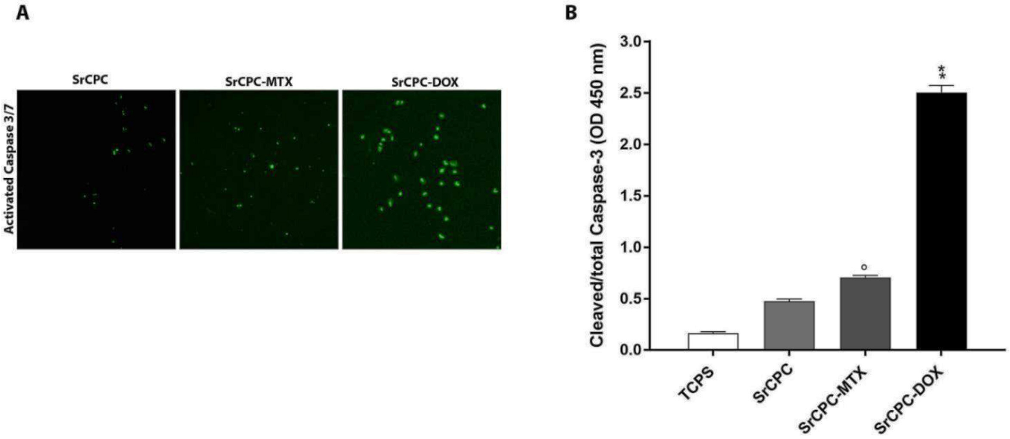

***Figure 73**. Evaluation of induction of apoptosis in SAOS-2 grown on SrCPC, SrCPC-MTX and SrCPC-DOX scaffolds. **(A)** Immunostaining of activated caspase 3/7 in SAOS-2 cells grown on SrCPC, SrCPC-MTX and SrCPC-DOX scaffolds. **(B)** Protein expression of cleaved Caspase-3*

Characterization and cytocompatibility of SrCPC scaffold

The scaffold cytocompatibility was analysed using human ASCs grown on SrCPC scaffold and tissue culture polystyrene (TCPS, the control). As reported below (Figure 74), SEM, metabolic activity, live/dead and cytoskeletal architecture analyses were performed in the two experimental groups at different time points. In addition, to evaluate the scaffold cytocompatibility, SAOS-eGFP cells grown on SrCPC scaffold and on TCPS were used on day 14.

SEM analysis of SrCPC scaffold cytocompatibility

Microstructure and morphology of SrCPC scaffolds without and with hASCs grown on it up to day 14 was analysed by SEM at high magnification (80-400×) (Figure 74a). hASCs grown on the scaffold showed a normal cell morphology, exhibiting pseudopodium-like structures, which connect them to the biomaterial surface (Figure 74a). Indeed, human stem cells can adhere to non-doped material, as indicated by the arrows.

Live/Dead analysis of hASCs grown on SrCPC scaffold.

The Live/Dead assay was used to analyse the cell viability of hASCs grown on the scaffold and TCPS, at day 3, 6 and 14. Cyto-dye, a green-fluorescent dye and propidium iodide, a red fluorescent dye, were used to stain live and dead cells, respectively. At each experimental time point, carried out on hASCs grown in contact with the scaffold, digital images showed the presence of live cells, which were indistinguishable from those grown on the control. Dead cells were no detected (Figure 74b). In addition, live cells were identified in the scaffold by confocal microscopy in 0.5 µm sections (z) at days 3, 6 and 14. A time-dependent increase was observed. The cytocompatibility of the SrCPC scaffold is demonstrated by these data.

Metabolic activity of hASCs grown on SrCPC scaffold

Alamar Blue assay was carried out to analyse the effects of the scaffold on hASCs cells viability. Cell metabolic activity of each time point was converted into the number of viable cells by calculating the interpolated X value of hASCs calibration curve. Results showed an increase cell number of hASCs grown on the SrCPC scaffold and TCPS, up to day 7 (Figure 74c). At day 1 and 2 there were no significant differences between the two experimental groups (Fig. 6c; $p>0.05$). Contrariwise, there are statistical differences in hASCs grown on the SrCPC scaffold compared to hASCs grown on TCPS, at day 7 (Figure 60c; $p<0.05$). Nevertheless, SrCPC scaffold induced hASCs growth and did not cause any cytotoxicity.

Cytoskeleton analysis of hASCs and SAOS-eGFP grown on SrCPC scaffold.

The cytoskeleton architecture of hASCs grown on the SrCPC scaffold and TCPS, was analysed by performing phalloidin-TRITC staining, at day 14 (Figure 74d). The cytoskeleton showed a well- organized structure in hASCs grown on scaffold and TCPS, demonstrating that the scaffold had not influence on the cytoskeleton architecture, up to day 14. In the digital images at 10X, 20X magnification and 40X magnification (Figure 74d), actin filaments appear unaltered, confirming the cytocompatibility of the SrCPC scaffold. The cytoskeleton architecture of SAOS-eGFP cells grown on the SrCPC scaffold and TCPS, analysed at day 14 and the cytoskeleton architecture showed a well-organized structure (Figure 74d). SAOS-eGFP cells grown on SrCPC scaffold demonstrate a regular cytoskeleton architecture (Figure 74e).

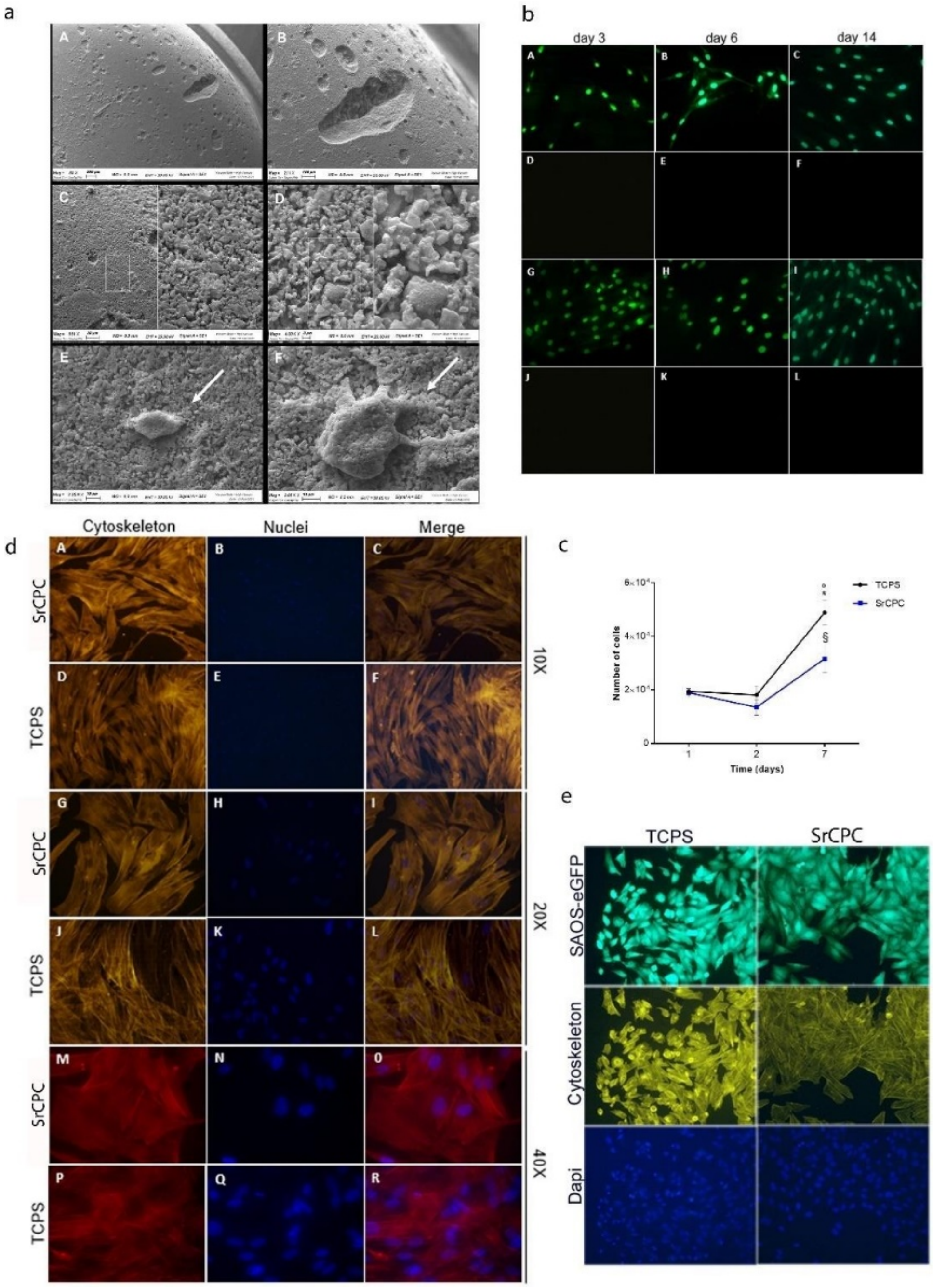

Figure 74. *Characterization of vitality and proliferation of hASC grown on SrCPC scaffold.* ***a)*** *SEM of SrCPC scaffold, Scale bar: 200 µm, Scale bar: 100 µm, Scale bar: 200 µm and Scale bar: 3 µm respectively (A-D). hASCs (white arrows) on the substrate, Scale bar 10 µm; Scale bar 10 µm, respectively (E-F).* ***b)*** *Cell viability analysis of hASCs using Live/Dead assay. Live cells (hASCs) grown in contact with SrCPC at day 3, 6, 14 (A-C). Dead cells were no detected (D-F). Live cells (hASCs) grown on TCPS at day 3 ,6, 14 (G-I). Dead cells were no detected (J-L). Scale bar: 100 µm. (c) hASCs metabolic activity, (d) Cytoskeleton analysis of hASCs grown on the SrCPC scaffold Scale bar: 100 µm, (e) Cytoskeleton analysis of SAOS-eGFP grown on the SrCPC scaffold.*

Modulation of the extracellular matrix and adhesion molecules' genes in hASCs by SrCPC scaffold

The ECM and adhesion molecules gene expression profiles were investigated using PCR array technology in hASCs cultured on the SrCPC scaffold and TCPS to evaluate the scaffold cytocompatibility. Analyses were carried out at day 3, 6 and 14 (Figure 75).

At day 3, a total of 27 differential expressed genes (DEG), including 9 up-regulated genes (>1 log2 fold change; $p<0.05$; red) and 18 down-regulated genes (<-1 log2 fold change; $p<0.05$; green), were identified in hASCs grown on scaffold, compared to the control.

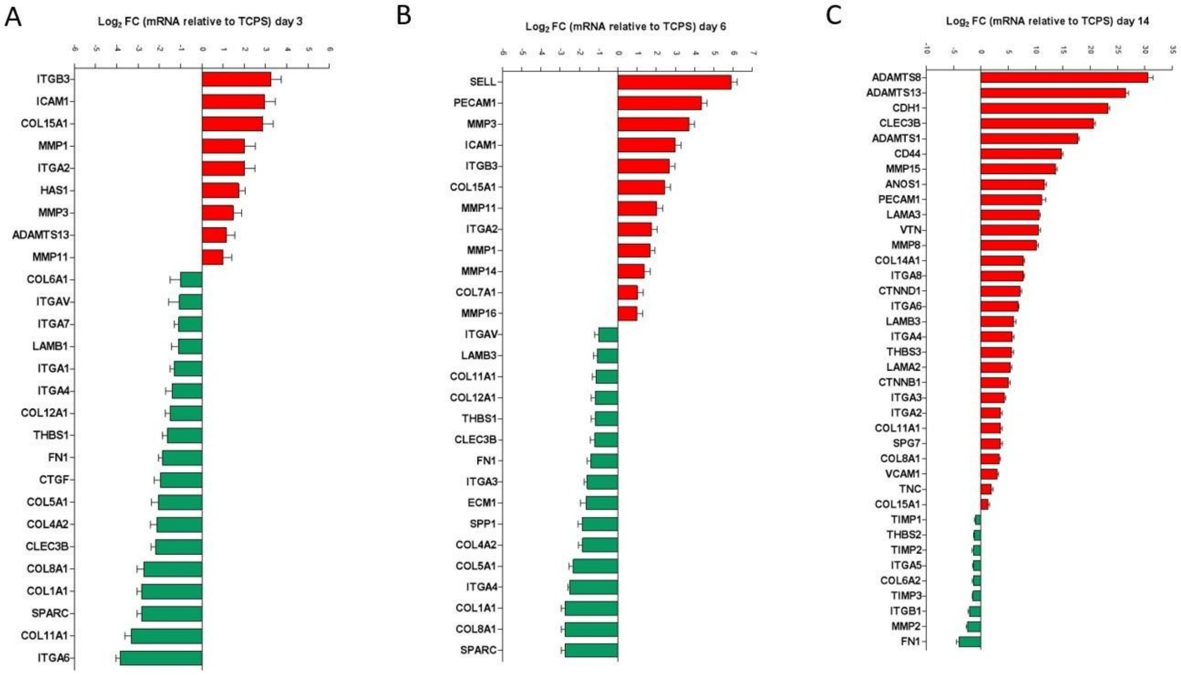

Figure 75*. Extracellular matrix and adhesion molecules genes modulated by SrCPC scaffold in hASCs. (A) At 3 days n= 27 differentially expressed genes, including 9 up-regulated genes (>1 log2 fold change; p<0.05; red) and 18 down-regulated genes (<-1 log2 fold change; p<0.05; green), were identified in hASCs grown on scaffold compared with control. (B) At day 6, n=28 differentially expressed genes, including 12 up-regulated genes (>1 log2 fold change; p<0.05; red) and 16 down-regulated genes (<-1 log2 fold change; p<0.05; green), were identified in hASCs grown on scaffold compared with control (TCPS). (C) At day 14, 38 differentially expressed genes, including n=29 up-regulated genes (p<0.05; red) and n=9 down-regulated genes (p<0.05; green), were identified in hASCs grown on scaffold compared with control.*

Osteogenic gene expression induced by SrCPC scaffold in hASCs.

In the second part of our study, the effect of SrCPC scaffold in the osteogenic gene expression were assessed employing hASCs cultures. Matrix mineralization, OCN protein expression and osteogenic genes expression were investigated in hASCs grown on the scaffold, up to day 14 (Figure 76 a-d).

Mineral matrix deposition of hASCs grown on SrCPC scaffold.

Alizarin Red staining was used to evaluate the mineralized matrix in hASCs grown on SrCPC scaffold and TCPS in basal medium. Cell cultures for the two experimental groups were stained with alizarin red and imaged using a bright-field microscope. Digital images show that SrCPC scaffold promotes mineral matrix deposition differently compared to TCPS (Figure 76a). Afterwards, alizarin red staining was eluted to perform optical density measurements. Results showed an increased calcified matrix in hASCs grown on the SrCPC scaffold compared to TCPS ($p < 0.0001$; Figure 76b), at day 14.

OCN protein expression in hASCs grown on SrCPC scaffold.

OCN protein expression in hASCs grown on SrCPC scaffold and TCPS, up to day 14, were analysed using ELISA test. In hASCs grown on SrCPC the assay revealed 38.25 ng of OCN/µg of proteins and 17.95 ng of OCN/µg of proteins, in TCPS. Data show a significant increase of OCN protein expression in hASCs grown on the scaffold compared to control ($p<0.0001$; Figure 76c).

Osteogenic genes modulated by SrCPC scaffold in hASCs.

In this study, osteogenesis RT2 Profiler PCR Array was used to investigate the differentially expressed genes in hASCs grown on SrCPC scaffolds, at day 3, 6 and 14 (Figure 76d). Results of experimental replicates obtained at day 3 revealed the ability of the scaffold to up-regulate (>1 log2 fold change; $p<0.05$; red) different genes involved in skeletal development. In summary, in hASCs the scaffold strengthened the expression of those genes implicated in ossification, osteoblast differentiation and bone mineralization during the experimental time course, whereas the modulation of genes involved in cell adhesion process decreased over time, up to day 14.

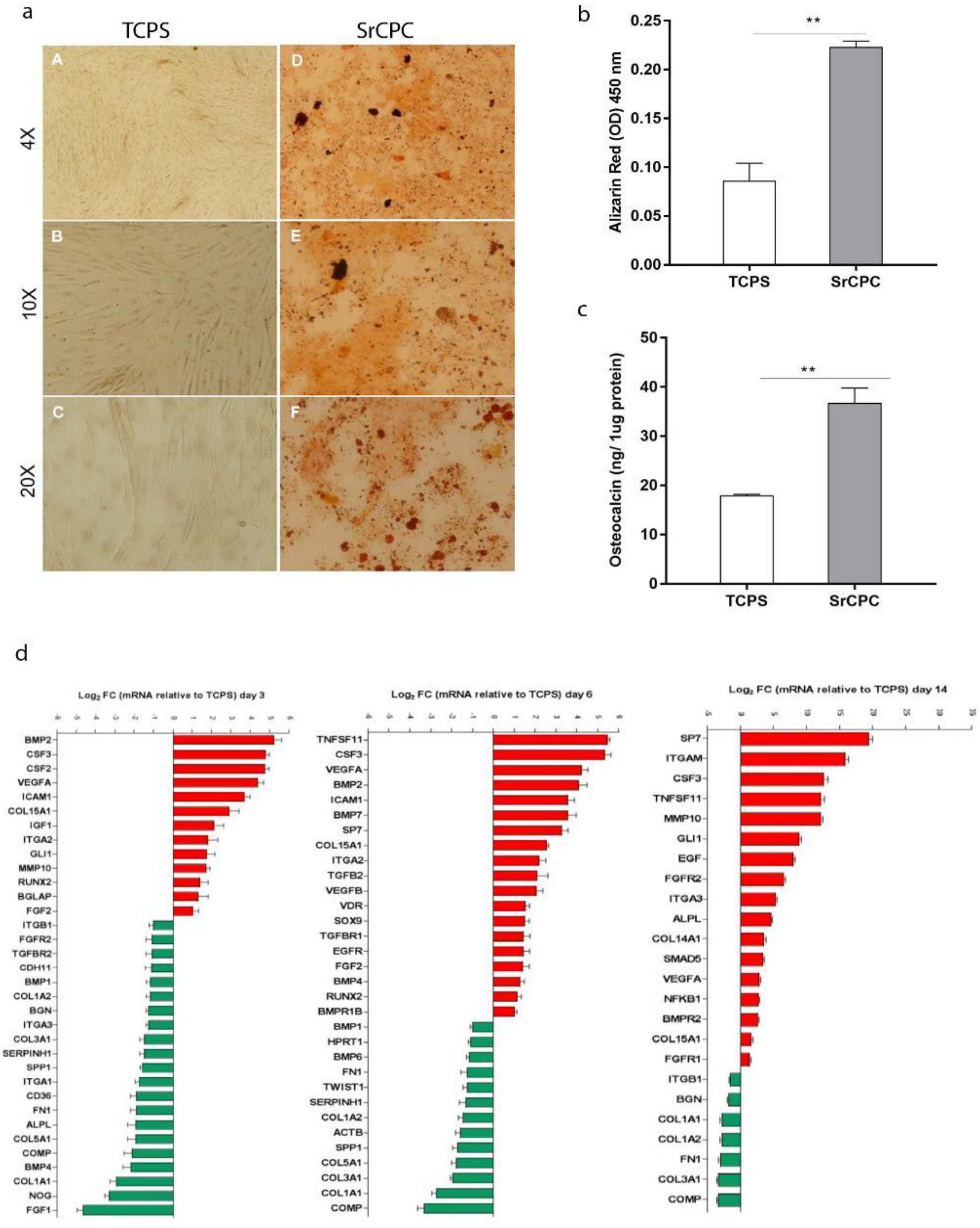

Figure 76. Osteoinductivity properties of SrCPC scaffold evaluated with hASCs culture. (a) Alizarin red staining in hASCs grown on TCPS and SrCPC at 4X (A,D), 10X (B,E) and 20X (C,F) magnifications. Scale bar for each magnification: 100 μm. (b) Quantification of Alizarin Red staining measured in hASCs grown on control and SrCPC. (c) OCN protein expression quantified using the ELISA test in hASCs grown on SrCPC scaffold and TCPS at day 14. (d) Osteogenic gene expression (mRNA) modulated by SrCPC scaffold in hASCs at days 3,6 and 14 day.

Discussion

The effects of doxorubicin or methotrexate drugs released on self-hardening apatitic scaffolds were investigated on SAOS-2 cells, particularly analyzing the putative mechanisms of cell death induced in vitro model of SAOS-2. In this work it was assessed in vitro the ability of drug-loaded SrCPC scaffolds to contrast OS cell proliferation, using the SAOS-eGFP cell line, which represents an appropriate study model, as previously reported[15,17-19].

As regards drug loading concentrations, in literature, there are heterogeneous data about MTX, which range from 0.1–100 µM28 to >100µM in the case of primary SAOS cell line[20]. About DOX, the tested concentration range is 10-320 µM for several 3D cultures, including OS cell line (U2OS)[21]. In this study, SrCPC-MTX and SrCPC-DOX scaffolds were prepared to achieve the release of drugs into these ranges, in fact, we obtained MTX and DOX release of approximately 48µg/mL and 5µg/mL after 3 days, respectively[17].

We show that both SrCPC-MTX and SrCPC-DOX scaffolds exert an in vitro anti-proliferative activity against cancer cells. Indeed, a decreasing number of SAOS-eGFP cells was observed at day 7 in MTX/DOX-conjugated scaffolds compared to drug-free SrCPC. These data were supported by qualitative and quantitative results obtained by fluorescence analysis of engineered SAOS-eGFP cells. Indeed, images from confocal microscopy analysis and measurement of fluorescence intensity revealed a reduced number of cancer cells grown on SrCPC-MTX compared to the control (52%) and a higher decrease of SAOS-eGFP cells grown on SrCPC-DOX scaffold (28%). Similarly, SEM investigation allowed us to analyse the morphology of cells grown on scaffolds. Microscopic analyses verified that the drug-free SrCPC scaffold surface was completely covered with SAOS-eGFP cells, with unaltered morphology. Contrariwise, SAOS-eGFP cells in contact with SrCPC-MTX presented an altered morphology. Furthermore, only a few SAOS-eGFP cells were observed on the SrCPC-DOX scaffold.

SrCPC-DOX induced apoptosis on SAOS-2 after four days of culture. To test the potential to induce apoptosis of the doped materials on the SAOS-2 culture, three different methods were employed. Apoptosis is a form of programmed cell death that is initiated by a tightly regulated signalling cascade, that results in caspase activation. Our results demonstrated that SrCPC-DOX material induces the apoptosis process in SAOS-2 cells through the activation of the protein caspase 3/7 compared to the control material. In addition, higher expression of caspase-3 is quantified in SAOS- 2 lines with respect to cell lines grown on SrCPC-MTX and on the control material. Further in vitro investigations are needed to deepen the genetic and epigenetic influences of drug-delivery scaffolds. Overall, these results report on the cytotoxic effects of MTX and DOX drugs in the used concentrations. On the other hand, 5μg/mL of DOX displayed a cell-killing effect on SAOS-eGFP cells higher than 45 μg/mL of MTX. This suggests that the MTX concentration used herein is not sufficient to kill all SAOS cells. Contrariwise, DOX concentration could159 be reduced[19].

The SrCPC scaffold was tested in terms of cytocompatibility and osteoinductivity using hASCs. The SrCPC scaffolds were selected for controlled drug delivery, as they exhibit a chemically active surface, especially for apatitic phases, favoring the chemical binding of drugs[15], as well as a microporous structure, given by nanosized acicular apatitic grains physically interlaced to form a mechanically resistant construct. Viability analyses for metabolic activity and cell morphology on drug-loaded SrCPCs report on an increasing number of live cells, as well as on the control. In addition, hASCs grown in contact with the SrCPC scaffold exhibit a well-organized cytoskeleton architecture with actin filaments being distributed uniformly in cell cytoplasm, at day 14. In addition, the SrCPCs studied herein present a granular structure offering a good microenvironment for adhesion and proliferation of hASCs, as shown by SEM analysis where cells grew well on the scaffold surface.

Cellular biology results were supported by molecular genetic/biology data, such as gene expression analysis carried out using a PCR array technique to evaluate the extracellular matrix and cell adhesion molecules profile. In bone, the extracellular matrix regulates cell adhesion, proliferation, and differentiation, producing collagen, integrin, fibronectin, and connective tissue growth factor[22]. Moreover, osteogenic differentiation during the ECM secretion phase in MSCs induces morphological changes in immature osteoblasts, immediately followed by the formation of mature osteoblasts[26]. In hASCs, genes encoding cell adhesion molecules were up-regulated in the presence of SrCPC scaffold, demonstrating the ability of the scaffold to mediate cell-cell and/or cell-scaffold interactions. Among them, ICAM1, PECAM1, VCAM1, SELL, and CD44 molecule up-regulation was observed. SELL is a calcium-dependent lectin that mediates cell adhesion by binding to glycoproteins on neighboring cells[27], whereas CD44 molecule is responsible for cell-cell interactions engaging extracellular matrix components, such as hyaluronan, collagen, growth factors, cytokines or proteases[28]. ECM-cell interaction is crucial for tissue morphogenesis and architecture; thus, such actions are mediated by integrin and cadherin[29]. The SrCPC scaffold stimulated the up- regulation of genes encoding integrins and cadherins in hASCs. Early expressed integrins are ITGA2 and ITGB3 followed by ITGA3/4/6/8, which were up regulated up to day 14. The gene expression levels of ITGA2 and ITGA3 agreed in the two different PCR-Array for ECM and Osteogenesis, as well as ITGA1, which resulted down-regulated in both assays, at the first time point. Of all, the cadherin CDH1, a calcium-dependent cell adhesion protein, resulted up-regulated in hASCs grown on the biomaterial. Integrins and cadherins have an important role in proper development, function, regeneration of skeletal tissue and MSCs osteogenic differentiation[29,30]. Collagen is the most abundant constituent of the ECM acting as a mechanical support for cells[31]. In vitro results demonstrated that the SrCPC scaffold promoted the expression of genes encoding for collagen proteins including COL7/8/11/14/15A1. The latter is constantly up expressed during the experimental time course in both the PCRs assay thus highlighting its important role in osteogenic differentiation and mineralization[32].

Matrix metalloproteinases (MMP), with the ability to cleave collagens and proteoglycans, are among the most active proteases in ECM regulation[26]. Such proteinases are involved in wound healing and tissue remodelling[33]. MMP1/3/11 gene expression was promptly induced by SrCPC in hASCs. MMP8/15 were positively modulated by the scaffold later. Indeed, while MMP15 is a membrane-type metalloproteinase[33], MMP8 is expressed in osteoblastic progenitors, differentiated osteoblasts and osteocytes[34]. Moreover, MMP10, which is essential for human bone development[35] and takes part in the physiological processes of bone growth[36], resulted positively modulated by the SrCPC scaffold. The BMP2 gene resulted up-regulated in our experiments suggesting hASCs osteogenic differentiation upon contact with the scaffold. Further, it has been reported that MMP10 enhances BMP-2-induced osteoblast differentiation in vitro[37]. The crucial signalling pathways leading MSCs towards osteogenesis differentiation are transforming growth factor-beta (TGF-β) and bone morphogenetic protein (BMP)[39,39]. Our results demonstrate that SrCPC scaffold up-regulated genes are involved in these two signalling cascades. Specifically, three of the most important BMPs, involved in osteogenesis, i.e., BMP2/4/7, resulted up-regulated alongside other BMP signalling like BMPR1A, BMPR2 and SMAD5[40]. On the other hand, among factors involved in the TGF-β cascade, TGFBR1/2 were positively regulated by the scaffold. The activation of cited signalling pathways leads to the expression of master osteogenic transcription factors, such as RUNX2 and Osterix (OSX), also known as SP7. More precisely, OSX is a downstream RUNX2 gene[41]. Our results agree with previous reports in as much as they demonstrated that the RUNX2 gene was up regulated at day 3 and 6, whereas SP7 expression with high fold change is observed at day 14, when RUNX2 modulation disappears[41]. Finally, RUNX2 and SP7 activity results in specific osteoblast gene expression of including OCN and collagen[41]. SrCPC biomaterial induced osteocalcin up-regulation in term of gene (BGLAP) and protein (OCN) expressions. In agreement, matrix mineralization analysis showed an increase matrix deposition in hASCs grown on the scaffold, as well as the up regulation of ALPL gene. Other osteogenic genes involved in the skeletal development process were modulated in hASCs by the scaffold. Of these, up-regulation of GLI1 and EGFR was observed. GLI1 is a transcriptional activator involved in signalling-mediated specification for osteoblast lineage inducing early osteoblast differentiation[39]. On the other hand, EGFR take part in EGFR/ERK/IGFBP-3 signalling pathway inducing osteoblast differentiation and maturation[14]. Additionally, the CLEC3B gene was found to be expressed in hASCs grown on the biomaterial, up to day 14[43].

It is well known that when MSCs differentiate into osteoblasts many osteoclast-associated cytokines are secreted, including CSF, RANKL stimulating osteoclasts differentiation[44]. Our experiments revealed the up regulation of TNFSF11, also known as RANKL and CSF2/3 genes. Thus, in hASCs the mechanism of bone resorption is activated together with the bone formation process. The coupled mechanisms continuously lead to bone remodelling.

Conclusion

This study shows an anti-proliferative ability of nanostructured apatitic bone cements (SrCPC) loaded with drugs on OS cells, with a greater effect of the SrCPC-DOX scaffold compared to SrCPC-MTX.

Here, it is demonstrating the ability of Sr-doped bone cement to deliver clinically relevant doses of anticancer drugs. Drug release kinetics vary depending on the chemical structure of the drug and its interaction with HA nanocrystals, resulting in different release mechanisms. Hindered Fickian diffusion is the mechanism by which MTX is released, while Dox follows an anomalous transport mechanism. Furthermore, the porous structure present in bone cement allow a sustained release of the drugs, resulting in a mechanism deflecting the classical Fickian diffusion.

The SrCPC scaffold, free of any loaded drugs, exhibits cytocompatibility and inductive effects on hASCs osteogenic differentiation. However, further studies should be carried out to evaluate if SrCPC-DOX and SrCPC-MTX may affect different hASCs biological processes depending on drug concentration.

These combined effects are promising for new therapeutic strategies against OS, addressing both tumour eradication and bone regeneration. A critical point is related to the setup of appropriate dosage of anticancer drugs with time, which must be tuned to balance toxic effects given by the drugs and the positive osteogenic signalling provided by the scaffold, as induced by their inherent physico-chemical and structural features. In this respect, nanostructured apatitic scaffolds, such as SrCPC, are particularly promising as the chemically active surface and the diffuse microporosity typical of self-hardened apatitic cements permit chemical linking of a variety of drugs and their incorporation into hollow cavities from which drugs can be released by diffusive mechanisms.

REFERENCES

1. Jackson, T. M., Bittman, M. & Granowetter, L. Pediatric Malignant Bone Tumors: A Review and Update on Current Challenges and Emerging Drug Targets. *Curr. Probl. Pediatr. Adolesc. Health Care* **46,** 213–228 (2016).
2. Belayneh, R., Fourman, M. S., Bhogal, S. & Weiss, K. R. Update on Osteosarcoma. *Curr. Oncol. Rep.* **23**, 71 (2021).
3. Jafari, F. et al. Osteosarcoma: A comprehensive review of management and treatment strategies. *Ann. Diagn. Pathol*. **49**, 151654 (2020).
4. Morelli, C. et al. Cell morphology, markers, spreading and proliferation on orthopaedic biomaterials. An innovative cellular model for the 'in vitro' study. *J. Biomed. Mater. Res. A* **83**, 178–183 (2007).
5. Manfrini, M. et al. Osteoconductivity of Complex Biomaterials Assayed by Fluorescent-Engineered Osteoblast-like Cells*. Cell Biochem. Biophys*. **71**, 1509–1515 (2015).
6. Mazzoni, E. et al. Hydroxylapatite-collagen hybrid scaffold induces human adipose-derived mesenchymal stem cells to osteogenic differentiation in vitro and bone regrowth in patients. *Stem Cells Transl. Med.* **9**, 377–388 (2020).
7. Iaquinta, M. R. et al. In Vitro Osteoinductivity Assay of Hydroxylapatite Scaffolds, Obtained with Biomorphic Transformation Processes, Assessed Using Human Adipose Stem Cell Cultures. *Int. J. Mol. Sci*. **22**, (2021).
8. Mazzoni, E. et al. Enhanced Osteogenic Differentiation of Human Bone Marrow-Derived Mesenchymal Stem Cells by a Hybrid Hydroxylapatite/Collagen Scaffold. Front. cell *Dev. Biol*. **8**, 610570 (2020).
9. Eilenberger, C. et al. Optimized alamarBlue assay protocol for drug dose-response determination of 3D tumor spheroids. *MethodsX* **5**, 781–787 (2018).
10. Kazantseva, L., Becerra, J. & Santos-Ruiz, L. Oridonin enhances antitumor effects of doxorubicin in human osteosarcoma cells. *Pharmacol. Reports* **74**, 248–256 (2022).
11. Sharma, N., Arya, G., Mankamna Kumari, R., Gupta, N. & Nimesh, S. Evaluation of Anticancer activity of Silver Nanoparticles on the A549 Human Lung Carcinoma Cell Lines through Alamar Blue Assay. Bio-protocol 9, 1–9 (2019).
12. Zhu, Y. et al. Evaluation of the proliferation and differentiation behaviors of mesenchymal stem cells with partially converted borate glass containing different amounts of strontium in vitro. *Mol. Med. Rep*. **7**, 1129–1136 (2013).
13. Giorgi, C. et al. Intravital imaging reveals p53-dependent cancer cell death induced by phototherapy via calcium signaling. *Oncotarget* **6**, 1435–1445 (2015).

14. Bruschi, M. L. Mathematical models of drug release. *Strategies to Modify the Drug Release from Pharmaceutical Systems* 63–86 (Elsevier, 2015). doi:10.1016/B978-0-08-100092-2.00005-9.

15. Sarda, S. et al. Interaction of Folic Acid with Nanocrystalline Apatites and Extension to Methotrexate (Antifolate) in View of Anticancer Applications. *Langmuir* **34**, 12036–12048 (2018).

16. Mukesh, U., Kulkarni, V., Tushar, R. & Murthy, R. S. R. Methotrexate loaded self stabilized calcium phosphate nanoparticles: A novel inorganic carrier for intracellular drug delivery. *J. Biomed. Nanotechnol*. **5**, 99–105 (2009).

17. Iafisco, M. et al. Superparamagnetic iron-doped nanocrystalline apatite as a delivery system for doxorubicin. *J. Mater. Chem. B* **4**, 57–70 (2016).

18. Suksiriworapong, J. et al. Synthesis and properties of a biodegradable polymer-drug conjugate: Methotrexate-poly(glycerol adipate). *Colloids Surf. B. Biointerfaces* **167**, 115–125 (2018).

19. Zhou, Z.F. et al. Calcium phosphate-phosphorylated adenosine hybrid microspheres for anti-osteosarcoma drug delivery and osteogenic differentiation. *Biomaterials* **121**, 1–14 (2017).

20. Sramek, M., Neradil, J., Sterba, J. & Veselska, R. Non-DHFR-mediated effects of methotrexate in osteosarcoma cell lines: epigenetic alterations and enhanced cell differentiation. *Cancer Cell Int*. **16**, 14 (2016).

21. Baek, N., Seo, O. W., Kim, M., Hulme, J. & An, S. S. A. Monitoring the effects of doxorubicin on 3D-spheroid tumor cells in real-time. *Onco. Targets. Ther*. **9**, 7207–7218 (2016).

22. Ren, J. et al. Global transcriptome analysis of human bone marrow stromal cells (BMSC) reveals proliferative, mobile and interactive cells that produce abundant extracellular matrix proteins, some of which may affect BMSC potency. *Cytotherapy* **13**, 661–674 (2011).

23. Dapporto, M., Gardini, D., Tampieri, A. & Sprio, S. Nanostructured Strontium-Doped Calcium Phosphate Cements: A Multifactorial Design. *Appl. Sci*. **11**, 2075 (2021).

24. Sprio, S. et al. Novel Osteointegrative Sr-Substituted Apatitic Cements Enriched with Alginate. *Materials*. **9**, 763 (2016).

25. Dapporto, M. Development of new bioactive and porous apatitic scaffolds for the regeneration of load-bearing Bones. *Univ. degli Stud. di Bol.* (2016).

26. Paiva, K. B. S. & Granjeiro, J. M. Matrix Metalloproteinases in Bone Resorption, Remodeling and Repair. *Prog. Mol. Biol. Transl. Sci*. **148**, 203–303 (2017).

27. Wedepohl, S. et al. Reducing Macro- and Microheterogeneity of N-Glycans Enables the Crystal Structure of the Lectin and EGF-Like Domains of Human L-Selectin To Be Solved at 1.9 Å Resolution. *Chembiochem* **18**, 1338–1345 (2017).

28. Midgley, A. C. et al. Transforming growth factor-β1 (TGF-β1)-stimulated fibroblast to myofibroblast differentiation is mediated by hyaluronan (HA)-facilitated epidermal growth factor receptor (EGFR) and CD44 co-localization in lipid rafts. *J. Biol. Chem*. **288**, 14824–14838 (2013).

29. Di Benedetto, A. et al. Osteogenic differentiation of mesenchymal stem cells from dental bud: Role of integrins and cadherins. Stem Cell Res. 15, 618–628 (2015).

30. Docheva, D., Popov, C., Alberton, P. & Aszodi, A. Integrin signaling in skeletal development and function. *Birth Defects Res. C. Embryo Today* **102**, 13–36 (2014).

31. Saito, M. & Marumo, K. Effects of Collagen Crosslinking on Bone Material Properties in Health and Disease. *Calcif. Tissue Int*. **97**, 242–261 (2015).

32. Wu, J. et al. Mmu_circ_003795 regulates osteoblast differentiation and mineralization in MC3T3-E1 and MDPC23 by targeting COL15A1. *Mol. Med. Rep*. **22**, 1737–1746 (2020).

33. Liang, H. P. H., Xu, J., Xue, M. & Jackson, C. Matrix metalloproteinases in bone development and pathology: current knowledge and potential clinical utility. *Met. Med.* Volume **3**, 93–102 (2016).

34. Sasano, Y. et al. Gene expression of MMP8 and MMP13 during embryonic development of bone and cartilage in the rat mandible and hind limb. *J. Histochem. Cytochem. Off. J. Histochem. Soc*. **50**, 325–332 (2002).

35. Bord, S., Horner, A., Hembry, R. M. & Compston, J. E. Stromelysin-1 (MMP-3) and stromelysin-2 (MMP-10) expression in developing human bone: potential roles in skeletal development. *Bone* **23**, 7–12 (1998).

36. Ortega, N., Behonick, D. J. & Werb, Z. Matrix remodeling during endochondral ossification. *Trends Cell Biol.* **14**, 86–93 (2004).

37. Reyes, R. et al. Combined sustained release of BMP2 and MMP10 accelerates bone formation and mineralization of calvaria critical size defect in mice. *Drug Deliv*. **25**, 750–756 (2018).

38. Lanzillotti, C. et al. Long Non-coding RNAs and MicroRNAs Interplay in Osteogenic Differentiation of Mesenchymal Stem Cells. *Front. cell Dev. Biol*. **9**, 646032 (2021).

39. Mazziotta, C. et al. MicroRNAs Modulate Signaling Pathways in Osteogenic Differentiation of Mesenchymal Stem Cells. *Int. J. Mol. Sci*. **22**, (2021).

40. Martini, F. et al. Bone Morphogenetic Protein-2 Signaling in the Osteogenic Differentiation of Human Bone Marrow Mesenchymal Stem Cells Induced by Pulsed Electromagnetic Fields. *Int. J. Mol. Sci*. **21**, (2020).

41. Iaquinta, M. R. et al. The role of microRNAs in the osteogenic and chondrogenic differentiation of mesenchymal stem cells and bone pathologies. *Theranostics* **11**, 6573–6591 (2021).

42. Hojo, H. et al. Gli1 protein participates in Hedgehog-mediated specification of osteoblast lineage during endochondral ossification. *J. Biol. Chem*. **287**, 17860–17869 (2012).

43. Larsen, K. H., Frederiksen, C. M., Burns, J. S., Abdallah, B. M. & Kassem, M. Identifying a molecular phenotype for bone marrow stromal cells with in vivo bone-forming capacity. *J. bone Miner. Res. Off. J. Am. Soc. Bone Miner. Res.* **25**, 796–808 (2010).

44. Meng, B. et al. Interleukin-20 differentially regulates bone mesenchymal stem cell activities in RANKL-induced osteoclastogenesis through the OPG/RANKL/RANK axis and the NF-κB, MAPK and AKT signalling pathways. Scand. J. *Immunol*. **91**, e12874 (2020).

4.2.3. Strontium-doped apatitic bone cement for local treatment of bone metastasis

This work was supported by the *Italian Ministry of Health* in *Progetto Nazionale Finalizzato - GR-2016-02364704*, BIOBOS: “*An in vitro and ex vivo model of biomimetic regenerative devices to treat bone metastases and soft tissue tumors*” and by *Progetto POR-FESR 2014-2020 - PG/2018/632022*, DINAMICA: *“Development and validation of nanostructured medicated biomaterials for the treatment and regeneration of metastatic bone tissue*”.

BIOBOS and DINAMICA Projects aimed to develop new ideas for future technologies. Specifically, they aimed to create a therapeutic approach based on bio-inspired materials that have regenerative abilities. These materials would be combined with antitumor and bone-targeted agents/anti-inflammatory drugs and applied as grafts to heal and regenerate cancerous bones while inhibiting cancer cell growth. This revolutionary strategy couples the standard pharmacological treatment to an innovative approach of regenerative medicine aimed to restore of healthy tissues in different setting of patients. The implementation of medicated biomaterials specifically developed to heal and regenerate bone lesions will represent an important integrated treatment in the multidisciplinary approach of these patients.

Injectable bone cements were developed in this work by using calcium-phosphates powder mixed with natural polymers (CPC). Pastes were equipped with a bone-targeted molecule, Denosumab (Den), that inhibits bone resorption or anticancer drugs such as Doxorubicin (Dox) or Everolimus (Ev). The purpose of these projects was to create medicated implants that promote the regeneration of the bone matrix while locally targeting the disease.

To create the cement, powders of solid precursor Sr-doped α-tricalcium phosphate ($\alpha(Sr,Ca)_3(PO4)_2$: Sr-αTCP) were synthesized. Strontium was selected as the doping ion due to its capability to affect osteoblast and osteoclast cells activity, by stimulating the bone formation and reduce the bone resorption.

This study optimized the preparation of drug-loaded bone cement based on hydroxyapatite nanoparticles doped with carbonate ions and stabilized with citrate as a drug carrier for Dox and Den. Both Dox and Den were incorporated into the cement by mixing the powder precursor with Dox-loaded hydroxyapatite nanoparticles (Dox/CaPCO) or Den-loaded hydroxyapatite nanoparticles (Den/CaPCO), while Everolimus, a hydrophobic inhibitor of mTOR, was loaded into the bone cement by dissolving Ev in DMSO solution and then mixing it with the cement liquid phase. The adsorption process of Den and Dox onto CaPCO surface was optimized and the release profiles of each drug (Den, Dox, Ev) were investigated under physiological conditions.

Furthermore, a preliminary biologic evaluation was conducted on bone cells, including a Mesenchymal cell line (*MSC*) and Human peripheral blood mononuclear cells (*PBMCs*), as well as a tumour cells (triple-negative breast cancer cell line *MDAMB-231*)

The drug-loaded CPC was subjected to in vitro biologic evaluations, which were conducted by Dr. Laurea Mercatali, Dr. Claudia Cocchi, Dr. Tony Ibrahim and Dr. Alessandro De Vita from *Istituto Romagnolo per lo Studio dei Tumori "Dino Amadori*" IRCCS, Meldola, Italy. .

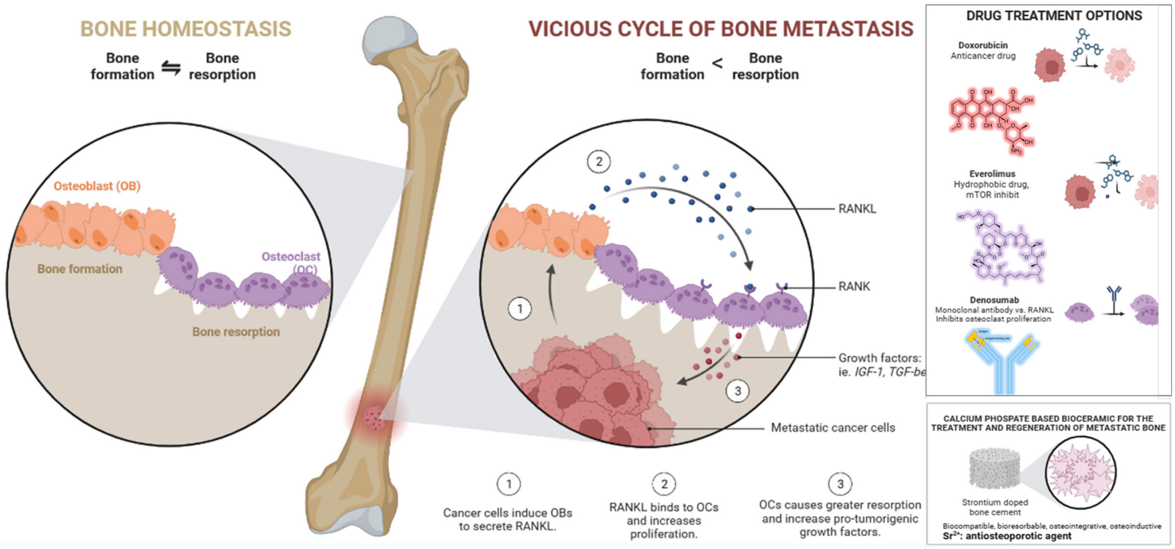

Figure 77. *Comparison between bone homeostasis and the vicious cycle of bone metastasis and the proposed treatment of bone metastasis in BIOBOS and DINAMICA projects.*

Experimental *methods*

Synthesis of hydroxyapatite nanoparticles stabilized with citrate (CaPCO)

Hydroxyapatite nanoparticles stabilized with citrate and doped with carbonated ions (CaPCO) were synthesized by the batch heating crystallization method according to the procedure previous developed[1,2]. Two solutions of i) 0.1 M $CaCl_2$ + 0.4M $Na_3(Cit)$ and ii) 0.12 M of Na_2HPO_4 + 0.2 M Na_2CO_3 were mixed at room temperature and the pH was adjusted to 8.5 with HCl. The obtained nanoparticles are referred to as CaPCO. Citrate anions were used as calcium complexing agent to prepare homogenous metastable solutions. The mixture was than introduced in flask and immersed in a water bath at 80°C for 24h. After the precipitation, the nanoparticles were repeatedly washed with water by centrifugation (10000 rpm for 5 min) and freeze-dried at −60 °C under vacuum (3 mbar) overnight.

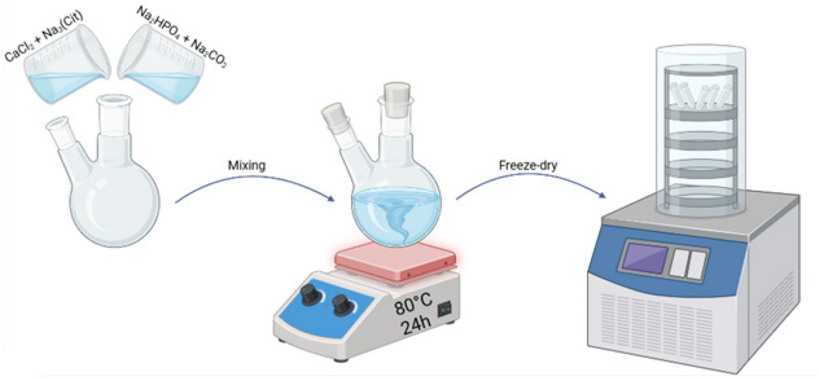

***Figure 78**. Synthesis of carbonated-hydroxyapatite nanoparticles stabilized with citrate.*

Functionalization of CaPCO with denosumab (Den/CaPCO)

Firstly, a 0,5 mg/mL batch of denosumab was prepared through the dilution of Xgeva, an injectable form of Denosumab that has a concentration of 70mg/mL. The adsorption kinetic of Den on CaPCO was determined by mixing 3 mg of nanoparticles with 1 mL of aqueous Den solution (500 µg/mL) and analysed by HPLC method (reported in the section 2.2.9), calibration curve between 1 and 250 µg/mL of Den, R^2=0,98, was construct. The mixtures were incubated at 37 °C for different times, up to a maximum of 24 h. Afterward samples were carefully washed three times with a 0,5 mL of ultrapure water to remove the physically adsorbed drug molecules. The amount of non-adsorbed Den in the supernatant was diluted 1:2 with ultrapure water and measured by HPLC (method reported in section 2.2.9).

Then, the adsorption of increasing amount of Den was also explored (100 and 1000 µg/mL), with the same solid/liquid ratio and temperature used to determine the adsorption kinetic. This protocol was used to determine the optimal incubation time and Den concentration to optimize the drug loading were defined.

Functionalization of CaPCO with doxorubicin (Dox/CaPCO)

The adsorption kinetic of Dox on the CaPCO was determined by mixing 20 mg of nanoparticles with 5 mL of aqueous Dox solution (0,05 and 0,1 mg/mL, LC and HC respectively). The mixtures were incubated at 37 °C for different times, up to a maximum of 24 h. Incubation was done under agitation in the dark since Dox is sensitive to photolytic decomposition. For the study of the adsorption isotherms, 20 mg of apatite were mixed with 5 mL of different concentrations (from 0.03 to 1 mg/mL) of aqueous Dox solutions. Mixtures were then incubated under agitation at 37 °C for 90 min. Drug loaded samples were separated from unbound drug molecules by centrifugation at 10.000 rpm for 5 min. Afterward samples were carefully washed three times with a 2 mL of ultrapure water to remove the physically adsorbed drug molecules. The amount of non-adsorbed Dox in the supernatant was measured by UV-Vis spectroscopy at a wavelength of λ = 480 nm.

In this work was selected nanoparticles with two different drug-loading, namely low concentration (LC) and high concentration (HC), to meet the request in terms of drug release concentration of clinicals.

Preparation of SrCPC containing Dox/CaPCO or Den/CaPCO

The 10% of drug loaded CaPCO (Dox/CaPCO_LC, Dox/CaPCO_HC or Den/CaPCO) respect to the powder precursor were mixed with solid cement phase. The powder and liquid components were mixed using a high-energy planetary shear-mixer (Thinky Mixer ARE-500, Thinky, Japan) at 1000 rpm for 90 seconds. The liquid component of the paste was made of aqueous solutions of (5wt%) disodium hydrogen phosphate dehydrate, and (2wt%) sodium alginate.

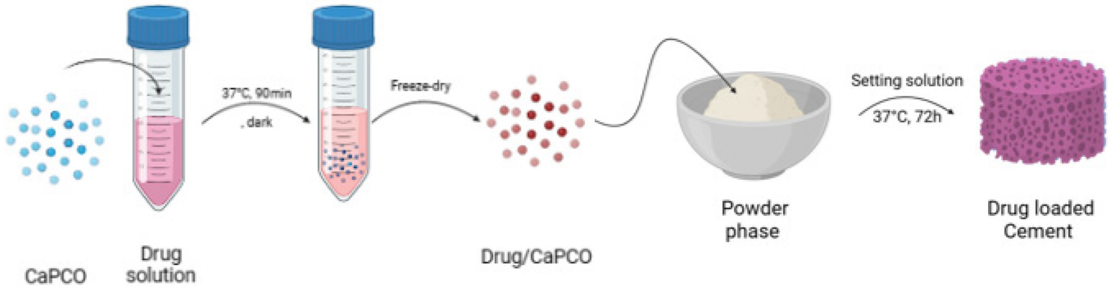

***Figure 79**. Schematic representation of the preparation of drug loaded carbonated- hydroxyapatite nanoparticles (Drug/CaPCO) and cement containing Drug/CaPCO*

Preparation of SrCPC containing Ev

Due to the intrinsic lipophilicity of the drug, a concentrated solution of Everolimus in DMSO was firstly prepared and added to the liquid phase of the cement formulation (aqueous solutions of disodium hydrogen phosphate dihydrate(5 wt%) and sodium alginate (2 wt%)); cements formulation (figure 80) used in this work are listed in the following table:

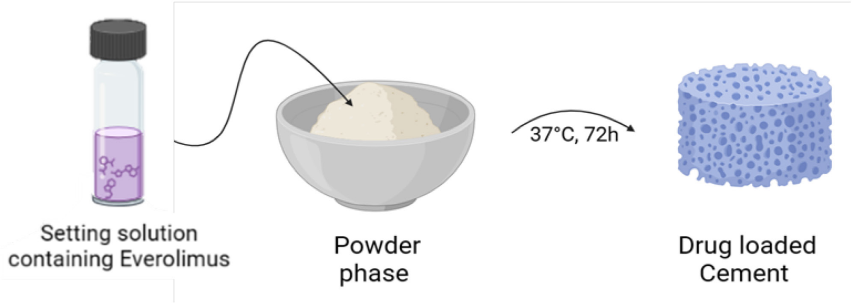

Figure 80. *Preparation of Ev-loaded bone cement.*

Table XXIII*. Cement containing everolimus formulations.*

	SrCPC	SrCPC-Ev_HC
L/P	0.6	0.6
aTCP (g)	2.000	2.000
Setting solution (g)	1.200	1.200
Ev 2 mL/mL (DMSO) (mL)	-	0.033

Drug release

Cement containing Den/CaPCO, Dox/CaPCO or Ev were immersed in 5mL of HEPES buffer solution (0.01M, with KCl 0.01M, pH 7.4), the drug release experiment was optimized based on drug chemical nature.

Denosumab: at each time point 50uL of HEPES solution was collected and renewed with the same volume and analysed by HPLC (see section 2.2.9).

Doxorubicin: at each time point 10% of HEPES solution was collected and renewed with the same volume and analysed by UV-Vis spectrophotometer at 480 nm.

Everolimus: at each time point, the whole solutions were collected, freeze-dried and resolubilized in DMSO solution, in order to better analyse samples by using UV-Vis spectrophotometer at 292 nm (the characteristic peak intensity are higher in DMSO solution than HEPES one).

Biological evaluations

Osteoclasts (OCs) are derived from blood mononuclear cells (PBMCS) following isolation by the Ficoll protocol. The differentiation medium consists of αMEM (Minimum Essential Medium - Alpha MEM Eagle, Lonza), 10% fetal bovine serum (FBS), 1% penicillin/streptomycin, and 1% L-glutamine. The differentiation factors MCSF 20 ng/mL (Macrophage colony-stimulating factor) are added from day 1 to day 7, and MCSF and RANK-L 20 ng/mL are added from day 7 to day 14. Following cell differentiation, fixation of the cells was performed using 4% PFA and staining was undertaken to evaluate the TRAP marker utilising the Acid Phosphatase Leukocyte Procedure kit. For an osteoclast to be considered mature, they must be TRAP positive and possess at least 4 nuclei[3]. The experiment, which had previously been optimised in 2D, was also conducted on SrCPC and SrCPC-drug samples. After fixation, the cells grown on the devices were subjected to staining with TRAP, phalloidin (F-actin), and DAPI before analysing them under a confocal microscope. Real-time PCR was optimized as a secondary detection method to assess the expression of osteoclastogenesis markers (ACP5, RANK, NFATC1, CTSK) at the genetic level.

The optimization of the osteoblastogenesis assay involved refining the differentiation protocol for mesenchymal stem cells in the osteoblastic direction (Merck Millipore) initially in 2D and subsequently on SrCPC. The differentiation medium is congruent with that used for osteoclasts, augmented with differentiation factors, namely dexamethasone at a concentration of 100 nM, β-glycerophosphate at a concentration of 10 mM, and ascorbic acid at a concentration of 200 µM determined through optimization as part of this study. After 14 days, the cells were fixed using 4% PFA and subsequently stained with Alizarin Red dye to detect the deposited matrix. The cells grown on the devices were then stained with osteocalcin, phalloidin (F-actin) and DAPI and viewed with a confocal microscope for analysis. Osteoblastogenesis was evaluated using Real Time PCR to assess gene expression of specific markers (alkaline phosphatase, osteocalcin, and runx2).

The effects of everolimus were assessed on tumour cells, denosumab on monocytes during osteoclastic differentiation, and doxorubicin on all three cell lines. The impact of doxorubicin and everolimus on tumour cells was evaluated using MTT or PrestoBlue assay, whereas the effect of each medication on the bone component was studied through immunofluorescence analysis under a confocal microscopy.

Results and discussion

Physico-chemical features of drug-loaded bone cement

As reported in the section 4.3.1 and 4.3.2, a preliminary set of experiments was carried out to determine the maximum extent of nanoparticles that could be added to SrCPCs without significant variations in setting times and injectability, considering the clinical need of initial setting time of ~15–20 min[4,5]. The addition of 10wt% CaPCO, in respect to Sr-αTCP amount was selected as optimal amount for the preparation of SrCPCs formulations with performance compliant for clinical applications.

The XRD analysis of CaPCO reveals the typical pattern of pure HA (hexagonal, space group P63/m, figure 81a), with marked peak broadening related to the small crystal size according to the synthesis temperature and no other crystalline phases were detected. The SSA of CaPCO was 202.82 m^2/g. The FTIR-ATR spectrum (figure 81b) confirms the vibrational signatures of HA, particularly all vibration modes of PO_4^{3-}, including the characteristic bands for v1, v2, v3 and v4 stretching modes at 963, 472, 1040 and 560–600 cm^{-1}, respectively, were detected[9]. The presence of carbonate ions in the samples was confirmed by the presence of a very weak carbonate band at ca. 870 cm^{-1} and by two weak bands at 1415 and 1455 cm^{-1}, suggesting a B-type carbonate doping (CO_3^{2-}ions substituting PO_4^{3-} ions)[6,7]. B-type carbonate doping was expected because carbonate ions enter the crystal lattice as phosphate substituent when HA is prepared by wet precipitation in presence of CO_3^{2-} ions, whereas A-type carbonate doping (CO_3^{2-} ions substituting OH− ions) is usually favored when HA is thermally reacted in presence of CO_2.[7]

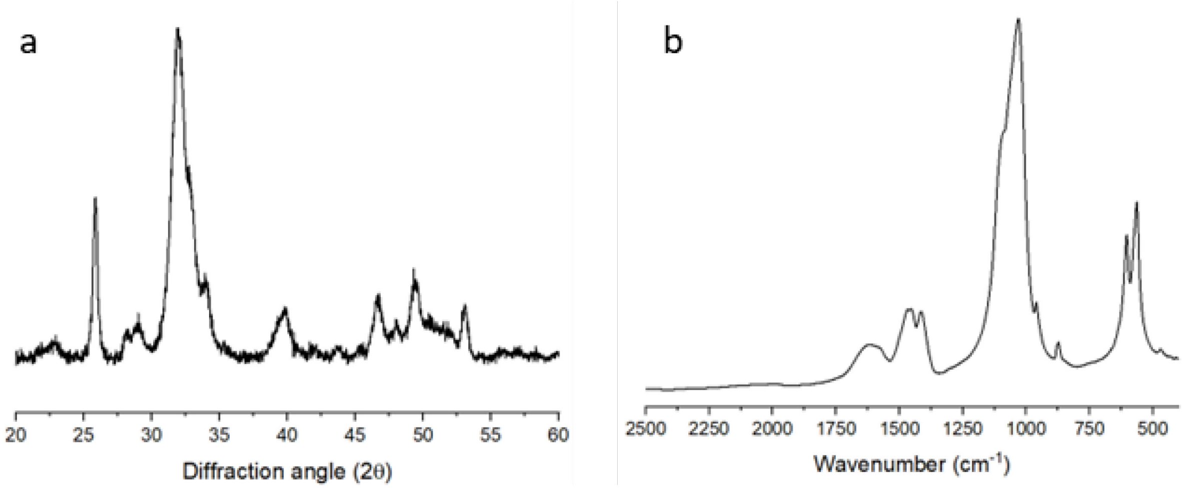

***Figure 81. a)** Diffraction pattern and **b)** ART spectra of CaPCO*

SEM analysis (figure 82) confirms the nano-size and the needle-like morphology of CaPCO, which is consistent with the high SSA value found by BET method.

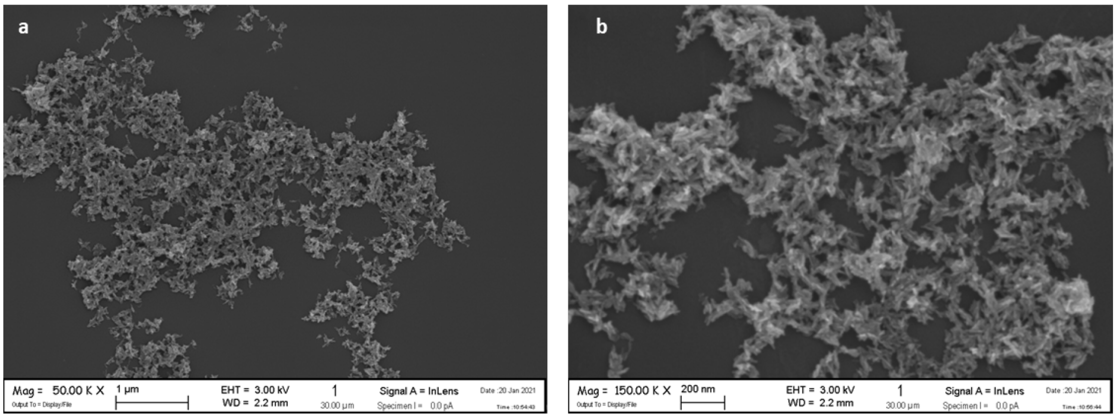

Figure 82. *SEM images of CaPCO. a) scale bar = 1um, b) scale bar 200 nm*

Firstly, the calibration curves of Dox in HEPES acidified with HCl 1 M (pH 2) a (showed in Figure 83a) was constructed by monitoring the optical density of Dox in standard solution ranging from 0,5 and 50 µg/mL, which were prepared by dilution of mother solution (100 µg/mL). Den in ultra-pure water calibration curve (showed in Figure 85a) was constructed by monitoring the optical density of Den in standard solution ranging from 1 and 250 µg/mL by HPLC method (reported in section 2.2.9). While a calibration curves of Ev in DMSO was constructed (Figure 83b) by monitoring the optical density of Ev in standard solution ranging from 0,01 and 20 µg/mL, which were prepared by dilution of mother solution (100 µg/mL).

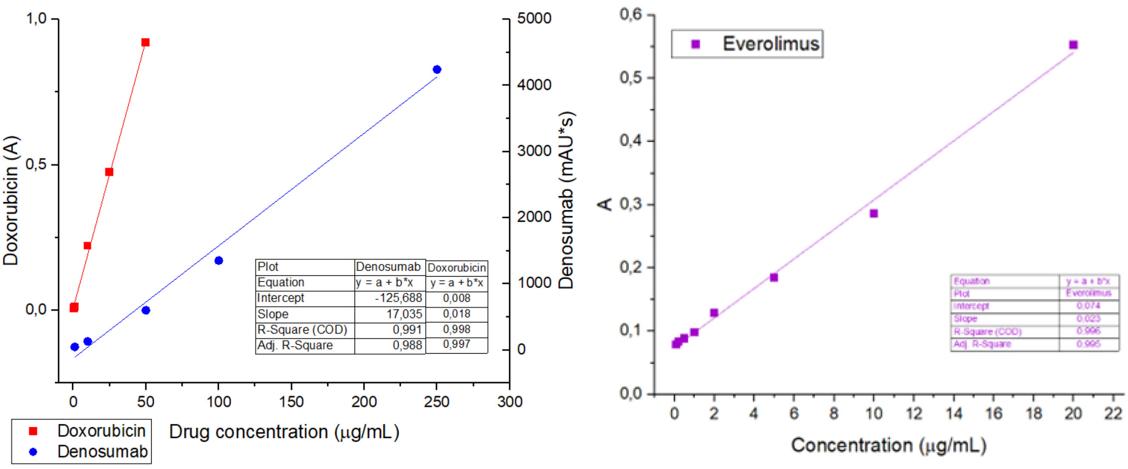

Plot	Denosumab	Doxorubicin
Equation	y = a + b*x	y = a + b*x
Intercept	-125,688	0,008
Slope	17,035	0,018
R-Square (COD)	0,991	0,998
Adj. R-Square	0,988	0,997

Equation	y = a + b*x
Plot	Everolimus
Intercept	0,074
Slope	0,023
R-Square (COD)	0,996
Adj. R-Square	0,995

Figure 83. *Calibration curve of a) Doxorubicin (red line), Denosumab (blue line) and Everolimus (purple line)*

Ev, Den and Dox kinetic release profiles from SrCPC are shown in Figure 84 and the result of the fitting with the mathematical models (Eq. 10) in the tables below (table XXVII).

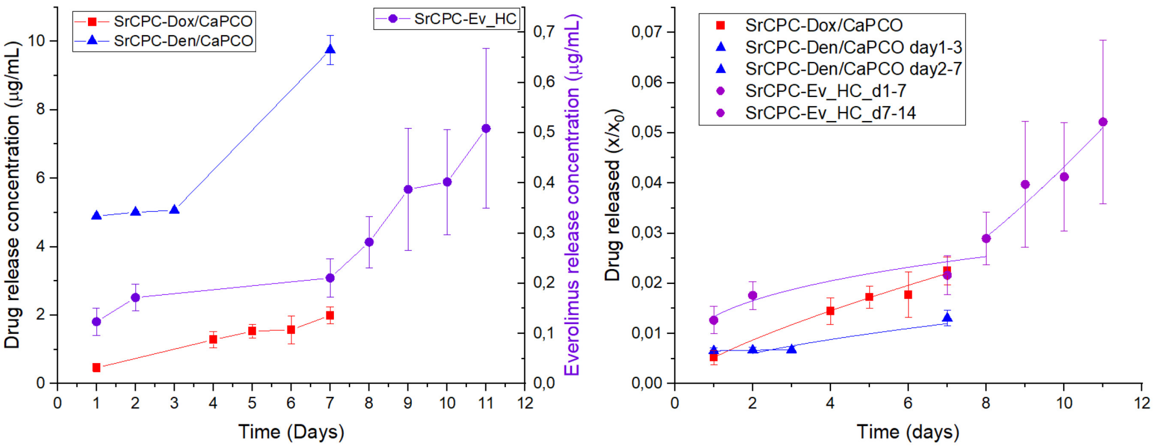

Figure 84. *Kinetic release profiles of doxorubicin from CPC-Dox/CaPCO_LC (red line), SrCPC-Dox/CaPCO_HC (dark red line) and denosumab from CPC-Den/CaPCO (blue line)*

Table XXIV. n *exponent value of Korsmeyer-Peppas model and relative release regime obtained by fitting the release profiles of drugs.*

Samples	Day	*n* value	Release regime	R^2	Drug release (µg/mL)
SrCPC-Den/CaPCO	1-3	0.031 ± 0.001	Hindered Fickian diffusion	0.958	5.1
	2-7	0.549 ± 0.238	Anomalous transport	0.611	-
SrCPC-Dox/CaPCO	1-7	0.739 ± 0.039	Anomalous transport	0.993	1.3
SrCPC-Ev	1-7	0.307 ± 0.083	Hindered Fickian diffusion	0.870	0.2
	7-14	1.752 ± 0.252	Super-case II	0.953	-

The release kinetics of Den shown in a “pseudo-sigmoidal” profile, characterized by a constant release for the first three days and second burst release between day 3 and 7. Therefore, the mechanism of Den kinetic release from SrCPC-Den/CaPCO was analysed by applied twice the KP model. Firstly, the KP model was applied from day 1 to 3, followed by its application from day 2 to day 7. The drug release in the first case was mathematically associated with a process of diffusive regime with hindered release. In contrast, during day 2-7, the drug release was governed by anomalous transport. This variation in release mechanism of Den is most probably due to the molecular size of the antibody (147 kDa) and due to the chemical interaction between HA present in cement formulation and the several functional groups of Den. The release kinetics of Dox from SrCPC-Dox/CaPCO were linked to an anomalous transport mechanism, consisting of a combination of diffusion other phenomena which depend on the porous network.

Ev release shown a sigmoidal profile; hence the mathematical model was applied two times. During the first week, the release mechanism was associated with hindered Fickian diffusion, while during the second week with super-case II. It is probable that the initially hampered release within the initial 7-day period is a consequence of everolimus' hydrophobic nature as well as its interaction with calcium ions. Subsequently, during the second week, non-linear kinetics occur within the super-case II mechanism, whereby the release rate gradually intensifies over time, rather than diminishing. In the field of drug release from monolithic systems, "super-case II" refers to a drug release mechanism that exceeds the traditional case II release (Zeroth order kinetics)[8]. In the transport mechanism of super-case II, drug release from the matrix follows a complex and anomalous kinetics. This release mechanism is affected by several factors, such as the matrix's composition, drug solubility, drug-matrix interactions and the matrix's physical properties. As a result, drug release rates may vary from those predicted by the case II model.

The following figure (Figure 85a) shows the typical microstructure of self-hardening apatitic bone cements featuring elongated interlocking nanocrystals. Comparison between the SEM images shows that the adding of CaPCO nanoparticles (Figure 85b) and the loading with Dox/CaPCO (Figure 85c), Den/CaPCO (Figure 85d) or Ev (Figure 85e) does not affect the structural features of the scaffold.

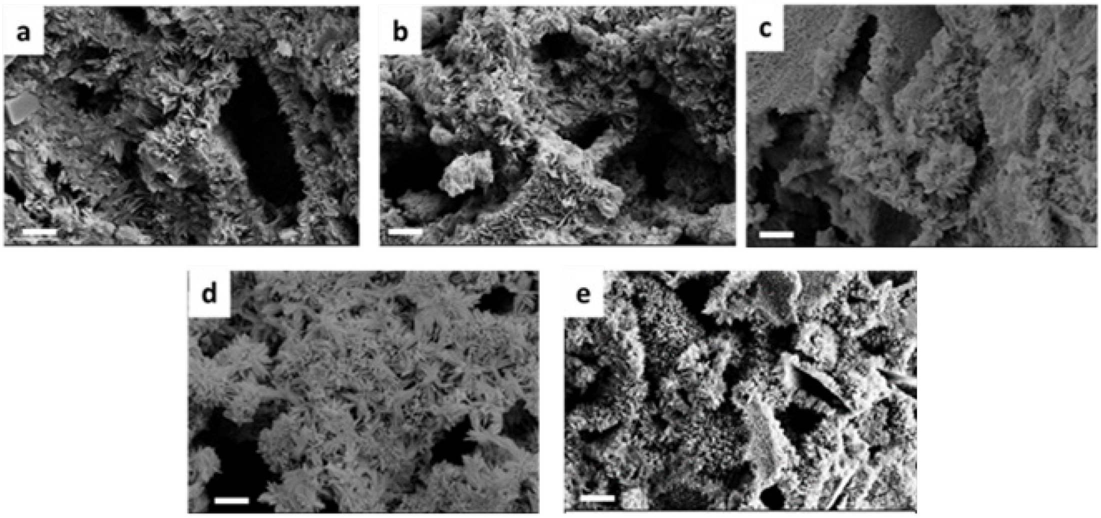

Figure 85. *SEM images of a) SrCPC, b) SrCPC-CaPCO, c) SrCPC-Dox/CaPCO, d) SrCPC-Den/CaPCO and e) SrCPC-Ev; scale bar: 1μm.*

Osteoblastogenesis and osteoclastogenesis on SrCPC.

Osteoblastogenesis differentiation from hMSCs (Merck Millipore) in 2D standard cultured was optimized identifying the correct cell density and the concentration of ascorbic acid to be added to the differentiation medium. To evaluate OBs differentiation, cell morphology was observed at the microscope and Alizarin Red Staining was performed to detect the calcium deposition. After optimization, the experiment parameters were set in 3000 cells/cm^2 and 50 µM of ascorbic acid. Furthermore, the differentiation procedure was shortened from 26 day to 14 days to be homogeneous with timing of osteoclastogenesis differentiation. Then, the obtained parameters were translated and adjusted culturing hMSCs directly on bone cements. 3x10^5 hMSCs were used per cement. OBs and OCs differentiations were analyzed by confocal microscopy.

After 14 days of differentiation, the presence of mature OCs on SrCPC was confirmed by immunofluorescence staining and confocal imaging (Figure 86).

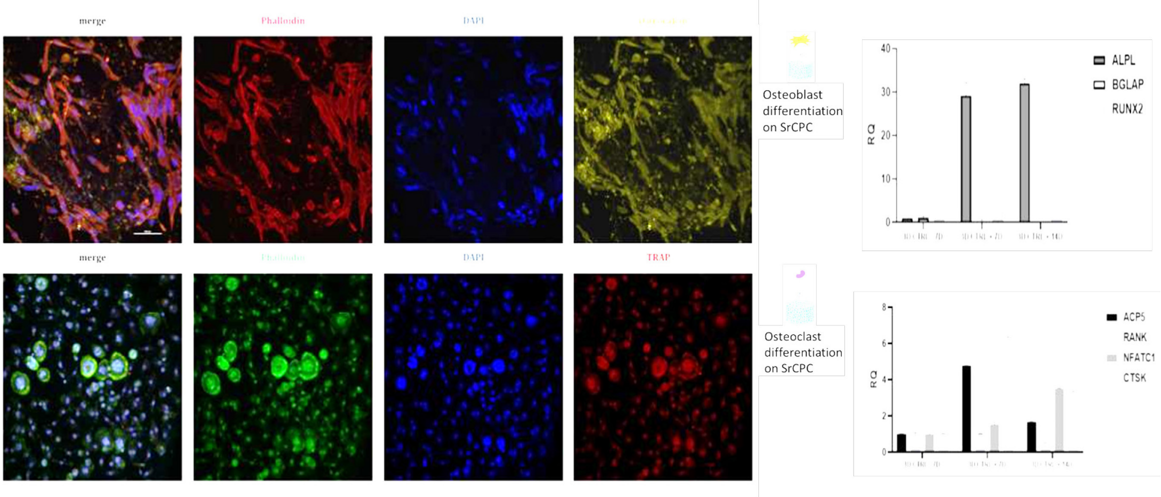

Figure 86. Confocal images of osteoblast and osteoclast differentiations on SrCPC and relative gene expressions

OCs were characterized by the disposition of the cytoskeleton as an acting ring, the presence of 4 or more nuclei and positivity to TRAP marker. OBs changed morphology to become more spindle-like with respect to negative control and were positive for the osteoclastogenesis marker osteocalcin. For all analyzed markers a significant increase over time was observed compared to negative controls.

Assessing the impact of Dox, Den and Ev released from Sr-doped bone cement.

The ability of SrCPC scaffolds factionalized with everolimus (SrCPC-Ev) to contrast bone metastasis was analyzed *in vitro* on *MDAMB-231* cells, up 7 days.

Everolimus released from SrCPC-Ev led to an inhibition of cancer cell proliferation, as shown in Figure 87.

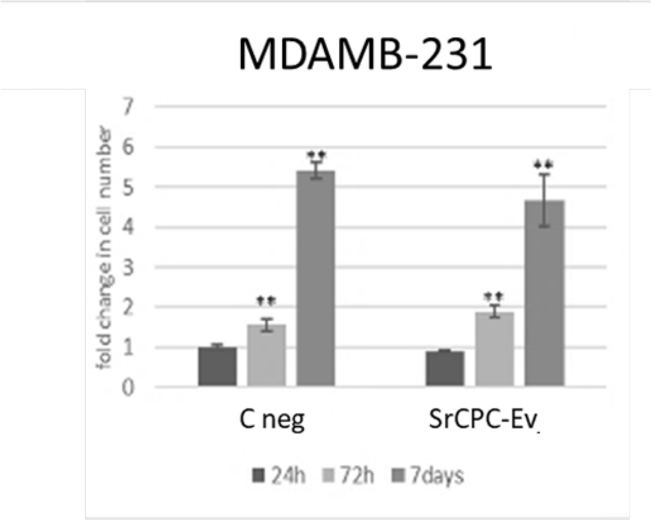

Figure 87*. MDAMB-231 proliferation on negative control and SrCPC-Ev at different time-point.*

The ability of SrCPC scaffolds factionalized with doxorubicin (SrCPC-Dox/CaPCO) was analysed *in vitro* on *MSC, PBMCS* (Figure 88) through immunofluorescence analysis under a confocal microscopy and *MDAMB-231* cells (Figure 89) by MTT assay, up 7 days.

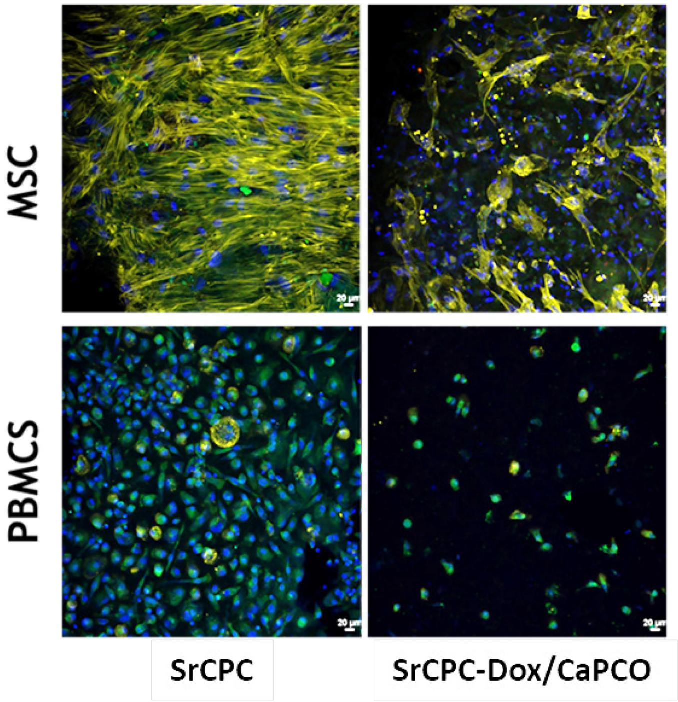

Figure 88. *Confocal images of MSC and PBMCs on SrCPC and SrCPC-Dox/CaPCO after 7 days.*

Figure 89 shown the confocal images of *MSC* and *PMBC* after 7 days of proliferation of SrCPC and SrCPC-Dox/CaPCO after 7 days. As expected, both cell lines well-spread on free-drug cement surface, while a decreasing in cell proliferation was observed for cells grown onto SrCPC-Dox/CaPCO surface.

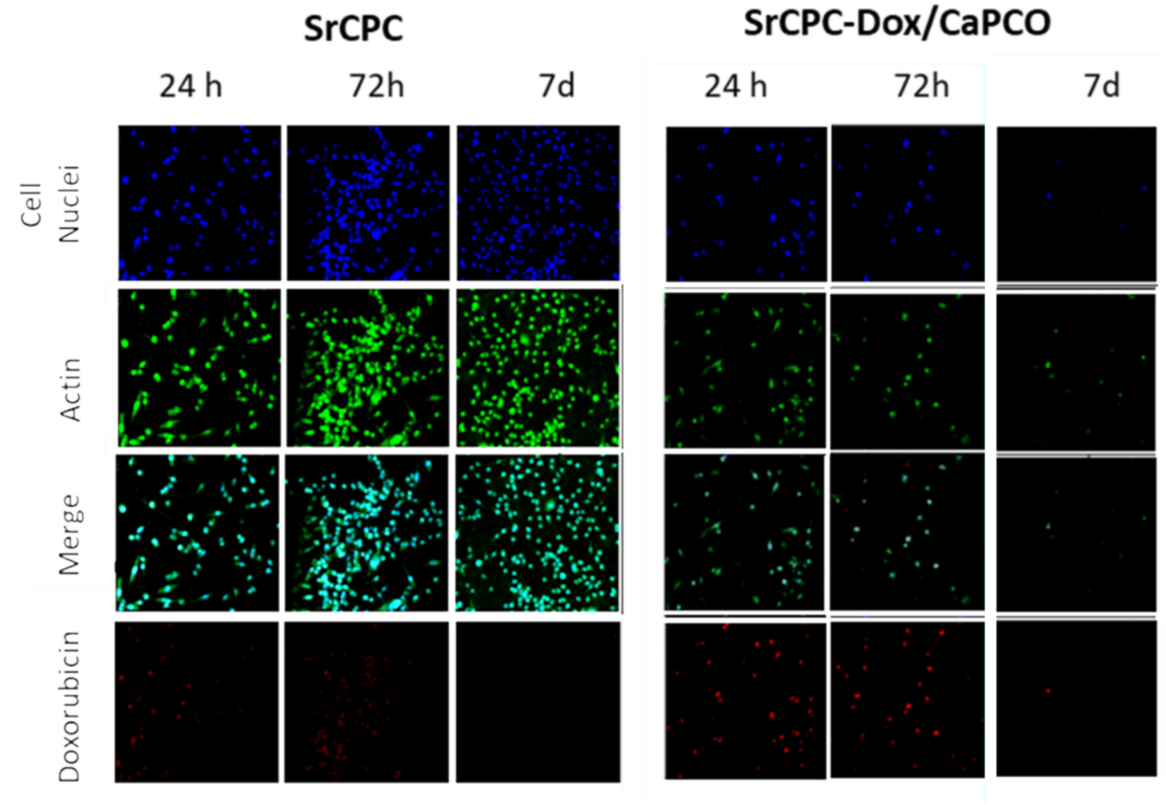

Figure 89*. MTT assay of MDAMB-231 grown on SrCPC and SrCPC-Dox/CaPCO*

A noteworthy reduction in *MDAMB-231* viability is noted merely after 72 hours because of the cytotoxicity of doxorubicin.

The ability of SrCPC scaffolds factionalized with denosumab (SrCPC-Den/CaPCO) to reduce the osteoclast activity was analysed *in vitro PBMC*, up 7 days (Figure 90). The key to the anti-RANKL mechanism is the prevention of bone resorption by limiting the differentiation of mature osteoclasts (the effectors of resorption). The goal is to achieve this inhibitory effect, which is particularly important when treating lytic bone metastases. The experiment involved introducing an anti-RANKL releasing device to the culture after 7 days of differentiation of PBMC cells.

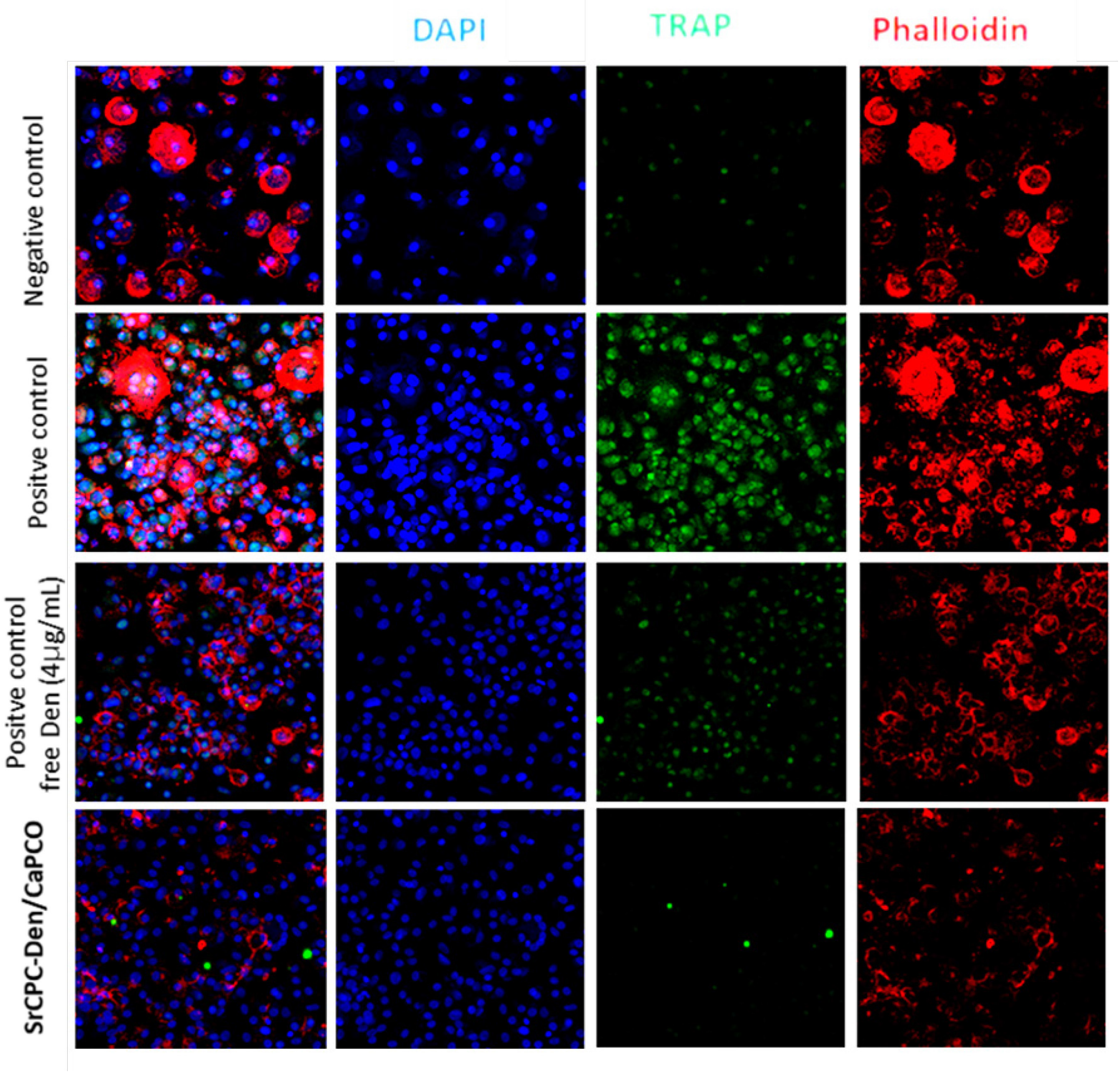

Figure 90. *Confocal images of PBMCs on SrCPC and SrCPC-Den/CaPCO after 7 days.*

The immunofluorescence observations of the cells under the confocal microscope indicated reduced differentiation, as evidenced by reduced TRAP marker positivity and a lower total cell count.

Conclusions

Injectable self-hardening bone cement partially substituted with Sr^{2+} ions and capable of sustained drug release have been developed in this study. Everolimus, a hydrophobic mTOR inhibitor, doxorubicin, a hydrophilic broad-spectrum anticancer drug or denosumab, a monoclonal antibody with anti-RANKL ability, were added to bone cements. The loading methodology was optimized depending on the chemical properties of the drug. For Ev, the process of drug loading entails dilution of the concentrated Ev solution in DMSO solvent, along with the liquid phase of the cement, prior to being mixed with the powder precursor.

On the contrary, drugs such as Dox and Den, which had already been loaded on the surface of carbonated hydroxyapatite (CaPCO) nanoparticles, were loaded into the cement by incorporating 10% drug loaded CaPCO with the solid precursor, before being mixed with the liquid phase. All cement formulations were able to release the drug in clinically relevant doses, as confirmed by the biological evaluation of SrCPC-drug on different cell lines.

The drug release kinetics of each sample were subsequently fitted with the Korsmeyer-Peppas model to comprehend the mechanisms of drug release. In all SrCPC-drug studied in this work, the drug release is governed by mechanisms different from the classical Fickian-diffusion and it is consequence of the combination effect of chemical interactions between drug and the bioactive composition of the matrix, drug size and chemical nature and the pore network of the cement matrix.

In particular, the porosity network that characterizes bone cement may poses obstacle drug molecules to diffuse through the system. The tortuous path of the pores increases the distance that drug molecules must travel, thereby reducing the overall release rate, resulting in a sustained and controlled release profile ensuring sustained therapeutic effect.

REFERENCES

1. Rodríguez-Ruiz, I. et al. PH-responsive delivery of doxorubicin from citrate-apatite nanocrystals with tailored carbonate content. *Langmuir* **29**, 8213–8221 (2013).
2. López-Macipe, A., Gómez-Morales, J. & Rodríguez-Clemente, R. Nanosized hydroxyapatite precipitation from homogeneous calcium/citrate/phosphate solutions using microwave and conventional heating. *Advanced Materials* vol. **10** 49–53 (1998).
3. Mercatali, L. et al. The effect of everolimus in an in vitro model of triple negative breast cancer and osteoclasts. *Int. J. Mol. Sci*. **17**, (2016).
4. Dricssens, F. C. M., Flanell, J. A., Boltong, M. G., Khairoun, I. & Ginebra, M. P. Osteotransductive bone cements. *Proc. Inst. Mech. Eng. Part H J. Eng. Med*. **212**, 427–435 (1998).
5. Bohner, M. Reactivity of calcium phosphate cements. *J. Mater. Chem*. **17**, 3980–3986 (2007).
6. Antonakos, A., Liarokapis, E. & Leventouri, T. Micro-Raman and FTIR studies of synthetic and natural apatites. *Biomaterials* **28**, 3043–3054 (2007).
7. Degli Esposti, L., Adamiano, A., Siliqi, D., Giannini, C. & Iafisco, M. The effect of chemical structure of carboxylate molecules on hydroxyapatite nanoparticles. A structural and morphological study. *Bioact. Mater*. **6**, 2360–2371 (2021).
8. Bruschi, M. L. Mathematical models of drug release. in *Strategies to Modify the Drug Release from Pharmaceutical Systems* 63–86 (Elsevier, 2015). doi:10.1016/B978-0-08-100092-2.00005-9.

4.3. Conclusions and future perspectives

The first part of this Chapter was dedicated to a preliminary study of the hardening process of bone cement, demonstrating that the L/P and the presence of a setting accelerator play a role in the kinetic of the hydrolysis reaction of αTCP into HA.

Instead, the second part reports the results obtained from different research on the development of drug delivery systems based on strontium-doped apatitic bone cement. Depending on the clinical need and the chemistry of different drugs tested (tetracycline, methotrexate, doxorubicin, denosumab, and everolimus), the drug loading approach was optimized. Alldrug-loaded bone cements developed in this work have been shown to release drugs at clinically relevant doses, as demonstrated by *in-vitro* studies, resulting in a very promising scaffold for the local treatment of different bone disorders.

As extensively explained in sections 1.7.2 and 1.7.3., the release kinetics of drugs depend on various factors such as the cement matrix feature, drug feature, physicochemical interaction between drug and carrier and overall experimental condition. Regarding the properties of the cement matrix, the porosity is considered to be one of the most important characteristics influencing the kinetic release of the drug. The setting reaction of apatitic bone cements takes place under in vivo conditions and occurs by dissolution-precipitation mechanism, without variations in temperature and pH, which lead to the formation of a calcium-deficient hydroxyapatite matrix characterized by diffuse microporosity. Strontium-doped apatitic bone cement developed in this work is characterized by nano- and sub-microporosity, with an average porosity degree of about 40% and pore size of 60% ranging from 0.01 to 0.1 µm and 40% from 0.5 to 1 µm, as shown in table XXII in section 4.2.3. This bimodal distribution of pore dimensions may suggest the possibility of obtaining a diffuse and interconnected microporosity, which can create a deviation for drug molecules as they diffuse through the system. The complexity of the microporous network can increase the diffusion path length that drug molecules have to travel, slowing the overall release rate and providing a prolonged therapeutic effect.

Other factors that influence the kinetics of drug release from the bone cement are the solubility of the drug in the medium, the molecular size, and the presence of a functional group that may interact with the bioactive matrix. Furthermore, environmental factors like pH, temperature, and more in general experimental set-up, could impact the drug release. Therefore, any change in these factors can alter the solubility and diffusion characteristics of the drug, ultimately affecting its release kinetics.

Therefore, when drawing these conclusions, it should be noted that the drug loading approach, the total amount of loaded drug as well and some of the experimental setups of release experiments were different depending on the type of drug and the research project[c].

The differences in experimental setup are shown in the following table (Table XXIV):

***Table XXV**. Differences in the experimental setup of drug release experiments.*

Sample	Drug loading amount (ug in 1 sample)	Total volume of HEPES solution (pH 7,4)	% of medium replacement	Time points	Drug release concentration in last time point (ug/mL)
SrCPC-TC and **SrCPC-TC/NPs**	2000	5 mL	100%	1-7-14-21-28-35 day	SrCPC-TC: 71.1 ± 5.2 SrCPC-TC/NPs: 54.7 ± 7.4
SrCPC-MTX and **SrCPC-Dox**	1000	2 mL	100%	6h, 1-2-3-4-7 day	SrCPC-MTX: 48.7 ± 14.2 SrCPC-Dox 5.2 ± 0.4
SrCPC-Dox/CaPCO	500	5 mL	10%	1-4-5-6-7 day	2.0 ± 0.1
SrCPC-Den/CaPCO	2500	5 mL	1%	1-2-3-7 day	9.6 ± 0.4
SrCPC-Ev	50	5 mL	100%	1-2-7-8-9-10-11 days	0.5 ± 0.1

In this research activity, different type of drugs was functionalized into bone cement in different ways depending on their chemical nature and solubility. The release kinetics of each drug were then fitted with the Korsmeyer-Peppas model.

In particular, for the delivery of TC, Dox, and Den, two different types of hydroxyapatite nanoparticles were used. Here, the 10% of drug-loaded nanoparticles were mixed with the solid precursor of bone cement before mixing with the liquid phase. TC was functionalized on hydroxyapatite nanoparticles (NPs) that was prepared by neutralization reaction by

---

[c] Parts of experiment of some research projects were conducted in 2020/2021 during the COVID-19 pandemic.

dropping H_3PO_4 solution into $Ca(CH_3COOH)_2$ one. While Dox or Den was loaded on nanoparticles that was prepared through a one-pot synthesis by mixing a $CaCl_2$ and a Na_2HPO_4 solutions. In this reaction mix were also added $Na_2CO_3 \cdot H_2O$ for enhancing the biocompatibility of the final material and to increase its solubility by inhibiting its crystallization, and $Na_3(C_6H_5O_7) \cdot 2H_2O$ to stabilize the final nanoparticles suspension, namely CaPCO. The obtained NPs and CaPCO were characterized by XRD, ATR, SEM and BET. MTX and Dox were loaded in cement by mixing solid drug into cement powder precursor before mixing with liquid phase. While Ev, due to its hydrophobicity, was loaded by diluting concentrated Ev solution (in DMSO solvent) in the liquid phase before mixing with the powder one.

The following figure (Figure 91) show the mechanism calculated for each cement formulation.

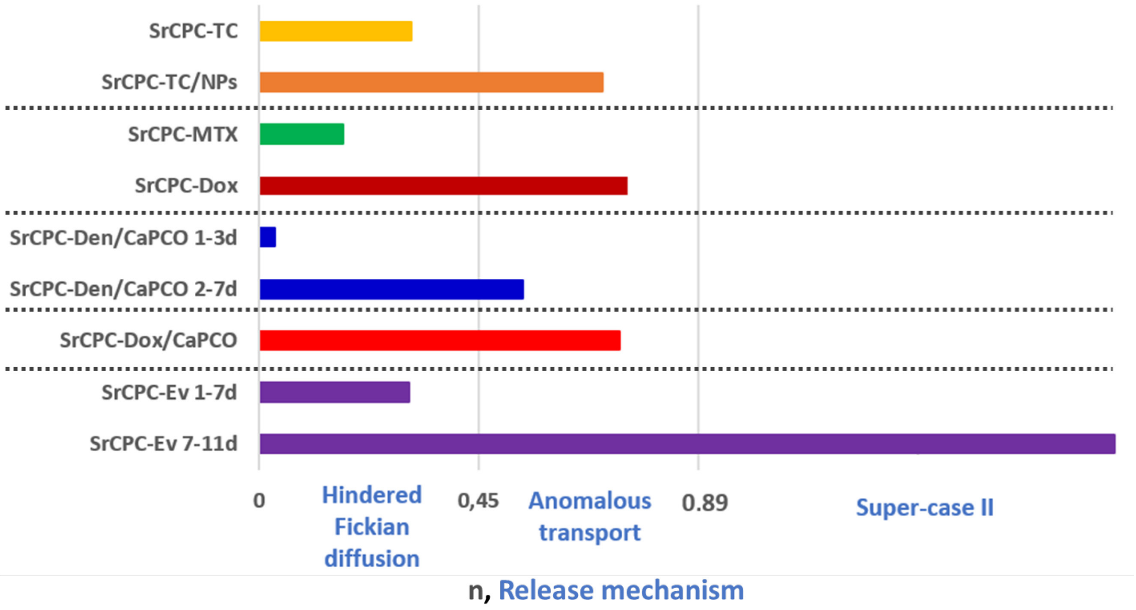

***Figure 91**. Mechanism calculated for each cement formulations.*

Specifically, the *hindered Fickian diffusion* mechanism is representative of system characterized by diffusive regime with hampered release, the *anomalous transport* is characteristic of those case where in addition to diffusion other mechanisms contribute to the drug release (e.g., adsorption/desorption of the drug during the diffusion into the matrix), while *super-case II* mechanism is a drug release mechanism that exceeds the traditional case II release (zeroth order kinetics) and follow a complex kinetics, whereby the release rate gradually intensifies over time, rather than diminishing.

Comparing the release of tetracycline from SrCPC-TC and SrCPC-TC/NPs, it is possible to appreciate how the presence of nanoparticles in the cement formulation allows a more sustained release of the antibiotic over time, modifying its release mechanism. The mechanism changes from hindered Fickian diffusion for the formulation without nanoparticles to anomalous transport in the case of cement containing TC/NPs. The results of this research suggest that the addition of nanocarriers may be an effective approach to the development of tuneable drug delivery bone cement. While the comparison of drug release kinetics from SrCPC-MTX and SrCPC-Dox highlights how the chemical interaction between drug and apatitic nanocrystals play a role in drug release mechanism. Here, the drug loading approach was the same and in the same amount of drugs: MTX shown a faster release with hindered-Fickian diffusion, while Dox a slower release with anomalous transport mechanism. This difference can be ascribed to the different functional groups present in the chemical structure of the drugs and therefore to their affinity, hence the strength of chemical interaction, with hydroxyapatite.

As mentioned above, one of the most important features of the scaffold that affects drug release kinetics is porosity. By varying the overall characteristics of the porosity, such as the degree of porosity, the pore size and the extent and complexity of the pore network, the kinetics and mechanism of drug release can be altered. In this regard, 3D printing is an additive manufacturing method able to produce devices with complex geometry and design. Direct Writing Ink (DWI) is a straightforward manufacturing technique that enables the production of diverse structures ranging from solid monolithic parts to highly complex porous scaffolds. In this context, a preliminary study on the optimization on the ink-based αTCP for DWI applications were carried out at the Universitat Politècnica de la Catalunya during a 45-days stage. Particularly, Sr-αTCP and Mg-doped hydroxyapatite nanoparticles (MgHA) or tetracycline-loaded MgHA (TC/MgHA) were used as powder phase of the inks. As liquid phase was used a sodium alginate solution enriched with carboxymethylcellulosa or pluronic®. MgHA was synthetized by neutralization reaction by mixing $Ca(OH)_2$ and $MgCl_2 \cdot 7H_2O$ with H_3PO_4, then characterized by XRD, ATR, ICP, SEM and BET. After, TC was linked to MgHA nanoparticles by incubating MgHA in a 1mg/mL of TC solution for 2h at 37°C. To prepare TC-loaded magnesium and strontium doped self-hardening inks, liquid and powder phases were mixed using a speed-mixer at 3500 rpm for 2 minutes at different

L/P. A cylindrical model of the scaffolds (10 mm diameter and 4 mm height) was designed using Simplify3D software and converted to 3D scaffold with a rectangular pattern, an infill of 0.50 and 0.35, and different layer height of 0.30 and 0.15 mm. The produced scaffolds were therefore characterized by different porosity. However, as it is still a preliminary research, further studies will be needed to evaluate the kinetic release and mechanism of tetracycline.

The porosity of cement can be tuned basically by modulating the L/P or by adding porogen agents. In this respect, future studies will focus on the development of drug-loaded strontium-doped apatitic bone cements characterised by different porosities by modulating the L/P.

As previously reported, the L/P significantly influences the kinetics of the self-hardening process and thus the rheological properties of the paste. Therefore, a comprehensive study of the rheological properties of these pastes will be carried out with the aim of correlating the physico-chemical characteristics with the rheological behaviour of the pastes, to obtain an accurate modelling of the viscosity and extrudability of drug-loaded self-hardening calcium phosphate pastes and cement, which are also particularly crucial for the application of self-hardening inks in 3D printing.

CHAPTER 5 –BIOMORPHIC SCAFFOLD BASED ON MULTI-ION DOPED HYDROXYAPATITE FOR LOCAL DRUG DELIVERY

This work was supported by *Progetto POR-FESR 2014-2020 - PG/2018/632022, DINAMICA: "Development and validation of nanostructured medicated biomaterials for the treatment and regeneration of metastatic bone tissue*".

This chapter reportsreports on the research activites carried out on the b.Bone™ Bone substitute scaffold, supplied by *Greenbone Ortho S.p.A* as a partner of *DINAMICA Project,* with the aim of to developing it as a drug delivery system for the local administration of everolimus or denosumab to obtain smart material for the treatment of metastatic bone tissue and the regeneration of long-bearing bone.

b.Bone™ Bone substitute is a biomorphic scaffold that is highly biomimetic and biocompatible with natural bone. The scaffold has a compositional structure that mimics the architecture of natural bone and is designed to support bone regeneration. Importantly, b.Bone™ can promote new bone formation, making it a promising solution for complex bone defects. In particular, these scaffolds possess a highly interconnected hierarchical porosity that mimics human bone and are intended to facilitate natural bone healing and optimize bone quality. They additionally promote bone healing by assisting in homing and cell differentiation. Furthermore, b.Bone™ is characterized by nanostructure and bioactive composition (HA and β-TCP with the presence of Mg^{2+} and Sr^{2+}), reflecting the composition of bone. This unique combination of nanostructural characteristics and chemical composition similar to that of human bone allows intercellular communication along the signalling pathway, promoting the progression of bone regeneration[1].

b.Bone™ are produced by biomorphic transformation of natural structure, which consists in a complex multistep process based on heterogeneous chemistry to convert rattan wood into biomimetic multi-ion-doped HA. This scaffold is commonly used in the regeneration of load-bearing bone *in-vivo* and is characterized by hierarchical porosity that mimic the osteon 3D structure[1-4].

In this research activity, drugs release kinetics of everolimus and denosumab from b.Bone™ bone substitute were studied, hereafter referred to as GB. Moreover, to better understand the mechanism of the release of drugs, the Korsmayer-Peppas mathematical model (paragraph 1.7.4., Eq. 10) was applied to the experimental data.

The *in vitro* biological evaluations of drug-loaded CPC were investigated by Dr. Laurea Mercatali, Dr. Claudia Cocchi, Dr. Tony Ibrahim and Dr. Alessandro De Vita from *Istituto Romagnolo per lo Studio dei Tumori "Dino Amadori*" IRCCS, Meldola, Italy.

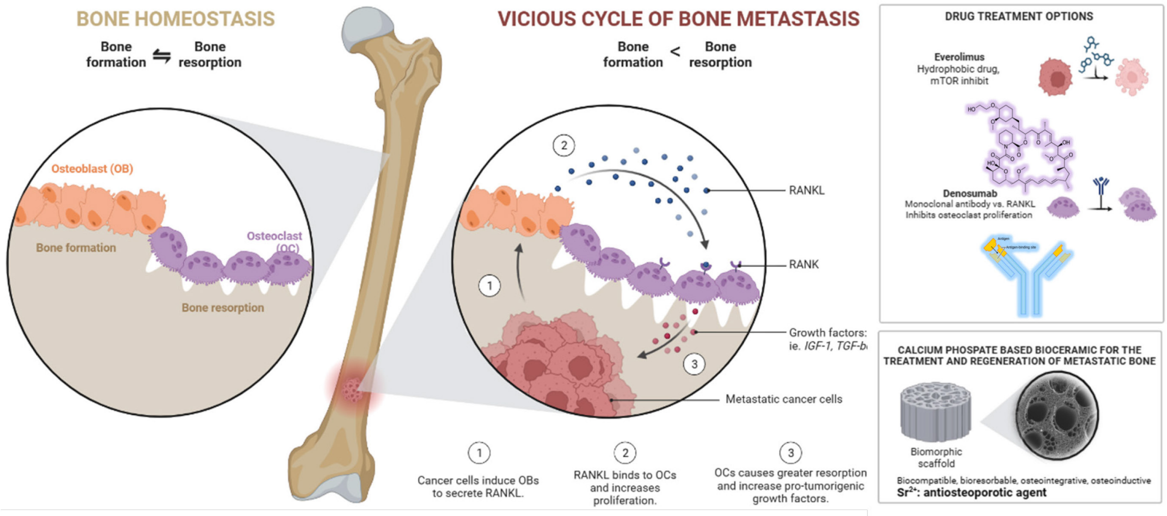

Figure 92. *Comparison between bone homeostasis and the vicious cycle of bone metastasis and the proposed treatment of bone metastasis in DINAMICA projects*

5.1. Experimental methods

5.1.1. Drug loading and release.

Everolimus: the Ev loading was performed by pipetting 5 drops of 20 µL of 200 µg/mL of Ev solution onto the surface of the GB scaffolds to load 20 µg of drug (hereafter referred to as GB-Ev). Calibration curve was reported in Figure 83 in section 4.2.3.

Everolimus release experiment was conducted after the DMSO evaporation (2h, RT in solvent hood). GB-Ev samples were immersed in 5 mL of HEPES solution (0.01M, with KCl 0.01M, pH 7.4) in thermostatic stirrer in dark condition at 37°C up to 14 days. At each time-point, the whole volume of HEPES solution were collected and lyophilized O/N. The lyophilized samples were than dissolved in 0,5 mL of DMSO solution and spectrophotometrically analysed by monitoring the optical density of Ev at 277 nm.

Denosumab: firstly, a 10 mg/mL batch was prepared through the dilution of Xgeva, an injectable form of Denosumab that has a concentration of 70mg/mL. Then, denosumab loading was performed by pipetting 2 drops of 25 µL of 10 mg/mL of Den solution onto the surface of the GB scaffolds to load 500 µg of Den (hereafter referred to as GB-Den). Calibration curve was reported in Figure 83 in section 4.2.3.

Denosumab release experiment was conducted after water evaporation (2h, RT in solvent hood). GB-Den samples were immersed in 5 mL of HEPES solution (0,01 M with KCl 0,01 M, pH 7,4) in thermostatic stirrer in dark condition at 37°C up 7 days. At each time point 50 µL of HEPES solution was collected and renewed with the same volume and analysed by HPLC (see section 2.2.9).

Drug loading and release approach is schematized in the following figure (Figure 93).

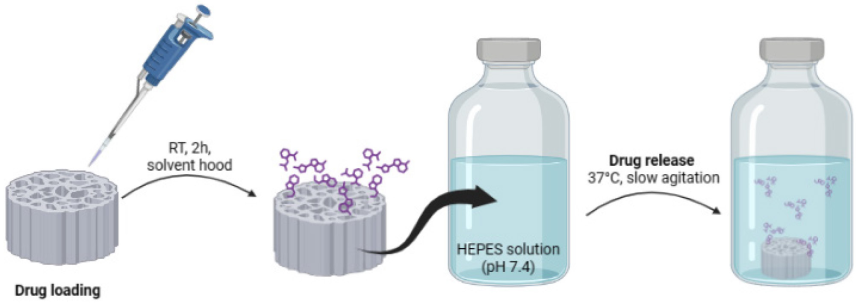

Figure 93. *Schematic representations of everolimus loading biomorphic scaffold approach and drug release experiment.*

5.1.2. Biological evaluations

The biological effect of GB, GB-Ev and GB-Den were evaluated on *MSC* (mesenchymal cells) and *PBMCs* (human peripheral blood mononuclear cells) in osteoblastic and osteoclastic differentiation respectively, and on three different tumoral cell lines: *MDAMB-231* (triple-negative human breast adenocarcinoma cells) *, MFC7* (human breast cancer cell with estrogen, progesterone and glucocorticoid receptor) *and Caki-2* (human clear cell renal cell carcinoma).

Osteoclasts (OCs) are derived from blood mononuclear cells (PBMCS) following isolation by the Ficoll protocol. The differentiation medium consists of αMEM (Minimum Essential Medium - Alpha MEM Eagle, Lonza), 10% fetal bovine serum (FBS), 1% penicillin/streptomycin, and 1% L-glutamine. The differentiation factors MCSF 20 ng/mL (Macrophage colony-stimulating factor) are added from day 1 to day 7, and MCSF and RANK-L 20 ng/mL are added from day 7 to day 14. Following cell differentiation, fixation of the cells was performed using 4% PFA and staining was undertaken to evaluate the TRAP marker utilizing the Acid Phosphatase Leukocyte Procedure kit. For an osteoclast to be considered mature, they must be TRAP positive and possess at least 4 nuclei[3]. The experiment, which had previously been optimized in 2D, was also conducted on GB and GB-drug samples. After fixation, the cells grown on the devices were subjected to staining with TRAP, phalloidin (F-actin), and DAPI before analysing them under a confocal microscope. Real-time PCR was optimized as a secondary detection method to assess the expression of osteoclastogenesis markers (ACP5, RANK, NFATC1, CTSK) at the genetic level.

The optimization of the osteoblastogenesis assay involved refining the differentiation protocol for mesenchymal stem cells in the osteoblastic direction (Merck Millipore) initially in 2D and subsequently on GB. The differentiation medium is congruent with that used for osteoclasts, augmented with differentiation factors, namely dexamethasone at a concentration of 100 nM, β-glycerophosphate at a concentration of 10 mM, and ascorbic acid at a concentration of 200 µM determined through optimization as part of this study. After 14 days, the cells were fixed using 4% PFA and subsequently stained with Alizarin Red dye to detect the deposited matrix. The cells grown on the devices were then stained with osteocalcin, phalloidin (F-actin) and DAPI and viewed with a confocal microscope for analysis. Osteoblastogenesis was evaluated using Real Time PCR to assess gene expression of specific markers (alkaline phosphatase, osteocalcin, and runx2).

The effects of everolimus were assessed on three-lines of tumor cells and denosumab coculture of MCS and PBMC during osteoclastic differentiation. The impact of everolimus on tumor cells was evaluated using PrestoBlue assay, whereas the effect of denosumab on the bone components was studied through immunofluorescence analysis under a confocal microscopy.

5.2. Results and discussion

5.2.1. Physico-chemical features of drug-loaded biomorphic scaffold

XRD analysis of the biomorphic scaffold (Figure 94a) indicates the presence of HA (hexagonal, space group P63/m) with distinct and narrow peaks, indicating the high crystallinity of HA in the biomorphic scaffold due to the biomorphic transformation process. Additionally, a trace amount of β-TCP (rhombohedral, space group R3c) was detected. The FTIR-ATR spectrum (figure 94b) confirms the vibrational signatures of HA, particularly all vibration modes of PO_4^{3-}, including the characteristic bands for ν1, ν2, ν3, and v4 stretching modes at 963, 472, 1040, and 560–600 cm^{-1}, respectively, were detected[5].

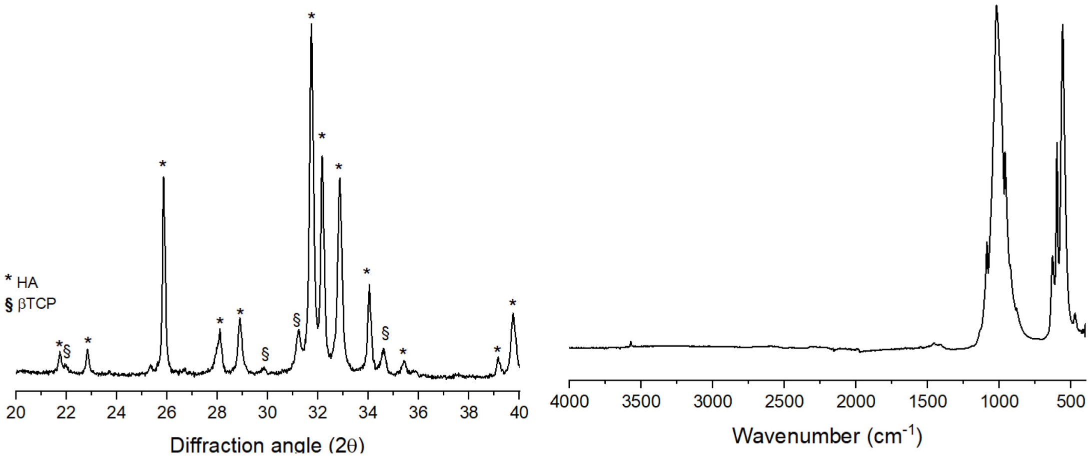

Figure 94. a) Diffraction profiles and b) ATR spectra of biomorphic scaffolds.

Table XXIV lists the physical characteristics of a biomorphic scaffold (provided by the company *Greenbone Ortho s.r.l.*): Young's modulus, porosity, and pore size.

Table XXVI. *Physical features of biomorphic scaffold (GB): Young's modulus, porosity and pore size*

	Young's modulus	Porosity	Pore size
Biomorphic scaffold	1.011 ± 0.4 GPa	60 ± 5%	0.01-600 nm

SEM micrographs, at two different scale bars: 100 and 10 μm (Figure 95a,b respectively), show the typical microstructure of a biomorphic scaffold, showing the hierarchical pore network with canicular pore distribution.

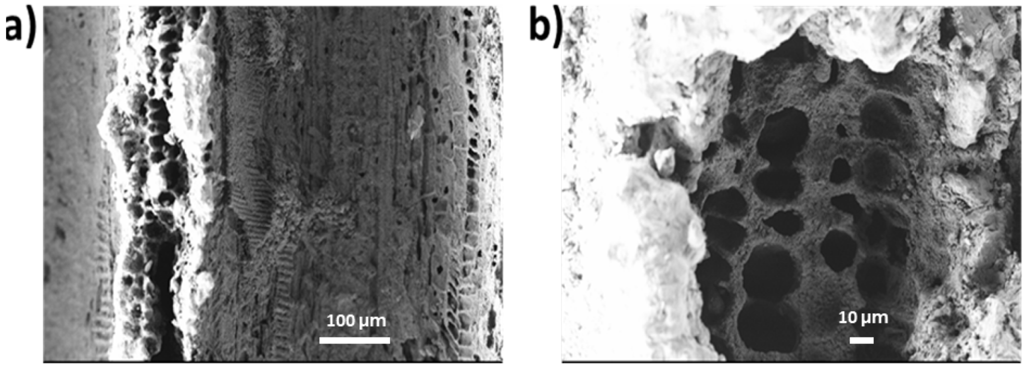

Figure 95. SEM images of biomorphic scaffolds a) scale bar 100 µm, b) scale bar 10 µm.

The elemental analysis, presented in Table XXV, indicates the existence of magnesium and strontium ions, in levels comparable to the biogenic multi-ion doped HA (natural bone).

Table XXVII. *Elemental composition of biomorphic scaffold.*

	${Ca + Mg + Sr}/{P}$	**Mg (mol%)**	**Sr (mol%)**
Biomorphic scaffold	1.55 ± 0.01	2.28 ± 0.41	0.82 ± 0.16

The drug release profile of GB-Ev and GB-Den scaffolds was performed for up to 14 days for Ev and 7 days for Den and fitted with the Korsmeyer-Peppas model (Eq. 10)

The calibration curves of Ev and Den were reported in Figure 83, section 4.2.3.

Den and Ev kinetic release profiles from the biomorphic scaffold are shown in Figure 96 and the result of the fitting of experimental data with the mathematical model in the tables below (table XXVII).

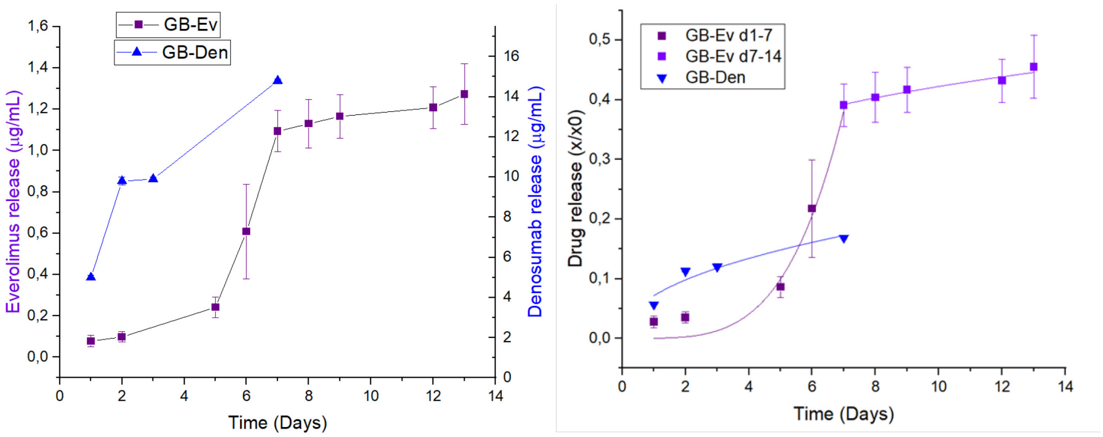

Figure 96*. Kinetic release profiles of everolimus (purple line) and denosumab (blue line) from biomorphic scaffolds.*

Table XXVIII. n *exponent value of the Korsmeyer-Peppas model and relative release regime obtained by fitting the Everolimus release profiles.*

Sample	**Day**	***n* value**	**Release regime**	R^2	**Drug release at day 2 (µg/mL)**
GB-Den	1-7	0.452 ± 0.096	Fickian diffusion (first-order kinetics)	0.926	9.6
GB-Ev	1-7	4.001 ± 1.502	Super-case II	0.801	0.09
	7-14	0.207 ± 0.029	Hindered Fickian diffusion	0.944	-

The release kinetics of Den follow a classical Fickian diffusion mechanism, resulting in a first-order kinetics. This mechanism is therefore characterized by a slow release of the drug over time. The antibody hence diffuses from the scaffold surface in a controlled manner, resulting in a predictable release profile.

Ev release showed a sigmoidal profile; hence the mathematical model was applied two times. During the first week, the release mechanism was associated with the Super-case II mechanism, whereby the release rate gradually intensifies over time, rather than diminishing. Here, it could be associated with the existence of Ev concentration gradients on the scaffold surface. Subsequently, during the second week, a hindered Fickian diffusion was calculated. It is probable that the hampered release is a consequence of the hydrophobicity of Ev.

5.2.2. Osteoblastogenesis and osteoclastogenesis on biomorphic scaffold.

Osteoblastogenesis differentiation from hMSCs (Merck Millipore) in 2D standard cultured was optimized as reported in section 4.2.3. Then, the obtained parameters were translated and adjusted culturing hMSCs directly on the biomorphic scaffold surface. 5x10^4 hMSCs were used per biomorphic scaffold. OBs and OCs differentiations were analyzed by confocal microscopy. After 14 days of differentiation, the presence of mature OCs on GB was confirmed by immunofluorescence staining and confocal imaging (Figure 97).

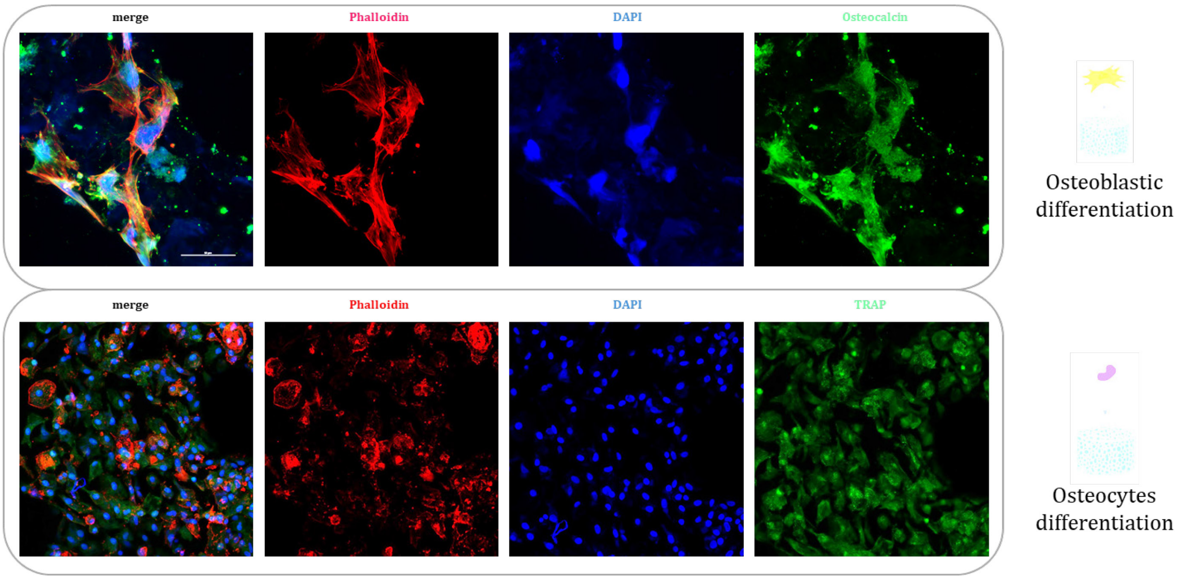

***Figure 97**. Confocal images of osteoblast and osteoclast differentiation on GB.*

OCs were characterized by the disposition of the cytoskeleton as an acting ring, the presence of 4 or more nuclei, and positivity to the TRAP marker, while OBs were positive for the osteoclastogenesis marker osteocalcin. Moreover, OB and OC differentiation was confirmed also by gene expression analysis of early and late markers of osteoblastogenesis and osteoclastogenesis (Figure 98).

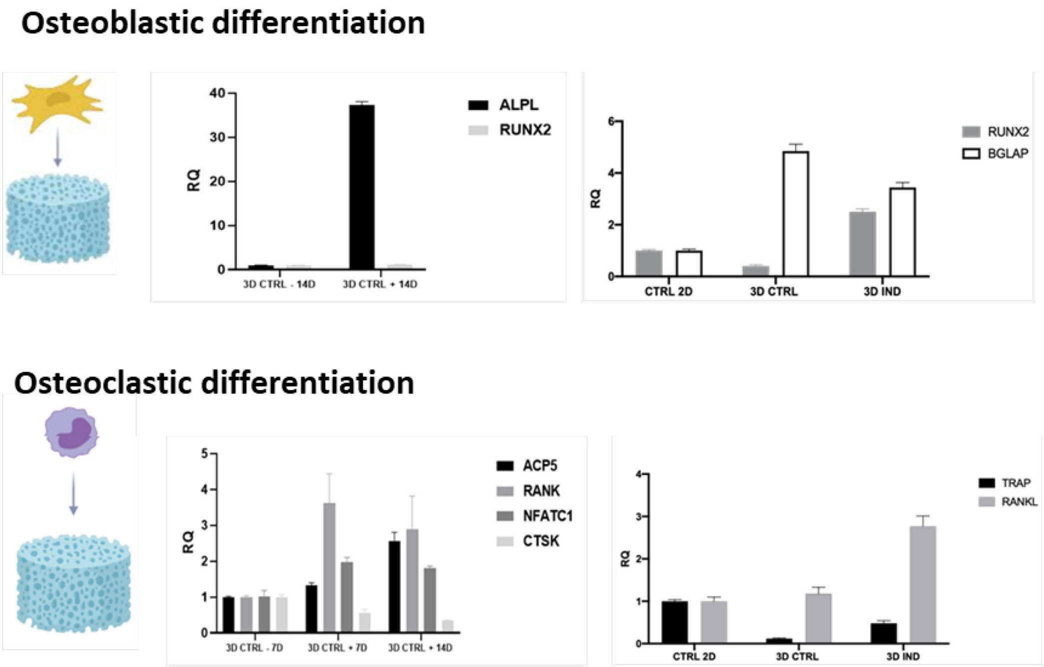

***Figure 98**. Gene expression of osteoblastogenesis and osteoclastogenesis on biomorphic scaffold surface*

These results confirm the high biocompatibility of biomorphic scaffold, supporting both osteoblast and osteoclast differentiation.

5.2.3. Assessing the impact of Dox, Den, and Ev released from the biomorphic scaffold.

The ability of biomorphic scaffolds factionalized with everolimus (GB-Ev) to contrast bone metastasis was analyzed *in vitro* on *Caki-2, MCF7,* and *MDAMB-23*1 cells, up 7 days, as shown in Figure 99.

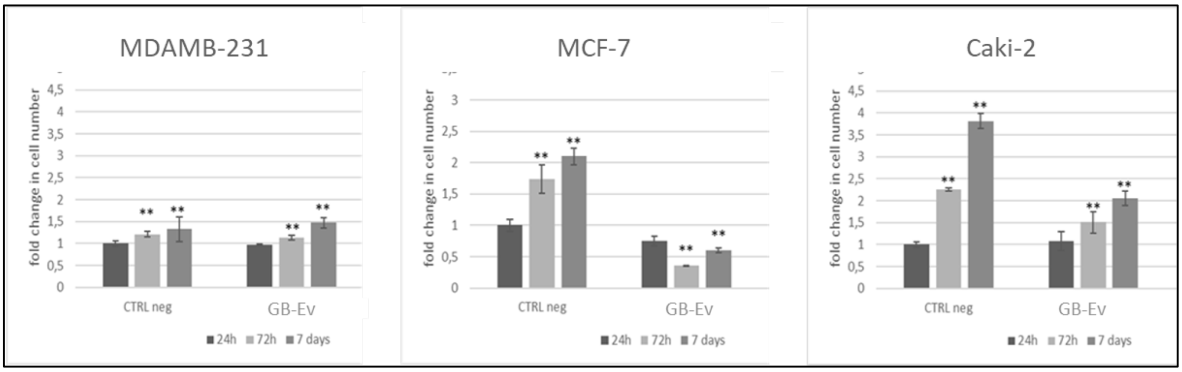

***Figure 99**. MDAMB-231 proliferation on negative control and SrCPC-Ev at different time points.*

The MTT test indicates inhibition of cell proliferation in both Caki-2 and MCF-7 cell lines.

However, the effects of the drug were not appreciated in the case of the triple-negative breast cancer cell line MDAMB-231.

Moreover, GB-Den, as well as GB-Ev, were tested in a co-culture experiment in which both *MSC* and *PBMCs* cell lines were seeded onto the scaffold surface and analyzed by immunofluorescence assay after 7 days of differentiation (Figure 100). As previously mentioned, the key to the anti-RANKL mechanism is the prevention of bone resorption by limiting the differentiation of mature osteoclasts. The goal is to achieve this inhibitory effect, which is particularly important when treating lytic bone metastases.

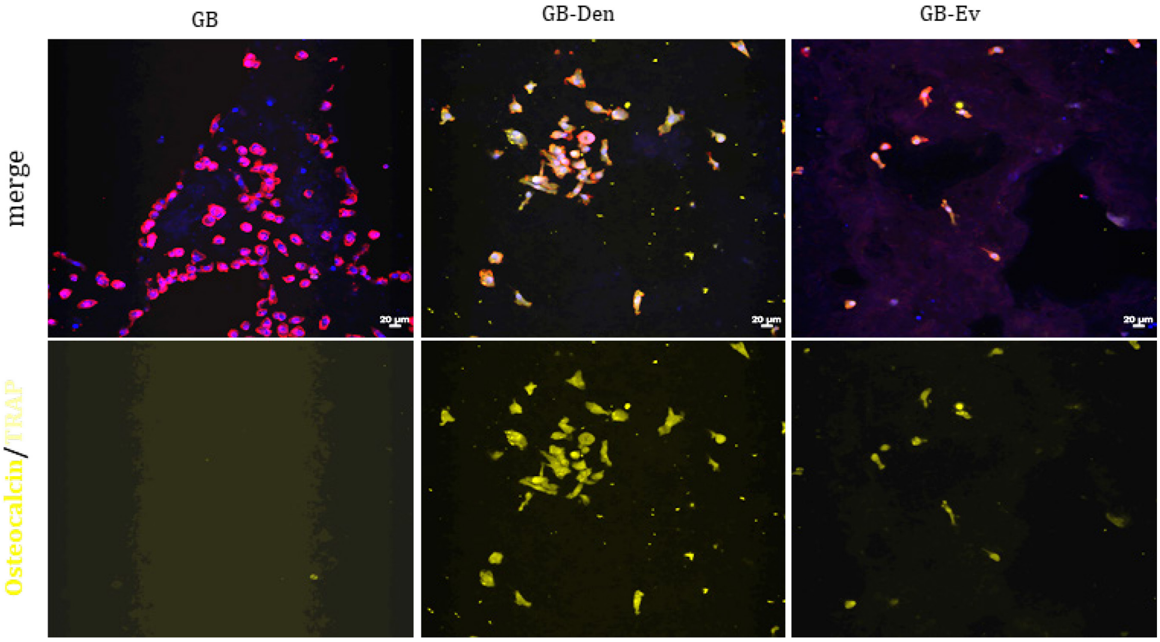

Figure 100. *Confocal images of MSC and PBMCs co-culture on GB, GB-Den, and GB-Ev after 7 days.*

The immunofluorescence observations of the cells under the confocal microscope indicated reduced differentiation, as evidenced by reduced TRAP marker positivity and a lower total cell count. In particular, a reduction in the number of osteoclasts is observed during denosumab treatment and a decrease in cell number occurred after treatment with everolimus. During the experiment, we encountered issues with the scaffold control. As illustrated in Figure 99, no Osteocalcin/TRAP markers were detected. Consequently, further analysis is required to assess the effectiveness of the control scaffold in coculture. Nevertheless, this scaffold is currently utilized as a bone substitute in clinical practice, and its biocompatibility and osteogenic activity have been extensively researched[1-3].

5.3. Conclusions

This study aimed to investigate the efficacy of biomorphic scaffolds as delivery platforms for Everolimus, a hydrophobic mTOR inhibitor, and Denosumab, a monoclonal anti-RANKL antibody. Alongside its established biomimicry and biocompatibility, biomorphic scaffolds possess the capacity to control the delivery of a wide range of molecules, promoting bone regeneration and the efficient on-site therapy of bone metastases.

The biomorphic scaffolds are endowed with a hierarchical porosity that mimics the 3D architecture of osteons, as well as a bioactive composition and a nanostructure. These features allow for surface functionalization and long-term drug release. In particular, the antibody is released from the scaffold surface with first-order kinetics, indicating that the bioactive apatitic surface interacts with the various functional groups of the antibody chemical structure, enabling a diffusive release mechanism. In contrast, the hydrophobic anticancer drug (Ev) in the initial 7-day period follow an exponential trend. This is attributable to the drug's hydrophobicity, its interaction with the scaffold's bioactive surface, and the presence of a gradient Ev concentration on the scaffold surface.

The hierarchical pore structure can also have a significant effect on drug release, influencing diffusion pathways, surface area, and loading capacity. This allows for precise control over drug release kinetics. A hierarchical pore structure refers to the presence of diverse pore sizes and interconnected channels, providing diverse diffusion pathways for drugs. The presence of larger pores accelerated drug release, while smaller pores act as reservoirs, ensuring a sustained release of the drugs over time.

However, further research is necessary to investigate the effect of the functionalization process and the initial concentration of the functionalized drug on the surface of the biomorphic scaffolds. In addition, to evaluate the potential of the biomorphic scaffold as a bone metastatic niche model, future studies will aim to establish a three-culture experimental model including bone and tumor cells on biomorphic scaffolds. *Ex-vivo* and *in-vivo* investigations of a drug-loaded biomorphic scaffold will be conducted to ensure its effectiveness.

REFERENCES

1. GreenBone Ortho srl. b.bone. Date accessed: 13/10/2023 https://greenbone.it/b-bone.
2. Iaquinta, M. R. *et al.* In Vitro Osteoinductivity Assay of Hydroxylapatite Scaffolds, Obtained with Biomorphic Transformation Processes, Assessed Using Human Adipose Stem Cell Cultures. *Int. J. Mol. Sci.* **22**, (2021).
3. Alt, V., Walter, N., Rupp, M., Begué, T. & Plecko, M. Bone defect filling with a novel rattan-wood based not-sintered hydroxyapatite and beta-tricalcium phosphate material (b.Bone^{TM}) after tricortical bone graft harvesting – A consecutive clinical case series of 9 patients. *Trauma Case Reports* **44**, (2023).
4. Tampieri, A. *et al.* Heterogeneous chemistry in the 3-D state: An original approach to generate bioactive, mechanically-competent bone scaffolds. *Biomater. Sci.* **7**, 307–321 (2019).
5. Degli Esposti, L., Adamiano, A., Siliqi, D., Giannini, C. & Iafisco, M. The effect of chemical structure of carboxylate molecules on hydroxyapatite nanoparticles. A structural and morphological study. *Bioact. Mater.* **6**, 2360–2371 (2021).

SUMMARY AND CONCLUSIONS

This research work was dedicated to the design and development of various types of bioactive porous bioceramic scaffolds, designed for specific applications in bone regeneration, as drug delivery systems, with the aim of future development of new therapies providing effective medical treatment to repair bone tissue damaged by trauma or other pathologies.

Apatitic-based bone scaffolds studied in this research activity, which are particularly promising for diverse applications in bone tissue engineering, have been: -macroporous sintered scaffolds (MSS), -strontium-doped apatitic bone cements obtained both as injectable pastes suitable for in vivo hardening and in form of 3D-printed scaffolds (SrCPC), and -biomorphic scaffolds (GB, *Greenbone Ortho S.p.A.*). Apatitic bone scaffolds were functionalized with different types of drugs ranging from antibiotics (tetracycline) to anti-cancers (doxorubicin, methotrexate, everolimus and denosumab), characterized by different chemical structure and properties. Particularly, the functionalization approach was optimized for each drug-carrier combination, depending on the chemical nature of the drugs and the physico-chemical-structural characteristics of the scaffolds.

A relevant objective of this thesis was to understand the mechanisms regulating the release process from the different scaffolds, which is a fundamental knowledge for the development of medicated devices, to achieve clinically effective drug delivery. This work attempts to correlate the physico-chemical with the structural properties of the scaffold influence the release mechanism by applying the Korsmeyer-Peppas model (a semi-empirical mathematical model that correlates release exponentially with time). The different release mechanism of drugs from each scaffold were found to depend on several factors, including the drug features, the scaffold properties, the physico-chemical interaction between drug and scaffold and the overall experimental setup and condition. The scaffold composition and structure (i.e. in terms of porosity extent, pore size, pore distribution and interconnectivity) are the most important features that may have a major impact on the kinetic release mechanism. In this respect, the scaffolds studied in this thesis are all based on hydroxyapatite, however the different synthesis method yielded 3D constructs featuring substantial differences in terms of chemical composition (particularly ion doping), nanostructure and porosity (summarized in Table XXIX).

Table XXIX. *Composition and porosity features of macroporous sintered scaffold (MSS), strontium-doped apatitic bone cement (SrCPC) and biomorphic scaffold (GB)*

Scaffold	Composition	Porosity degree %	Pore size (µm)
MSS	Crystalline HA	83 ± 1	Average: 218 Modal: 742
SrCPC	Low crystalline CHDA doped with strontium	40 ± 5	40%: 0.01 – 0.1 60%: 0.5 – 1
GB	Crystalline HA and β-TCP doped with magnesium and strontium	60 ± 5	0.01-600

In summary:

- Macroporous sintered scaffolds (MSS) were prepared by direct foaming, a template-free technique that guarantee about 80% of open and interconnected macroporosity. Then, scaffolds were functionalised with tetracycline and coated with cross-linked sodium alginate acting as a diffusive layer to modulate the drug release. The overall results demonstrate the possibility of creating a multilayer sodium alginate can lead to different tetracycline release both in terms of mechanism and drug concentration.
- Strontium-doped apatitic bone cements (SrCPC) were prepared by mixing Sr-αTCP, synthesized by solid-state chemical reaction, and an aqueous solution eventually containing sodium phosphate and sodium alginate. The first part of this work was dedicated to a preliminary study of the hardening process of bone cement, demonstrating that the liquid/solid (L/P) ratio and setting accelerators play a key role in the kinetics of the hydrolysis reaction of αTCP into HA. The second part of the work reports the results obtained from different research on the development of drug delivery systems based on strontium-doped apatitic bone cement. Here, a SrCPC characterized by nano- and sub-microporosity, with bimodal distribution of pores dimensions, were developed. Depending on the clinical need and on the chemistry of different drugs tested the drug loading approach was optimized. One of the most important results suggest that the addition of hydroxyapatite nanoparticles linked to drugs in cement formulation may be an effective approach to the development of tuneable drug delivery bone cement, permitting to tune the release mechanism of tetracycline. All the drug-loaded SrCPC developed in this work have been shown to release drugs at clinically relevant doses, as demonstrated by *in-vitro* tests, resulting in

promising biomaterial for the local treatment of different bone diseases. Moreover, a preliminary study was conducted on the optimization of strontium and magnesium doped HA-based inks for the development of tetracycline-loaded 3D-printed porous bone scaffolds using DWI technology.

- Biomorphic scaffolds (GB) are characterized by bioactive composition (HA and β-TCP both doped with Mg^{2+} and Sr^{2+} ions), by lamellar nanostructure and hierarchic multiscale porosity. Alongside its established biomimicry and biocompatibility, in this research work it was demonstrated that biomorphic scaffolds possess the ability to deliver denosumab or everolimus at clinically significant doses, as demonstrated by *in-vitro* test, thus being promising to promote the regeneration of load-bearing bones and to establish efficient on-site therapies.

The comprehensive results obtained by Korsmeyer-Peppas model are summarized in Figure 101.

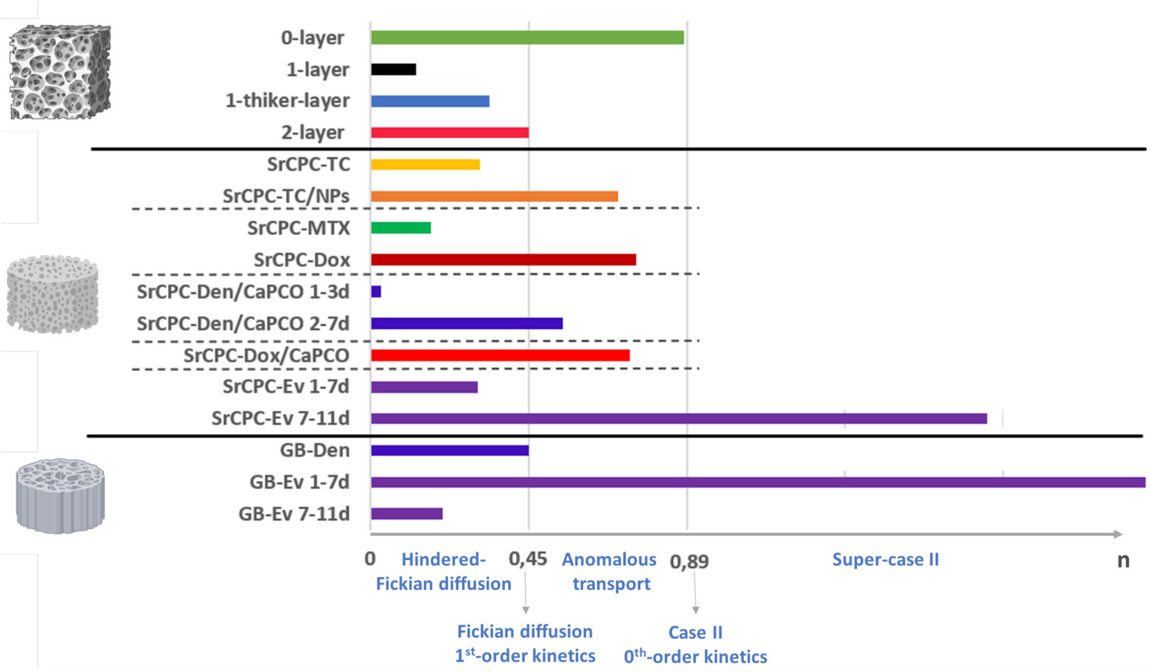

Figure 101. Mechanism calculated for each drug-scaffold: MSS, SrCPC and GB.

Along the differences in experimental set-up and conditions (drug loading amount, approach of drug loading, total volume of the medium, medium replacement), it is possible to draw some general conclusions regarding the importance of bioactive composition, of nanostructure promoting chemically active surface and high specific surface area as well as porosity features (porosity degree, pore size, distribution, and interconnectivity) suitable for osteconduction osteointegration and controlled drug delivery.

The biomorphic scaffold is characterized by bioactive composition, lamellar nanostructure and hierarchic multiscale porosity, all achieved thanks to a synthesis process preventing the use of sintering for final consolidation. These features allowed surface functionalization and long-term drug release without the need to introduce additional diffusive layers. Particularly, the presence of larger pores allows accelerated drug release, while smaller pores act as reservoirs, ensuring sustained release of the drugs over one week. Conversely, MSSs have an interconnected macroporosity but, due to the sintering process used for their consolidation, they exhibit relatively low surface activity preventing strong linking to the drug, thus leading to burst drug release. To slacken and modulate the drug release kinetics, it was necessary to cover the scaffold with a polymeric diffusive layer acting as a barrier extending the diffusion path of the drug. Conversely, SrCPC are characterized by bioactive composition and a diffuse microporosity with random pore distribution, which can increase the diffusion path length for drug molecules, slowing the overall release rate and useful to provide a prolonged therapeutic effect.

In conclusion, the results obtained in this research work can be useful as a proof-of-concept opening to the development of innovative medicated scaffolds for the treatment of bone diseases in different bony districts, once the required drug doses released from the scaffold in different clinical contexts are known.

Certainly, further investigation is required to gain a better understanding of the role of porosity in drug release, as it is a critical factor in the design of tailored bone scaffolds for drug delivery. In this regard, the overall bioactivity, the possibility of introducing drugs into the scaffold matrix rather than functionalising them on the scaffold surface, and the possibility of tailoring the porosity by modulating the L/P and/or adding porogenic agents, make bone cement the ideal scaffold for this study.

PEER-REVIEWED JOURNAL PUBLICATIONS

1. Massimiliano Dapporto, Marta Tavoni, Elisa Restivo, Francesca Carella, Giovanna Bruni, Laura Mercatali, Livia Visai, Anna Tampieri, Michele Iafisco and Simone Sprio. *"Strontium-doped apatitic bone cements with tunable antibacterial and antibiofilm ability."* Frontiers in Bioengineering and Biotechnology: 2297, doi: 10.3389/fbioe.2022.969641
2. Federico Pupilli, Andrea Ruffini, Massimiliano Dapporto, Marta Tavoni, Anna Tampieri, Simone Sprio *"Design Strategies and Biomimetic Approaches for Calcium Phosphate Scaffolds in Bone Tissue Regeneration",* Biomimetics 2022, 7(3), 112; doi: 10.3390/biomimetics7030112
3. Marta Tavoni, Massimiliano Dapporto, Anna Tampieri, Simone Sprio "*Bioactive Calcium Phosphate-Based Composites for Bone Regeneration*" Journal of Composites Science, 2021, 5,227, doi: https://doi.org/10.3390/jcs5090227

MANUSCRIPTS UNDER REVIEW

1. *"Lanzillotti C., Iaquinta M.R., Mosaico M., Patergnani S., Giorgi C., Sprio S., Dapporto M., Tavoni M., Tampieri A., Montesi M., Martini F., Mazzoni E. - Calcium phosphate cements for the treatment of bone tissue affected by osteosarcoma",* Journal of Cellular Physiology.

2. "Campisi S., Folliard V., Tavoni M., Sprio S., Tampieri A., Aurox A., Gervasini A. - *Uncovering the effects of magnesium and strontium incorporation on acid/basic surface features of hydroxyapatites with and without carbonates*", Physical Chemistry Chemical Physics

SCIENTIFIC CONTRIBUTION TO CONGRESS AND SCHOOLS

1. M. Tavoni, M. Dapporto, A. Tampieri, S. Sprio, F. Martini, E. Mazzoni, M. Montesi. *Strontium-doped apatitic scaffolds functionalized for sustained release of anticancer drugs against osteosarcoma.* 24th Conference on Material Science, YUCOMAT 2023 - Herceg Novi - Montenegro, 4-8 September 2023
2. M. Tavoni, M. Dapporto, A. Tampieri, E. Restivo, L. Visai, S. Sprio. *Investigating the physicochemical and antibacterial properties of nanocrystalline hydroxyapatite co-doped with silver and carbonate*. Conference and Exhibition of the European Ceramic Society – Lyon – France, 2-6 July 2023
3. M. Tavoni, M. Dapporto, E. Restivo, F. Carella, G. Bruni, L. Visai, A. Tampieri, M. Iafisco, S. Sprio. *Injectable strontium-doped apatitic bone cements with tunable antibacterial and antibiofilm ability.* Emerging Antimicrobial Biomaterials for Orthopaedic Applications – Zagreb - Croatia, 22,23 February 2023
4. M. Tavoni, M. Dapporto, F. Carella, L. Mercatali, A. De Vita, M. Iafisco, A. Tampieri, S. Sprio, *Toward new therapies for the treatment of bone cancer: calcium phosphate-based cement as tuneable system for Doxorubicin delivery.* 20th Young Researchers' Conference – Belgrade – Serbia, 30 November – 2 December, 2022
5. M. Tavoni, M. Dapporto, F. Carella, L. Mercatali, A. De Vita, M. Iafisco, A. Tampieri, S. Sprio. *New delivery systems made of self-hardening Calcium Phosphates functionalized with drug-loaded apatite nanoparticles*. International Conference: 32nd Meeting of the International Society of Ceramics in Medicine, Bioceramics32– Venezia Mestre – Italy, 20-23 September 2022
6. M. Tavoni, M. Dapporto, A. Tampieri, S. Sprio. *Macroporous hydroxyapatite scaffolds modified for sustained drug delivery*. International Conference: 32nd Meeting of the International Society of Ceramics in Medicine, Bioceramics32– Venezia Mestre – Italy, 20-23 September 2022
7. M. Dapporto, F. Carella, M. Tavoni, L. Degli Esposti, E. Restivo, L. Visai, L. Mercatali, A. Tampieri, M. Iafisco, S. Sprio. *Controlled release of Tetracycline from injectable apatitic*

bone cement. International Conference: 32nd Meeting of the International Society of Ceramics in Medicine, Bioceramics32– Venezia Mestre – Italy, 20-23 September 2022

8. E. Restivo, M. Dapporto, M. Tavoni, F. Carella, G. Bruni, L. Mercatali, A. Tampieri, M. Iafisco, S. Sprio, L. Visai. *Promising strontium-doped apatitic bone cement for the treatment of bacterial infection*. International Conference: 32nd Meeting of the International Society of Ceramics in Medicine, Bioceramics32– Venezia Mestre – Italy, 20-23 September 2022
9. M. Tavoni, M. Dapporto, F. Carella, E. Restivo, L. Visai, L. Mercatali, T. Ibrahim, A. Tampieri, M. Iafisco, S. Sprio. *Apatitic bone cements with effective antibacterial and antibiofilm effect*. 31st Conference of the European Society for Biomaterials (ESB2021) – Porto – Portugal, 5-9 September 2021
10. M. Tavoni, F. Carella, M. Dapporto, C. Cocchi, A. De Vita, A. Tampieri, M. Iafisco, S. Sprio. *Doxorubicin-loaded hydroxyapatite nanoparticles as trigger for anticancer bone cement*. 31st Conference of the European Society for Biomaterials (ESB2021) – Porto – Portugal, 5-9 September 2021
11. M. Tavoni, M. Dapporto, F. Carella, E. Restivo, L. Visai, L. Mercatali, T. Ibrahim, A. Tampieri, M. Iafisco, S. Sprio. *Apatitic bone cements with effective drug release: from antibacterial and antibiofilm ability to anticancer therapy*. Congresso Nazionale Biomateriali 2021 (SIB2021) – Lecce – Italy, 11-14 July 2021
12. M. Tavoni, E. Campodoni, M. Dapporto, A. Ruffini, C. Cocchi, A. De Vita, T. Ibrahim, L. Mercatali, M. Sandri, S. Sprio, A. Tampieri, M. Montesi. *Nanostructured medicated scaffolds for the local treatment of bone metastasis.* Congresso Nazionale Biomateriali 2021 (SIB2021) – Lecce – Italy, 11-14 July 2021

ACKNOWLEDGEMENTS

Funding:

The Author is grateful to the following funding agencies:

- *Italian Ministry of Health* for the project: *Progetto Nazionale Finalizzato - GR-2016-02364704*, BIOBOS: “An in vitro and ex vivo model of biomimetic regenerative devices to treat bone metastases and soft tissue tumours”.
- *Regione Emilia Romagna* for the project: *Progetto POR-FESR 2014-2020 - PG/2018/632022, DINAMICA: “*Development and validation of nanostructured medicated biomaterials for the treatment and regeneration of metastatic bone tissue”.
- *Italian Ministry of University and Research (MUR)* for the project: *Progetto Nazionale PRIN – 017 C8RYSS*, RE-GROWTH: “Osteosarcoma and mesenchymal stem cells to assay innovative materials, bioactive injectable bone cements, with drug delivery ability, to contrast spine tumour recurrence and to enhance healthy bone regrowth”.

Scientific contribution

The Author is grateful to the following researchers:

- Elisa Restivo of Molecular Medicine Department, Center for Health Technologies, UdR INSTM of University of Pavia, Prof. Giovanna Bruni of Department of Chemistry, Physical Chemistry Section, Center for Colloid and Surfaces Science, University of Pavia, and Prof. Livia Visai of Medicina Clinica-Specialistica, UOR5 Laboratorio di Nanotecnologie, ICS Maugeri, IRCCS, for the microbiological evaluations of SrCPC-TC and SrCPC-TC/NPs.
- Dr. Carmen Lanzillotti, Dr. Maria Rosa Iaquinta, Dr. Raffaella De Pace and Dr. Maria Mosaico a of Laboratories of Cell Biology and Molecular Genetics, Department of Medical Sciences, University of Ferrara, Dr. Simone Patergnani and Dr. Carlotta Giorgi of Laboratories of Cell Signalling, Department of Medical Sciences, University of Ferrara, Dr. Martini Fernanda of Technological Laboratory for Advanced Therapy

(LTTA), University of Ferrara, and Dr. Elisa Mazzoni of Department of Chemical, Pharmaceutical and Agricultural Sciences, University of Ferrara, for the *in vitro* test of SrCPC-MTX and SrCPC-Dox.

- Dr. Laurea Mercatali, Claudia Cocchi, Dr. Tony Ibrahim and Dr. Alessandro De Vita from Istituto Romagnolo per lo Studio dei Tumori "Dino Amadori" IRCCS, Meldola, Italy, for the *in-vitro* test of SrCPC-DenC/CaPCO, SrCPC-Dox/CaPCO, SrCPC-Ev and on GB.
- Dr. Anna Diez-Escudero and Prof. Maria-Pau Ginebra of Biomaterials, Biomechanics and Tissue Engineering Group, Department of Materials Science and Metallurgical Engineering, Technical University of Catalonia (UPC) for supervising the research on 3D-printed scaffold.
- Dr. Elisabetta Campodoni, Dr. Massimiliano Dapporto, Dr. Francesca Carella, Federico Pupilli, Cesare Melandri and Andreana Piancastrelli of the Institute of Science, Technology and Sustainability for Ceramics, National Research Council, for materials characterizations.